EXPERIMENTAL AND THREE DIMENSIONAL NUMERICAL ANALYSIS OF CYLINDRICAL SOLAR COOLING ADSORBENT BEDS WITH CIRCULAR HEAT EXCHANGE COILS

A THESIS SUBMITTED TO
THE GRADUATE SCHOOL OF NATURAL AND APPLIED SCIENCES
OF
MIDDLE EAST TECHNICAL UNIVERSITY

BY

ARİF CEM GÖZÜKARA

IN PARTIAL FULFILLMENT OF THE REQUIREMENTS
FOR
THE DEGREE OF DOCTOR OF PHILOSOPHY
IN
MECHANICAL ENGINEERING

FEBRUARY 2016

Approval of the thesis:

EXPERIMENTAL AND THREE DIMENSIONAL NUMERICAL ANALYSIS OF CYLINDRICAL SOLAR COOLING ADSORBENT BEDS WITH CIRCULAR HEAT EXCHANGE COILS

submitted by **ARİF CEM GÖZÜKARA** in partial fulfillment of the requirements for the degree of **Doctor of Philosophy in Mechanical Engineering Department, Middle East Technical University by,**

Prof. Dr. Gülbin Dural Ünver
Dean, Graduate School of **Natural and Applied Sciences** _____

Prof. Dr. Tuna Balkan
Head of Department, **Mechanical Engineering** _____

Assoc.Prof. Dr. Cemil Yamalı
Supervisor, **Mechanical Engineering Dept., METU** _____

Examining Committee Members:

Assoc.Prof. Dr. Ahmet Yozgatlıgil
Mechanical Engineering Dept., METU _____

Assoc.Prof. Dr. Cemil Yamalı
Mechanical Engineering Dept., METU _____

Prof. Dr. Mecit Sivrioğlu
Mechanical Engineering Dept., Gazi University _____

Prof. Dr. Derek K. Baker
Mechanical Engineering Dept., METU _____

Prof. Dr. Atilla Bıyıkoğlu
Mechanical Engineering Dept., Gazi University _____

Date: **05.02.2016**

I hereby declare that all information in this document has been obtained and presented in accordance with academic rules and ethical conduct. I also declare that, as required by these rules and conduct, I have full cited and referenced all material and results that are not original to this work.

Name, Last name : Arif Cem GÖZÜKARA
Signature :

ABSTRACT

EXPERIMENTAL AND THREE DIMENSIONAL NUMERICAL ANALYSIS OF CYLINDRICAL SOLAR COOLING ADSORBENT BEDS WITH CIRCULAR HEAT EXCHANGE COILS

Gözükara, Arif Cem
PhD., Department of Mechanical Engineering
Supervisor: Assoc. Prof. Dr. Cemil Yamalı

February 2016, 382 pages

In this study three dimensional cylindrical adsorbent bed designs with circular heat transfer fluid paths had been investigated numerically and experimentally. Three dimensional high fidelity numerical coupled heat and mass transfer analyses of the proposed design alternatives are performed. Numerical analysis results are compared with the results of experiments using the temperature distributions within the adsorbent bed. In addition to geometric design features, effects of initial adsorption capacity, heat transfer fluid flow rate and inlet temperature are also investigated. In the numerical analyses both local thermal equilibrium and local thermal non-equilibrium approaches are used in comparison for modeling the heat and mass transfer within the bed. The results of experimental and numerical analyses are used for evaluating the heat recovery effectiveness of adsorbent beds. The maximum value of the axial temperature gradients within the bed is used as a measure of heat recovery effectiveness. Results had shown that reduced initial adsorption capacity, increased Heat Transfer Fluid (HTF) inlet temperature and flow rate increases the maximum value of the axial temperature gradients within the bed thus the heat recovery efficiency for same duration of operation.

Additionally, effect of non-adsorbing (condensing) gas existence in the adsorption cooling system, had been discussed based on the two dimensional axisymmetric numerical analyses. Under the conditions analyzed, it had been shown that existence of non-condensing gas in the system had been significantly affects the temperature and adsorption capacity distribution within the bed during adsorption process. Whereas, its effect is less emphasized during desorption process.

Keywords: Adsorption, Adsorbent bed, Numerical modeling, Experimental study

ÖZ

GÜNEŞ ENERJİSİ İLE SOĞUTMADA KULLANILAN DAİRESEL ISI DEĞİŞTİRİCİLİ SİLİNDİRİK ADSORPSİYONLU YATAKLARIN DENEYSEL VE ÜÇ BOYUTLU SAYISAL OLARAK İNCELENMESİ

Gözükara, Arif Cem
Doktora, Makine Mühendisliği Bölümü
Tez yöneticisi: Doç.Dr. Cemil Yamalı

Şubat 2016, 382 sayfa

Mevcut çalışmada dairesel ısı transfer akışkanı yollarına sahip farklı üç boyutlu silindirik yatak tasarımları hem deneysel hem de sayısal olarak incelenmiştir. Bu kapsamdan üç boyutta, yüksek çözünürlükle, kütle ve ısı transferinin birlikte çözüldüğü gerçekleştirilmiş sayısal analizler sonlu elemanlar yöntemi kullanılarak gerçekleştirilmiştir. Bu analizlerden elde edilen yatak içi sıcaklık değerleri, deneysel çalışmadan elde edilen sonuçlarla karşılaştırılmıştır. Çalışmada farklı yatak tasarımlarının yanı sıra başlangıç yatak adsorpsiyon kapasitesi, ısı transfer akışkanı debisinin ve giriş sıcaklığının etkileri de incelenmiştir. Sayısal analizlerde ısı ve kütle transferi, hem gaz fazı ve katı fazı arasında lokal ısıl dengenin olduğu hem de bu fazlar arasında lokal ısıl dengenin olmadığı durum kabulleri yapılarak modellenmiştir. Bu iki farklı kabul ile gerçekleştirilen sayısal analiz çalışmalarının sonuçları karşılaştırmalı olarak verilmiştir. Deneysel çalışma ve sayısal analizlerden elde edilen sonuçlar yatağın ısı geri kazanım etkinliğini değerlendirilmesinde kullanılmıştır. Isı geri kazanım değerlendirmesinde yatak içerisindeki eksenel sıcaklık gradyanının en yüksek değeri ölçüt olarak olarak kullanılmıştır. Sonuçlara

bakıldığında, başlangıç adsorpsiyon kapasitesindeki düşüşün, ısı transfer akışkanı debisi ve giriş sıcaklığındaki artışın, yatak içerisindeki eksenel sıcaklık gradyan en yüksek değerlerini artırdığı, dolayısıyla aynı çalışma süresinde yatağın ısı geri kazanım etkinliğinde artışa neden olduğu gözlenmiştir.

Ayrıca sistemde adsorbe edilemeyen bir gaz olması durumu da iki boyutlu eksenel simetrik model üzerinde sayısal analizler ile incelenmiştir. Analiz edilen şartlar altında, sistemde adsorbe edilemeyen bir gazın bulunması durumunun, adsorpsiyon işlemi esnasında yatak içerisindeki sıcaklık ve adsorpsiyon kapasitesi dağılımlarını desorpsiyon işlemine göre daha fazla etkilediği görülmüştür.

Anahtar kelimeler: Adsorpsiyon, Adsorban yatak, Sayısal modelleme, Deneysel çalışma

to my family **…**

ACKNOWLEDGEMENTS

I would like to express my sincere appreciation to my co-supervisor, Assoc.Prof. Dr. Cemil YAMALI for his boundless support, excellent supervision and endless patience in addition to invaluable comments and contributions.

I also would like to thank Prof. Dr. Mecit SİVRİOĞLU and Assoc. Prof. Dr. Ahmet YOZGATLIGİL for their guidance as members of thesis progress committee.

I would like to thank Prof. Dr. Derek K. BAKER for guidance and valuable comments in addition to his efforts on detailed proofreading.

I would like to express my special thanks to Dr.Güvenç CANBALOĞLU his continuous moral support, invaluable advices and efforts during the establishment and maintenance of the experimental setup.

I would like to express my special thanks to my colleague Argün KATIRCI for sharing his experiences about experimenting and his valuable guidance about measurement equipment and methods.

I am thankful to my superior Dr. Ali Mürteza ÇOLAKOĞLU for his support, encouragement and mentoring throughout my professional life and for my study.

I would like to state my thanks to Mustafa YALÇIN for his intense efforts during the construction and operation of the experimental setup.

I would like to state my thanks to Asst. Prof. Dr. Murat BARIŞIK for his technical support, helpful advice and friendship.

Also I would like to thank my managers Dr. İhsan Özsoy and Sabri Çetin for their support throughout this work.

I would like to thank to my colleagues Dr.Berkan ERDOĞMUŞ and Dr.Mustafa OCAK for their support and helpful advice.

I would like to thank to Uğur Selim GENÇOĞLU, for his helps on the illustrations and recommendation on visual aspects of the manuscript.

Also I would like to thank to ASELSAN Inc. for supporting my research activities.
I would like to thank to my father, Yılmaz GÖZÜKARA beyond his support and encourage, for his meticulous efforts on constructing the heat transfer fluid piping of the experimental test setup.
I owe a sincere appreciation to my ancestors, who had survived through misery, poverty and wars, for the inspiration to overcome the difficulties that I had came across.

I wish to express my deepest gratitude to my family who had endlessly and unconditionally supported me throughout my life. Especially I would like to state my sincere appreciation to my grandmother for her endless love, encouragement, and support. Unfortunately, words would be inconclusive to express my feelings toward my family.

TABLE OF CONTENTS

LIST OF TABLES

TABLES

LIST OF FIGURES

FIGURES

LIST OF SYMBOLS

SYMBOLS

c_p	specific heat at constant pressure, J/kg-K
COP	coefficient of performance
SCP	specific cooling power
D_o	reference diffusivity, m^2/s
D_m	mass diffusion coefficient, m^2/s
$\dot{E}$	energy, kJ
E_a	activation energy of surface diffusion, J/mol
h	specific enthalpy, kJ/kg
h_{tg}	convective heat transfer coefficient between tube and fluid, W/m^2K
HTF	heat transfer fluid
HTT	heat transfer tube
Q_{ad}	heat of adsorption, kJ/kg
ΔH_{ad}	heat of adsorption, kJ/kg
k	thermal conductivity, W/m-K
k_m	internal mass transfer coefficient, 1/s
P	pressure, Pa
q	heat transfer, W
R	universal gas constant, J/mol-K
t	time, s
T	temperature, K
u	specific internal energy, kJ/kg
u	vapor velocity vector, m/s
X	adsorption capacity, $kg_{water}/kg_{adsorbent}$
V	velocity, m/s
V	volume, m^3

Greek Symbols

ε	porosity
κ	permeability, m^2
μ	dynamic viscosity, kg/m-s
ρ	density, kg/m^3
ω	mass fraction

Subscripts

a	air
h	high
l	low
eq	equivalent
e	equilibrium
eff	effective
f	fluid, HTF
s	(solid) adsorbent
g	gas
v	vapor
l	liquid
sat	saturation
t	tube

CHAPTER 1

INTRODUCTION

The global economic growth and increase in population together with the prosperity levels, emerges a dramatic increase in the energy demands. The data provided by U.S Energy Information Administration [137] shows that the world total primary annual energy consumption had been increased 31 % from 2000 to 2012, while the portion of energy production based on renewable sources is increased 0.6 %. The 41 % of the primary energy had been consumed by the buildings in 2010, according to the data provided by Lior [138]. The one third of the energy consumption in buildings in the U.S reported to be caused by the Heating Ventilating and Air Conditioning (HVAC) systems and as an insight, the ratio of energy consumption based on HVAC systems is going to be increased with increasing life standard around the world [139]. Today conventionally the cooling and refrigeration technologies are mainly based on the vapor compression cycles which are powered by electricity and according to the data of International Institute of Refrigeration in Paris, 15 % of the global electricity had been consumed for the various kinds of refrigeration and air conditioning purposes [112].

Based on the provided information it could be inferred that the energy consumption in the form of electricity will tend to increase more rapidly than the increase in the amount of energy governed from the sustainable sources. As a consequence, to provide the demanded energy in the future, more fossil fuels will be consumed which will raise environmental pollution and related unwanted effects.

The conventional vapor compression cooling and refrigeration systems are solely depending on the electric energy which reduces the overall efficiency of such systems. In addition to the inefficient energy utilization as a result of electricity dependence, the traditional vapor compression cooling and refrigeration cycles uses refrigerants which have potential for ozone depletion. Regarding these environmental aspects conventional cooling and refrigeration systems could become a major category that augments the global warming potential.

The concerns mentioned above, impelled the researchers to develop and implement more environmentally friendly and energy efficient systems for cooling and refrigeration, besides the improvement of conventional vapor compression cooling and refrigeration systems [80]. One of the main area of focus of the researchers in the last decade is the thermally driven cooling and refrigeration systems which are capable of direct utilization of thermal energy sources. The thermal energy that will be used by the system can be obtained from, industrial waste heat, fossil fuel combustion, solar and geothermal sources [140].

Being a globally available heat source regardless of urbanization and owing to the fact that the peak times of demand for cooling and refrigeration coincide with the solar radiation availability [112] solar thermal driven systems become one of the outstanding alternative among the others. The researchers are more interested in the sorption technologies for direct utilization of low grade thermal energy sources in cold production. Therefore most of the recent studies involved in solar thermal energy driven cooling and refrigeration systems are based on the sorption phenomena.

Sorption is a common general name used for adsorption and absorption phenomena together. The absorption is a sorption process which involves diffusion of distinct materials into each other and interacting chemically to form a solution. The absorption process can be characterized by the volumetric chemical interaction

between two different materials. On the other hand, adsorption is a surface phenomenon which can be defined as accumulation of one substance on the others surface as a result of unbalanced surface forces at the interface of two substances.

In the sorption based cooling and refrigeration systems, physical or chemical attraction between two substances are used to obtain a cooling effect. The substance which adsorbs or absorbs the other can be named as sorbent (adsorbent or absorbent according to the process) generally while the substance which is adsorbed or absorbed can be called as refrigerant or sorbate (adsorbate or absorbate according to the process). In absorption processes the absorbent can be solid or liquid and in the adsorption processes adsorbent is generally in solid phase. Therefore in some cases adsorption is also called as solid-sorption.

As stated previously in the absorption process, sorbent absorbs the refrigerant going through a volumetric interaction which results in chemical and/or physical changes. Whereas during the adsorption process, refrigerant molecules are bonded on the the adsorbent surface by means of chemical and/or physical forces but, the adsorbent does not goes through a chemical nor physical change during this process.

Both absorption and adsorption based refrigeration and cooling systems have their own advantages and disadvantages. However, the advantages of adsorption based systems over absorption based systems make their usage more suitable for various kinds of applications in different fields.

The advantages of adsorption based cooling and refrigeration systems compared to the absorption based systems can be summed up as follows.

Thermal sources with wide range of temperatures can be used for powering adsorption based systems. The temperature of the heat source that may be utilized by a adsorption cooling system can be as low as 50 ^{o}C or can be as high as 500 ^{o}C. The

thermal source temperature should be 70^{o}C at minimum for the absorption systems and operating temperatures over 200 ^{o}C will cause severe corrosion problems in these systems [15]. Based on the qualitative and quantitative comparisons made between a LiBr-H_2O absorption cooling system and a silica gel-water adsorption system, it had been reported that for low temperature, low grade thermal energy utilization silica-gel water adsorption cooling system is more suitable option [140].

The adsorption based systems are suitable to operate under dense vibration conditions which can be observed in air, land and sea vehicles. However, in absorption systems absorbent may be displaced in the system undesirably since it is in fluid phase. The flow of absorbent from evaporator to generator or condenser to absorber will result in malfunctioning of the system [15].

The adsorption based systems are relatively simpler and does not require auxiliary systems like absorption based cooling and refrigeration systems do [15].Additionally the adsorption based cooling systems do not suffer from crystallization and distillation which is common for the absorption based cooling and refrigeration systems [80].

The wide operating temperature range, stability, reliability and inherently safe nature of the adsorption cooling systems makes them a promising environmentally friendly alternative for the conventional vapor compression cooling and refrigeration systems. Therefore in the last decades researchers are interested in development and implementation of adsorption based cooling and refrigeration systems which may replace the conventional systems, in terms of performance, reliability and cost [80].

Beneath their environmental friendly nature, the adsorption cooling systems are still far from being a feasible alternative for the conventional vapor compression based cooling and refrigeration cycles. The adsorption cooling systems still needed to be improved in terms of cooling capacity and cost efficiency. Basically the low Specific

Cooling Power (SCP) and low Coefficient of Performance (COP) values are the most significant disadvantages of the adsorption cooling systems [80]. Therefore many ongoing research activities are focused on eliminating these disadvantages and to make adsorption based cooling systems a comparable alternative for the conventional systems. These activities can be summarized as analytical, numerical and experimental investigations based on new cycle and system designs, adsorbent bed designs, development of new synthetic adsorbents. The details of the research activities related with the adsorption cooling systems will be given in detail in the following sections.

1.1 Basics of Adsorption

The process of adsorption is taking place at the interface of two different phases and involves separation of molecules of one phase due to its accumulation or concentration at the surface of other as a result of unbalanced surface forces at the phase boundary [1, 17].

As stated earlier in the process of adsorption physical and/or chemical forces are involved. The types of adsorption processes can be further classified according to the forces involved in the process. In the physical adsorption the mechanism which binds the molecules of adsorbate on the adsorbent is van der Waals forces [15]. In the adsorbents with mesopores the accumulation of adsorbate will be in form of layers one top of another and in the adsorbents with micropores, adsorbate fills the micropores [15]. As a result of relatively weak intermolecular forces between adsorbate and adsorbent, physical adsorption is easier to revert. Since the adsorbent and adsorbate does not interact chemically, they preserve their original state while undergoing adsorption process.

On the other hand, in chemical adsorption the first layer of accumulated adsorbate reacts with the adsorbent. As a result of chemical bonds, electron transfer atom

rearrangement, the adsorbent do not preserve its initial state after undergoing a chemical adsorption process. Since relatively strong chemical forces are involved in the chemical adsorption, reversion of this process is relatively more difficult. Therefore in the adsorption cooling and refrigeration systems, physical adsorption phenomenon is more favorable and preferred. The adsorbents that are generally used in physical adsorption process can be listed as, activated carbon and activated carbon fiber, silica gel and zeolite. Activated carbon and activated carbon fibers can be made from coal, wood, organic substances such as bone, coconut shell etc. [15]. The specific surface area and heat transfer performance of activated carbon fiber is higher than the activated carbon however the anisotropic nature of the fiber makes it a less favorable alternative [115]. Silica gel is an amorphous synthetic material that can be used when high capacity is required at moderate pressures and low temperatures. Silica gels are classified according to the pore size and named as Type A, B and C. Type A has a micro pore size of approximately 2.5 nm and can be used for all desiccation conditions regardless of the relative humidity [15]. Zeolites are the porous alumina silicates which are naturally formed and can be formed as a result of artificially by synthesis. There are about 40 different type of natural zeolite while 150 different synthetic types are exists. The artificially synthesized zeolites are more expensive than the natural ones however they have superior heat transfer characteristics and more stable structure [65]. Therefore in the adsorption cooling systems synthetic zeolites are preferred and used generally. The types of zeolites that are common for these applications can be named as 4A, 5A, 10 X, 13X. In addition to these adsorbents, researchers are also working on composite adsorbents obtained by, mixing, and impregnation and consolidation methods. The details of the composite adsorbents can be found in the following sections.

In addition to the adsorbent, another important contributor of the adsorption phenomena is the adsorbate (refrigerant). Among the all possible adsorbent-adsorbate pairs the ones that are most commonly used in adsorption cooling and refrigeration applications can be listed as, ammonia, methanol, ethanol and water.

Ammonia is called as positive pressure refrigerant since it has a boiling point of 10 ^{o}C at the 1 atm pressure [15]. On the other hand being a highly toxic fluid is the main disadvantage of ammonia. Most common application is to use ammonia with activated carbon in adsorption cooling systems. Ethanol and methanol are similar refrigerants in terms of saturation pressure and flammability characters. Since these refrigerants have a freezing point lower than 0^{o}C, they are mostly used in the adsorption based ice makers. The main disadvantage of ethanol and methanol is the low latent heat of evaporation compared to water and ammonia. Water is one of the most favorable refrigerants when environmental and health aspects are considered. Additionally the latent heat of evaporation of water is two times higher than methanol. Unfortunately by using the water as refrigerant it is not possible to obtain refrigeration temperatures below 0^{o}C. Moreover the extremely low saturation pressure requirement for obtaining low temperatures is another disadvantage of water as a refrigerant. Water is usually used with silica gel and zeolite as a refrigerant.

One other important concept related with the adsorption and the working pairs is the adsorption equilibrium. Adsorption equilibrium is used in various state equations which are also known as isotherms of adsorption and there are several approaches which had been proposed for defining the equilibrium adsorption capacity. All of these approaches aim to express and define the equilibrium adsorption capacity of adsorbent adsorbate pairs in a global manner; however the approach should be chosen specifically according to the adsorbent-adsorbate pairs and operation conditions. Some of the basic approaches that are used for defining equilibrium adsorption capacity are Henry's Law, Langmuir's approach, Brauner, Emmet and Teller (BET), Gibbs' theory and adsorption potential theory.

The most popular equations that are applicable for physical adsorption of gases and vapors on microporous solids are the ones based on the adsorption potential theory. Since these equations proved their capability in correlating large amount of data they had been widely used for defining the adsorption capacity [116]. Some of the well-

known equations are Dubinin-Radushkevich (DR) and Dubinin-Ashtakov (DA). Also there are many variants of these equations, but as mentioned earlier each equation has its own strengths and weaknesses according to the application.

The equilibrium adsorption capacity is usually expressed as the ratio of mass of adsorbed phase to mass of adsorbent. The adsorption capacity will be denoted by letter *x* in this text.

Equilibrium adsorption capacity of an adsorbent-adsorbate pair is a function of pressure and temperature. The adsorption capacity definitions are specific to the adsorbent-adsorbate pairs; additionally it differs for the adsorbents of different manufacturers. Therefore most accurate equilibrium adsorption capacity definition for a pair can be obtained by the experimental results. The experimental determination of the equilibrium adsorption capacity correlations can be made with the measurements of saturation pressure the temperature of the adsorbent together with the adsorbed amount.

The adsorbed mass ratio, saturation pressure and the temperature of the adsorbent recorded at different adsorbent loading conditions by changing the adsorbent temperature and the saturation pressure. The experiments are generally repeated for adsorption and desorption processes to include the effect of hysteresis on the average equilibrium adsorption capacity definition. After obtaining a data set of adsorbed amount mass ratio, adsorbent temperature and the corresponding saturation temperature it is possible to correlate it with the equilibrium adsorption capacity of the working pair. DA equations are one of the forms that can be used for correlation of the experimentally obtained data. The general form of DA equation can be expressed as follows [17],

$$X = X_0 \exp(-\mathrm{kA}) \tag{1.1}$$

Where the A in Equation 1.1 can be written as,

$$A = \left(\frac{T_{ad}}{T_{sat}} - 1\right)^{n} \tag{1.2}$$

The parameters used for fitting experimental data to DA equation are the X_0, k and n.

As stated earlier the equilibrium adsorption capacity of an adsorbent-adsorbate pair is specific to the manufacturer of the adsorbent. The isotherms of the adsorbent that will be used in this study had been experimentally determined by Solmuş [17] and expressed in form of modified DA equation. Therefore the definition given there will be used without alteration.

Another concept that is related with the adsorption phenomenon is the heat of adsorption. During the adsorption process the free adsorbate molecules gathered in more ordered structure when they are adsorbed. This decrease in entropy is the underlying reason for the exothermic characteristic of adsorption process [65]. In adsorption processes the heat release may be %30-100 higher than the heat released due to condensation of adsorbate [1,4]. The heat released in the adsorption process could be determined by using adsorption isotherms or experimental methods that utilizes calorimetry.

For the theoretical methodology there are three different definitions exist for the released heat during adsorption. The first one is the integral heat of adsorption, which describes the total heat released between two states of adsorbate loading under constant temperature. The second one is the differential heat of adsorption which describes the heat released under incremental adsorbate loading condition. The third one is the isosteric heat of adsorption. Since the isosteric process, leads to a process under constant loading the isosteric heat of adsorption can be determined with the help of adsorption isotherms and Clausius-Clapeyron relationship [87, 17].

Clasisus-Clapeyron equation basically relates the change in enthalpy with the entropy change during adsorption process. The change in enthalpy under isosteric (constant loading) conditions also named as the isosteric heat of adsorption and denoted as Q_{ad}. The isosteric heat of adsorption can be expressed in terms of temperature and pressure as follows,

$$Q_{ad} = -R\left(\frac{d\ lnP}{d\left(\frac{1}{T}\right)}\right)_X \tag{1.3}$$

As can be seen from the Equation 1.3, the isosteric heat of adsorption is equal to the slope of curve connecting constant adsorption capacity points of the isotherms on a *lnP* vs *1/T* graph, multiplied by the universal gas constant [17,15].

1.2 Adsorption Cooling and Refrigeration Cycle

The adsorption cooling and refrigeration cycles are based on the adsorption phenomenon to obtain net cooling effect by utilizing heat energy.Basic adsorption cycle is composed of four thermodynamic steps. These four steps are generally demonstrated on a Clapeyron diagram (*lnP* vs *-1/T*).However a schematic representation of a basic adsorption cycle will help to understand the steps of an adsorption cooling cycle. Basic adsorption cooling system could be defined as two linked vessels. The schematic representation working principle of a simple adsorption cooling system can be seen in Figure 1[20]. One of the vessels seen in the figure contains the adsorbent media (the vessel on the left hand side in the Figure) and the other is containing adsorbate (the vessel on the left hand side in the Figure). The vessel containing the adsorbent will be named as adsorbent vessel and the other vessel will be named as condenser/evaporator.

Initially both adsorbent and adsorbate is at low pressure and low temperature. The first step of the adsorption cooling cycle, adsorbent side is heated which causes the

increase of temperature and the pressure of the system. The heating process continues until the pressure of system reaches the pressure that is corresponding to the pressure of saturation at a predetermined temperature. This temperature is the condensation temperature; at which adsorbed refrigerant will condensate in the condenser/evaporator. During the first step the adsorbed amount in the adsorbent vessel is constant therefore; the first step is called as isosteric heating step. In the second step the heating continues on the adsorbent vessel while condensation is taking place in the condenser/evaporator vessel by rejecting heat from the system. At this step the system pressure is constant but the adsorbent loading starts to decrease due to discharge to the condenser. The second step is called as isobaric heating or the desorption step. Desorption is the reverse of the adsorption process. The third step of the cycle is the isosteric cooling step. In this step the adsorbate loading in the adsorbent vessel is constant but the pressure and temperature of the adsorbent vessel decreases as a result of heat rejection from the adsorbent vessel. This step can be named as isosteric cooling step. The adsorbent vessel is cooled down so that the pressure of the system reduces to evaporation pressure. After the reduction of pressure to the evaporation pressure of the adsorbate in the condenser/evaporator vessel, adsorbate in liquid form, starts evaporate. During the evaporation of adsorbate, the pressure of the system is constant. The temperature of the condenser/evaporator vessel temperature decreases due to evaporation. On the other hand heat should be rejected from the adsorbent vessel to facilitate the continuation of adsorption, since adsorption is an exothermic process. The cycle is completed at the end fourth step where temperature and pressure of the adsorbent is low.

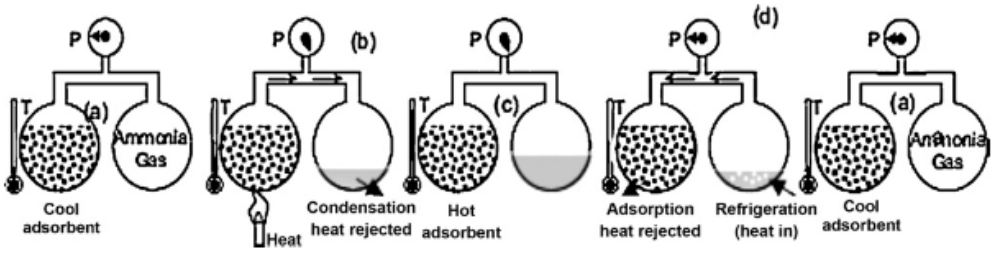

Figure 1.1 Schematic representation of adsorption cooling system working principle [20]

The process can also be demonstrated on a Clapeyron diagram. The Clapeyron diagram for an ideal adsorption cooling and refrigeration cycle can be seen in Figure 1.2. As described above, basic, ideal adsorption cycle is composed of four main steps.

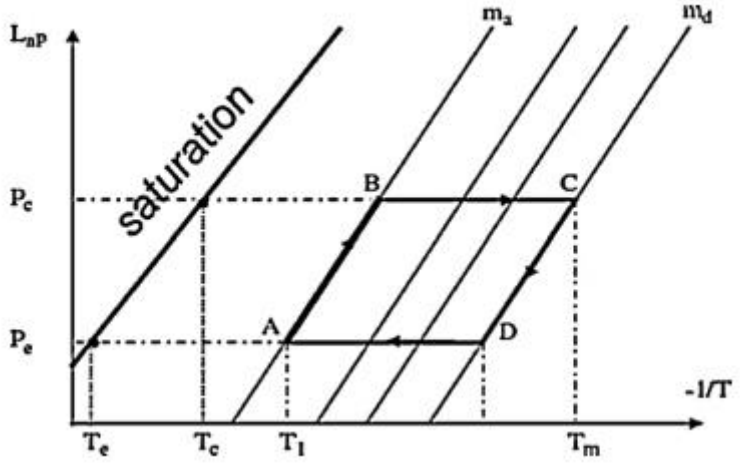

Figure 1.2 The Clapeyron diagram of an ideal basic adsorption cycle [20]

In the beginning of the cycle adsorbent is at low temperature T_l and low pressure (P_e, evaporation pressure). The cycle starts at point A. The first step is the isosteric heating step; the adsorbent is heated while the loading is constant. During the heating step from A to B, the adsorbed amount in the adsorbent bed is constant and heating continues until the pressure of the adsorbent reaches the condensation pressure P_c.

Upon completion of the isosteric heating step, heat addition to the adsorbent bed continues. However from point B to C the pressure of the adsorbent is constant due to condensation taking place in the condenser which is connected to the adsorbent bed. The adsorbed amount starts to reduce as the heat added to the adsorbent bed. The heat is rejected from the condenser for keeping the condensation pressure constant. The step from B to C can be called as isobaric heating or desorption step. Desorption step continues until desired amount of adsorbate is desorbed and condensed at the condenser. At the end of desorption step, the system is at high pressure (P_c) and at high temperature (T_m). The next step will be the isosteric cooling step which is required for reducing the pressure of the adsorbent bed to evaporation pressure P_e. From poing C to point D, the adsorbent bed is cooled by rejecting heat. During this step the system adsorbed amount is kept constant by disconnecting adsorbent bed from condenser. At the end of isosteric cooling step, when adsorbent bed pressure lowers to evaporator pressure P_e, the adsorbent bed will be connected to evaporator.upon connecting the evaporator, adsorbent bed starts to adsorb refrigerant which is in liquid phase and produce a cooling effect by receiving heat from cooling space. The adsorbent temperature further reduced by releasing heat during the adsorption process. The cooling of adsorbent bed facilitates the continuation of adsorption process. The adsorption will be ceased if the pressure of the adsorbent bed increases. Therefore the temperature of the adsorbent bed should be lowered from point D to A to keep the adsorption pressure constant while the adsorbed amount is increasing. The cycle is completed when the adsorbent bed reaches its initial point, point A.

The efficiency of a cooling or refrigeration system is generally defined as the ratio of its capacity of removing heat from a cooling space to energy supplied to this system for maintaining its operation [86]. This ratio is called as the Coefficient of Performance (COP) of a cooling and refrigeraiton cycle. The thermal COP definition can be written as,

$$COP_C = \frac{cooling\ energy\ (energy\ removed)}{energy\ receieved\ by\ the\ system} \quad (1.1)$$

Specific to adsorption based cooling systems; the heat energy supplied to the system will be equal to the sum of heat used in isosteric heating and the regeneration (desorption-isobaric heating) phases of the cycle. Referring to the Clapeyron diagram given in Figure 1.2, the heat supplied from point A to point C is the energy received by an adsorption cooling and refrigeration system. The heat received by the cold space is equal to the latent heat of evaporation multiplied by the amount of evaporated refrigerant. The amount of evaporated refrigerant is equal to the mass of adsorbed refrigerant in the cycle. With the light of this information the COP for an adsorption cooling system can be decomposed into its components and expressed as,

$$COP = \frac{Q_c}{Q_{in}} = \frac{L\Delta m_{adsorbed}}{m_{desorbed}\Delta H + \sum m_{system} c_p \Delta T} \quad (1.2)$$

The heat received by the system will be utilized for desorption of the adsorbed phase and the preheating and pressurization of the desorbing bed to condensation pressure. The heat required for preheating or the isosteric heating stage can be called as the sensible heat consumption. The sensible heat of the system is the second term in the denominator of the COP definition given in Equation 1.2. It can be seen from Equation 1.2 that the COP value can be increased by reducing the sensible heat consumption of the system. The details of the COP improving approaches will be given in the literature survey section.

On the other hand there are two different approaches can be used for calculation of the cooling power of an adsorption cycle. The one of the approaches is to calculate the total cooling effect that can be obtained by evaporation of the desorbed and condensed mass of refrigerant. In this approach, the heat rejected during cooling of refrigerant from condensing temperature to evaporation temperature is subtracted from the total cooling effect due to evaporation of the refrigerant mass. The COP

value calculated by using this method is named as gross COP of refrigeration. The second method of calculation will be based on the heat removed from the cold space by the system. In this method heat removed from the cold space will be divided by the heat received by the system to obtain the net COP of the system [86]. Most of the time in the literature, the calculation method of COP values had not been specified, therefore the COP values presented in this study are assumed to be net COP unless otherwise mentioned.

Moreover another concept had been introduced for defining the efficiency of cooling and refrigeration systems that are powered by solar energy. The concept is the solar COP of the system. Solar COP of the system can be expressed as follows [112],

$$COP_C = \frac{cooling\ energy(energy\ removed)}{energy\ receieved\ by\ the\ solar\ collector} \quad (1.3)$$

Another measure of performance in the adsorption based cooling and refrigeration systems is the average volumetric and average mass specific cooling density values. The average volumetric specific cooling power density is obtained by dividing the net cooling energy received from the cold space divided by the cycle time and the volume occupied by the adsorbent bed. Similarly the average mass specific cooling power density is defined as the energy removed from the cold space divided by the cycle time and the mass of the adsorbent bed. The average volumetric and mass specific cooling power density can be expressed as follows,

$$SCP_v = \frac{Q_c}{V_{adsorbent} t_{cycle}} \quad (1.4)$$

$$SCP = \frac{Q_c}{m_{adsorbent} t_{cycle}} \quad (1.5)$$

1.3 Survey of Literature

As stated above, adsorption cooling and refrigeration is a promising technology when the advantageous aspects are considered. The main advantages of adsorption cooling systems can be briefly recited as,

- Direct utilization from low grade energy sources (e.g. solar energy)
- Can be operated with a wide range of heat source temperature
- Relatively simple construction and design, does not dependent on mechanical actuators such as electric motors.
- Environmentally friendly, non-toxic refrigerants can be used
- Suitable for operation and usage on mobile platforms

Besides the advantages listed above, low performance characteristics, low SCP and COP values of adsorption cooling and refrigeration systems is hindering their commercialization and wide spread usage. As mentioned earlier the ongoing research activities are focused to improve the performance characteristics of these systems. In addition to the performance improvements, the method of implementation on the industrial use and commercialization of the adsorption cooling systems is also attracting attention of the researchers.

The research activity in the field of adsorption cooling systems can be classified in three main groups according to the main focus of the efforts. One of the main branch of research activity is focused on the improvement of the adsorbent-adsorbate pairs which is vital to the adsorption based cooling and refrigeration systems. The research efforts on of working pairs is mainly concentrated to develop new adsorbents or new methods to improve the heat and mass transfer characteristics of the commonly used adsorbents to obtain better adsorption performance.

Another group of research activity involved with the performance improvement of adsorption cooling and refrigeration cycle through heat and mass transfer enhancements on the adsorbent bed and new cycle designs and operation procedures. Some of these works can be briefly mentioned as design of heat and mass recovery, multi-staged, cascading and thermal wave cycles. Beyond the cycle design, studies on the heat and mass transfer enhancement within the adsorbent bed are generally related with the enhancing heat exchange performance between the heat source and the adsorbent particles by increasing the heat transfer surface area or by reducing the thermal resistance between heat transfer surfaces and the adsorbent particles. The details of the efforts in this area will be cited in the related subsection.

The last part of the literature survey will be dedicated to the solar powered adsorption cooling and refrigeration systems and the research efforts up to date. In this subsection mainly, the experimental and numerical efforts and real case applications will be discussed.

1.3.1 Adsorbent-Adsorbate Pairs

As stated earlier, the adsorbent bed is the main component of the adsorption cooling and refrigeration systems which corresponds to the compressor of the conventional vapor compression cooling and refrigeration cycles [81].

The performance of the adsorbent used in the physical adsorption mainly determined by both material and geometric properties. The material properties can be exemplified as the hydrophobic or hydrophilic behavior of the adsorbent material. This property is a result of polar or non-polar atomic structure of material. The non-polar materials are generally hydrophobic while the polar materials are hydrophilic. The geometric properties of the adsorbent may be listed as the surface area, pore sizes, pore shapes, grain sizes. Since the adsorption is a surface phenomenon, larger surface area is a favorable geometric property which can be achieved by porous structure. Another important geometric property is the pore size distribution which

affects the accessibility of the adsorption sites. Today, it is possible to design adsorbent beds which possess the desired geometric and material properties. The selection of adsorbent and adsorbate media has a great impact on the adsorption system since; the performance is substantially affected by the working media and the temperatures [14, 17]. Some of the desired properties of an adsorbent could be listed as [87, 14,117];

- Low specific heat capacity and high thermal conductivity which increases the heat transfer rates and reduces the cycle times.
- High adsorption capacity in a relatively small temperature range
- Non-toxic, non-corrosive
- Available and low cost
- No deterioration and aging

Some of the most popular adsorbents that are used in the adsorption systems can be listed as activated carbon and activated carbon fibre, zeolite and silica gel [15, 14, 17].

As mentioned earlier activated carbons can be obtained from coal, wood, bone, and coconut shell by processing. The heat of adsorption of the activated carbons is lower compared to other popular adsorbents since its surface is covered by a oxide layer and/or some inorganic substances which reduces the surface polarity of activated carbon. However, it is a low cost and widely available substance. The activated carbon fiber has better mass transfer characteristics compared to activated carbon due to the more uniform distribution of pores. However an anisotropic thermal characteristic is a significant disadvantage of activated carbon fiber [15, 14].

Zeolites are another group of popular adsorbent. There are approximately 40 natural and 150 types of artificially synthesized types of zeolites exists. The pore size and distribution of the artificially synthesized zeolites can be adjusted by the process

parameters during production. Therefore heat and mass transfer characteristics of artificially synthesized zeolites are superior to natural ones. However the cost of artificially synthesized zeolites is more expensive than the natural zeolite. The artificially synthesized zeolites are named with extensions like 4A, 13X which refers to the manufacturing process [15].

Silica gel posesses most of the desired properties listed above. It is an synthetic amorphous adsorbent, that can be used when high capacity is required at moderate pressures and low temperatures. Silica gels are classified according to the pore size and named as Type A, B and C. Type A is the most common type since it can be used for all desiccation conditions regardless of the relative humidity [15]. Due to the low binding energy, silica gel is easy to regenerate by using low temperature heat sources. Therefore it is ideal adsorbent for the solar applications [101]. One of the main drawbacks of silica compared to the other common adsorbents (zeolite, activated carbon) is the high cost and low availability [101, 83].

Similarly some of the desirable properties for an adsorbate could be listed as [14, 15, 17, and 101];

- Low viscosity values, and smaller molecular size would be preferable to ease the adsorption
- High thermal conductivity and low specific heat to increase heat transfer rate.
- High latent heat of adsorption
- Chemically and thermally stable under operation conditions
- Low viscosity
- Available and low cost

Some of the most popular adsorbate (refrigerants) that are used in the adsorption systems can be listed as, ammonia, ethanol, methanol and water.

Having a boiling point below -10^{o}C at 1 atm, ammonia is a positive pressure refrigerant while; ethanol, methanol and water are vacuum refrigerants. The systems which operate under vacuum pressures are susceptible to immediate failure in case of air leakage into the system. The positive pressure systems which utilize ammonia as a refrigerant can tolerate the air leakage up to a level [101, 118]. However ammonia is a toxic and corrosive refrigerant which requires relatively higher pressure values for condensation at moderate temperatures [101].

Methanol and ethanol are similar in terms of freezing point and latent heat of evaporation values. The low freezing point of methanol and ethanol make them favorable in cooling and refrigeration applications where temperatures below 0^{o}C are desired. Also being, non-corrosive makes methanol and ethanol advantageous over ammonia. However chemical stability is and over regeneration temperatures of 120^{o}C and flammability is an issue for methanol. The latent heat of evaporation for ammonia, ethanol, methanol and water is respectively 1368 kJ/kg, 842 kJ/kg, 1102 kJ/kg, 2258 kJ/kg. [15] Regarding the latent heat of evaporation water is the most favorable refrigerant. Furthermore, being non-corrosive, non-toxic and inflammable makes water seems to be the most suitable refrigerant for adsorption cooling and refrigeration purposes among the others. However, as a result of its high freezing point water cannot be used as a refrigerant for cooling purposes which requires temperatures below 0^{o}C, [15, and 83].

There are several studies evaluating the performance of different adsorbent-adsorbate pairs [15, 101, 119 and 120]. As stated earlier the most commonly used adsorbent-asorbate pairs can be listed as, activated carbon-methanol, activated carbon-ammonia, zeolite-water, and silica gel-water. [15, 101]

Silica gel-water is considered to be the most suitable working pair for solar powered adsorption cooling and refrigeration applications due to its low regeneration temperature.[101,15] since refrigeration temperatures below 0^{o}C are not possible to

obtain with this working pair, silica gel-water is used commonly in the adsorption based chillers and air conditioning systems.[101]. The experiments had shown that silica gel-water pair can perform cyclic operations without experiencing any significant performance and stability degradation [111]. Moreover water is the environmental friendly and highest safety class refrigerant among the mentioned ones [97]. However, low adsorption capacity, low vapor pressure requirements are the major disadvantages of this working pair.

Another working pair is the zeolite-water. The heat of adsorption for zeolite-water pair is higher than the heat of adsorption of silica gel-water pair. The regeneration temperature of zeolite-water pair is above the 200^{o}C but zeolite-water pair can operate in a wide range of condensation temperatures without experiencing any performance degradation.[15] Similar to silica gel-water pair, the mass transfer performance of zeolite-water pair is low due to low operating pressures. Likewise it is not possible to obtain refrigeration temperatures below 0^{o}C with the zeolite-water pair.

Activated carbon-methanol pair is another favorable and common working pair for adsorption cooling and refrigeration systems. The activated carbon-methanol pair can operate by using low temperature heat sources. As stated earlier, above 120 ^{o}C methanol becomes chemically and thermally unstable, therefore lower operation temperatures should be preferred while working with this pair. Another important characteristic of activated carbon-methanol pair is its high adsorption capacity. Additionally the low freezing point of methanol makes this pair suitable for adsorption based ice makers. Low thermal conductivity of activated carbon and toxicity and flammability of methanol are the disadvantages of the activated carbon-methanol pair. [101, 15]

The main advantage of activated carbon-ammonia pair is the high working pressure compared to the other working pairs. As stated previously ammonia is a positive

pressure refrigerant which does not requires vacuum environment. The high operating pressure results in better mass transfer characteristics and low cycle times. On the other hand working at high pressures with a toxic refrigerant is not a favorable situation from the safety aspect [101, 15, and 87].

The brief comparison of the mentioned working pairs together with the most common application area is given in Table 1.1.

Table 1.1 Comparison of the commonly used working pairs in adsorption cooling and refrigeration systems

Working Pair	Operating Temperature [^{o}C]	Operating Pressure [barA]	Specific Cooling Capacity	Common Application
Silica gel-Water [121,80]	<90	0.01-0.3	High	Air Conditioning-Water chiller
Activated Carbon-Methanol[87,121]	<120	0.01-0.35	Normal	Ice Maker
Activated Carbon-Ammonia[121,80]	<150	3-10.4	Highest	Refrigeration-Ice Maker
Zeolite-Water [87]	<200	3.4-8.5	Normal	Air conditioning-Water chiller

In addition to the common adsorbents that are generally used researchers are trying to develop new adsorbent with desirable properties as mentioned above. One of the main purposes of working on new or composite adsorbents is to improve the heat transfer performance of these substances. The granular and porous nature of the adsorbents results in low thermal conductivity and low thermal performance.

One of the methods for improving the thermal conductivity of an adsorbent substance is to mix it with additives which have relatively high thermal conductivity. These materials can be metallic pieces [14], metal powders and carbon fibers.

However, carbon fibers when used as an additive to improve heat transfer characteristics of an adsorbent may not create the desired improvement due to its anisotropic thermal characteristics. In some of the cases existence of carbon fibers in the adsorbent even increased the thermal resistance at the heat exchange interface [15]. Addition of metallic pieces or metal powders will increase the dead mass of the adsorbent which may result in higher sensible heat consumption and lower COP values at the cost of increasing the thermal conductivity. Another approach is to mix different sized adsorbent particles to improve the thermal conductivity of the adsorbent bed [121].

Another method that is used for improving the heat transfer performance of the adsorbents is consolidation. Consolidated adsorbents can be obtained by compressing the adsorbent particles with binder and/or other high thermal conductivity materials. As a result of consolidation high thermal conductivity values can be reached since a continuous conduction path had been established by the binder matrix. However with the introduction of interstitial filling, the permeability and the mass transfer performance of the adsorbent bed significantly decreases relative to granular packed beds. This degradation in the mass transfer performance would likely reduce the adsorption rates especially under vacuum conditions which will result in elongated cycle times [14].

The investigations on the consolidated adsorbents yields higher COP values up to compared to unconsolidated beds [122, 123]. However in some of the cases, the adsorption duration need to be 7 times longer than desorption durations for the best COP results [88]. The possible cause of longer adsorption durations may be the reduced mass transfer performance of the bed. Therefore a new material is reported to be developed to eliminate the adverse effects of binder materials used in consolidation [81]. According to the results of experiments the developed host matrix material does not affect the mass transfer performance of the base adsorbent (silica gel) significantly.

1.3.2 Enhancement of Heat and Mass Transfer in Adsorbent Bed

The low COP and SCP values of the adsorption systems associated with the poor heat and mass transfer within the adsorbent bed is a well-known drawback of the adsorption based cooling and refrigeration systems [80]. Therefore, the research activities in the field of adsorption cooling and refrigeration are aiming to improve the performance of these systems and seek for the ways of commercialization through possible implementations of these systems [89,114].

Since adsorbent bed is the main component of these systems, the enhancements in heat and mass transfer performance of the adsorbent bed will directly influence the performance of adsorption cooling system. Effectiveness of the heat exchange between source and the adsorbent bed characterizes the thermal performance of the adsorbent bed. In some of the solar applications the adsorbent bed directly exposed to solar radiation and heated by the source itself [92, 96, and 100] but in general the heat is transferred from source to the adsorbent bed by an intermediate medium. The medium which facilitates the heat transfer between the bed, source and environment is named as Heat Transfer Fluid (HTF) [1, 14, 17, and 93]. The HTF flows through a heat transfer tube (HTT) or duct which separates the HTF and the adsorbent particles. Mainly the adsorbent bed is composed of HTF flow path and adsorbent particles but the thermal performance of the adsorbent bed depends on various parameters such as, HTF thermophysical properties, HTF flow velocity, dead mass of the bed and the thermal resistance between HTT and adsorbent particles.[6, 7, 8, 38]

Furthermore mass transfer performance of the bed is equally important as the thermal performance. Since the bed needs to adsorb and desorb required amount of refrigerant during operation, mass transfer characteristics of the bed should be at desired level. The mass transfer performance is influenced by the interparticle flow and intrapartice diffusion of the refrigerant [14, 37]. Moreover, as stated earlier some

of the enhancements in the heat transfer performance of adsorbents (e.g. consolidation) may detract the mass transfer performance of the bed [14, 88]. As a consequence, the adsorbent bed heat and mass transfer performance could be enhanced by determining the necessary design parameters according to the operation and performance requirements.

The enhancement efforts on the thermal conductivity of the adsorbent particles had been presented in the previous part. Another bottleneck in the heat transfer pathway is the thermal resistance between HTT and the adsorbent particles. The thermal resistance at the HTT interface reduces the heat exchange rate between HTF and adsorbent particles and affects the thermal performance of adsorbent bed. Thus researchers also interested in methods to reduce this resistance.[124] One of the popular methods that had been used for reducing the thermal resistance between the HTT wall and the adsorbent particles is to coat the heat exchange surfaces with the adsorbent particles[50,125]. In the coating process of the heat exchange surfaces, dip coating [127], spray coating, coil coating [125] methods could be used. In the mentioned coating methods the adsorbent particles are coated on the metal surfaces by using a binding agent, however it is also possible to directly growing the adsorbent material on the metal surfaces [126]. It had been reported that by coating the metal heat exchange surfaces of the adsorber with adsorbent particles, the heat transfer coefficient at the interface increased from 10 W/m2K to 150 W/m2K, while the SCP value of the system increases 15 times. [128]. Likewise by coating of annular fins of an adsorber bed, a heat transfer coefficient of 3000 W/m2K had been obtained [129]. The results show that the heat transfer resistance at the metal surface-adsorbent particle interface could be reduced by coating of the heat exchange surfaces. On the other hand, similar to consolidation methods improved thermal performance comes along with a reduction in the mass transfer performance of the bed which negatively affects the overall performance and further investigation is required [50].

Another approach that is used for enhancing the heat transfer performance of an adsorbent bed is to increase the heat exchange surface area. In this approach generally adsorbent beds obtained by packing adsorbent particles around conventional heat exchangers. A general method of manufacturing an adsorbent bed is to fill the annulus of a circular finned tube with adsorbent particles [23, 93, 110, 114, 130, 131, 132]. In some other cases plate fins [96], plate type heat exchangers [20] or corrugated finned structures [89] can be used as extended surfaces to increase the heat transfer surface area. The usage of extended surfaces on the HTF flow path generally increases the thermal performance of the adsorbent beds as a result of increased heat transfer surface area; however the increased mass of the adsorbent bed may reduce the COP and SCP values if not appropriate trade study is performed [52, 131].

From the mass transfer point of view the amount of adsorbent (its layer thickness around the HTT) and the grain size are the main parameters that can be used for performance enhancements. The results of the investigations showed that the smaller adsorbent grain sizes together with the less number of layers(less amount of adsorbent around HTT) lead to better COP and SCP values of the adsorption cooling systems in which adsorption phenomenon is dominated by mass transfer. .[133, 90]

Consequently, it can be said that the design of the adsorbent bed is important for the performance improvement of adsorption cooling systems. The enhancements in the performance through an efficient adsorbent bed design should not be based on the thermal aspects solely since mass transfer and heat transfer in the adsorbent always contradicts [52]. The enhancements in the thermal performance generally decrease the mass transfer performance of the bed. Therefore an effective bed design should establish a compromise between the enhancements of heat transfer and mass transfer characteristics.

1.3.3 Adsorption Cooling Cycles

The earliest version of the adsorption cooling system is based on the basic cycle which had been described above. The systems operating on basic adsorption cycle found out to have low performance metrics. Additionally the adsorption cooling applications are based on the basic cycle are operating in an intermittent manner. Beyond the low efficiency, intermittent operation is a major drawback for these systems compared to conventional vapor compression based cooling systems. Therefore researchers are interested in new cycle designs which improve the performance of the adsorption cooling systems while facilitating the continuous operation.

The continuous operation in an adsorption cooling system could be achieved by switching the mode of operation from adsorption to desorption alternately between two adsorbent beds, in a cycle [83]. For this type of operation at least two adsorbent beds are required in the system. Regarding the nature of alternating operation of adsorbent beds, the consumed heat by the system in a cycle can be reduced by exchanging the heat between adsorbing and desorbing beds [113]. As it had been stated in the definition of COP, some of the heat received by the system is utilized as sensible heat in the isosteric heating step of the cycle [52]. The heat required for the preheating and pressurization stage of desorption process can be supplied by the heat released by the adsorbing bed. The cycles in which heat is exchanged between the adsorbent beds of the system in this manner are called as the heat recovery cycles.

The heat transfer between source and the beds need to be achieved by means of a HTF for this type of cycles. In a classical heat recovery cycle, the HTF receives heat from the adsorbing bed and directed to the heat exchanger for further heat addition and heated HTF flows through the desorbing bed for achieving desorption. Similarly the high temperature HTF leaves the desorbing bed at a lower temperature and upon further cooling in the heat exchanger directed to the adsorbing bed. The external

heating and cooling requirements of the system is reduced and performance increased by this way. According to the experimental studies, heat recovery in a two bed adsorption chiller increases the COP of the system 38 % [134, 7]. The COP increase as a result of heat recovery is a better working mechanism when the sensible heat load to the latent heat load ratio of the adsorbent bed is high[3].

Another type of adsorption cycle combines the heat and mass recovery processes. The mass recovery is achieved by the refrigerant (adsorbate) transfer between desorbing and adsorbing beds of the system. At the end of a half cycle one bed is at condensation pressure (at the end of desorption process) and the other one is at evaporation pressure (at the end of adsorption process). The bed which completes the desorption will be depressurized and cooled down before performing adsorption similarly the bed which completes the adsorption step will be heated and pressurized before the desorption step. The high pressure bed will be depressurized while the low pressure bed is pressurized by the transfer of adsorbate through a connecting line between adsorbent beds. Both beds reach to an intermediate equilibrium pressure by this process. As a result of this mass transfer between beds the SCP and the adsorption capacity of the system increases. Solely mass transfer process reported to be capable of enhancing the system performance [135, 136]. However, in general mass recovery is accompanied by the heat recovery for further performance improvements. The cycles utilizing heat and mass exchange between the adsorbent beds are called as heat and mass recovery cycles [52, 170]. The SCP and COP improvements by utilizing mass and heat recovery can be achieved with the determination of recovery times specific to the system [33, 22].

A further improvement in the heat recovery systems had been proposed by with the introduction of thermal wave cycle [5]. Similar to the previously mentioned cycles for the thermal wave heat recovery there should be at least two adsorbent beds in the system. Similar to the other heat recovery cycles, the adsorbent beds should be heated or cooled by a HTF. In the thermal wave heat recovery cycle, the adsorbent

beds are connected in series with the two heat exchangers (heater/cooler). The heat exchangers are used for adding or removing heat from the HTF. A schematic representation of a thermal wave cycle can be seen in Figure 1.3.

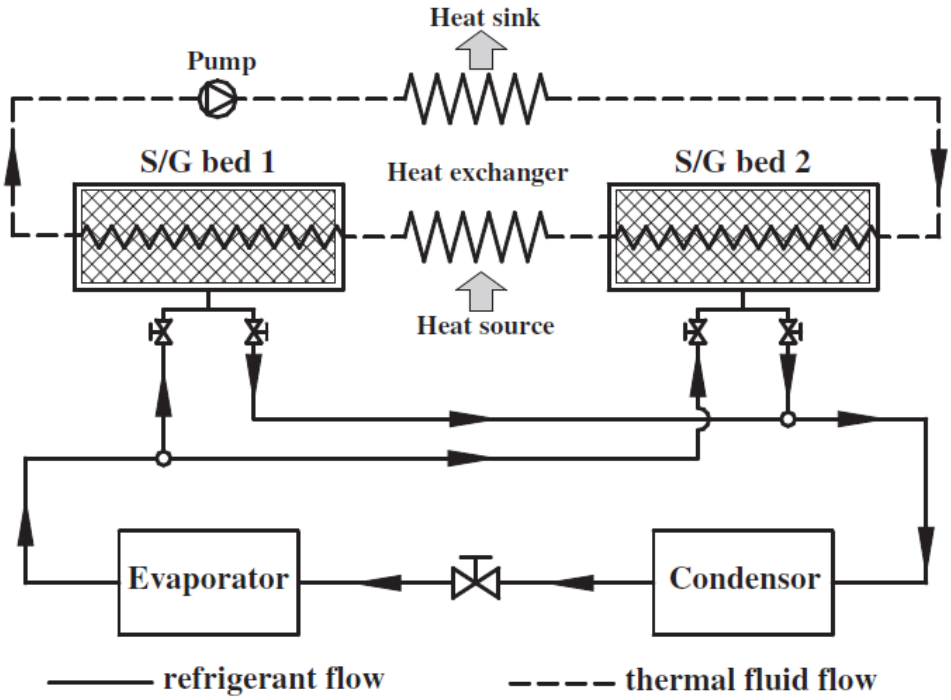

Figure 1.3 Schematic representation of thermal wave heat recovery adsorption cooling system [83]

The thermal wave heat recovery adsorption cooling system shown in Figure 1.3 can be operated continuously by only switching the direction of fluid flow. The operating principle of the system is similar to heat recovery cycles mentioned above. In the beginning of the first cycle the bed 1 is at low temperature and the adsorbate loading is high while the bed 2 is at high temperature and the adsobate loading of the bed is low. The HTF flows in the direction shown in Figure 1.3. Cooled HTF enters the bed 2 which is at high temperature and as a result of heat exchange between HTF and the bed, temperature of the HTF increases as it advances in the bed while the bed is cooled. The heated HTF leaves the bed 2 and enters the heat exchanger for further

heat addition. Upon leaving the heat exchanger at a high temperature HTF enters the bed 1 which is at low temperature. The HTF cools down while heating the bed 1 during its advancement in bed 1. The cooled HTF is directed to the heat exchanger where it is further cooled down. In this cycle bed 2 is adsorbing and connected to evaporator and the bed 1 is desorbing and connected to condenser. In the second cycle, the connections between beds and condenser and evaporator will be interchanged while the HTF flow direction is reversed [83, 14]. The operation of the thermal wave recovery cycle is not different from a simple heat recovery cycle. The main distinctive property of the thermal wave type heat recovery cycle is to maximize the heat recovery by establishing large temperature gradients in the HTF while flowing through the adsorbent beds [5, 14, 1, and 52]. The temperature profile variation for the HTF within the beds during operation can be graphically represented in Figure 1.4 [83, 14].

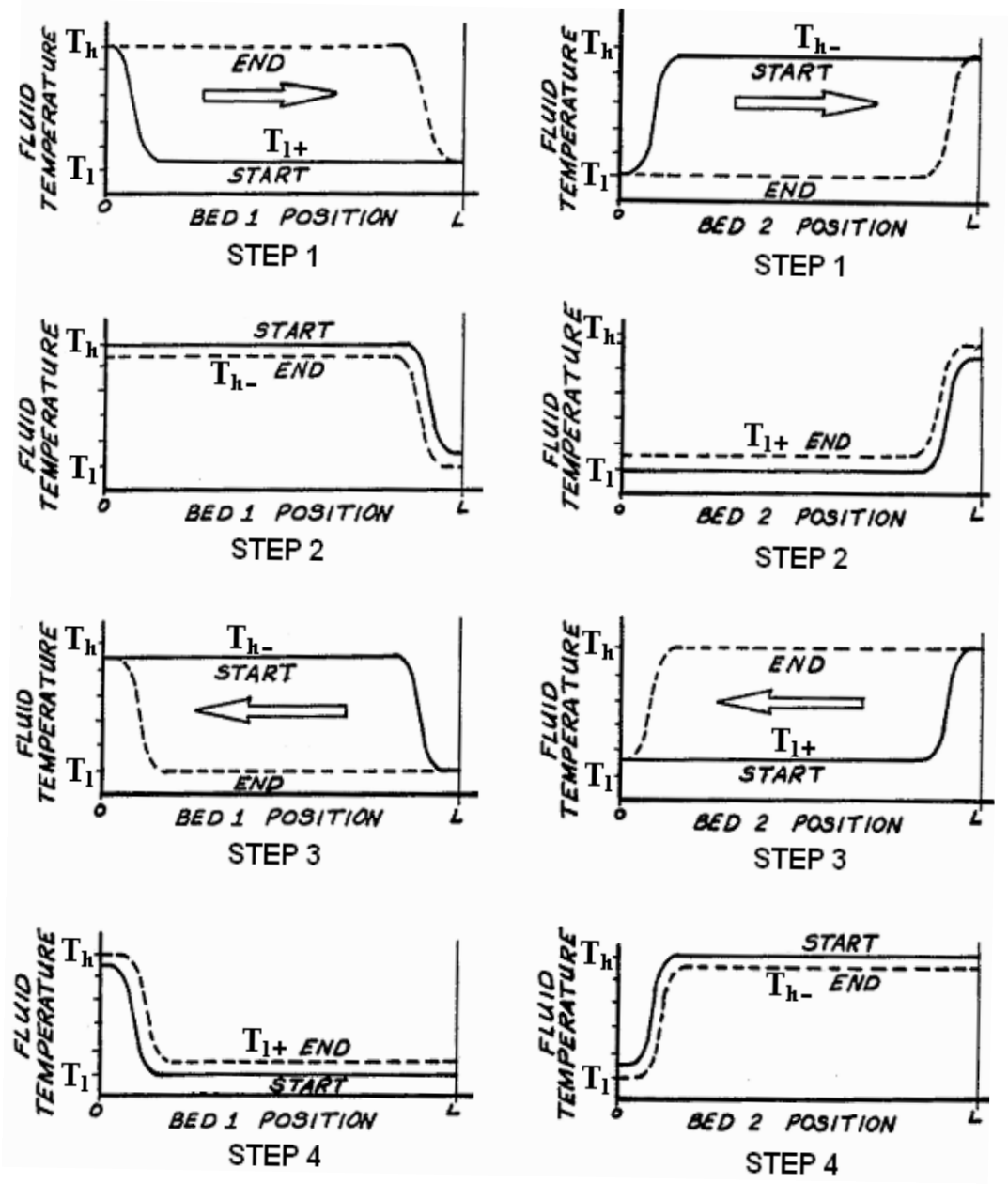

Figure 1.4 Schematic representation of thermal wave heat recovery adsorption cooling system [83, 14]

In Figure 1.4 the temperature variation of the HTF while passing through the adsorbent beds of an thermal wave heat recovery adsorption system is graphically presented [83,14]. The solid lines in the graphics represent the initial condition while

the dashed lines are representing the final condition reached upon completion of the step.

In Step 1 the bed 1 is at low temperature T_l and the bed 2 is at high temperature T_h initially. T_h is the upper operating temperature of the system and T_l is the lower operating temperature. During the first cycle bed 1 will be heated by the HTF and desorb refrigerant, while bed 2 will be cooled by the HTF and adsorption process will take place in bed 2. The HTF entering the bed 1 is at high temperature T_h and leaves the bed with a low temperature T_{l+} which is slightly higher than the lower operating temperature of the system. The HTF leaving bed 1 with T_{l+} is further cooled to temperature T_l in the heat exchanger before entering bed 2. The low temperature HTF enters bed 2 and leaves the bed at temperature T_{h-} which is slightly lower than the bed 2 temperature T_h. The temperature profile of HTF follows a wave like shape while flowing through the beds, but the shape of the temperature profiles in bed 2 is opposite of the bed 2. In step 1 the wave fronts in both beds proceeds to the right end of the beds as the time proceeds.

Upon completing the desorption in bed 1 and adsorption in bed 2 under constant pressure conditions the next step will be a pressurization step for bed 2 and a depressurization step for bed 1. Since bed 1 was at condenser pressure at the end of the step 1 an isosteric cooling (depressurization) step will follow step 1. Similarly the bed 2 was adsorbing and initially at evaporator temperature therefore step 1 need to be followed by an isosteric heating (pressurization) step. In step 2 the HTF flow is reversed, therefore HTF enters the beds from right end. The high temperature HTF entering bed 2 increases the temperature of the bed which is required to reach the condenser pressure. The cold HTF leaving the bed 2 further cooled in the heat exchanger and directed to bed 1. The bed 1 temperature need to be reduced to reach the evaporator pressure before starting adsorption in the next step.

The third step is similar to step 1 but in step 3 bed 1 will be adsorbing while bed 2 is desorbing. During step 3 the HTF is circulated in the opposite direction of step 1. Similar to step 2, step 4 will be the isosteric heating and cooling step for bed 1 and bed 2 respectively. The cycle times in the thermal wave regenerative systems are defined by the travel of the wave from one end of the bed to another.

As demonstrated and explained above, the existence of thermal wave type temperature variations within the adsorbent bed and HTF, it is possible to minimize the heat addition and rejection to/from the system by the heat exchangers. Minimization of the external heat addition increases the COP and SCP values directly [14, 1, 2, and 5].

Based on this thermal wave concept numerous research activities had been performed. One of them is the two dimensional numerical investigation heat and mass transfer on an adsorbent bed operating in a thermal wave regenerative cycle [7]. As a result of numerical analyses, the performance of a thermal wave regenerative heat pump has higher COP compared to uniform temperature heat pump. Additionally the results had shown that COP values higher than unity is also possible with the thermal wave heat recovery. The efficiency of a thermal wave heat recovery cycle could be increased with the reduced thermal wave thickness [5, 83]. The results of a theoretical study [2] had showed that the COP improvement by the thermal wave type regeneration depends on various operation parameters such as condensation temperature and dead mass of the adsorbent bed. On the contrary to the common engineering intention, a high COP thermal wave regenerative adsorbent bed design should have a large dead mass. Based on the results obtained it is also concluded that the mass recovery does not increase the COP value of the thermal wave heat recovery cycle under the conditions of investigation [2].

The two dimensional numerical analyses that neglect the axial conduction in the adsorbent bed and the HTF had demonstrated that a thermal wave shaped

temperature distributions could be obtained [48]. The experimental and numerical analysis results on a finned tube adsorbent bed had showed that HTF flow velocity is the most significant parameter affecting the operation of an adsorbent bed which operates in a thermal wave heat recovery cycle [14,23].On the other hand the experimental reports on the inadequate performance improvements by the thermal wave heat recovery and lack of a successful adsorption system prototype operating on thermal wave principle [1] brings up the question on practical applicability of this concept.

Also it had been reported that by enhancing the heat transfer within the adsorbent bed it is difficult to satisfy the necessary conditions to obtain a thermal wave type temperature variation. As an another option for increasing the heat exchange rate between adsorbent bed and the HTF, flow velocity could be decreased or HTF flow path could be elongated but these design approach will result in decreased energy density and SCP[52].

Consequently it could be stated that by using appropriate design parameters and under suitable operating conditions it is possible to develop and operate an adsorbent bed which can demonstrate the thermal wave type heat recovery characteristics.

Since one of the main drawbacks of thermal wave heat recovery cycle is the low power density as a result of poor heat transfer between HTF and the adsorbent bed, a new cycle which heats and cools the adsorbent bed by using the adsorbate had been developed and named as convective thermal wave adsorption cycle [9]. The low power density In convective thermal wave cycle the adsorbate transfer heat between source or sink and used for heating or cooling of the adsorbent bed. The high surface area of the adsorbent particles yields an effective heat transfer rate during cooling and heating of the bed. The adsorbate flow through the beds is facilitated by a low power pump. Theoretical studies had shown that the COP of a convective thermal wave cycle can be as high as 0.9 [24].

Up to this point all the cycles discussed were single stage cycles. Moreover, there are also multi-stage and cascading cycles which are composed of more than one single stage cycles. A multi-stage cycle is designed for performing adsorption and desorption at different pressure and temperature levels and to utilize form the energy of the source more effectively by recovering heat between different stages of the cycle [1]. Each stage of a multi-stage cycle uses the same working pair. The main idea behind using a multi-stage cycle is to improve the efficiency of a system which can be operated by using a low temperature heat source [52].

Moreover, the cascading cycle is used when there is a large temperature difference exists between heat source and refrigeration space. Therefore cycles using different working pairs are connected in series to utilize from the high temperature heat source more efficiently [80].

1.3.4 Solar Powered Adsorption Cooling Applications

As stated previously the increasing cooling and air conditioning loads as a result of economic growth and increase in prosperity levels [80] also impacts the energy consumption based on air-conditioning and cold production in Turkey [2]. The importance of solar energy utilization in cold production can be explained by the coincidence of peak cold production need with the peak of solar irradiation [112,101]. Especially the west and south coastal regions of Turkey are the areas at which utilization of solar energy is at feasible levels. Furthermore in these areas air conditioning and cooling needs are more intensified with the contribution of developing tourism industry [2]. Therefore a cooling and refrigeration systems utilizing solar energy will contribute for reducing the energy demand which will have significant positive impact on the economy.

Beyond the advantages mentioned above, being an attractive alternative for the conventional systems, solar powered adsorption cooling and refrigeration systems

become the most fast pacing adsorption based cooling system among the others in terms of commercialization [B26]. Today various companies had their commercially available solar refrigeration systems. Some of these companies are Brissoneau et Lotz-Marine (France), EG Solar(Germany), Solaref (France), Zeopower (USA), SorTech AG (Germany) [101, 106]. The photograph of some of the commercially available systems in the market can be seen in Figure 1.5.

Figure 1.5 Solar adsorption chillers of SorTech AG [106](on the left) LBM Solar ice makers tested in Morocco [50](on the right)

The above mentioned commercialized products are all technically successful but they are unable to dominate the market of solar refrigeration [101]. The competitor of the solar powered adsorption based cooling and refrigerations systems in the solar refrigeraiton market is the photo-volatic powered vapor compression refrigerators. PV powered vapor compression refrigeration systems are still leading in the solar refrigeration market as a result of their cost efficiency [101]. On the other hand from the COP point of view, it could be said that both PV powered vapor compression refrigeration systems and solar powered adorption cooling systems are at a comparable level. The practical COP values of the solar based adsorption cooling and refrigeration systems are ranging from 0.1 to 0.2. Actually there are higher COP values demonstrated by simulations but these values had not been practically demonstrated yet [101]. The electric conversion efficiency of modern commercially available PV cells is on the order of 10 % and the COP values of a vapor compression refrigeration system will vary between 1.1 and 3.3 while operating with

an evaporator temperature between -5 and 15 ^{o}C at an ambient temperature which ranges between 45 and 61 ^{o}C. Resultantly the overall COP for PV solar refrigeration system will be ranging between 0.11 and 0.33 [141]. As a conclusion it is possible to state that the solar COP of solar powered adsorption cooling system and solar vapor compression refrigeration system are close to each other. However to become a feasible alternative for the conventional refrigeration systems, solar powered adsorption cooling systems required to be improved in terms of cost efficiency and/or performance.

The need for improving the performance and cost of the solar powered adsorption systems attracted the attention of researchers and prepared a ground for various research activities. Based on the cooling temperature range the adsorption cooing and refrigeration systems can be classified into three main categories as follows [112],

- Solar powered adsorption based air conditioning applications, cooling temperature range 8-15^{o}C
- Solar powered adsorption based refrigeration applications for food and vaccine storage, cooling temperature range 0-8^{o}C
- Solar powered adsorption based ice making and freezing applications, cooling temperature range below 0^{o}C

The solar adsorption cooling systems generally adopted the basic adsorption cycle and operate with a single bed on an intermittent manner [101]. Since the heat source is not available continuously [109] intermittent operation is more advantageous for the solar adsorption cooling systems. The solar powered adsorption cooling systems which adopt the basic cycle do not require any mechanical and electrical energy, reliable and cost effective. In the most basic versions of solar adsorption cooling and refrigeration systems solar collectors contains the adsorbent bed and adsorbent beds directly heated by the solar irradiation [91, 99, 100]. In some of the systems, solar collectors are used for heating the HTF which transfer heat to the adsorbent bed

[93].In some applications also Parabolic Through Collectors (PTC) are also used for heating the HTF [104, 105]. The operation mode and principle of basic solar adsorption cooling cycle is presented in Figure 1.6.

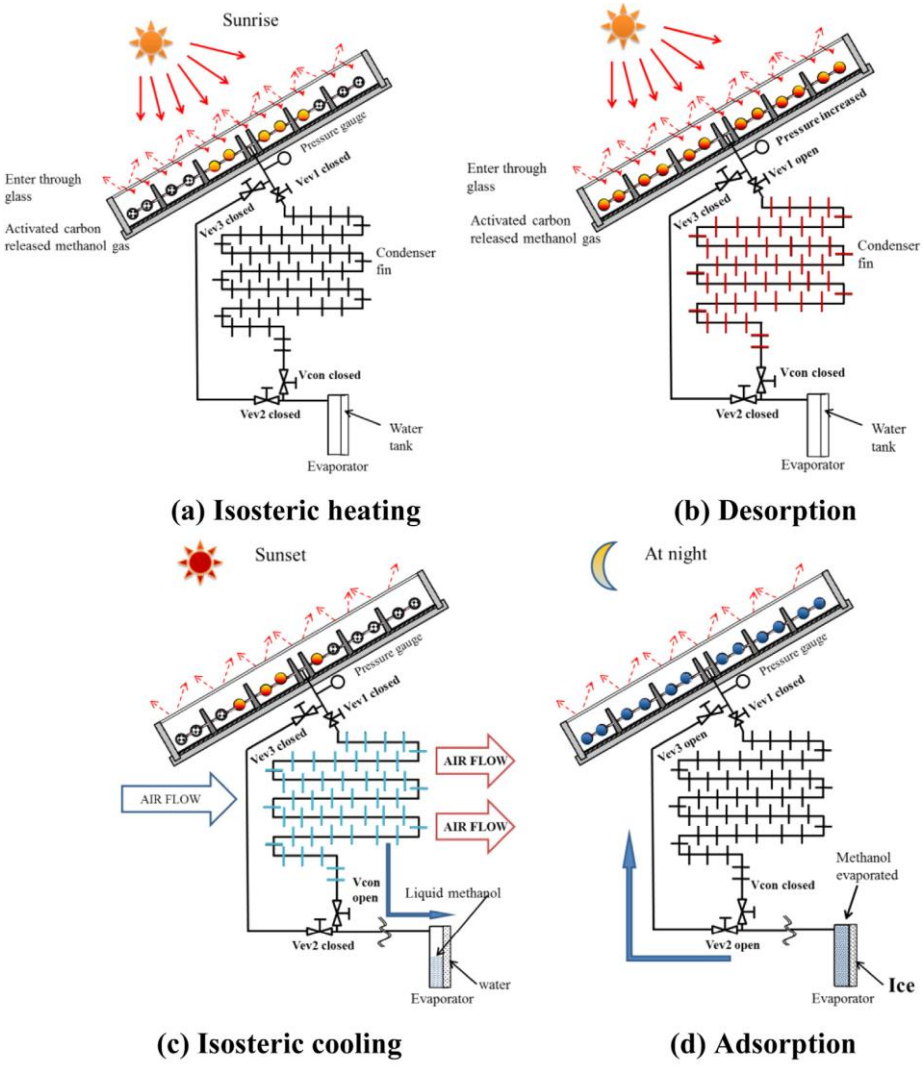

Figure 1.6 Schematic of operation modes of a basic solar adsorption cycle [100]

As can be seen from Figure 1.6, the isosteric heating step of the adsoption cycle starts with the sunrise. During the isosteric heating all the valves connected to the adsorbent bed is closed. As soon as the adsorbent bed pressure reaches the condenser pressure, adsorbent bed is connected to condenser and the desorption step starts. The

desorption continues until sunset since heat supplied to the system is received in the form of solar irradiation. At the end of sunset, the isostreic cooling step starts, during isosteric cooling, the valves of the adsorbent bed are closed. The isosteric cooling step is completed when the adsorbent bed pressure is lowered to evaporator pressure. The adsorption process starts upon completion of the isosteric cooling step and during adsorption the valve between the adsorbent bed and the evaporator is opened. The adsorption process continues until sunrise.

Fernandes et al.[101] had surveyed the experimental and simulation studies in the field of solar based adsorption cooling from 1982 to 2014. Regarding surveyed studies, most of the solar adsorption cooling applications are solar ice makers. Other applications of the solar powered adsorption cooling systems are water chillers, refrigerators, air-conditioning systems. Mostly used pairs for solar powered adsorption cooling applications are activated carbon/methanol, activated carbon/ammonia, zeolite/water and silica gel/water.

Activated carbon-methanol pair is widely utilized in solar powered ice makers. The experimentally obtained highest solar COP of the solar powered adsorption cooling system uses activated carbon/methanol is 0.19 [142, 101]. Similar to the all other cases there are also higher COP values obtained from the simulation and theoretical analyses but these result does not have a practical demonstration. Another adsorbent-adsorbate pair that is used popularly in solar powered cooling applications is the activated carbon-ammonia. Activated carbon-ammonia pair is mostly used in solar powered adsorption ice makers and refrigerators [101, 52]. Zeolite-water pair is also used in the solar powered adsorption cooling applications. The application area of the systems utilizing zeolite and water is ice makers, refrigerators and water coolers.[101,] The experimentally obtained typical solar COP values for a solar powered adsorption ice maker that uses zeolite-water working pair is on the order of 0.1 [143, 144]. One other common working pair that is used in solar powered adsorption cooling systems is the silica gel-water. Experimentally obtained highest

solar COP among the all solar powered adsorption systems, belongs to a solar powered ice maker which uses silica gel-water [145, 101]. The reported solar COP value is 0.16. The systems using silica gel-water pair are also used in air conditioning, refrigeration and water cooling purposes.

There are also hybrid solar powered systems which can be used for cooling during summer and heating in the winter seasons [145]. Additionally it is also possible to design solar powered adsorption cooling systems which will also perform desalination. The numerical studies had shown that for combined desalination/adsorption cooling system designs most suitable working pair is silica gel and water [84, 85].

In addition to the experimental an intensive effort is spent on the theoretical analysis of the solar powered adsorption cooling systems. In most of the cases the operation and the performance of the solar powered systems are generally simulated by using a lumped parameter method [84, 85, 90, 91, 92 95, 97, 98, 102,104]. In the lumped parameter analyses temperature variation along the adsorbent bed is assumed to be uniform. The heat transfer and mass transfer resistances within the adsorbent bed is neglected and the adsorbent is assumed to adsorb the refrigerant uniformly. Most of the time these models are used to predict the dynamic behavior of the adsorption cooling systems owing to the simplicity of the system of equations solved [47]. In some cases the dynamic behavior predictions of adsorption cooling systems based on lumped parameter models correlates well with the experimental data [91, 96]. In addition to the lumped parameter models, more sophisticated 2-D numerical models that solves the heat and mass transfer in the adsorbent bed also used for performance prediction of the solar powered adsorption cooling systems and shape the design parameters [96, 108]

However, the COP values and system characters which are much different than the experimentally investigated prototypes had pointed out numerical models are

neglecting or not accounting for the some of the important factors limiting the performance of experimental prototypes [101]. Based on the critics about the reliability of the numerical simulations, a more preferred way of using numerical simulations is to make comparisons between different cases and determine the effect of parameters [90, 92, 94, 95, 96, and 97].

1.3.5 Mathematical Investigations

Researchers also interested in mathematical modeling of the adsorption cooling systems since it would be helpful to understand the phenomena, predict the trends and understand the effect of parameters. There are various approaches in the field of mathematical modeling of adsorption phenomenon.

One of the mathematical modeling approaches is to build a thermodynamic model of the system. In the thermodynamic models generally the details of heat and mass transfer is disregarded. The thermodynamic models are involved in first and second law analyses of the adsorption system. The first law analysis is utilized for performance prediction while the second law analysis is made for determining the reasons of performance degradation [145]. The thermodynamic models of adsorption systems based on the adsorption equilibrium equations. Different approaches used for describing the adsorption equilibrium had been stated previously. The thermodynamic models are capable of determining the performance limits of adsorption based systems. In particular the COP trends and the limits of the adsorption cooling and refrigeration systems are investigated by using thermodynamic models [2, 3, 4, and 31].

The second group of numerical models that is generally used for predicting the dynamic behaviors of the adsorption systems is lumped parameter model. The lumped parameter models are simplified numerical models which are based on some simplifying assumptions. In the lumped parameter models, the adsorbent bed is

assumed to be isothermal and there exist a single variable for the bed temperature. Therefore both vapor and solid phase are assumed to be in thermal equilibrium. The adsorbed amount and adsorbate loading in adsorbent bed is assumed to be uniform. These assumptions points out the fact that the heat and mass transfer characteristics of the adsorbent bed is neglected in lumped parameter models [47]. The results obtained from lumped parameter numerical analyses are generally the time variation of adsorbent bed temperature and the adsorbent bed loading. An example of lumped parameter numerical analysis is performed for predicting the performance of a silica gel-water chiller and the results compared with the experiments [12]. The dynamic characteristics and performance of different adsorption cooling systems are generally analyzed by using lumped parameter method [84, 85] since it is relatively simpler and fast responding method.

The last category of modeling approaches is the heat and mass transfer modeling. In numerical heat and mass transfer modeling, beyond the time variation of temperature and adsorbate loading of the adsorbent bed, also spatial variation of these parameters can be obtained. These numerical analyses are more sophisticated and capable of giving detailed information about the dynamics, heat and mass transfer characteristics of the adsorbent bed. Additionally with numerical heat and mass transfer analyses of adsorption systems can be utilized for shaping the adsorbent bed design or optimization of a design [47]. In detailed heat and mass transfer modeling conservation equations for mass, momentum and energy is employed together with the adsorption equilibrium equation. All these transient governing equations are solved numerically on a spatial grid. In the numerical solution of the governing equations conventionally, finite difference, finite volume and finite element methods can be used. Owing its simplicity finite difference is commonly used [6, 7, 10, 17, 32, and 39]. The numerically analyzed geometries are generally two dimensional axissymmetrical geometries, which are also suitable for finite volume numerical analyses [11, 33, 35, 36, and 38]. In some of the cases also finite element methods are used for numerical solution of the governing equations [14, 23, 146].As another

way of categorization the heat and mass transfer models can be grouped with the number of spatial dimensions. The adsorbent bed geometries are generally in tubular or annular forms which could be modeled as two dimensional axisymmetric geometries. Therefore most of the time two dimensional numerical analyses are performed [33,35,36,38,17,10,32,39]. There are only a few three dimensional numerical analyses exist in the literature which are performed on axissymmetric geometries by using periodic boundary conditions [11, 147]. One other criterion that can be used in categorizing the heat and mass transfer models is the way of treating the solid phase and vapor phase temperature variables. In some of the numerical models the solid and the vapor phase within the adsorbent bed is assumed to be in thermal equilibrium. This approach is called as Local Thermal Equilibrium (LTE) heat transfer modeling. However it had been shown that the LTE assumption is valid under certain conditions [39]. The LTE assumption is valid if the particles of the adsorbent are sufficiently small and there is no significant heat generation in any of the phases. Actually the conditions are defined in a qualitative manner therefore it is not possible to make a justification on the validity of LTE assumption solely with these criteria. There are several LTE based adsorbent bed numerical analysis studies exists in the literature [11, 23, 35, 36, 48] some of which had been satisfactorily correlated with the experimental results. The LTNE based numerical analyses [39, 17, 10, and 148] are not as common as the LTE based numerical analysis work. The main reason could be the additional complexity of the LTNE based numerical models compared to the LTE based ones.

The modeling of the mass transfer is another issue for the numerical analyses. In some of the studies the mass transfer resistance within the adsorbent bed is totally neglected by making a uniform pressure assumption. In these numerical analyses the pressure distribution within the bed is not solved therefore the momentum conservation equation is not needed [149, 48]. However in vast majority of the numerical analyses the mass transfer resistance within the adsorbent resistance is accounted and pressure and velocity distribution in the adsorbent bed is modeled by

the Darcy's equation [7, 11, 33, 35, 37, 17, 39, and 147]. Darcy's equation is widely used for describing the flows in porous media. However it is applicable to very low speed incompressible flows with under uniform temperature conditions and does not accounts for the inertial effects [56]. Another equation that is used for modeling the mass transfer resistance of the adsorbent bed is the Ergun's Equation which accounts for the inertial effects in porous media flows [56, 76]. All the above mentioned mass transfer resistances are the external mass transfer resistance of the adsorbent bed. There is also internal mass transfer resistance which can be accounted by modeling the intraparticle mass diffusion of vapor. The intraparticle mass diffusion of adsorbate depends on the adsorbate loading of the adsorbent. Internal mass resistance can be included in the numerical models by using different approaches [17, 14, 10, 23, 39, 11, 33, 37, and 149]. In some of the approaches the internal mass transfer is neglected by assuming that the adsorbate diffusion in adsorbent particles are independent of adsorbate concentration within the adsorbent particles[26, 38, 48, 96]. In such analyses the adsorbed amount is assumed to be equal to equilibrium adsorption capacity of the adsorbent. This approach is called as assumption of adsorption equilibrium. One of the popular models used for accounting the intraparticle mass transfer resistance is the Linear Driving Force model proposed by Sakoda and Suzuki [9]. LDF is used widely as a result of its simplicity and accuracy [10, 11, 14, 17, 33, 37, and 39]. LDF model is based on the assumption that the concentration profile of adsorbate within the adsorbent particle is parabolic [17, 47]. Thus in LDF model the adsorption capacity variation of the adsorbent with time is related with the equilibrium adsorption capacity via a mass transfer coefficient as follows.

$$\frac{\partial X}{\partial t} = k_m\left(X_{eq} - X\right) \tag{1.6}$$

In Equation 1.6 k_m represents the internal mass transfer coefficient while X_{eq} represents the equilibrium adsorption capacity of the adsorbent at a definite

temperature and pressure. The details of the LDF equation can be found in following sections.

Another method that can be used for modeling the internal mass transfer resistance in numerical models is the solid diffusion model which is based on the Fick's law of diffusion [47].However these models imposes an additional complexity on the numerical models and not widely used [149].

There are various numerical analysis studies performed in the field of adsorption cooling systems as mentioned above. Even each analysis study based on different assumptions and mathematical modeling approach main aim is to use them as a design tool for determining the effect of design parameters and operating conditions [7, 33 ,37 ,48, 17, 14, 23, 10]. The numerical analysis results of some numerical studies are compared with the experimental results and/or the available analytical solutions. The comparison studies are performed more commonly on the lumped parameters analyses made for predicting the dynamical behavior of adsorption cooling systems [12, 84, 85, 90, 91, 107, and 96]. Additionally, in a limited number of studies the coupled hat and mass transfer solutions are compared with the experimental data. Regarding the lumped parameter models a good agreement could be observed with the experimental results. In addition to lumped parameter models, the detailed heat and mass transfer models are also demonstrated good agreement with the experimental data trends in terms of temperature variations [14, 23, 11, 39, 40, and 44]. On the other hand there is still a lack of agreement among the numerical studies available in the literature in terms of modeling approaches and methodologies [47]. One example of these discrepancies is the definition of thermal contact resistance between adsorbent particles and the metal surface of HTT. Different values are used by different researchers [6, 48, 14, 17,11,16,38, 131, and 132] and still neither a consistent method for calculation nor a reliable experimentally measured value had been presented. A similar disagreement among the researchers

can be seen in the definition of the effective stagnant thermal conductivity of porous adsorbent beds in LTE type heat transfer models [23, 37, 17, 81, 150, and 152].

Results and philosophy behind several numerical studies had been presented; however an optimal agreed and validated method for numerical analyses cannot be addressed for utilization in adsorption system designs. Therefore the need for extra work is still essential in development and validation of numerical approaches that can be used optimization of adsorption system designs. [47]

1.4 Motivation and Objective of the Study

As mentioned previously global economy growth and increasing prosperity levels will result in increase in the energy consumption based on the air conditioning and refrigeration applications. The increase in demand for cooling and refrigeration applications is more significant in the regions which are rich in terms of solar resources. The need for air conditioning and refrigeration has it peak times in the hot summer days which coincides with the peak of solar irradiation availability. The relation between cooling needs and solar energy sources leads to the result that, with the utilization of solar energy in air conditioning and refrigeration purposes may provide a great contribution in the economic growth and reduce the detrimental effects caused by the electricity production based on fossil fuels. Therefore adsorption cooling and refrigeration is a promising technology from economic and environmental viewpoints.

As stated earlier, the poor performance characteristics and high initial costs of adsorption based cooling and refrigeration systems is a hindrance that need to be confronted before becoming a an alternative for the conventional vapor compression cooling and refrigeration systems. Based on the overall COP comparison, solar powered adsorption based cooling systems are in a comparable level with the PV solar driven vapor compression cycles, but they are not feasible in terms of initial

and operation costs. Therefore most of the studies in the literature, mainly involves with the performance improvement of adsorption based cooling and refrigeration systems to make them economically feasible alternative for the conventional systems.

As way of improving the COP of adsorption cooling and refrigeration systems heat recovery cycles can be proposed as a suitable option. Further COP improvement of a heat recovery system is also theoretically possible with thermal wave type operation [5]. Thermal wave principle is simple and a promising technology in terms of performance enhancement. However, lack of a successful adsorption system prototype operating on thermal wave principle [1] brings up the question on practical applicability of this concept.

The thermodynamic analyses on the adsorption based cooling systems had shown that the COP limits are much higher than the experimentally obtained values [1, 2, and 26]. This result suggests that there are unforeseen factors limiting the performance of the adsorption cooling and refrigeration systems in practice. This discrepancy between performance predictions based on theoretical or numerical models and actual systems can be caused by the underestimated or neglected effects of different parameters [26].

Some of the common disagreements in the numerical models available in the literature is the calculation of thermal resistance between the HTT and the adsorbent particles [6, 48, 14, 17, 11, 16, 38, 131, 132], three dimensional effects, pressure difference between the evaporator and the adsorbent bed during adsorption process [26] and the definition of effective thermal conductivity of the adsorbent bed [23, 37, 17, 81, 150, 152]. These differences point out the lack of agreement among the numerical studies available in the literature in terms of modeling approaches and methodologies. Therefore the need for extra work is still essential in development

and validation of numerical approaches that can be used optimization of adsorption system designs. [47]

In the light of the information given above, current study ultimately aims to contribute the efforts on improving the performance of adsorption based cooling and refrigeration systems. For this purpose detailed numerical analyses will be performed on a three dimensional adsorbent bed for developing an understanding about the effects of different parameters and numerical modeling approaches. There are two novel numerical modeling activities performed in the scope of this study which can be introduced as,

- LTNE based coupled heat and mass transfer of a complete adsorbent bed in three dimensions will be numerically analyzed.
- The effect of co-existence of non-adsorbing specie (air) together with the refrigerant in the adsorbent bed will also be numerically modeled.

As stated previously, it is practically difficult [1, 52] to build a prototype which obeys the exact thermal wave type heat regenerative principle [5]. However the principle of obtaining large axial gradients within the adsorbent bed could be adopted for heat recovery performance enhancements. Therefore, to obtain large axial temperature gradients in the adsorbent bed, three dimensional cylindrical adsorbent bed designs equipped with circular HTTs which increases the radial and reduces the axial heat transfer rate [48, 52] will be proposed. The proposed designs will be manufactured, numerically modeled and experimentally investigated in the scope of this study. Another novel part of the study is the uncommon adsorbent bed designs which had not been proposed before. In the literature numerically and experimentally investigated adsorbent beds are generally manufactured by using a straight finned tube, annular spacing filled with adsorbent particles and in some of the cases flat plate and corrugated finned heat exchangers are adopted as adsorbent beds. Therefore the proposed designs are novel in the literature and strongly three

dimensional thus these designs cannot be modeled by any kind of reduced numerical modeling approach.

The numerical and experimental analyses will be based on the adsorbent beds which use silica gel/water as working pair. Silica gel/water is chosen since this working pair since it is widely used in adsorption cooling and refrigeration systems which requires low grade thermal energy source utilization such as solar applications.

1.5 Outline of Thesis

As mentioned the adsorbent bed is the main component of the adsorptive cooling systems. In the scope of this study the heat and mass transfer characteristics of a cylindrical adsorbent bed with circular heat transfer tube will be investigated by using numerical and experimental methods.

The first chapter of thesis starts with the introduction of adsorption phenomenon and operation principles adsorption cooling and refrigeration systems. The survey of literature part is also in the first chapter of thesis. In the literature survey part, adsorbent and adsorbate pairs used in different adsorption cooling and refrigeration systems had been presented together with the research activities on improving the performance of adsorbent-adsorbent pairs. The second subsection of literature survey is dedicated to the studies which are focused on improving the heat and mass transfer in the adsorbent bed of adsorption cooling and refrigeration systems. Literature about the solar application of the adsorption cooling and refrigeration systems and the mathematical modeling approaches and methodologies had been given in the last two subsections of the literature survey.

The second chapter of the study is mainly contains the governing equations, the derivations, and the simplifying assumptions used in the numerical modeling. Four

different set of equations for four different numerical models had been presented in Chapter 2. These numerical models are,

- Model based on LTE approach, where gas phase is composed of refrigerant (water) vapor only.
- Model based on LTE approach, where gas phase is composed of refrigerant (water) vapor and air.
- Model based on LTNE approach, where gas phase is composed of refrigerant (water) vapor only.
- Model based on LTNE approach, where gas phase is composed of refrigerant (water) vapor and air.

The analyses performed on a two dimensional axissymetrical model by using the numerical models that had been described above will be presented in Chapter 3. In this chapter numerical analysis procedure, boundary and initial conditions used in the analyses will be given. The results obtained from different analysis models during adsorption and desorption processes will be given and the results will be discussed in comparison.

The fourth chapter dedicated to the experimental investigation performed in the scope of this study. The experimental setup will be described together with the proposed adsorbent bed designs. The experimental procedure followed will be given. The results obtained by using LTE based and LTNE based numerical analyses will be given together with the experimental measurements for different initial and boundary conditions.

In the last chapter the results of this study and the outcomes will be summarized.

CHAPTER 2

THEORY

2.1 Introduction

The governing equations that will be used in modeling are basically the conservation equations. However in addition to conservation equations, auxiliary equations will be utilized for defining the equilibrium parameters and as equation of state. Governing equations will be separately solved for each component in the porous media. Since HTF is flowing in the heat transfer tube and exchanging heat with the packed bed through the heat transfer tube, conservation of mass, momentum and energy equations will also be solved for HTF. On the other hand, heat transfer tube is a solid pipe with a certain thickness, for this reason, in this domain only conservation of energy equation will be solved. As mentioned above, the coupled heat and mass transfer is taking place within the packed bed due to the adsorption process. In some of the cases, packed bed domain may contain adsorbate and non-adsorbing specie in addition to adsorbed phase and solid particles. As a result of this coexistence, conservation of mass for species, conservation of momentum and conservation of energy equations need to be solved for each phase within the porous media. According to the assumptions made in modeling, in some cases, different phases can be considered as a mixture for simplification. Additionally as stated earlier, governing equations will be solved by suing auxiliary equations that accounts for the mass transfer resistance and density variation for the gas phases. Details of assumptions made and the equations that are used in different modeling approaches will be discussed in the following parts.

2.2 Definition of Porous Media

Problems involving the porous structures are commonly encountered in the discipline of engineering. However direct solution or exact mathematical modeling of porous media is highly complicated. For this reason, various approaches are proposed for the simplification of the modeling and description attempts. All of these approaches are based on different methods used for the characterization of the porous medium.[56] Some of the remarking approaches and models used for description of porous media could be listed as [61,14];

- Bundle of capillary tube model
- Pack of solid grain model
- Averaging of microscopic field equations
- Dimensionless empirical correlation methods
- Hybrid models

The method that will be followed to obtain the governing equations in this study is the averaging of microscopic field equations. This method is preferred since it is based on the conservation equations of the microscopic level which enables the handling of the problem by using fundamental and consistent theoretical approaches.

Before going through the governing equations some basic concepts, terms and conventions that will be used in this study related to the porous media need be declared. The transport of any property within a porous material is generally characterized by geometric properties of the porous media and the physical properties of the phase in which transport takes place. The geometric properties belonging to the porous medium could be listed as, pore space, connectedness, tortuosity and porosity [54]. In addition to these geometrical properties another important parameter used for characterization of the porous media is the permeability. Permeability is a derived parameter which is a function of the

geometrical properties of the porous medium and can be expressed in terms of these geometric properties by using certain approaches.

The first important property is porosity. Porosity is also named as the void fraction because it is the volume fraction of void space in a porous material. The total porosity of a medium is composed of the void space formed between the particles and much smaller pores within the particles. The volume fraction of the void space between the particles could be named as bed porosity while the volume fraction of smaller pores within the particles is called as intraparticle porosity.

The bed porosity, intraparticle porosity and total porosity can be expressed as follows [14];

$$\varepsilon_b = \frac{\text{void volume between particles}}{\text{total volume of the medium}} \tag{2.1}$$

$$\varepsilon_p = \frac{\text{void volume within particles}}{\text{total volume of the medium}} \tag{2.2}$$

$$\varepsilon_t = \varepsilon_b + (1 - \varepsilon_b)\varepsilon_p \tag{2.3}$$

The permeability is the measure of porous media resistance to volumetric flux of mobile phase [162]. Since it is difficult to measure permeability directly, it is usually calculated by using different methods [54]. As mentioned above there are various approaches exist which relates the permeability to the porous medium geometric parameters. The details of approach used for calculating permeability in this study will be discussed later.

2.3 Mathematical Modeling

The adsorbent beds subject to investigation in this study is composed of three main parts. The first one is the heat transfer fluid, the second one is the heat transfer tube, and the third one is the porous bed. Mass, momentum and heat conservation equations for all of these components differ and for this reason governing equations for each component will be treated separately. In addition to the components, different mathematical models will be presented here which are differing in terms of assumptions, conservation equations boundary and operating conditions.

2.3.1 Modeling Approach and Assumptions

The first component is heat transfer fluid (HTF). HTF is encapsulated by the heat transfer tube and flow of HTF is driven by an external pump. Main duty of HTF is heating or cooling the porous bed by exchanging heat with the bed through heat transfer tube (HTT). The variables that need to be calculated for HTF are pressure, velocity and temperature distribution for the fluid. For this reason in the mathematical model conservation of mass, momentum and energy equations will be solved in the HTF domain. During the construction of mathematical model for HTF some assumptions made. The assumptions made while derivation of conservation equations can be listed as follows:

- The thermal conductivity, specific heat and the density of the HTF assumed to be constant
- The viscous dissipation and radiative heat transfer within the HTF domain assumed to be negligible
- The flow regime is assumed to be totally laminar according to the Reynolds number range.
- Kinetic, potential energy differences and effect of body forces are neglected.

The second component of the system is heat transfer tube. This component is composed of solid material and immobile. For this reason only energy conservation equation will be solved in this domain and the interaction with both HTF and the packed porous bed will be defined through proper boundary conditions. Similar to the other components, also some simplifications and assumptions are made in the mathematical modeling of heat transfer tube. The assumptions and simplifications made could be listed as:

- The thermal conductivity, specific heat and the density of the HTT assumed to be constant
- The heat transfer tube (HTT) assumed to exchange heat with the porous bed through the outer surface of the tube which is in contact with the bed. Sketch representing the heat exchange interface between HTT and porous bed can be seen in Figure 2.1.

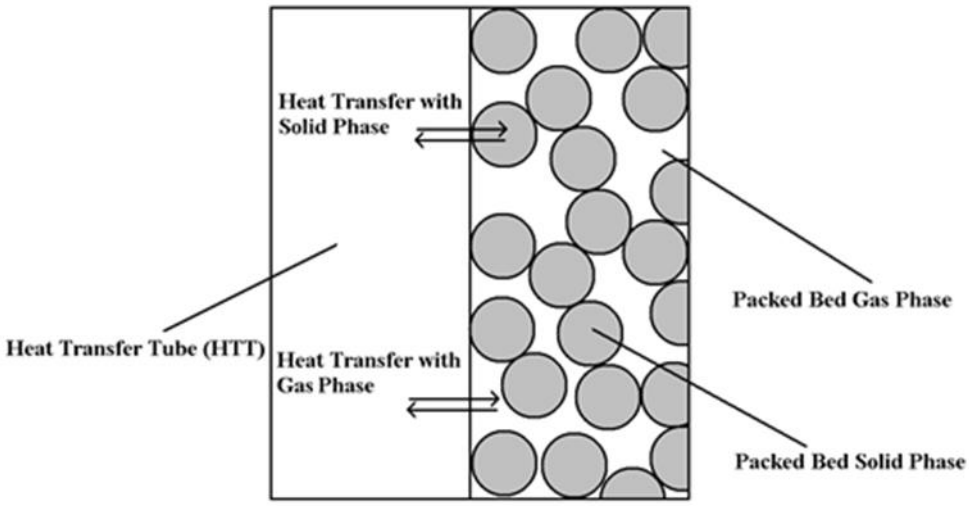

Figure 2.1 Representative sketch of the heat exchange interface between HTT and porous bed

In the mathematical models heat exchange between HTT and solid and gas phases of the porous bed cannot be directly implemented, therefore simplifying approach had

been followed. The heat exchange between HTT and porous bed is modeled by defining a thermal resistance to that interface. The contact resistance is calculated by using Equation 2.4 [132] with the thermal conductivity of solid adsorbent, gas phase (adsorbate) and porosity values.

$$R_{contact} = \frac{L_g}{(1-\varepsilon_t)\frac{2k_s k_t}{k_t + k_s} + \varepsilon_t k_g} \tag{2.4}$$

In Equation 2.4 L_g represents the solid particle diameter, k_s represents the thermal conductivity of the solid phase, where k_g represents the conductivity of gas phase, k_t represents the thermal conductivity of heat transfer tube material and ε_t represents the total porosity of the bed.

The third component is the packed porous bed, where adsorption and desorption process take place. As mentioned earlier mathematical modeling of this component is the most rigorous one. Within this domain, conservation of mass, momentum, and energy equations will be solved. According to the modeling approach and assumptions, the form and number of the equations will differ. Two different modeling approaches had been followed in this study. One of them is the Local Thermal Equilibrium approach which is based on the assumption that, the mobile gas phase is in thermal equilibrium with the immobile solid phase. The second one is the Local Thermal Non-Equilibrium (LTNE) approach in which mobile gas phase and immobile solid phase are not in thermal equilibrium and thermally interacting with each other. In the LTE approach both phases temperature distribution is defined by a single temperature variable whereas in the LTNE approach there are two temperature fields exists for solid and gas phases.

Additionally for being able to discuss the effects due to existence of non-adsorbing species during adsorption and desorption processes, two different mathematical models had been developed. In one of these models the mobile (gas) phase is composed of adsorbing specie only which is defined as vapor. In the second model

the gas phase is composed of mixture of two different species. One of these species is adsorbing and the other is non-adsorbing. The adsorbing specie will be called as vapor while the non-adsorbing specie will be called as air throughout this text. The governing equation sets that will be used for modeling the gas phase composed of adsorbing (vapor) and non-adsorbing (air) species, contains two additional mass transport equations for defining the concentration distribution of these species.

According to the definitions given above there are four set of governing equations discussed in the scope of this study for the porous packed bed. These four sets are classified as given below. The model classification and naming is based on the existence of thermal equilibrium between solid phase and gas phase and composition of the gas phase

- Local Thermal Equilibrium(LTE), pure vapor
- Local Thermal Non-equilibrium(LTNE), pure vapor
- Local Thermal Equilibrium(LTE), vapor-air mixture
- Local Thermal Non-equilibrium(LTNE), vapor-air mixture

Except the thermal equilibrium conditions and the gas phase composition there are common assumptions and simplifications used in the modeling of packed porous bed. Most of these assumptions and simplifications are adopted from the literature [14, 17, 37, and 33]. The assumptions and simplifications used in modeling of packed bed modeling could be presented as;

- The packed bed porosity is assumed to be uniform
- Adsorbent particle diameter is assumed to be constant
- Adsorbed phase and adsorbent are assumed to be immobile
- The gas phase is assumed to behave like ideal gas
- Specific heat, thermal conductivity and viscosity values assumed to be not varying with temperature.

- The surface porosity of the adsorbent particles is assumed to be equal to the total porosity of bed.
- Local Thermal Equilibrium (LTE) between solid phase and gas phase is assumed for some cases. In some cases, Local Thermal Non-Equilibrium (LTNE) is assumed and the gas phase and solid phase temperature is calculated by different governing equations.
- In some cases gas phase is composed of air and vapor. In these cases gas phase is assumed to be a mixture of air and vapor. The concentration distribution of each species governed by solving mass transport equation for both components.
- When LTE assumption is made, the packed bed is modeled as a continuous media and as thermal conductivity of the packed bed is calculated by an equivalent expression.
- The porosity value of the packed bed assumed to be not varying with the adsorbed liquid content

As mentioned earlier there are different domains in the mathematical model of the adsorption system. The governing equations for each domain will be different and their derivation will be given separately. The derivation steps of governing equations are given in Appendix C in detail. The equations used for different models will also be cited in the related sections with its final form.

2.3.2 Conservation Equations for the Heat Transfer Fluid (HTF)

First the governing equations will be given for the Heat Transfer Fluid (HTF) domain. As mentioned above, temperature, velocity and pressure distribution within the HTF will be governed by mass, momentum and energy conservation equations. The set of governing equations for the HTF can be seen below. As stated earlier detailed derivation of these equations are given in Appendix C.

Mass conservation equation for the HTF

$$\frac{\partial \rho}{\partial t} + \boldsymbol{\nabla}(\rho \mathbf{V}) = 0 \tag{2.5}$$

Momentum conservation equation for the HTF

$$\frac{D\mathbf{V_f}}{Dt} = -\frac{1}{\rho_f}\boldsymbol{\nabla} p_f + \frac{\mu_f}{\rho_f}\boldsymbol{\nabla^2}\mathbf{V_f} \tag{2.6}$$

As mentioned earlier, it had been assumed that the effect of body forces is negligibly small. Therefore body forces are not included in the momentum conservation equation for HTF.

Energy conservation equation for the HTF

$$\rho_f c_f \frac{DT_f}{Dt} = k_f \boldsymbol{\nabla^2} T_f \tag{2.7}$$

2.3.3 Conservation Equations for the Heat Transfer Tube (HTT)

As mentioned earlier, for modeling HTT domain only energy conservation equation will be used since temperature distribution within the HTT can be governed by solution of energy conservation equation. The detailed derivation of energy conservation equation for HTT is given in Appendix C.

$$\rho_t c_t \frac{\partial T_t}{\partial t} = k_t \boldsymbol{\nabla^2} T_t \tag{2.8}$$

2.3.4 Conservation Equations for the Porous Packed Bed

As stated above, there are various approaches in mathematical modeling of the packed bed. The derivation of governing equations procedure is mainly based on the treatment of the phases. Based on the LTNE assumption, phases are treated separately and the governing equations for each phase will be derived by using volume averaging method. On the other hand when phases are assumed to be at local thermal equilibrium (LTE) and all the phases within the packed bed will be treated as a single phase, the governing equation derivation will be based on control volume approach.

Moreover it should be noted that the mobile phase within the packed bed is gas and, this phase may be pure vapor or mixture of vapor and air depending on the case. There are also immobile phases exist in the packed bed. The immobile phases are liquid and solid phases but according to the assumptions immobile phases (solid and liquid phases) are treated as a single phase which will be mentioned as solid phase. Throughout this work the quantities and parameters that belong to mobile phase will be denoted with the subscript *g* referring to the gas state of the phase. Similarly, the quantities and parameters that belong to solid phase will be denoted with subscript *s*. The properties and variables belonging the liquid phase will be denoted by a subscript *l*.

2.3.4.1 Governing Equations for the Porous Packed Bed Based on Local Thermal Equilibrium (LTE) Approach

As stated in the previous sections, there exists two different governing equation sets for the porous packed bed based on LTE approach. In the first set, the gas phase is composed of single adsorbing specie. The second set of equations is derived for modeling the coexistence of two different species in the gas phase. In this second set of equations gas phase is composed of a mixture of two species and additional mass transport equations for each species will be solved.

The detailed derivation of these equations can be found in Appendix C.The governing equations for the porous packed bed based on LTE approach where gas phase is composed of only adsorbing specie can be written as follows,

Mass conservation equation for the gas phase in porous packed bed based on LTE approach

$$\varepsilon_t \frac{\partial \rho_g}{\partial t} + (1-\varepsilon_t)\rho_s \frac{\partial X}{\partial t} + \nabla . \mathbf{V_g} = 0 \tag{2.9}$$

One of the important parameters in the mass conservation equation is the adsorption capacity *X* which is a dimensionless quantity representing the ratio of kilograms of adsorbed amount to kilograms of adsorbent. The distribution of the adsorption capacity within the bed is yielded by a adsorption-desorption rate equation. In this study the adsorption rate defined by using the Linear Driving Force (LDF) model which accounts for the internal mass transfer resistance within the adsorbent particles. The adsorption-desorption rate equation based on LDF approach can be expressed as follows [9, 10, 14, 17, 30].

$$\frac{\partial X}{\partial t} = k_m \left(X_{eq} - X\right) \tag{2.10}$$

In Equation 2.10 the k_m denotes the mass transfer coefficient where X_{eq} represents the equilibrium adsorption capacity. The equilibrium adsorption capacity value defines the adsorption capacity values corresponding to adsorbent temperature and adsorbate pressure. For the purpose of correlating the equilibrium adsorption capacity of silica gel-water pair with adsorbent temperature and adsorbate pressure modified form of Dubinin-Ashtakov (D-A) equation will be used [17, 14, 10]. The equilibrium adsorption capacity for silica-gel water pair can be written as,

$$X_{eq} = 0.346 \exp\left[-5.6\left(\frac{T_{gs}}{T_{sat}} - 1\right)^{1.6}\right] \tag{2.11}$$

In Equation 2.11 T_{gs} is the temperature of solid phase which is identical with the gas phase for the LTE based models. The T_{sat} term in Equation 2.11 denotes the saturation pressure of the adsorbate corresponding to a particular pressure. The vapor pressure and saturation temperature for water can be related via expression given below,

$$T_{sat} = \left[\frac{1730.63}{8.0713 - \log_{10}(7.0063 p_g)} + 39.724\right] \tag{2.12}$$

Another parameter that should be defined is the internal mass transfer coefficient that is used in the adsorption capacity rate equation [12].

$$k_m = 15\frac{D_e}{r_p^2} \tag{2.13}$$

In Equation 2.13 r_p is the radii of the spherical adsorbent particles and D_e in is the equivalent diffusivity and defined as [12],

$$D_e = D_0 \exp\left(\frac{E_a}{RT_s}\right) \tag{2.14}$$

In Equation 2.14 D_0 represents the reference diffusivity, E_a represents the activation energy for surface diffusion, T_s represents the adsorbent temperature and R represents the universal gas constant for the adsorbate (water).

Momentum conservation equation for the gas phase in porous packed bed based on LTE approach is given as follows. The momentum conservation equation which relates the pressure gradient and mobile phase velocities in the porous media is also known as Darcy Law.

$$\mathbf{V_g} = -\frac{\kappa_g}{\mu}\boldsymbol{\nabla} p_g \tag{2.15}$$

In Equation 2.15 κ_g denotes the permeability of the packed bed. The permeability of the bed can be related with the bed total porosity and the particle diameter (d_p) by using Kozeny-Carman relation which is given as [68];

$$\kappa_g = \frac{d_p^2 \varepsilon_b^3}{180(1-\varepsilon_b)^2} \tag{2.16}$$

As stated previously for the LTE approach the gas and solid phases are assumed to be at the same temperature within the packed bed domain, therefore a single temperature variable exists for the energy conservation equations based on the LTE approach. The temperature belonging both phases will be denoted by a subscript of *gs*. The final form of the energy conservation equation for the porous packed bed, based on LTE approach can be written as follows,

$$\begin{aligned}&\varepsilon_t \rho_g c_{pg} \frac{\partial T_{gs}}{\partial t} - \varepsilon_g \frac{\partial p_g}{\partial t} + (1-\varepsilon_t)\rho_s c_{ps} \frac{\partial T_{gs}}{\partial t} + (1-\varepsilon_t)\rho_s X c_{pl} \frac{\partial T_{gs}}{\partial t} \\ &= \nabla\left(k_{eq} \nabla T_{gs}\right) + (1-\varepsilon_t)\rho_s \frac{\partial X}{\partial t} \Delta H_{ad} - \rho_g \mathbf{V_g} c_{pg} \boldsymbol{\nabla}. T_{gs}\end{aligned} \tag{2.17}$$

In Equation 2.17 one of the important parameters is the equivalent thermal conductivity of the porous packed bed. In the literature there are various formulae available for calculation of the equivalent thermal conductivity of porous medium. The equivalent thermal conductivity of the bed had been defined by the following relation based on the definition given in [37],

$$k_{eq} = {k_s}^{(1-\varepsilon_g)} {k_g}^{\varepsilon_g} \tag{2.18}$$

Based on the assumption that the gas phase is an ideal gas, the equation of state for this set of governing equations will be the ideal gas law given below,

$$p_g = \rho_g R_g T_{gs} \tag{2.19}$$

In Equation 2.17 ΔH_{ad} term represents the heat of adsorption. The heat addition or rejection is defined in terms of rate of adsorption-desorption and heat of adsorption with the second term on the right hand side of Equation 2.17 [36]

As stated in the previous parts the second set of governing equations will be used for modeling the gas phase as a binary mixture of air and vapor. In such cases the mass transport equations for each component in the gas phase will be added to the mathematical model. These equations will define the transport of species within the packed bed by convection and diffusion. The derivation procedure for the mass transport equation for each species is given in detail in Appendix C.

The mass conservation equation for the gas phase is composed of mass transport equations for air and vapor species. The sum of these two mass transport equations will yield a mass conservation equation for the gas phase. The mass transport equation for vapor and air can be written as,

$$\frac{\partial(\rho_g \omega_v)}{\partial t} + (1-\varepsilon_t)\rho_s \frac{\partial X}{\partial t} + \nabla.(\rho_g \omega_v \mathbf{V_g}) = \nabla.(\rho_g \mathfrak{D}_{vaeq} \nabla \omega_v) \tag{2.20}$$

$$\frac{\partial(\rho_g \omega_a)}{\partial t} + \nabla.(\rho_g \omega_a \mathbf{V_g}) = \nabla.(\rho_g \mathfrak{D}_{aveq} \nabla \omega_a) \tag{2.21}$$

These two mass conservation equation for air and vapor species are solved by using a mass constraint. The mass constraint used is sum of mass fraction of air and vapor which is equal to 1.

$$\omega_a + \omega_v = 1 \tag{2.22}$$

The terms in Equation 2.20 and 2.21 ω_v and ω_a represents the mass fraction of vapor and air in gas phase respectively. While $\mathfrak{D}_{vaeq}$ and $\mathfrak{D}_{aveq}$ terms represents the equivalent mass diffusivity of vapor in air and air in vapor.

The equivalent diffusivity value for the porous packed bed is defined by Nield and Bejan [75] as,

$$\mathfrak{D}_{vaeq} = \varepsilon_t D_{va} \tag{2.23}$$

In Equation 2.23 D_{va} stands for the mass diffusivity of vapor in air. In addition to this definition it had been stated by Bird et al.[63] the mass diffusivity value for both species in a binary mixture will be identical which means,

$$D_{va} = D_{av} \tag{2.24}$$

The binary diffusion coefficient for vapor and air can be expressed based on Chapman-Enskog kinetic theory as [79],

$$D_{va} = D_{av} = 0.0018583 \frac{1}{p\sigma_{av}^2 \omega_{av}} \sqrt{T_{gs}^3 \left(\frac{1}{M_a} + \frac{1}{M_v}\right)} \tag{2.25}$$

In Equation 2.25 the M_a and M_v represents the molecular weight of air and vapor respectively. Where σ_{av} represents the collision diameter for Lennard-Jones potential and ω_{av} represents the collision integral.

The momentum and energy conservation equations will not differ when gas phase composed of two species. The gas phase thermophysical properties that will be used in the conservation equations will be computed by using the binary mixture relations.

The binary mixture properties that will be used in the conservation equations are the viscosity, density, thermal conductivity and specific heat. These values will be expressed in terms of molecular weight and mass/molar fraction of species.

The density of the gas phase is related with pressure with ideal gas law. The ideal gas law can be written as follows, for a binary gas mixture, which is composed of air and water-vapor in this case.

$$p_g = \rho_g R T_{gs} \left(\frac{M_v \omega_a + M_a \omega_v}{M_v M_a} \right) \tag{2.26}$$

In Equation 2.26 M_v and M_a are the molecular weight of air where and vapor species and R is the universal gas constant.

The other parameter is the gas phase viscosity which is a function of molar fractions of species in case of air vapor mixture models. The gas phase viscosity is defined by using the expression based on Chapman-Enskog theory [63] as,

$$\mu_g = \mu_a + \mu_v + \frac{\left[8 \left(1 + \frac{M_a}{M_v} \right) \right]^{\frac{1}{2}}}{\left[1 + \left(\frac{\mu_a}{\mu_v} \right)^{\frac{1}{2}} \left(\frac{M_v}{M_a} \right)^{\frac{1}{4}} \right]^2} \left[\frac{(1 - x_v)\mu_a}{x_v} + \frac{x_v \mu_a}{(1 - x_v)} \frac{M_v}{M_a} \right] \tag{2.27}$$

In Equation 2.27 μ_g is the gas phase dynamic viscosity and similarly μ_a and μ_v are the dynamic viscosities of air and vapor. M_a is the molecular weight of air and M_v is molecular weight of air. x_a and x_v are the molar fractions of air and vapor respectively.

The thermal conductivity of the gas phase in case of air-vapor mixture can be expressed as a function of molecular weight, viscosity and molar fraction of species as,

$$k_g = k_a + k_v + \frac{\left[8\left(1+\frac{M_a}{M_v}\right)\right]^{\frac{1}{2}}}{\left[1+\left(\frac{\mu_a}{\mu_v}\right)^{\frac{1}{2}}\left(\frac{M_v}{M_a}\right)^{\frac{1}{4}}\right]^2}\left[\frac{(1-x_v)k_a}{x_v}+\frac{x_v k_v}{(1-x_v)}\frac{\mu_a}{\mu_v}\frac{M_v}{M_a}\right] \quad (2.28)$$

In Equation 2.28 k_g is the gas phase thermal conductivity k_a and k_v are the thermal conductivity values of air and vapor respectively.

The specific heat of the gas phase is also defined in a similar form as,

$$c_{pg} = c_{pa}x_a\frac{M_a}{M_g} + c_{pv}x_v\frac{M_v}{M_g} \quad (2.29)$$

In Equation 2.29 c_{pg} is the gas phase constant pressure specific heat, likewise c_{pa} and c_{pv} are the constant pressure specific heat values of air and vapor respectively.
The momentum and energy conservation equations remained same regardless of the composition of the gas phase therefore these equations will not be cited here again.

2.3.4.2 Governing Equations for the Porous Packed Bed Based on Local Thermal Non-Equilibrium (LTNE) Approach

The second approach that had been used in the mathematical modeling of the porous packed bed is the Local Thermal Non-Equilibrium approach. As mentioned earlier, in this approach, the temperature of the immobile (solid) phase and the mobile (gas) phase will be treated separately since these phases are not in thermal equilibrium. The governing equations based on the LTNE approach had been derived by using the volume averaging method. In the volume averaging method governing equations for the microstructures in porous media are averaged over a finite volume for obtaining the governing equations for macro scale. The final form of the governing equations which are obtained by volume averaging will be cited here. Further details about

volume averaging method and the derivation of governing equations based on the LTNE approach can be found in Appendix A and Appendix C.

Mass conservation equation for the porous packed bed based on LTNE approach can be written as,

$$\varepsilon_t \frac{\partial \rho_g}{\partial t} + \boldsymbol{\nabla}.\rho_g \mathbf{V_g} + (1-\varepsilon_t)\rho_s \frac{\partial X}{\partial t} = 0 \tag{2.30}$$

As can be seen from the Equation 2.30, the mass conservation equation based on the LTNE approach is identical with the mass conservation equation derived based on the LTE approach. The only difference is the derivation method. Similar to the LTE approach, the adsorption capacity (X) variation is defined by using the adsorption rate equation given by Equation 2.10 in the previous section.

Similar to the LTE approach, the velocity field will be yielded by Darcy's Law for the LTNE approach. The volume averaged momentum conservation equation can be written as,

$$\mathbf{V_g} = -\frac{\kappa_g}{\mu_g}\boldsymbol{\nabla} p_g \tag{2.31}$$

The details of volume averaging procedure and simplifications applied can be found in Appendix C.

The energy conservation equation for gas phase based on the LTNE approach can be written as follows,

$$\varepsilon_t \rho_g \frac{\partial (c_{pg} T_g)}{\partial t} + \rho_g \mathbf{V_g}.\boldsymbol{\nabla}(c_{pg} T_g) + c_{pg}(T_s - T_g)(1-\varepsilon_t)\rho_s \frac{\partial X}{\partial t} = \boldsymbol{\nabla}(K_{geq}.\boldsymbol{\nabla} T_g) - a_{gs} h_{gs}(T_g - T_s) \tag{2.32}$$

In Equation 2.32 th a_{gs} variable represents the gas-solid phase interface area per unit volume and expressed as a function of total porosity and adsorbent particle diameter as [39],

$$a_{gs} = \frac{6(1-\varepsilon_t)}{d_p} \tag{2.33}$$

In Equation 2.33 K_{geq} represents the equivalent thermal conductivity which is the sum of hydrodynamic dispersion and effective thermal conductivity tensors. The equivalent thermal conductivity tensor will be composed of constant values since the conductive heat transfer for the gas phase is assumed to be isotropic. The equivalent thermal conductivity for gas phase can be defined as a linear function of total porosity as [75],

$$K_{geq} = \varepsilon_t k_g \tag{2.34}$$

Likewise the energy conservation equation for the solid phase based on LTNE approach is derived by using the method of volume averaging. The details of derivation procedure can be found in Appendix C. The final form of the energy conservation equation for the solid phase in the porous packed bed can be written as,

$$\begin{aligned}&(1-\varepsilon_t)\rho_s\left(c_{ps}+Xc_{pl}\right)\frac{\partial T_s}{\partial t}+\\&=\ \boldsymbol{\nabla}\left(K_{seq}\boldsymbol{\nabla}T_s\right)+a_{gs}h_{gs}\left(T_g-T_s\right)+(1-\varepsilon_t)\rho_s\frac{\partial X}{\partial t}\Delta H_{ad}\end{aligned} \tag{2.35}$$

Similarly K_{seq} represents the isotropic equivalent thermal conductivity tensor for the solid phase and the diagonal values can be expressed as function of solid phase volume fraction by using the relation given below,

$$K_{seq} = (1-\varepsilon_t)k_s \tag{2.36}$$

The h_{gs} term in both energy conservation equations is the interfacial heat transfer coefficient which is the heat transfer coefficient between solid and gas phases.

Another parameter that will be defined is the heat transfer coefficient at the solid-gas phase interface, for the LTNE models. This convective heat transfer coefficient determined by using an expression which is a function of Reynolds and Prandtl number [39]. The correlation for the spherical solid particles can be written in expanded form as,

$$h_{gs} = \frac{k_g}{d_p}\left[2 + 1.8\left(\frac{\mu_g c_{pg}}{k_g}\right)^{0.33}\left(\frac{\rho_g d_p U}{\mu_g}\right)^{0.5}\right] \tag{2.37}$$

In Equation 2.37 U is the gas phase velocity magnitude.

Similar to the LTE approach the governing equations based on LTNE where gas phase is composed of an adsorbing (vapor) and a non-adsorbing (air) specie, only the mass conservation equation for the gas phase alters. The momentum and energy conservation equations remain same and the gas phase thermophysical properties are calculated by using the binary mixture relations. The mass conservation equation for the gas phase is expressed by the mass transport equations of the constituting species. The final form of the mass transport equations derived for the vapor and air species in the gas phase is identical with the ones that had been presented for the LTE approach. However these equations had been derived by using the volume averaging method. The details of derivation can be seen in Appendix C.

The mass transport equations used in the LTNE based models for vapor and air in the can be written as follows,

$$\varepsilon_t \frac{\partial(\rho_g \omega_v)}{\partial t} + \boldsymbol{\nabla}.(\rho_g \omega_v \mathbf{V_g}) + (1-\varepsilon_t)\rho_s \frac{\partial X}{\partial t} = \boldsymbol{\nabla}.(\rho_g \mathfrak{D}_{vaeq} \boldsymbol{\nabla} \omega_v) \quad (2.38)$$

$$\varepsilon_t \frac{\partial(\rho_g \omega_a)}{\partial t} + \boldsymbol{\nabla}.(\rho_g \omega_a \mathbf{V_g}) = \boldsymbol{\nabla}.(\rho_g \mathfrak{D}_{aveq} \boldsymbol{\nabla} \omega_v) \quad (2.39)$$

The notation and the parameters used in the equations above are defined in the previous section therefore will not be cited here again. The thermophysical properties of the gas phase that will be used in the energy conservation equation of the gas phase had been given in detail in the previous parts.

CHAPTER 3

MATHEMATICAL MODELING AND COMPARATIVE ANALYSES

3.1 Introduction

In the previous chapter, governing equations required for constructing a mathematical model for the adsorbent bed system had been presented. As previously mentioned there will be different mathematical models which are based on different assumptions and composition of gas phase. These assumptions which are used in the mathematical modeling are local thermal equilibrium (LTE) and local thermal non equilibrium (LTNE). The composition of the gas phase will also be affecting the governing equations used in the mathematical model. In this study two different situations will be discussed in terms of gas phase composition. The gas phase can be composed of pure vapor or a mixture of air and vapor. In the latter one, air is assumed to be non-adsorbing specie. According to these differences the four different mathematical model will be constructed for discussion of modeling approach and existence of a non-adsorbing specie during adsorption and desorption processes. These four different models can be listed as,

1. LTE based model with pure vapor as gas phase (Model 1)
2. LTE based model with air-vapor mixture as gas phase (Model 2)
3. LTNE based model with pure vapor as gas phase (Model 3)
4. LTNE based model with air-vapor mixture as gas phase (Model 4)

The comparative analyses will be made by using the four different models. For this purpose the governing equations for each mathematical model will be solved numerically in a coupled manner on a basic adsorbent bed design by using the software package COMSOL.

3.2 Geometric Model Used in Comparative Analyses

One of the requirements for making a numerical analysis by using a mathematical set of governing equations is to have a solution domain which is representative of the system that will be modeled. For this purpose a simple geometrical model is used which consist of a heat transfer tube (HTT) surrounded by a packed bed will be used. The heat transfer fluid (HTF) is flowing inside the heat transfer tube. As a result of complexity in the system of equations that will be solved, computation resource requirements can be dramatically increase. Therefore to reduce the minimum computer resource requirements and solution times, a simple 2-D axisymmetical model will be used. The sketch of the 2-D axisymmetrical model that will be used in the comperative analyses can be seen in Figure 3.1.

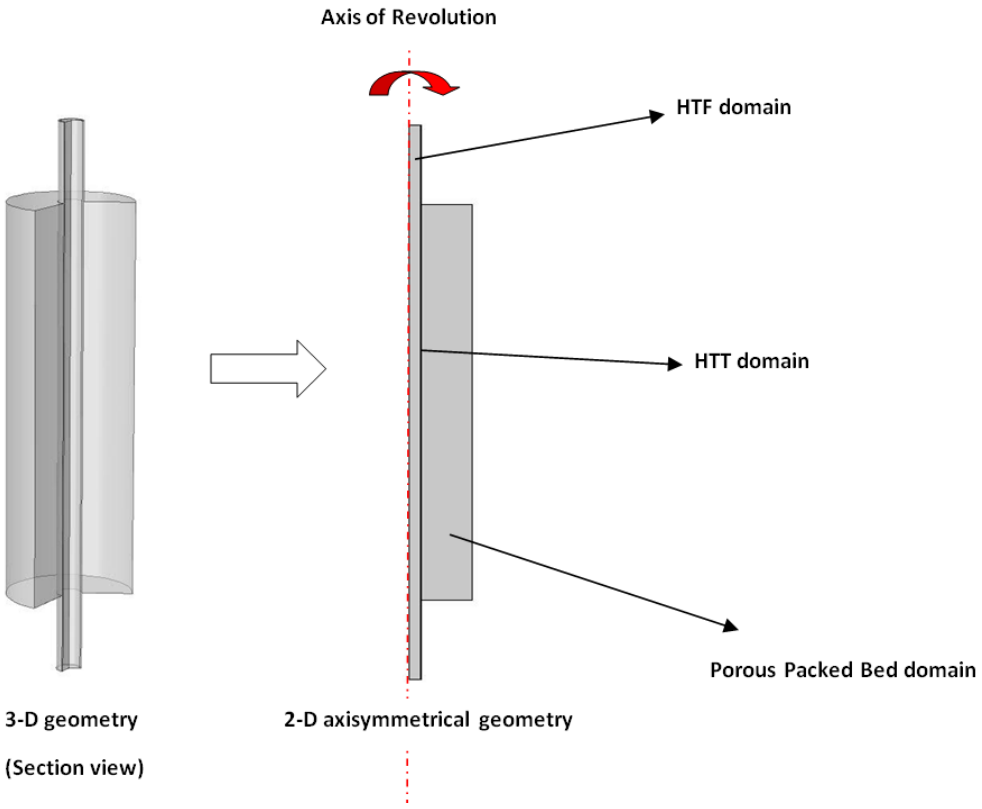

Figure 3.1 The sketch of 2-D axisymmetric model that is used in the base case analyses

The geometrical model consists of 3 main domains which are HTF, HTT and porous packed bed domain. The dashed red line shows the axis of revolution for the 2-D axisymmetrical geometry.

The boundaries of the 2-D axisymmetrical model is marked with numbers and shown on the sketch given in Figure 3.1. The boundary conditions that will be defined on these boundaries are going to be discussed in the following parts.

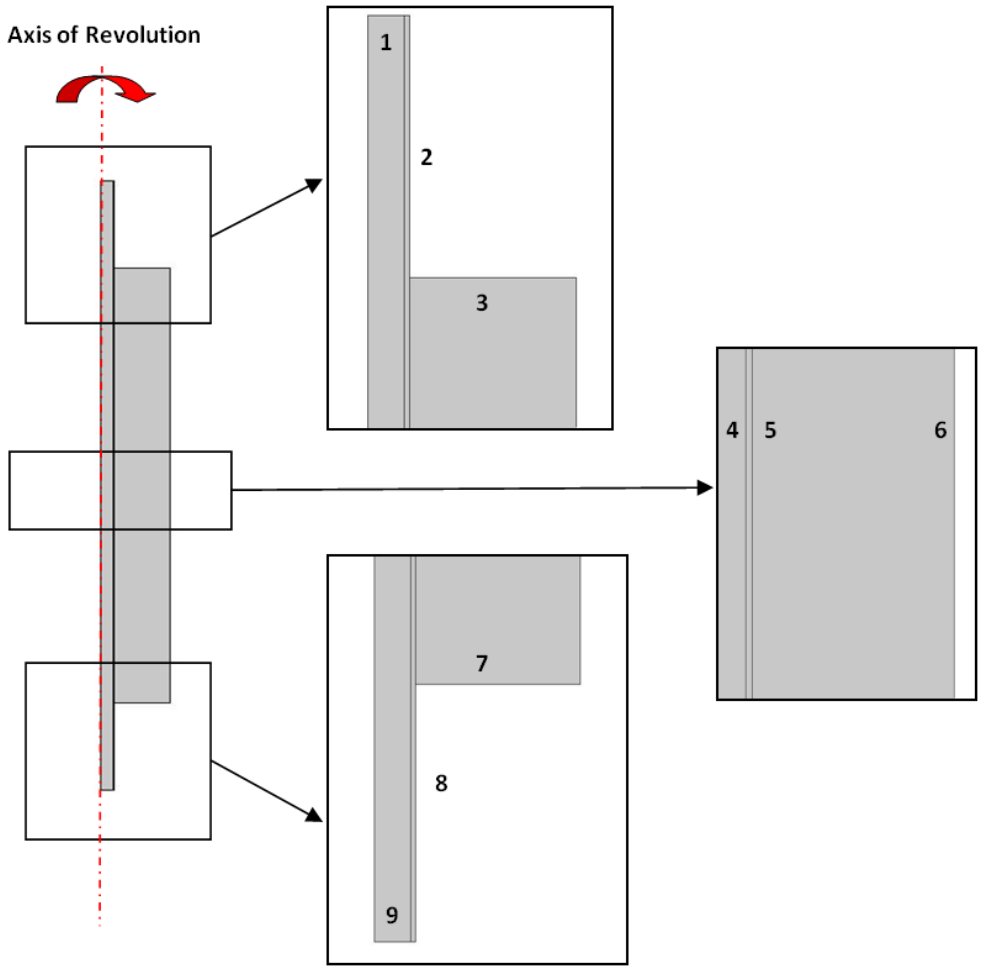

Figure 3.2 The boundaries of the 2-D axisymmetric analysis model

As given in Figure 3.2 boundary 1 is the inlet boundary for the heat transfer fluid (HTF), the boundary 2 and 8 are the outer surface of the HTT which are the interface between vacuum chamber space and the HTT. The boundary marked with number 3 is the upper outer boundary of the porous packed bed. The boundary number 4 is the boundary between HTF and HTT. Boundary number 5 is the boundary between HTT and the porous packed bed. The boundary with number 6 is the peripheral outer boundary of the porous packed bed. The boundary number 7 is the lower wall boundary of the porous packed bed which is similar to the number 3. Boundary

number 6 is the interface between vacuum chamber space and porous packed bed. Finally the boundary numbered with 9 is the outflow boundary of the HTF.

3.3 Governing Equations and Boundary Condition Definitions for the Comparative Analyses

As mentioned above the governing equations for different mathematical models will be solved on the computational 2-D axissymetrical domain numerically. In this part the governing equations that will be solved for each model, the boundary, initial conditions and operating conditions which defines the mode of operation will be discussed. In all of the cases the governing equations for HTF and HTT does not change. Therefore instead of repeating the same governing equations for each model first, these common equations will be given. The governing equations for modeling the fluid flow and heat transfer within the HTF and HTT will be referred here once. However the governing equations for the packed bed differ in each mathematical model and will be presented separately. In each part together with the governing equations the boundary conditions will also be defined for clarity.

Governing Equations for HTF

Mass, momentum and energy conservation equation for HTF used in all mathematical models are given below,

$$\rho_f \nabla . \mathbf{V_f} = 0 \tag{3.1}$$

$$\frac{D\mathbf{V_f}}{Dt} = -\frac{1}{\rho_f}\nabla p_f + \frac{\mu_f}{\rho_f}\nabla^2 \mathbf{V_f} \tag{3.2}$$

$$\rho_f c_f \frac{DT_f}{Dt} = k_f \nabla^2 T_f \tag{3.3}$$

Boundary conditions for HTF

As given in Figure 3.2 the HTF domain is surrounded by boundaries with number 1, 4, and 9 and an axis of revolution. The boundary 1 is the inflow boundary for HTF; the conditions defined at this boundary are as follows,

Boundary conditions for mass and momentum conservation equation:

Boundary 1

$$\mathbf{V_f} = -U_{inlet}\mathbf{n} \tag{3.4}$$

n represents the face normal for the boundary 1 and U_{inlet} is the inlet velocity value. Since momentum equation will be solved by coupling pressure and velocity the pressure of HTF at the inlet will be solved by using the outlet pressure condition.

Boundary 4

$$\mathbf{V_f} = 0 \tag{3.5}$$

As mentioned earlier there is no-slip condition defined at the wall of HTT which is in contact with the HTF.

Boundary 9

$$p_f = p_{outflow} \tag{3.6}$$

The boundary marked with number 9 is the outflow boundary of the HTF. At this boundary only pressure condition will be defined for solution of the momentum

equation. The pressure defined at the outflow boundary is uniform and constant valued. In all cases a gage pressure equal to 0 is defined at this boundary.

Boundary conditions for energy conservation equation:

Boundary 1

$$T_f = T_{inlet} \tag{3.7}$$

The HTF inlet temperature will be defined as uniformly and constant at the inlet. The value of inlet temperature will depends on mode of operation. The inlet temperature value will be set accordingly, for adsorption and desorption processes.

Boundary 4

$$T_f = T_t \tag{3.8}$$

The boundary marked with number 4 is the interface between HTF and HTF. At this boundary the temperature of HTF and HTT will be equal.

Boundary 9

$$-\mathbf{n} \,.\, (k_f \nabla . T_f) = 0 \tag{3.9}$$

The boundary type that will be used for the solution of energy conservation equation will be the insulation boundary which means the temperature gradient at outflow is equal to zero.

Governing Equations for HTT

As mentioned previously, heat transfer tube is rigid and immobile solid. Therefore only energy conservation equation will be solved for this domain.

$$\rho_t c_t \frac{\partial T_t}{\partial t} = k_t \nabla^2 T_t \tag{3.10}$$

Boundary conditions for HTT

As demonstrated in Figure 3.2 the HTT domain is surrounded by four boundaries. As mentioned above, the boundaries numbered as 2 and 8 are the interface of HTT and vacuum chamber space. As stated in the previous chapter according to the assumptions the radiative heat transfer is neglected in the vacuum space. Thus there will be no heat flow through these boundaries and these boundaries will be defined as no heat flux boundaries. The boundary numbers 4 is the interface between HTF and HTT and at this boundary the temperature of both domains are defined to be equal. The boundary number 5 is the interface between porous packed bed and HTT. As discussed in the previous chapter, heat transfer taking place at this boundary is both convective and conductive. As previously defined, a thermal contact resistance is defined at this boundary. The contact resistance is imposed on the numerical model by defining an explicit heat transfer coefficient to this boundary.

Since in LTE based models there is single temperature variable exist for the porous packed bed the heat transfer between HTT and porous bed is expressed in terms of this single temperature variable. In LTNE based models two separate temperature variables exist for the solid and gas phases. Therefore heat transfer between HTT and solid and gas phases are expressed by using temperature variables of gas and solid phase temperatures.

Boundary conditions for energy conservation equation:

Boundary 4

$$T_t = T_f \tag{3.11}$$

As mentioned above at the interface of HTF and HTT the temperatures of both domains are defined to be equal.

Boundary 5

For the LTE based models, the heat flux at the HTT-porous packed bed interface is defined as

$$-\mathbf{n} \,.\, (k_t \boldsymbol{\nabla} T_t) = h_{tg}\big(T_{gs} - T_t\big) \tag{3.12}$$

Similarly for the LTNE based models heat flux at the HTT-porous packed bed interface can be expressed as a combination of heat transfer between HTT and the solid and gas phases as follows,

$$-\mathbf{n} \,.\, (k_t \boldsymbol{\nabla} T_t) = \varepsilon_t h_{tg}\big(T_g - T_t\big) + (1 - \varepsilon_t) h_{tg}(T_s - T_t) \tag{3.13}$$

The ratio of area of contact with gas phase to the total interface area is assumed to be equal to total porosity. For this reason heat flux between HTT and the solid phase and heat flux between HTT and gas phases are multiplied by corresponding applicable area ratios.

Boundary 2 and 8

$$-\mathbf{n} \,.\, (k_t \boldsymbol{\nabla} T_t) = 0 \tag{3.14}$$

As mentioned earlier these boundaries are the interface of HTT and vacuum chamber spacing and since radiative heat transfer is neglected no-heat flux boundary condition is defined at these boundaries.

Governing Equations for the Packed Bed- Model 1

Up to this point the governing equations that had been used in the mathematical modeling of HTT and HTF are given. These equations are same for all of the mathematical models. On the other hand, the governing equations used for the modeling of packed bed will be different for the four different models stated above. The first model that will be discussed is named as Model 1: "LTE based model with pure vapor as gas phase". The governing equations used for this model can be presented as follows,

Mass conservation equation for the gas phase:

$$\varepsilon_t \frac{\partial \rho_g}{\partial t} + \left(1 - \varepsilon_g\right)\rho_s \frac{\partial X}{\partial t} + \boldsymbol{\nabla}.\mathbf{V_g} = 0 \tag{3.15}$$

Momentum conservation equation for the gas phase,

$$\mathbf{V_g} = -\frac{\kappa_g}{\mu}\boldsymbol{\nabla} p_g \tag{3.16}$$

Energy conservation equation for solid, gas and adsorbed phases,

$$\begin{aligned}&\varepsilon_t \rho_g c_{pg} \frac{\partial T_{gs}}{\partial t} - \varepsilon_g \frac{\partial p_g}{\partial t} + (1 - \varepsilon_t)\rho_s c_{ps} \frac{\partial T_{gs}}{\partial t} + (1 - \varepsilon_t)\rho_s X c_{pl} \frac{\partial T_{gs}}{\partial t} \\ &= \nabla\left(k_{eq} \nabla T_{gs}\right) + (1 - \varepsilon_t)\rho_s \frac{\partial X}{\partial t} \Delta H_{ad} - \rho_g \mathbf{V_g} c_{pg} \boldsymbol{\nabla}.T_{gs}\end{aligned} \tag{3.17}$$

Adsorption-desorption rate equation,

Since the adsorption equilibrium is not used in this study the adsorption rate defined by using the Linear Driving Force model which accounts for the internal mass transfer resistance within the adsorbent particles.

$$\frac{\partial X}{\partial t} = k_m\left(X_{eq} - X\right) \tag{3.18}$$

Equation of State

As an equation of state for the gas phase the ideal gas equation will be used to solve the system of equations by using numerical methods.

$$p_g = \rho_g R_g T_{gs} \tag{3.19}$$

Boundary conditions for the Porous Packed Bed-Model 1

The packed porous bed is surrounded by boundaries numbered as, 3, 5, 6 and 7 which had been shown in Figure 3.2. The boundary 6 is the peripheral interface between porous packed bed and the vacuum chamber. The boundaries 3 and 7 are defined as impermeable boundaries at the top and bottom of the bed. The boundary 5 is the interface between HTT and the adsorbent particles.

Boundary conditions for mass and momentum conservation equation:

Boundary 6

$$p_g = p_{chamber} \tag{3.20}$$

The gas phase intake and discharge to the vacuum chamber space will take place through these boundaries. For this reason the pressure at this boundary is defined to be equal to the vacuum chamber pressure and will be defined according to the mode of operation. During adsorption process vacuum chamber space will be connected to the evaporator and the pressure value defined for this boundary will be equal to

evaporator pressure, similarly the pressure value will be equal to condenser pressure during desorption process.

Boundary 3, 5 and 7

$$-\mathbf{n}.(\rho_g \mathbf{V_g}) = 0 \tag{3.21}$$

Boundary 5 is interface between HTT and the porous packed bed. Bondaries 3 and 7 area also defined as walls which is impermeable for vapor flow. Therefore for the gas phase flow and no-flow condition had been defined at these boundaries

Boundary conditions for energy conservation equation:

Boundary 6

$$-\mathbf{n}\,.(k_{eq}\boldsymbol{\nabla}\, T_{gs}) = 0 \tag{3.22}$$

Since boundary 6 is facing to the vacuum space and the radiative heat transfer is neglected in mathematical modeling, heat flux through this boundary will defined to be equal to zero. Similarly the top and the bottom boundaries surrounding the adsorbent bed (Boundary 3 and 7), zero heat flux boundary condition is used.

Boundary 5

$$-\mathbf{n}\,.(k_{eq}\boldsymbol{\nabla}\, T_{gs}) = h_{tg}\left(T_t - T_{gs}\right) \tag{3.23}$$

As defined above, this boundary is the interface between HTT and porous packed bed. Due to the previous definition of the thermal condition at this boundary the inward heat flux for the porous packed bed domain had been defined as the negative of the heat flux boundary condition used for the HTT Boundary 5.

Since the influx and outflow of the adsorption capacity from the porous packed bed is not possible, adsorption capacity fluxes are defined to be equal to zero at all boundaries of the porous packed bed.

Governing Equations for the Packed Bed- Model 2

The governing equations for Model 2: "LTE based model with air-vapor mixture as gas phase" will be discussed in this subsection. Only difference between model 1 and Model 2 governing equations will be the mass conservation equation. In Model 2 the mass transport equations for vapor and air species will be solved. Set of equations used for Model 2 are given below.

Mass transport equations for vapor and air species:

As mentioned above mass conservation equation for the gas phase is composed of mass transport equations for air and vapor species. The sum of these two mass transport equations will yield a mass conservation equation for the gas phase.

$$\frac{\partial(\rho_g \omega_v)}{\partial t} + (1-\varepsilon_t)\rho_s \frac{\partial X}{\partial t} + \boldsymbol{\nabla}.(\rho_g \omega_v \mathbf{V_g}) = \boldsymbol{\nabla}.(\rho_g \mathfrak{D}_{vaeq} \boldsymbol{\nabla} \omega_v) \tag{3.24}$$

$$\frac{\partial(\rho_g \omega_a)}{\partial t} + \boldsymbol{\nabla}.(\rho_g \omega_a \mathbf{V_g}) = \boldsymbol{\nabla}.(\rho_g \mathfrak{D}_{aveq} \boldsymbol{\nabla} \omega_a) \tag{3.25}$$

These two mass conservation equation for air and vapor species are solved by using a mass constraint. The mass constraint used is the sum of mass fraction of air and vapor is equal to 1.

$$\omega_a + \omega_v = 1 \tag{3.26}$$

Momentum conservation equation for the gas phase,

$$\mathbf{V_g} = -\frac{\kappa_g}{\mu}\boldsymbol{\nabla} p_g \tag{3.27}$$

Energy conservation equation for solid, gas and adsorbed phases,

$$\varepsilon_t \rho_g c_{pg} \frac{\partial T_{gs}}{\partial t} - \varepsilon_t \frac{\partial p_g}{\partial t} + (1-\varepsilon_t)\rho_s c_{ps} \frac{\partial T_{gs}}{\partial t} + (1-\varepsilon_t)\rho_s X c_{pl} \frac{\partial T_{gs}}{\partial t}$$
$$= \nabla\left(k_{eq} \nabla T_{gs}\right) + \left(1-\varepsilon_g\right)\rho_s \frac{\partial X}{\partial t} \Delta H_{ad} - \rho_g \mathbf{V_g} c_{pg} \boldsymbol{\nabla}. T_{gs} \tag{3.28}$$

Adsorption-desorption rate equation,

$$\frac{\partial X}{\partial t} = k_m\left(X_{eq} - X\right) \tag{3.29}$$

Equation of State

The density of gas phase is calculated by using the ideal gas law for mixture or species which is given below,

$$p_g = \rho_g R T_{gs}\left(\frac{M_v \omega_a + M_a \omega_v}{M_v M_a}\right) \tag{3.30}$$

Except the mass transport equations, all the boundary conditions that will be defined for Model 2 will be identical with the Model 1. Therefore these boundary conditions will not be rewritten here.

Boundary conditions for mass transport equations:

The porous packed bed domain is surrounded by boundaries 3, 5, 6 and 7. As defined above boundaries 3, 5 and 7 are impermeable for the gas phase flow. For this reason

at these boundaries no flow boundary condition will be defined for air and vapor species.

Boundary 3, 5 and 7

$$-\mathbf{n}.(-\rho_g D_{aveq}\nabla\omega_a + \rho_g \mathbf{V_g}\omega_a) = 0 \quad (3.31)$$

$$-\mathbf{n}.(-\rho_g D_{vaeq}\nabla\omega_v + \rho_g \mathbf{V_g}\omega_v) = 0 \quad (3.32)$$

Boundary 6

$$\omega_a = \omega_{a-chamber} \quad (3.33)$$

$$\omega_v = \omega_{v-chamber} \quad (3.34)$$

As stated above boundaries numbered as 6 is the interfaces between porous packed bed and the vacuum chamber spacing. At this boundary air and vapor mass fraction is dictated by the content of gas phase in the chamber. In the comparative analyses the air-vapor mass fraction at this interface is assumed to be constant which is equal to the vacuum chamber mass fractions for air and vapor.

Governing Equations for the Packed Bed- Model 3

The Model 3 is described as "LTNE based model with pure vapor as gas phase". Since Local Thermal Non-Equilibrium (LTNE) is assumed there will be two separate energy conservation equation for solid and gas phases within the packed bed. All the other governing equations of Model 3 will be identical with the Model 1.

Mass conservation equation for the gas phase:

$$\varepsilon_t \frac{\partial \rho_g}{\partial t} + (1 - \varepsilon_g)\rho_s \frac{\partial X}{\partial t} + \boldsymbol{\nabla}.\mathbf{V_g} = 0 \tag{3.35}$$

Momentum conservation equation for the gas phase,

$$\mathbf{V_g} = -\frac{\kappa_g}{\mu}\boldsymbol{\nabla} p_g \tag{3.36}$$

Energy conservation equation for solid phase,

$$\begin{aligned}&(1 - \varepsilon_t)\rho_s(c_{ps} + X c_{pl})\frac{\partial T_s}{\partial t} + \\ &= \boldsymbol{\nabla}(K_{seq}\boldsymbol{\nabla} T_s) + a_{gs}h_{gs}(T_g - T_s) + (1 - \varepsilon_t)\rho_s \frac{\partial X}{\partial t}\Delta H_{ad}\end{aligned} \tag{3.37}$$

Energy conservation equation for gas phase,

$$\begin{aligned}&\varepsilon_t \rho_g \frac{\partial(c_{pg}T_g)}{\partial t} + \rho_g \mathbf{V_g}.\boldsymbol{\nabla}(c_{pg}T_g) + c_{pg}(T_s - T_g)(1 - \varepsilon_t)\rho_s \frac{\partial X}{\partial t} \\ &= \boldsymbol{\nabla}(K_{geq}.\boldsymbol{\nabla}\langle T_g\rangle_g) - a_{gs}h_{gs}(T_g - T_s)\end{aligned} \tag{3.38}$$

Adsorption-desorption rate equation,

$$\frac{\partial X}{\partial t} = k_m(X_{eq} - X) \tag{3.39}$$

Equation of State

$$p_g = \rho_g R_g T_g \tag{3.40}$$

As stated above the difference between Model 3 and Model 1 is the energy conservation equations used. Therefore the boundary conditions for the energy conservation equations only will be redefined here for Model 3.

Boundary conditions for energy conservation equation:

Boundary 3, 6 and 7

$$-\mathbf{n} \,.\, (K_{geq} \boldsymbol{\nabla} T_g) = 0 \tag{3.41}$$

$$-\mathbf{n} \,.\, (K_{seq} \boldsymbol{\nabla} T_s) = 0 \tag{3.42}$$

These boundaries are interface between porous packed bed and vacuum chamber space. Since the radiative heat transfer is neglected in the calculations, the heat exchange between vacuum chamber and the packed bed at this boundary is assumed to be equal to zero. Therefore no heat flux boundary condition is defined at these boundaries.

Boundary 5

The heat transfer between HTT and porous packed bed interface can be expressed as a combination of heat exchange between the HTT and solid and gas phases as follows,

$$-\mathbf{n} \,.\, (k_t \boldsymbol{\nabla} T_t) = \varepsilon_t h_{tg} \left(T_g - T_t\right) + (1 - \varepsilon_t) h_{tg} (T_s - T_t) \tag{3.43}$$

The ratio of area of contact with gas phase to the total interface area is assumed to be equal to total porosity. For this reason heat flux between HTT and the solid phase and heat flux between HTT and gas phases are multiplied by corresponding applicable area ratios.

Governing Equations for the Packed Bed- Model 4

Model 4 is defined as "LTNE based model with air-vapor mixture as gas phase". Similar to Model 3 in Model 4 also based on Local Thermal Non-Equilibrium approach. Therefore there will be two separate energy conservation equations for solid and gas phases. Additionally the mass transport equation for air and vapor species will be solved since the gas phase is composed of these components.

Mass transport equations for the gas phase:

$$\frac{\partial(\rho_g \omega_v)}{\partial t} + (1-\varepsilon_t)\rho_s \frac{\partial X}{\partial t} + \boldsymbol{\nabla}.\left(\rho_g \omega_v \mathbf{V_g}\right) = \boldsymbol{\nabla}.\left(\rho_g \mathfrak{D}_{vaeq} \boldsymbol{\nabla} \omega_v\right) \tag{3.44}$$

$$\frac{\partial(\rho_g \omega_a)}{\partial t} + \boldsymbol{\nabla}.\left(\rho_g \omega_a \mathbf{V_g}\right) = \boldsymbol{\nabla}.\left(\rho_g \mathfrak{D}_{aveq} \boldsymbol{\nabla} \omega_a\right) \tag{3.45}$$

For being able to solve the mass transport equations a mass constraint is applied which had been used in Model 2 also. According to this constraint the sum of mass fraction of air and vapor should be equal to 1.

$$\omega_a + \omega_v = 1 \tag{3.46}$$

Momentum conservation equation for the gas phase,

$$\mathbf{V_g} = -\frac{\kappa_g}{\mu} \boldsymbol{\nabla} p_g \tag{3.47}$$

Energy conservation equation for solid phase,

$$(1-\varepsilon_t)\rho_s\left(c_{ps}+Xc_{pl}\right)\frac{\partial T_s}{\partial t}+$$
$$=\ \boldsymbol{\nabla}\left(K_{seq}\boldsymbol{\nabla}T_s\right)+a_{gs}h_{gs}\left(T_g-T_s\right)+(1-\varepsilon_t)\rho_s\frac{\partial X}{\partial t}\Delta H_{ad} \tag{3.48}$$

Energy conservation equation for gas phase,

$$\varepsilon_t\rho_g\frac{\partial\left(c_{pg}T_g\right)}{\partial t}+\rho_g\mathbf{V_g}.\boldsymbol{\nabla}\left(c_{pg}T_g\right)+a_{gs}c_{pg}\left(T_s-T_g\right)(1-\varepsilon_t)\rho_s\frac{\partial X}{\partial t}$$
$$=\ \boldsymbol{\nabla}\left(K_{geq}.\boldsymbol{\nabla}\langle T_g\rangle_g\right)-a_{gs}h_{gs}\left(T_g-T_s\right) \tag{3.49}$$

Adsorption-desorption rate equation,

$$\frac{\partial X}{\partial t}=k_m\left(X_{eq}-X\right) \tag{3.50}$$

Equation of State

$$p_g=\rho_g RT_{gs}\left(\frac{M_v\omega_a+M_a\omega_v}{M_vM_a}\right) \tag{3.51}$$

The boundary conditions used in Model 4 will not be rewritten since they had been defined previously. The boundary conditions used in Model 4 for mass conservation equation are identical with the boundary conditions used in Model 3. The boundary conditions that will be used in energy conservation equations of Model 4 is also identical with the boundary conditions used in Model 3.

3.4 Constants, Boundary and Initial Conditions Used in the Analyses

As stated in the previous sections the numerical analyses will be performed using LTE and LTNE approaches. Furthermore to understand the effect of a non-adsorbing species, additional analyses will also be performed during adsorption and desorption

processes. The governing equation system and the boundary conditions had been stated above. The adsorption cooling systems that had been investigated in the scope of this study is mainly based on the silica gel-water working pair. Therefore all the constants boundary and initial conditions are specific to this working pair. Additionally the operating conditions that are simulated in the analyses are chosen to represent the real conditions that can be experimentally simulated in the available adsorption-desorption experimental setups in the METU Heat Transfer Laboratory. The constant and parameters used in the analyses are taken from the available literature according to the simulated case. The constants and parameters used in the analyses are tabulated in Table 3.1 The unit for these parameters and the references where they had been taken are also given.

Table 3.1 Constants and used in the analyses

Parameter	Value	Unit	Definition and Reference
ε_b	0.37		Bed porosity [10,17,79]
ε_p	0.42		Particle porosity [10,17,79]
d_p	$2e^{-3}$	m	Adsorbent particle diameter[14]
μ_v	$1e^{-5}$	kg/m.s	Dynamic viscosity of water vapor [161]
k_v	0.024	W/mK	Thermal conductivity of water vapor[161]
c_{pv}	1880	J/kgK	Specific heat of water vapor [161]
M_v	18.02	kg/kmol	Molecular weight of water vapor [63]
μ_a	$1.983e^{-5}$	kg/m.s	Dynamic viscosity of air [161]
k_a	0.026	W/mK	Thermal conductivity of air[162]
c_{pa}	1005	J/kgK	Specific heat of air [162]
M_a	28.97	kg/kmol	Molecular weight of air [63]
ρ_s	670	kg/m^3	Density of the adsorbent particles [17,37]
k_s	0.198	W/m.K	Thermal conductivity of adsorbent particles[17,37]
c_{ps}	880	J/kg.K	Specific heat of adsorbent particles [17,37]
ρ_l	1000	kg/m^3	Density of adsorbed phase [162,37]
k_l	0.68	W/m.K	Thermal conductivity of adsorbed phase [162]
c_l	4180	J/kg.K	Specific heat of adsorbed phase [162]
ρ_f	914	kg/m^3	Density of HTF [14]
k_f	0.115	W/m.K	Thermal conductivity of HTF [14]
c_f	1930	J/kg.K	Specific heat of HTF [14]
μ_f	$1.002e^{-3}$	kg/m.s	Dynamic viscosity of air [162]
ρ_t	8700	kg/m^3	Density of HTT [162]
k_t	400	W/m.K	Thermal conductivity of HTT [162]
c_t	385	J/kg.K	Specific heat of HTT [162]
E_a	$1e^4$	J/mol	Surface diffusion activation energy [14,15]
D_0	$5.8e^{-9}$	m^2/s	Reference diffusivity [14,23]
h_{tg}	40	W/m^2	Convective heat transfer coefficient between packed bed and HTT [132]
R	8.314	kJ/mol. K	Universal gas constant [162]
Q_{ad}	2510	kJ/kg	Heat of adsorption [164]
σ_{av}	3.133	Å	Collision diameter of Lenneard Jones potential [63,163]

As stated earlier the base case analyses will be performed by using 4 different models with different boundary conditions. The boundary conditions will be different for adsorption and desorption cases. Additionally some of the boundary conditions are only applicable for the model used. Moreover, for being able to solve the governing equations, initial conditions need to be assigned for the variables according to the mode of operation. The initial conditions for the variables only change with the mode of operation and these will also be given in this section. The boundary and initial conditions that will be used in the comparative analyses are tabulated for each model and operation mode in the following tables. The comparative analyses had been performed under different scenarios which are based on the operating principle and the operating conditions of a two bed adsorption cooling system.

According to these scenarios, during adsorption phase of operation the adsorbent bed is initially at high temperature. During adsorption process cold heat transfer fluid starts to circulate with a fixed inlet temperature and flow rate to cool the adsorbent bed. The initial adsorption capacity of the bed is low at the beginning of adsorption process. In the desorption phase, the adsorbent bed is initially at low temperature and it is heated by the circulating high temperature HTF. HTF inlet temperature and flow rate is constant during the process. The bed is connected to condenser during desorption and connected to the evaporator during adsorption processes. The initial and boundary conditions are chosen based on the experience of the previous researchers that had been studied on the same laboratory test setup [14, 17, 10, and 23].

Table 3.2 Boundary and initial conditions of Model 1-adsorption analysis

Model 1-Boundary and Initial Conditions for Adsorption Analysis			
Variable	Value	Unit	Definition and reference
U_{inlet}	0.005	m/s	HTF inlet velocity [14,23]
$p_{outflow}$	1	atm	HTF outlet pressure
T_{inlet}	313	K	Temperature of the HTF at the inlet [17,10]
$p_{chamber}$	1.228	kPa	Vacuum chamber pressure, (evaporator pressure in case of adsorption)
$p_{initial}$	1.228	kPa	Initial pressure value for the gas phase in packed bed [17,10]
$T_{initial}$	473	K	Initial temperature value for, HTF, HTT and packed bed [17,10]
$X_{initial}$	0.0173	$kg_{water}/kg_{adsorbent}$	Initial value of the adsorption capacity at the packed bed

Table 3.3 Boundary and initial conditions of Model 2-adsorption analysis

Model 2-Boundary and Initial Conditions for Adsorption Analysis			
Variable	Value	Unit	Definition and reference
U_{inlet}	0.005	m/s	HTF inlet velocity [14,23]
$p_{outflow}$	1	atm	HTF outlet pressure
T_{inlet}	313	K	Temperature of the HTF at the inlet [17,10]
$p_{chamber}$	1.228	kPa	Vacuum chamber pressure, (evaporator pressure in case of adsorption) [17,10]
$\omega_{a\text{-}chamber}$	0.01	-	Mass fraction of air in the vacuum chamber
$\omega_{v\text{-}chamber}$	0.99	-	Mass fraction of vapor in the vacuum chamber
$p_{initial}$	1.228	kPa	Initial pressure value for the gas phase in packed bed [17,10]
$T_{initial}$	473	K	Initial temperature value for, HTF, HTT and packed bed [17,10]
$X_{initial}$	0.0173	$kg_{water}/kg_{adsorbent}$	Initial value of the adsorption capacity at the packed bed
$\omega_{a\text{-}initial}$	0.01	-	Initial air mass fraction within the packed bed
$\omega_{v\text{-}initial}$	0.99	-	Initial vapor mass fraction within the packed bed

Table 3.4 Boundary and initial conditions of Model 3-adsorption analysis

Model 3-Boundary and Initial Conditions for Adsorption Analysis			
Variable	Value	Unit	Definition and reference
U_{inlet}	0.005	m/s	HTF inlet velocity [14,23]
$p_{outflow}$	1	atm	HTF outlet pressure
T_{inlet}	313	K	Temperature of the HTF at the inlet [17,10]
$p_{chamber}$	1.228	kPa	Vacuum chamber pressure, (evaporator pressure in case of adsorption) [17,10]
$p_{initial}$	1.228	kPa	Initial pressure value for the gas phase in packed bed [17,10]
$T_{initial}$	473	K	Initial temperature value for, HTF, HTT and packed bed [17,10]
$X_{initial}$	0.0173	$kg_{water}/kg_{adsorbent}$	Initial value of the adsorption capacity at the packed bed

Table 3.5 Boundary and initial conditions of Model 4-adsorption analysis

Model 4-Boundary and Initial Conditions for Adsorption Analysis			
Variable	Value	Unit	Definition and reference
U_{inlet}	0.005	m/s	HTF inlet velocity [14,23]
$p_{outflow}$	1	atm	HTF outlet pressure
T_{inlet}	313	K	Temperature of the HTF at the inlet [17,10]
$p_{chamber}$	1.228	kPa	Vacuum chamber pressure, (evaporator pressure in case of adsorption) [17,10]
$\omega_{a\text{-}chamber}$	0.01	-	Mass fraction of air in the vacuum chamber
$\omega_{v\text{-}chamber}$	0.99	-	Mass fraction of vapor in the vacuum chamber
$p_{initial}$	1.228	kPa	Initial pressure value for the gas phase in packed bed [17,10]
$T_{initial}$	473	K	Initial temperature value for, HTF, HTT and packed bed [17,10]
$X_{initial}$	0.0173	$kg_{water}/kg_{adsorbent}$	Initial value of the adsorption capacity at the packed bed
$\omega_{a\text{-}initial}$	0.01	-	Initial air mass fraction within the packed bed
$\omega_{v\text{-}initial}$	0.99	-	Initial vapor mass fraction within the packed bed

The boundary and initial conditions that will be used in desorption analyses can be presented as follows.

Table 3.6 Boundary and initial conditions of Model 1-desorption analysis

Model 1-Boundary and Initial Conditions for Adsorption Analysis			
Variable	Value	Unit	Definition
U_{inlet}	0.005	m/s	HTF inlet velocity [14,23]
$p_{outflow}$	1	atm	HTF outlet pressure
T_{inlet}	473	K	Temperature of the HTF at the inlet [14,23]
$p_{chamber}$	4.247	kPa	Vacuum chamber pressure, (evaporator pressure in case of adsorption) [14,23,17,10]
$p_{initial}$	4.247	kPa	Initial pressure value for the gas phase in packed bed [14,23,17,10]
$T_{initial}$	313	K	Initial temperature value for, HTF, HTT and packed bed [14,23]
$X_{initial}$	0.3365	$kg_{water}/kg_{adsorbent}$	Initial value of the adsorption capacity at the packed bed

Table 3.7 Boundary and initial conditions of Model 2-desorption analysis

Model 2-Boundary and Initial Conditions for Adsorption Analysis			
Variable	Value	Unit	Definition and reference
U_{inlet}	0.005	m/s	HTF inlet velocity [14,23]
$p_{outflow}$	1	atm	HTF outlet pressure
T_{inlet}	473	K	Temperature of the HTF at the inlet [14,23]
$p_{chamber}$	4.247	kPa	Vacuum chamber pressure, (evaporator pressure in case of adsorption) [14,23,17,10]
$\omega_{a\text{-}chamber}$	0.01	-	Mass fraction of air in the vacuum chamber
$\omega_{v\text{-}chamber}$	0.99	-	Mass fraction of vapor in the vacuum chamber
$p_{initial}$	4.247	kPa	Initial pressure value for the gas phase in packed bed [14,23,17,10]
$T_{initial}$	313	K	Initial temperature value for, HTF, HTT and packed bed [14,23]
$X_{initial}$	0.3365	$kg_{water}/kg_{adsorbent}$	Initial value of the adsorption capacity at the packed bed
$\omega_{a\text{-}initial}$	0.01	-	Initial air mass fraction within the packed bed
$\omega_{v\text{-}initial}$	0.99	-	Initial vapor mass fraction within the packed bed

Table 3.8 Boundary and initial conditions of Model 3-desorption analysis

Model 3-Boundary and Initial Conditions for Adsorption Analysis			
Variable	Value	Unit	Definition and reference
U_{inlet}	0.005	m/s	HTF inlet velocity [14,23]
$p_{outflow}$	1	atm	HTF outlet pressure
T_{inlet}	473	K	Temperature of the HTF at the inlet [14,23]
$p_{chamber}$	4.247	kPa	Vacuum chamber pressure, (evaporator pressure in case of adsorption) [14,23,17,10]
$p_{initial}$	4.247	kPa	Initial pressure value for the gas phase in packed bed [14,23,17,10]
$T_{initial}$	313	K	Initial temperature value for, HTF, HTT and packed bed [14,23]
$X_{initial}$	0.3365	$kg_{water}/kg_{adsorbent}$	Initial value of the adsorption capacity at the packed bed

Table 3.9 Boundary and initial conditions of Model 4-desorption analysis

Model 4-Boundary and Initial Conditions for Adsorption Analysis			
Variable	Value	Unit	Definition and reference
U_{inlet}	0.005	m/s	HTF inlet velocity [14,23]
$p_{outflow}$	1	atm	HTF outlet pressure
T_{inlet}	473	K	Temperature of the HTF at the inlet [14,23]
$p_{chamber}$	4.247	kPa	Vacuum chamber pressure, (evaporator pressure in case of adsorption) [14,23,17,10]
$\omega_{a\text{-}chamber}$	0.01	-	Mass fraction of air in the vacuum chamber
$\omega_{v\text{-}chamber}$	0.99	-	Mass fraction of vapor in the vacuum chamber
$p_{initial}$	4.247	kPa	Initial pressure value for the gas phase in packed bed [14,23,17,10]
$T_{initial}$	313	K	Initial temperature value for, HTF, HTT and packed bed [14,23]
$X_{initial}$	0.3365	$kg_{water}/kg_{adsorbent}$	Initial value of the adsorption capacity at the packed bed
$\omega_{a\text{-}initial}$	0.01		Initial air mass fraction within the packed bed
$\omega_{v\text{-}initial}$	0.99		Initial vapor mass fraction within the packed bed

3.5 Numerical Solution Procedure and Spatial Discretization

The governing equations mentioned above together with the initial and the boundary conditions could only be solved by using the numerical methods. There are various numerical approaches exist however generating computational algorithms specific to certain purposes would be extensively time consuming. For this reason commercially available computation software will be used in this study. The analyses are performed in COMSOL Multiphysics 5.1. The 2-dimensional axissymmetric domain is spatially discretized into finite elements. The mesh generated by software can be seen in Figure 3.3. The mesh used for the solution is mapped type structured mesh and composed of quadrilateral elements. The HTF domain is meshed with finer

elements since coupled solution of pressure and velocity could be associated with large gradients and need to be resolved by using smaller mesh size.

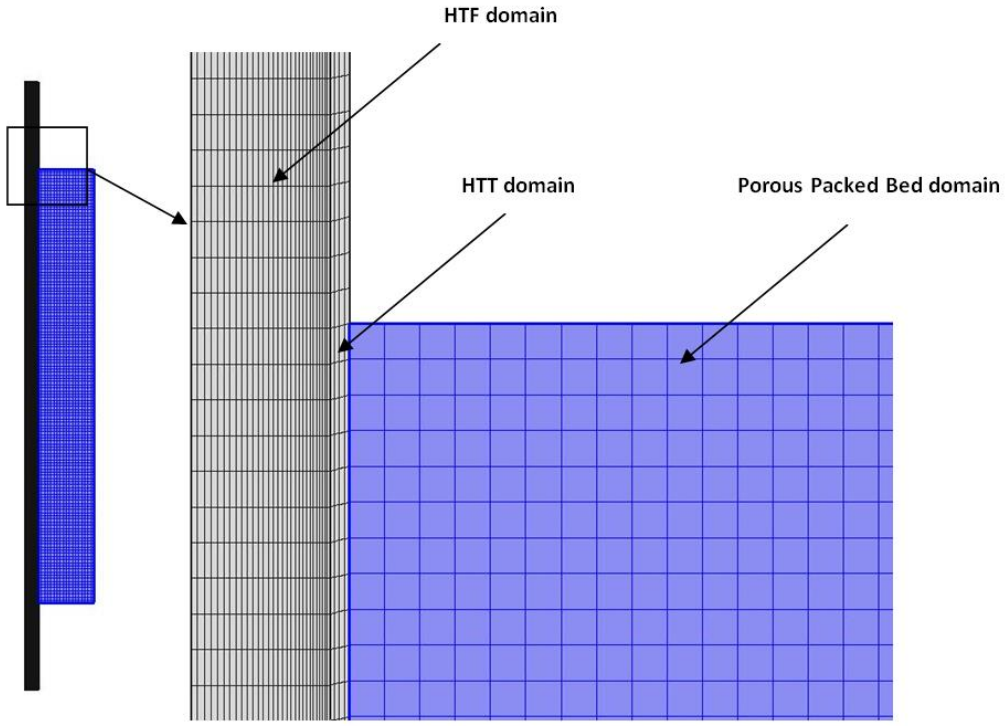

Figure 3.3 The meshed geometry that will be used in the computations

The equations solved are listed in the previous sections. Here the solution procedure and sequence will be mentioned in detail. For the solutions a segregated time dependent solver had been used. Fully coupled solutions in which all the variables are solved simultaneously requires higher amount of computer resources, in terms of memory and processor. Additionally the fully coupled numerical solutions have more tendency to diverge. Therefore segregated solution procedure had been followed which requires less amount of computer resources and relatively easier to converge.

The procedure followed in a single segregated solution step and the unsteady solution procedure followed can be described by the schematic given in Figure 3.4 and Figure 3.5 respectively.

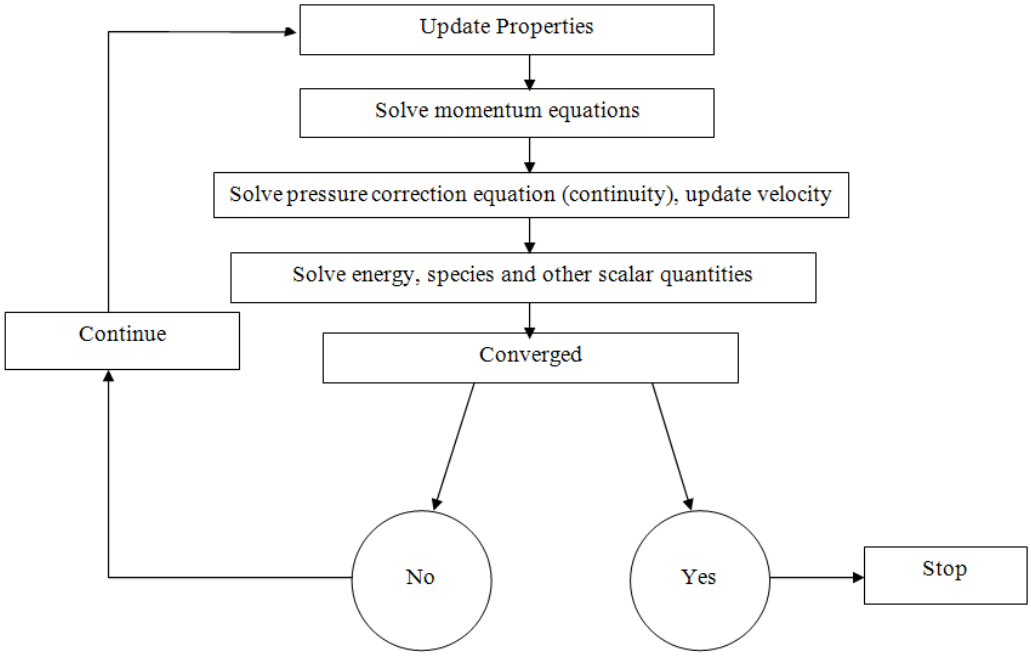

Figure 3.4 Segregated solution segregated step schematic

In a single segregated step, all the equations are solved separately by using the related variables obtained from previous iteration and this procedure will be repeated until a certain convergence criteria is satisfied. In this study the convergence criterion is the tolerance for each variable which is the scaled difference between two subsequent iterations. The segregated solution step will be repeated for each time step in a time dependent solution procedure. More details about the solvers available and the solution procedures in COMSOL can be found in [152].

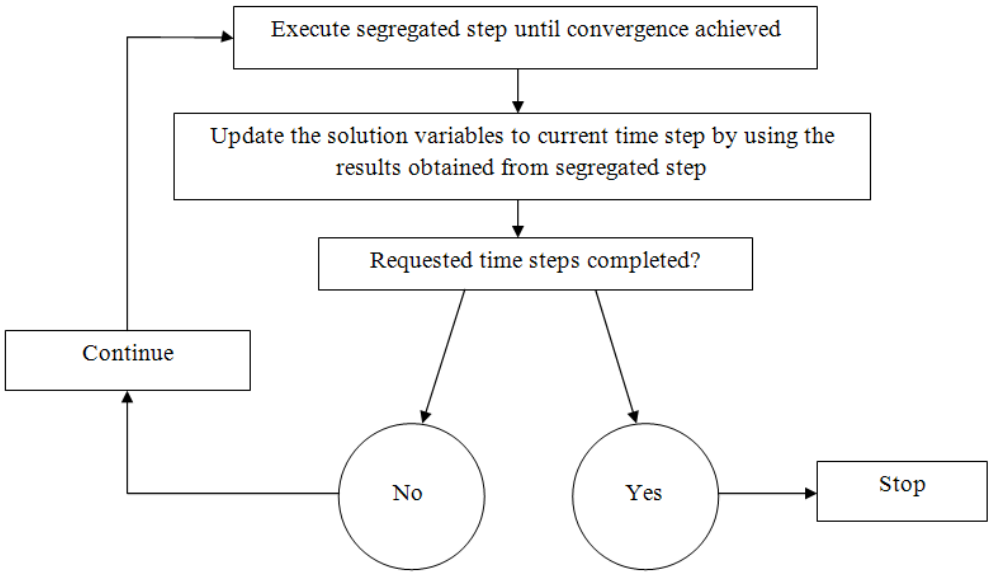

Figure 3.5 Time dependent segregated solution procedure schematic

3.6 Results of the Comparative Analyses

The results of the analyses performed will be presented for each model separately by using distribution contour plots and graphs of variation for solved quantities with time and location. Additionally for comparison, results obtained by using different models will be given together. Both adsorption and desorption analyses are performed for 18000 seconds by using the given boundary and initial conditions.

The graphs which are representing the variation of temperature with the time will be plotted by using the values taken from an arbitrary location. The location that will be used for extracting these values can be seen in Figure 3.6. The solid phase temperature will be used for the LTNE based models.

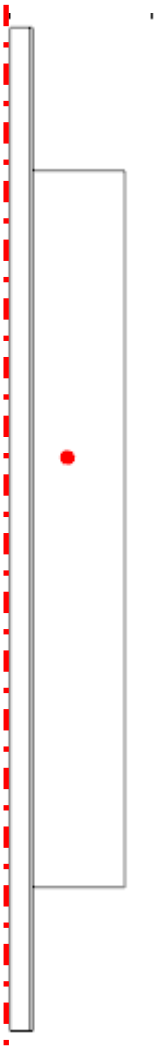

Figure 3.6 The point used for data extraction

As mentioned above the results will be presented in terms of distribution plots of temperature, adsorption capacity (X) and graphs plotted for demonstrating the variation of these quantities with location and time within the porous packed bed. The differences in mathematical modeling approaches and the effect of non-adsorbing gas will also be demonstrated based on these time variation plots and the contour plots.

The variation of temperature during desorption with time at the data point for all of the models can be seen Figure 3.7. The result of the models will be named based on the thermal equilibrium assumption and the composition of the gas phase in the plots for better understanding. The Model 1 results will be named as LTE-vapor while the results obtained from Model 2 is named as LTE-air-vapor. Likewise Model 3 and Model 4 results will be named as LTNE-vapor and LTNE-air-vapor respectively.

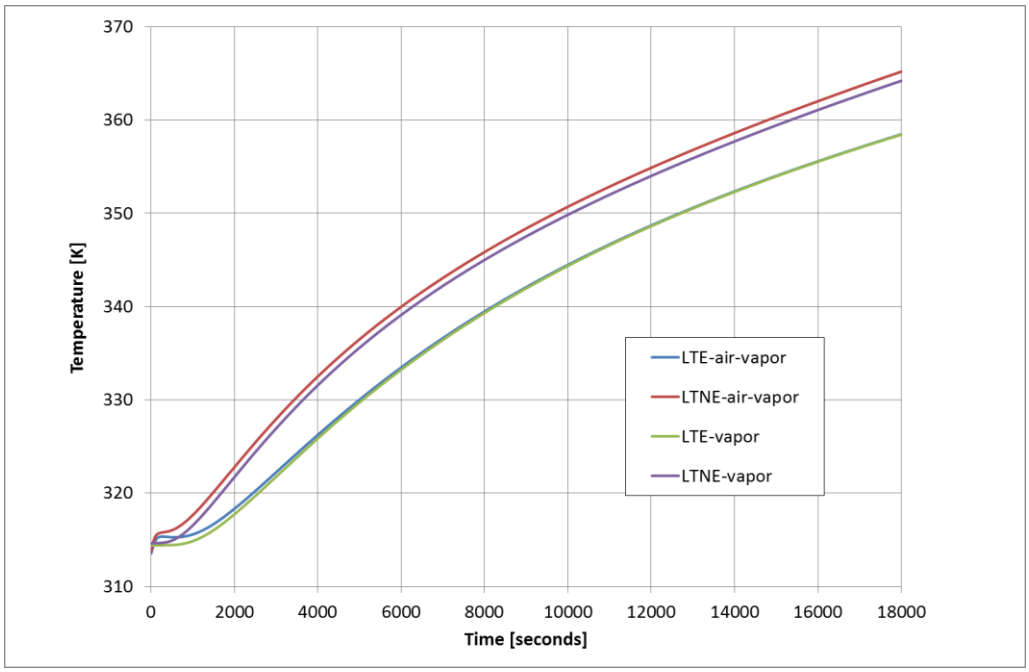

Figure 3.7 Time variation of the temperature at the data point for different models during desorption process

Regarding the temperature variations given in Figure 3.7, it can be said that, the LTE based models predicts the heat diffusion rate within the adsorbent bed less compared to LTNE based numerical models. The effect of air existence in the system is affected the temperature variation predicted by the LTNE based models. However the alteration in the temperature variation due to effect of air existence in LTE based numerical model is relatively small compared to LTNE based model results. Since heat exchange between solid and gas phase depends on the gas phase flow, in LTNE

based models air existence effect is more visible in the LTNE based models compared to LTE based ones. The adsorption capacity and temperature variations obtained from different analysis models are given in Figure 3.8 and Figure 3.9 for the desorption phase. The contour plots are taken at t=9600 s for comparison.

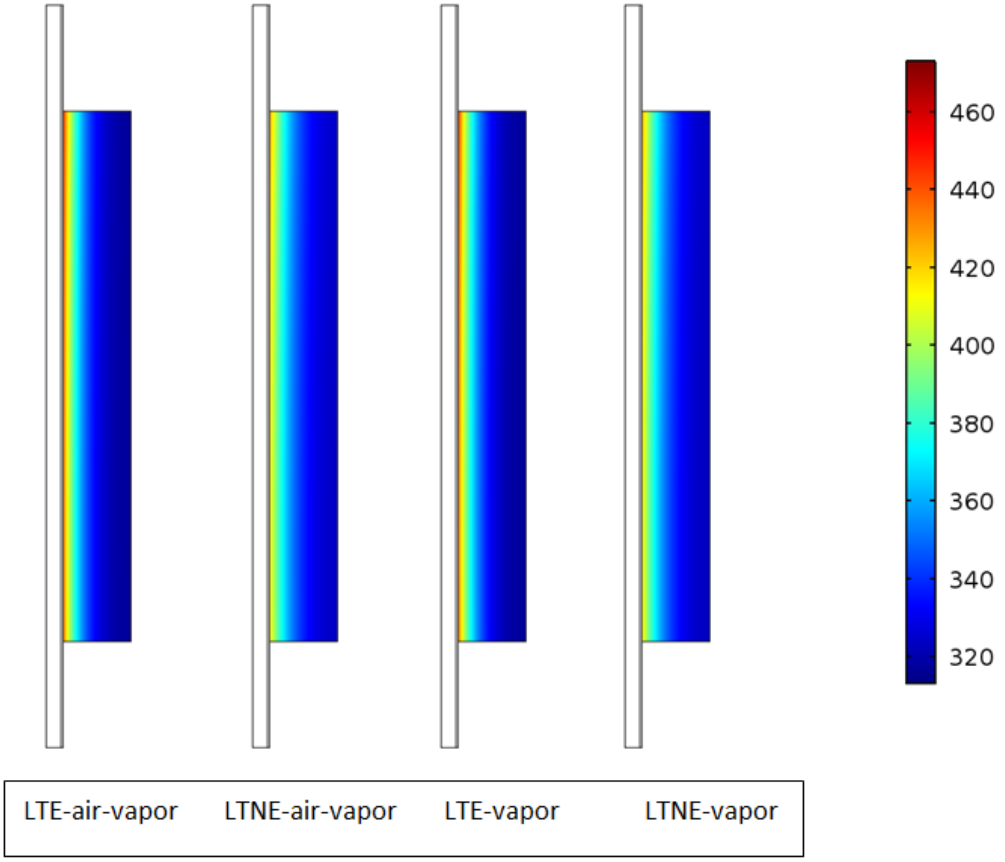

Figure 3.8 Temperature contour plots of the adsorbent bed at t=9600 taken from desorption analyses

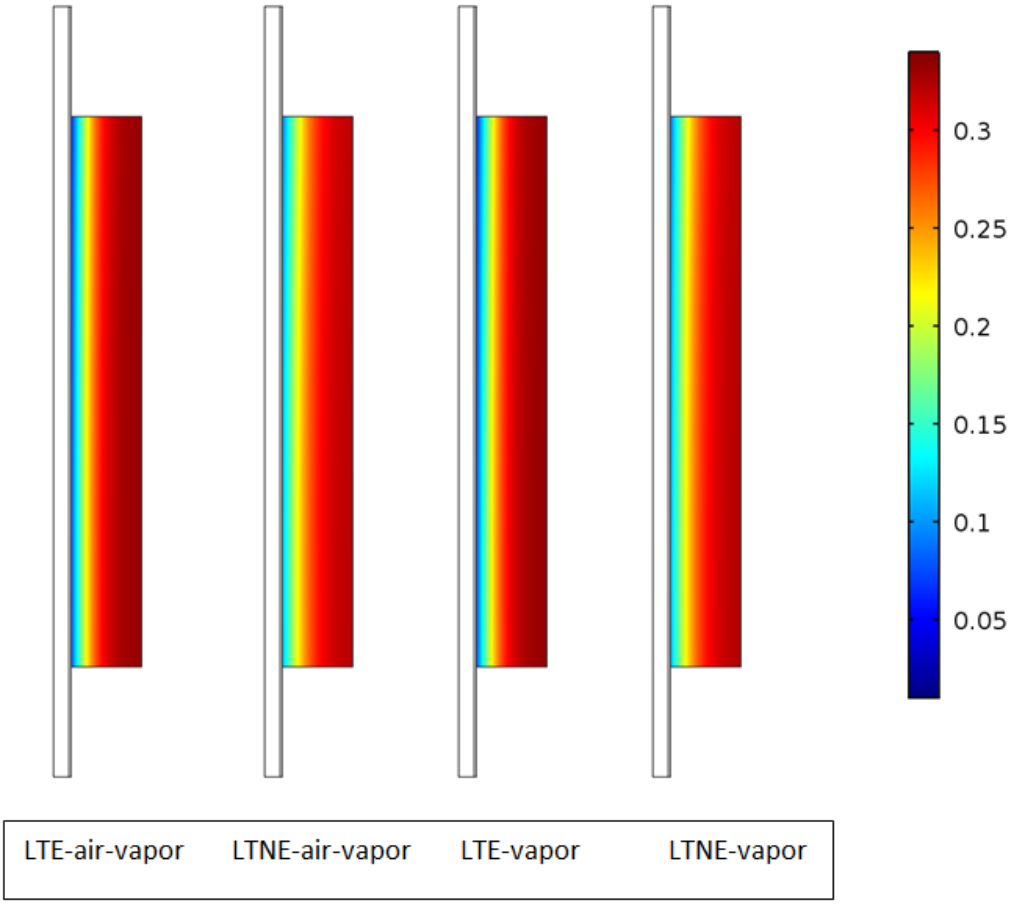

Figure 3.9 Adsorption capacity contour plots of the adsorbent bed at t=9600 taken from desorption analyses

When both, contour plots and the time variation plots of the numerical models are considered it could be concluded that during desorption process the differencs between results of LTNE and LTE based numerical models are not signifcant. Additionally the existence of air in the adsorbent bed does not dramatically changes the temperature and adsorption capacity distributions within the bed. Moreover the effect of the air is more emphasized by the LTNE based numerical model compard to

LTE based one.The time variation of the temperature at the same data point during the asdoprtion process is obtained by different models is given in Figure 3.10.

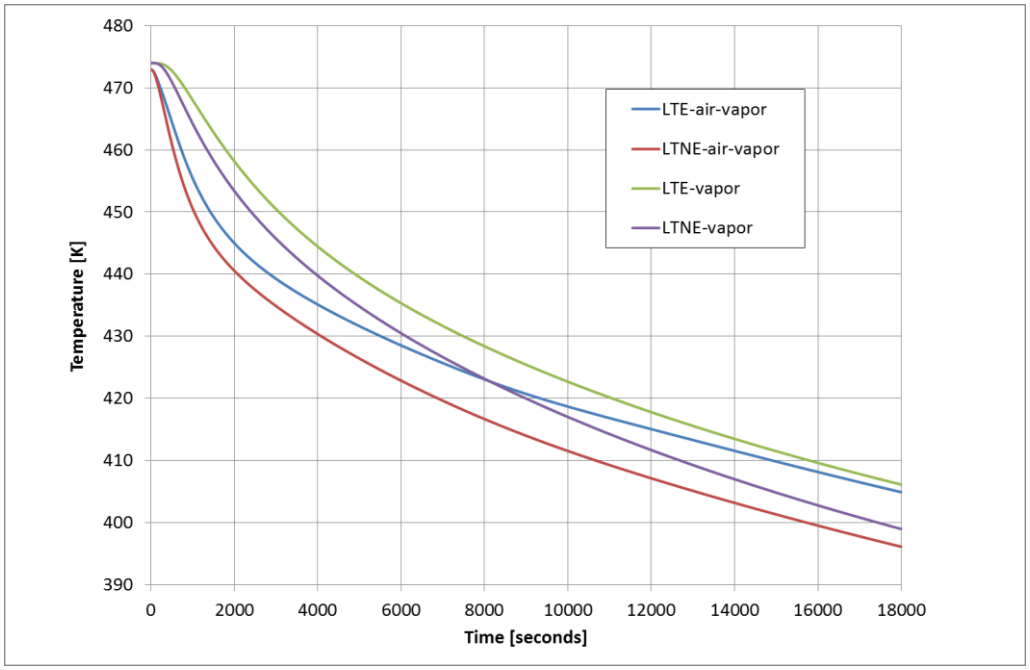

Figure 3.10 Time variation of the temperature at the data point for different models during desorption process

Unlike the temperature variations predicted during desorption process, the temperature variations due to air existence is more significant during adsorption regarding the results obtained from LTE and LTNE based numerical solutions. The difference between cases in which air exists and the ones with pure vapor decreases with time since adsorption process also slows down. The temperature and adsorption capacity distribution plots for the adsorption analyses also given in Figure 3.11 and 3.12 obtained from different numerical models at t=9600 second for comparison.

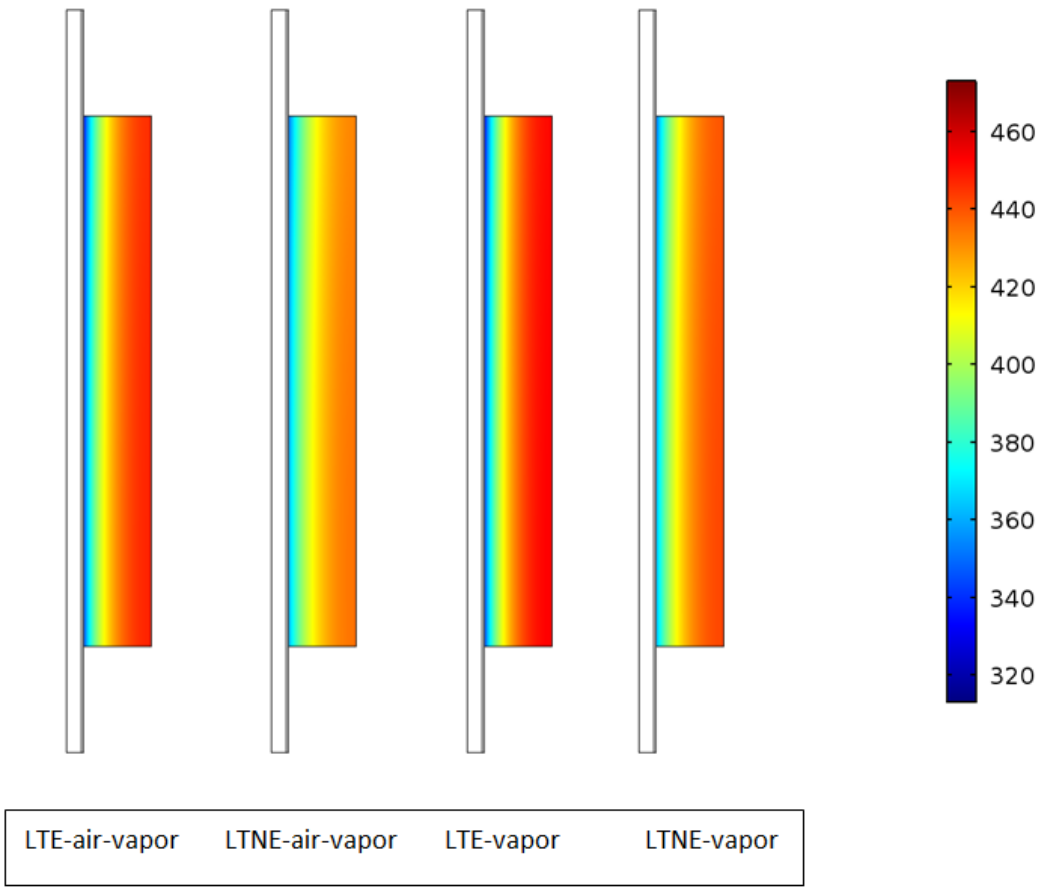

Figure 3.11 Temperature contour plots of the adsorbent bed at t=9600 taken from desorption analyses

Similar to the time variation plots obtained from different numerical models, it could be stated that the heat diffusion rate is higher for the LTNE based models compard to the LTE models. The difference between heat transfer rates of the LTE and LTNE models are probably caused by the definition of the effective thermal conductivity in LTE based models.

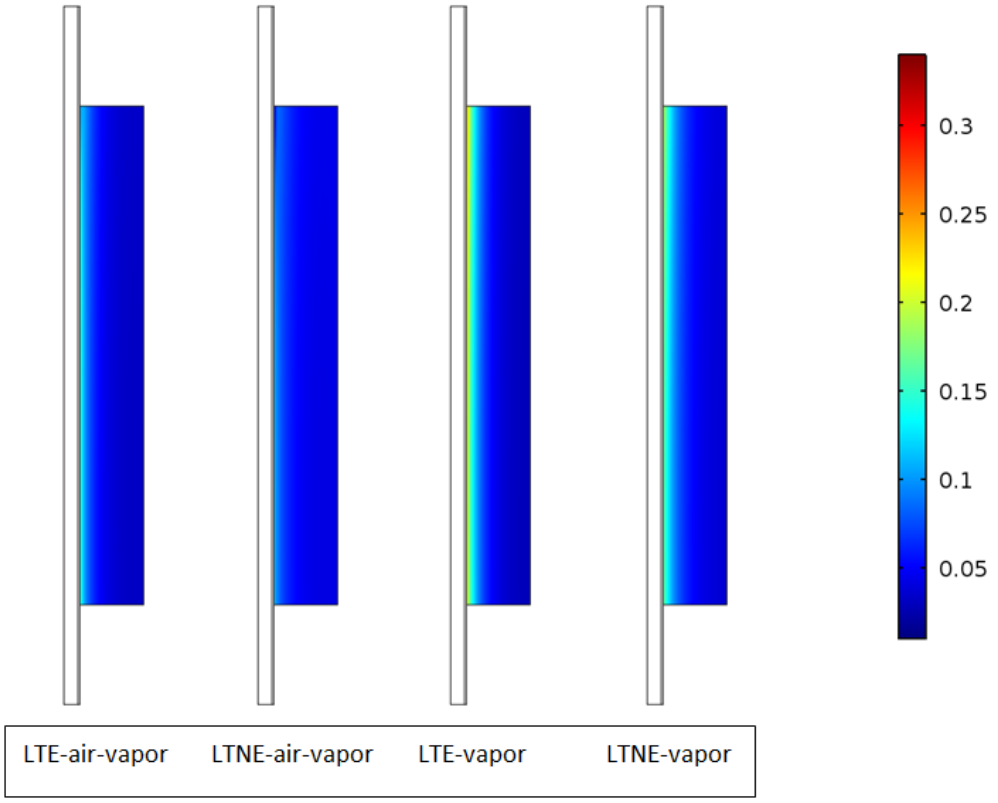

Figure 3.12 Adsorption capacity contour plots of the adsorbent bed at t=9600 taken from desorption analyses

Since adsorption process is taking place at low pressures the mass transfer rate within the bed is more affected by the mass transfer resistances. In case of air existence in the adsorbent bed, the air within the bed at the regions close to the HTT imposes an extra mass transfer resistance on the vapor flow into these regions. Therefore the adsorption capacity in the vicinity of HTT, adsorption capacity does not increase as high as the pure vapor conditions. Since vapor could not penetrate into the inner regions of the bed where the heat of adsorption is removed more effectively by the HTF, the adsorption rate of the bed is reduced due the existence of air in the bed. In the analyzed cases the mass fraction of air in the vapor is assumed to be equal to the 0.01. Regarding the differences resulted in adsorption capacity and temperature distributions, it could be concluded that, existence of a non-adsorbing gas in the

adsorbent bed would significantly affects the heat and mass transfer characteristics of the bed during adsorption process. The dramatic effect of non-adsorbing gas existence in the adsorbent bed also experimentally investigated and similar conclusions are drawn by Sapienza et al.[153]. On the other hand existence of a non-adsorbing gas has small effect on the heat and mass transfer characteristics of the adsorbent bed under desorption conditions. Desorption process is driven by the heat input to the bed via HTF therefore desorbed vapor concentration is higher at the inner regions in the vicinity of the HTT. The vapor at the inner regions flows through the bed toward the outer boundaries of the bed. While vapor is flowing outwards, it also thrust the air within the bed is towards the outer boundaries. Resultantly the effect of air existence is less emphasized on the mass and heat transfer characteristics of the bed during desorption process. However as a practical observation, existence of air in the adsorption system blocks the condensation in the condenser and would affect the bed eventually.

CHAPTER 4

EXPERIMENTAL INVESTIGATION

4.1 Introduction

The adsorption cooling systems suffers from low COP values compared to the conventional vapor compression refrigeration systems. One of the methods for improving the COP of adsorption cooling systems is the heat recovery method. Heat recovery methods can be applied to the systems which have two or more adsorbent beds which operate in an alternating manner. Additionally an intermediate medium which transfers heat (HTF) is also required for achieving heat recovery. In the heat recovery cycles a portion of sensible heat that is required for heating and pressurization of the desorbing bed is could be supplied by the rejected heat from adsorbing bed [113]. The most efficient way of heat recovery between two bed adsorption cycle could be achieved by the thermal wave type operation.[5,6,48]. The thermal wave heat recovery strategy is based on minimizing the external heat addition to the system [1, 5, 14, and 52]. When heat input to the system is at minimized the COP of cycle will be maximized. According to the numerical analyses performed, with the choice of radial thermal conductivity and high heat transfer coefficient between HTT and HTF it is possible to obtain COP values as high as 1.07 [7]. Another study which neglects the axial conduction within the adsorbent bed showed that COP values close to unity is also achievable [48].

According to the description in a thermal wave cycle temperature gradients in the axial direction of bed need to be large and a wave type temperature distribution should be obtained for HTF and the bed temperature variation with axial position [5].

The main idea behind the wave like temperature distributions is to obtain large temperature gradients in adsorbent bed and HTF along the axial distance. The described wave like temperature profile for bed along the adsorbent bed axial position can be seen in Figure 4.1

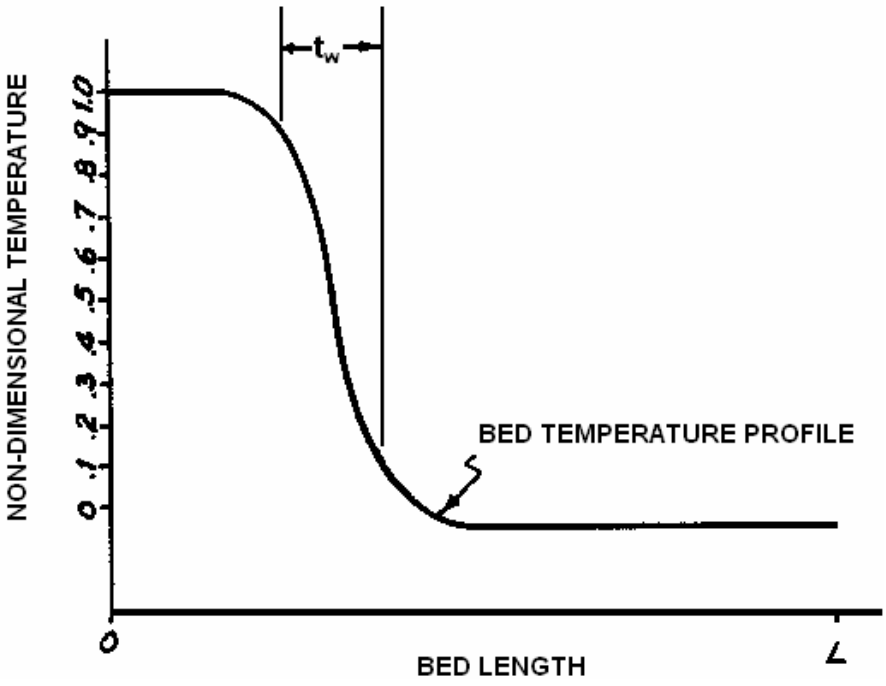

Figure 4.1 Wave like temperature distribution along the axial length of the bed and the thermal wave thickness [5]

The t_w shown in Figure 4.1 is denoted as the thermal wave thickness. The heat regeneration process would be more efficient with decreasing thermal wave thickness [2, 5, 14, and 83]. This temperature wave travels from one end of the bed to other during the process and the cycle is reversed. However, it is very difficult to obtain sharp thermal wave type temperature distributions within the adsorbent bed and HTF. Some of numerical analyses which neglect the axial conduction within the adsorbent bed demonstrated thermal wave type temperature variations with axial position [48,150]. Beyond these idealized cases a successful adsorption system prototype operating on thermal wave principle [1] had not been built yet. Since it is

practically difficult to obtain the thermal wave type temperature distributions in adsorbent bed with conventional design approaches, best design goal should be maximizing the axial temperature gradients within the adsorbent bed and increase the heat recovery efficiency of the system. The most successful implementation of this strategy is performed by Çağlar et al.[23]. The experimental results presented by Çağlar et al.[23] showed that practical approximations to thermal wave type temperature distributions within the adsorbent bed is possible. In the scope of this study two different bed designs will be proposed which are also expected to have large temperature gradients in the axial direction of the bed and HTF. Obtaining temperature gradients in the axial direction and similar temperature profiles like the thermal wave is desired since it would increase the heat recovery efficiency of the system.

There are a remarkable recommendations about the bed design exist in the literature for enhancing the heat recovery efficiency of the system by obtaining large axial temperature gradients within the bed and the HTF. These recommendations and the observations made by the researchers that guide the design approach followed in this study can be listed as,

- Heat transfer rate in the radial direction should be higher than the axial heat transfer rate [7, 48, and 23].
- Methods like consolidation could be used to increase the thermal conductivity of the adsorbent however it also causes high mass transfer resistance within the bed which would result in poor mass transfer performance. Therefore increase in the bed thermal conductivity at cost of poor mass transfer performance may deteriorate the performance of adsorbent bed [7].
- The increase in adsorbent bed radius will increase the amount of adsorbent and the cycled refrigerant. On the other hand increased the heat and mass transfer resistances within the bed would increase.[7,23]

- The HTF flow velocity is significantly affects the temperature gradients along the axial direction. Low HTF velocity or low advancement ratio of HTF in the axial direction is essential for obtaining thermal wave type large temperature gradients along the axial direction of the bed [23].
- The dead mass of the bed would not be design consideration since it does not affects the COP of the bed. Instead, design effort should be spent on obtaining sharp wavefronts within the bed and HTF [2].

In addition to the guidance of the results obtained by previous researchers, the adsorbent bed designs in the literature also surveyed and a novel design approach which had not been attempted before will be proposed. Some of the common adsorbent bed designs used in the adsorption cooling systems can be listed as,

- Straight circular HTT surrounded by cylindrical space filled with adsorbent particles [6, 7, 32, 33, 35, 36, 38, and 46]. Straight flat plate fins are added in some cases [11].
- Straight circular HTT with circular fins (finned tube) surrounded by cylindrical space filled with adsorbent particles [14, 23, 44, 53, 93, 105].
- Annular space between two concentric cylinders filled with adsorbents [17, 10, and 43]. In the solar collector/adsorbent bed applications, this shape also preferred but bed is heated by solar radiation instead of HTF. [92, 95, 100, 102, 103]
- In some of the practical applications spaces between the extended surfaces of conventional heat exchangers filled with adsorbent particles and used as adsorbent beds. Some of the different heat exchanger types used can be listed as; Shell and tube heat exchanger [85], plate finned tube heat exchangers [22,114], finned flat tube heat exchanger [89].

- In some of the solar applications adsorbent beds are obtained by filling the rectangular space between fins of flat plate solar collector. [42, 91, 96]

Another factor which shapes the design of the beds is the test environment available in the laboratory. Since the existing vacuum chamber has 22 mm ports available for the HTT the largest outer diameter for the HTT should be 22 mm. The vacuum chambers length and the diameter also restrict the dimensions of the adsorbent bed designs that will be proposed. Beyond the geometric aspects, one other property that adsorbent bed should possess is the long cycle times which enable continuous operation of a solar powered system with two adsorbent beds under intermittent solar energy source conditions. Therefore the cycled refrigerant amount and resultantly the adsorbent amount in the bed should be chosen accordingly. Moreover, silica gel-water pair is used owing to its high performance in solar powered adsorption cooling applications and its suitability for the available experimental setup.

In the scope of this thesis two different adsorbent bed designs will be proposed. These beds are manufactured, numerically analyzed and experimentally successfully investigated.

As stated the main aim of this numerical and experimental investigation is to develop an understanding about the heat and mass transfer principles in an adsorbent bed while trying to improve the heat recovery efficiency by obtaining large temperature gradients in the axial direction of the bed like thermal wave temperature distribution. For this purpose experiments are performed on the designed and manufactured adsorbent beds. The experiments performed are mainly based on the desorption process since the available experimental setup design and capability. The evaporator the experimental setup is suitable for cycling small amount of refrigerants at low adsorption rates however the beds that are tested in this study are relatively large and have high adsorption rate at low operating pressures. Since adsorption potential of the bed is high, most of the adsorption experiment attempts are resulted with the suction of liquid refrigerant in the vacuum line. When evaporator and the vacuum line fills with liquid refrigerant, evaporation take place at the free surface of the liquid refrigerant and the cooling effect cannot be observed in the cold space where it

is expected to be. Consequently, the experimental investigation will be mainly based on the desorption processes. The result of a successful adsorption experiment will also be shared to demonstrate the longer adsorption times compared to desorption and the cooling effect obtained.

The experimental results and the numerical analyses that will be presented in this chapter is restricted with five hours of duration due to the limitations of the data logger memory .Moreover increased analysis duration result in increase of the data file sizes which is approximately 17 GB for five hour transient analyses

4.2 Experimental Setup

The experimental setup that will be used for the investigation of the adorbent bed designs is capable of testing single adsorbent bed by imposing desired boundary conditions. As mentioned the experimental setup is a modified version of the setup that had been used by previous researchers [14, 17]. After the modifications the current configuration of the experimental setup can be demonstrated by the schematic given in Figure 4.2. As a general principle of operation experimental setup is designed to supply HTF to the adsorbent bed at desired temperature and flow rate. The vacuum chamber which contains adsorbent bed can be connected to evaporator or condenser due to the mode of operation. The chamber is connected to condenser during desorption process while it is connected to evaporator during adsorption process. The details on the operation of experimental setup are given in the experimental procedure subsection.

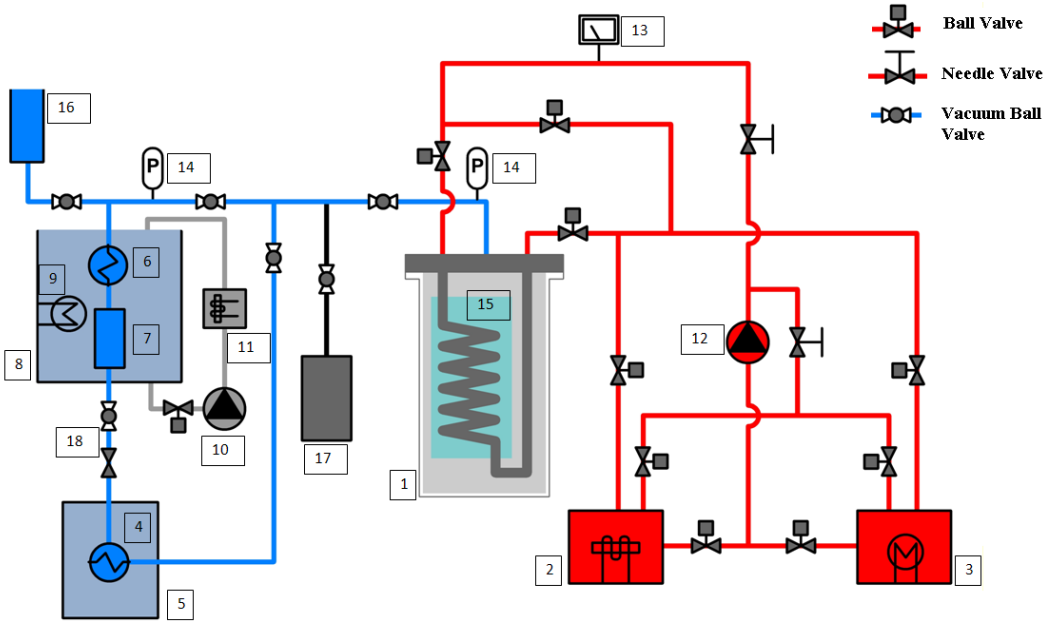

Figure 4.2 Schematic representation of the experimental setup used in the tests

In the Figure 4.2 numbered components of the experimental setup can be listed as follows,

1- Vacuum chamber
2- Cold HTF tank
3- Hot HTF tank
4- Evaporator
5- Cooling space of the evaporator
6- Condenser tube bundles
7- Condenser canister
8- Water bath of the condenser
9- Heater of the condenser water bath
10- Circulation pump of the condenser water bath
11- Heat exchanger of the condenser water bath
12- HTF pump
13- HTF flowmeter
14- Pressure transducers vacuum line

15- Adsorbent bed
16- Refrigerant (water) feed line
17- Vacuum pump
18- Capillary tube and throttling valve

The setup is composed of three main sections, one of which is the vapor (refrigerant) line. The vapor flow line is the blue colored line and the blue colored components belong to the vapor line. The second section is the HTF flow line which is shown by the red lines in Figure 4.2 and the last section is composed of data acquisition components.

The main components of the vapor line section are the
-Adsorbent Bed Assembly

- Adsorbent Bed
- Vacuum Chamber

-Evaporator
-Condenser
-Expansion valve and capillary tube

Similar to the vapor line, there are three main components exists in the HTF line. These components are

- Hot HTF tank
- Cold HTF tank
- HTF circulation pump

The data acquisition and logging section contains the sensors and the data logging device. The components of this section can be listed as,

- Pressure transducers

- Thermocouples
- Flowmeter
- Data logging device

In addition to these components listed above there are plenty of auxiliary components used for the construction of the setup such as HTF pipes, vacuum piping and the vacuum pump. These components will also be mentioned in the related subsections.

4.2.1 Adsorbent Bed Assembly

Adsorbent bed assembly is the main component of the experimental setup since this is the component subject to investigation in this study. Therefore extensive effort is made for design and manufacturing of the adsorbent beds that will be tested. Since this setup is a single-bed test setup each bed is tested separately. The beds can be tested during adsorption or desorption according to the operational conditions set. However the reasons for performing only desorption analyses had been presented in the introduction.

Adsorbent bed assembly is composed of subcomponents which can be listed as,

- Vacuum chamber
- Adsorbent bed

The adsorbent bed is composed of adsorbent particles, frame, metallic net and the HHT section. The whole assembly placed into the vacuum chamber will be named as the adsorbent bed. The vacuum chamber can be connected to evaporator during adsorption process or can be connected to the condenser during desorption process by the piping arrangement that can be seen in Figure 4.2

4.2.1.1 Vacuum Chamber

The vacuum chamber is constructed to satisfy the vacuum requirements and tested extensively for leaks. The chamber is manufactured by the Vaksis Company and had been used in the research project of Çağlar [14]. The material of the chamber is high temperature stainless steel. The chamber is composed of a body and a cap. The cap is clamped to the flange of the body via four clamps. To maintain the vacuum seal two O-ring channels machined to the flange of the body. The capped design enables the placement of suitably designed beds.

There are two ports on the vacuum chamber body. T-pipes are welded to these ports. One of them is used for evacuating the chamber and the other one is left as an auxiliary port. Additionally there are four ports exists in the cap of the chamber. Two of these ports are used as the HTF tube inlet and exit. The other two ports are used as a passage for the thermocouple connections. Two feed through connectors for thermocouples will be installed on these ports. All of the ports on the cap are facilitated with O-ring sealing to maintain the vacuum. The 3-D cad model of the chamber is reconstructed for placement of the designed bed assemblies. The 3-D cad model and a photograph of the vacuum chamber can be seen in Figure 4.5 and Figure 4.6.

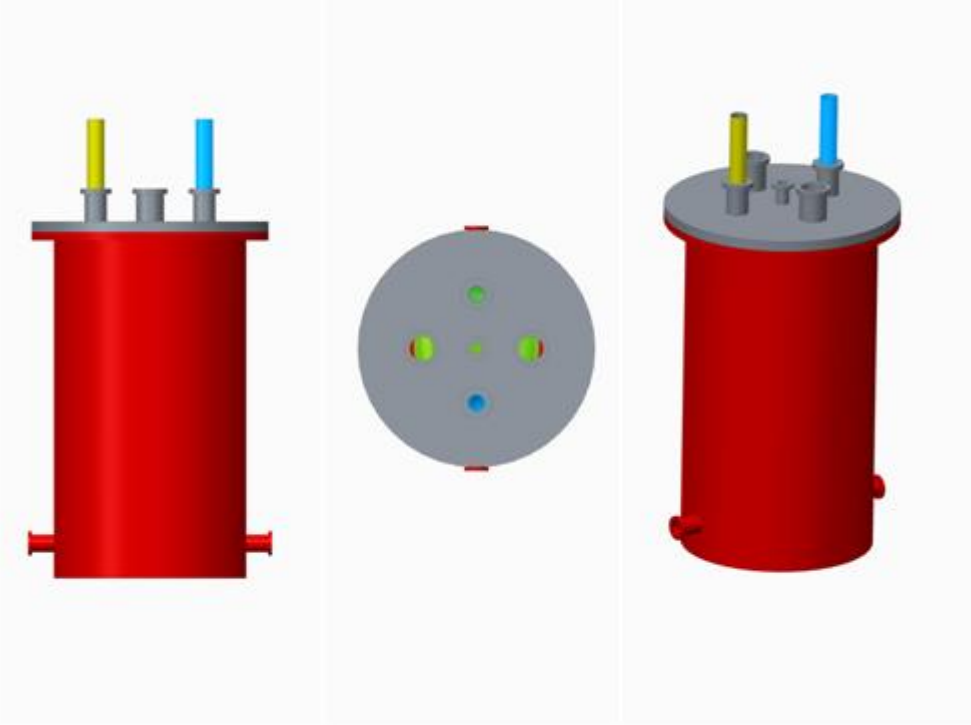

Figure 4.3 3-D CAD model of the vacuum chamber

Figure 4.4 Photograph of the vacuum chamber [14]

4.2.1.2 Adsorbent Bed

The adsorbent bed consists of bed frame, metallic net, HTT section and the adsorbent particles Main design and manufacturing efforts in this study is focused on the bed assembly. The details related with adsorbent bed designs will be given in the following sections.

4.2.1.2.1 Adsorbent Bed Design 1

As stated in the introduction part, the designs that will be proposed in the scope of this study are aiming to improve the heat recovery efficiency by obtaining large temperature gradients in the axial direction of the bed which resembles the thermal wave like temperature distribution. Based on the previously performed studies and used adsorbent bed designs, a design which had not been attempted before will be used here. The design can be called as uncommon since most of the studies in the literature are based on the same kind of adsorbent bed designs. Current design is based on the philosophy of increasing the radial heat transfer rate of the adsorbent bed while reducing the axial heat transfer rate to increase the temperature gradients in the axial direction. One of the approaches that can be used for increasing the radial heat exchange rate is the elongation of the HTF flow path in the radial direction while reducing the axial advancement rate of HTF.

One design alternative which can increase the radial heat transfer rate while reducing the axial one in the bed can be a cylindrical bed with a helical HTF flow path. Helical HTT placed concentrically in a hollow cylindrical adsorbent bed is one of the design alternatives proposed here. The 3-D CAD model of the Bed Design 1 can be seen in Figure 4.5

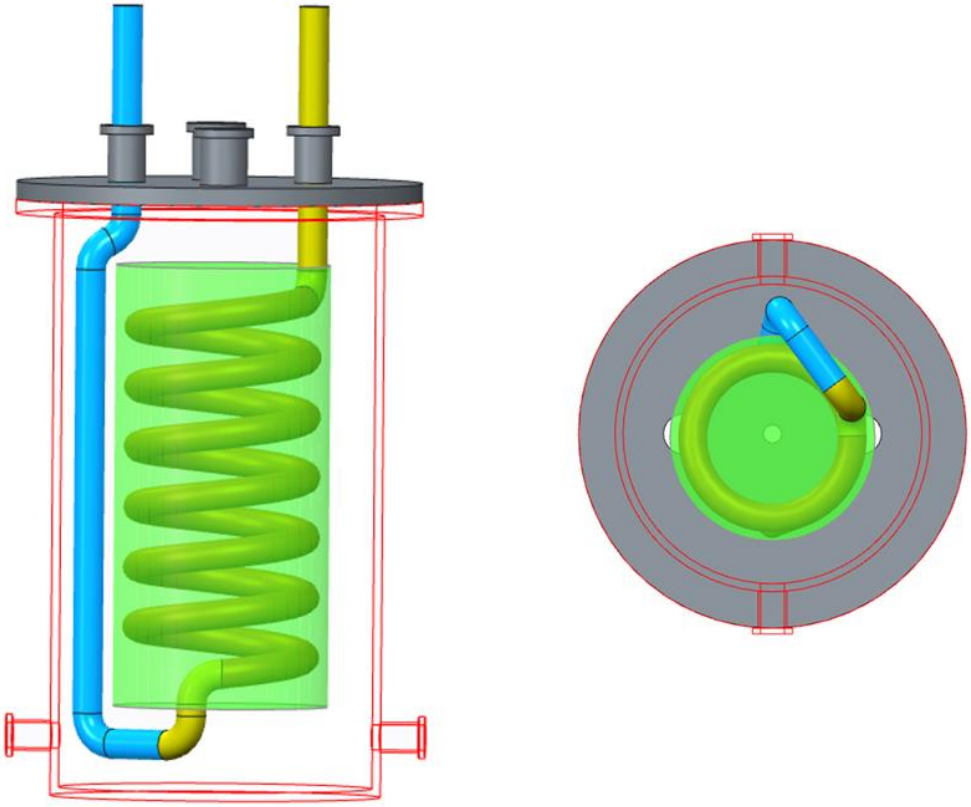

Figure 4.5 3-D CAD model of the Bed Design 1 with vacuum chamber, front and bottom views

The helical HTF flow path is a design attribute which is used for enhancing the heat transfer rate. Additionally it is also known that mass transfer rate is also important for bed design and should be considered. The bed is designed as a hollow cylinder to reduce the mass transfer resistance by reducing the number of adsorbent layers around the HTT. Hollow cylindrical design also facilitates refrigerant vapor flow from inner and outer peripheral surfaces. Moreover as it had been stated in the previous parts, the enhancements in the thermal conductivity by consolidation or similar methods generally increases the mass transfer resistances within the bed. Therefore the designs are constructed as standard packed beds since mass transfer rate of water is known to be low due to low operating temperatures.

The HTT is constructed from copper 20 mm diameter pipe. As stated one of the constraints for the design are the HTT ports available in the vacuum chamber. The maximum diameter of the HTT could be 22 mm since ports of the vacuum chamber has this dimension. The closest available copper pipe in the market was in 20 mm diameter so in the design of the adsorbent beds, 20 mm copper pipe with 1 mm wall thickness had been used. The helical section of the HTT is manufactured by winding process. The pipe is filled with metallic spheres and then wound around a mandrel. The manufacturing process is done by Deniz Yay A.Ş. The final shape of the HTT is obtained by the brazing straight pipe sections and elbows and the helical section together. The HTT before brazing operation can be seen for Bed Design 1 in Figure 4.6

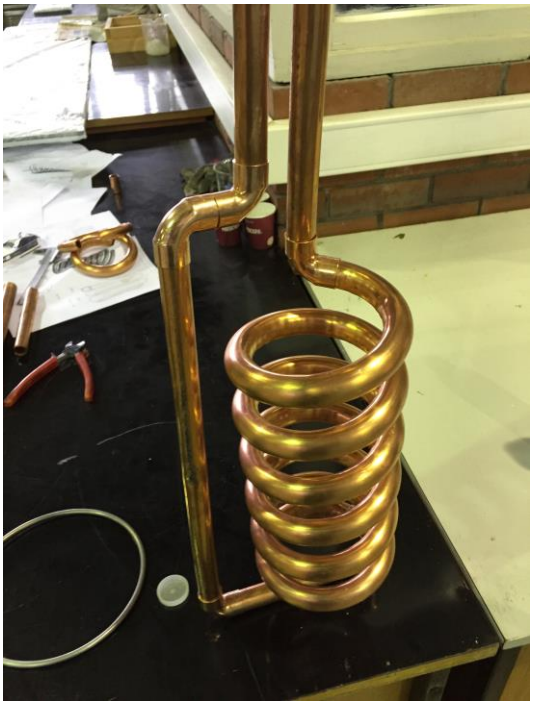

Figure 4.6 The HTT for Bed Design 1 before brazing operation

The silver brazing operation chosen for reducing the possible warping of work piece. The silver brazing operation of the HTT is made by Özsan A.Ş. The final shape of the HTT of Bed Design 1 after brazing operation can be seen in Figure 4.7

Figure 4.7 HTT of Bed Design 1 after brazing operation

In addition to the HTT the adsorbent bed also composed of adsorbent particles, metallic net that hold particles together and the metallic frame that supports the metallic net holding the adsorbent particles together around the HTT. The frame is constructed by using 6mm stainless steel sticks. The frame structure is formed by welding operation. TiG welding technique is used for construction of the adsorbent bed frame. The metallic net is stitched on the frame by hand. The metallic net is also manufactured from stainless steel with a mesh size of 18. The pictures showing the stitching stages of the metallic net for Bed Design 1 can be seen in Figure 4.8.

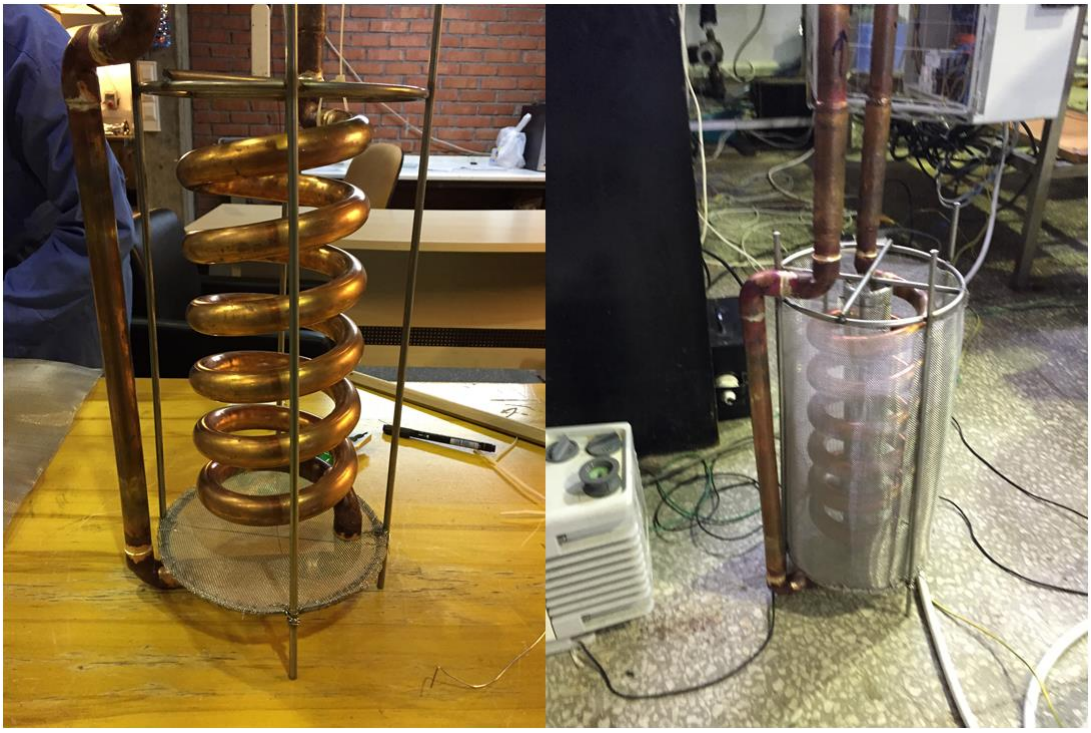

Figure 4.8 HTT of Bed Design 1 metallic net stitching operation

After completion of the stitching process of the metallic net on the frame the only missing component is the adsorbent particles. In the experiments silica gel with 4 mm average diameter produced by Damla Kimya A.Ş. will be used. The data sheet supplied by the producer for the silica gel used in the experiments can be seen in Appendix G. Since this silica gel had been used in the previous studies, the thermo physical properties that are not available in the data sheet are taken from [14 and 17].

The silica gel is filled to the bed after total regeneration in the electric oven. According to the suppliers data sheet regeneration should be done at 160-172 ^{o}C temperature at least for 4 hours. After total regeneration of the silica gel it is filled into the bed between metallic net and HTT. The amount of silica gel poured into the bed is weighed and recorded. Before replacing the adsorbent bed into the vacuum chamber, thermocouples are placed to the predefined measurement points. As stated above there are two thermocouple feedthrough ports exists in the the vacuum

chamber and also there are two K type thermocouple feedthrough s exists. Therefore it is possible to measure temperature of 10 different points within the vacuum chamber. The temperature measurement points shown on the crossectional view of Bed Design 1 can be seen in Figure 4.9

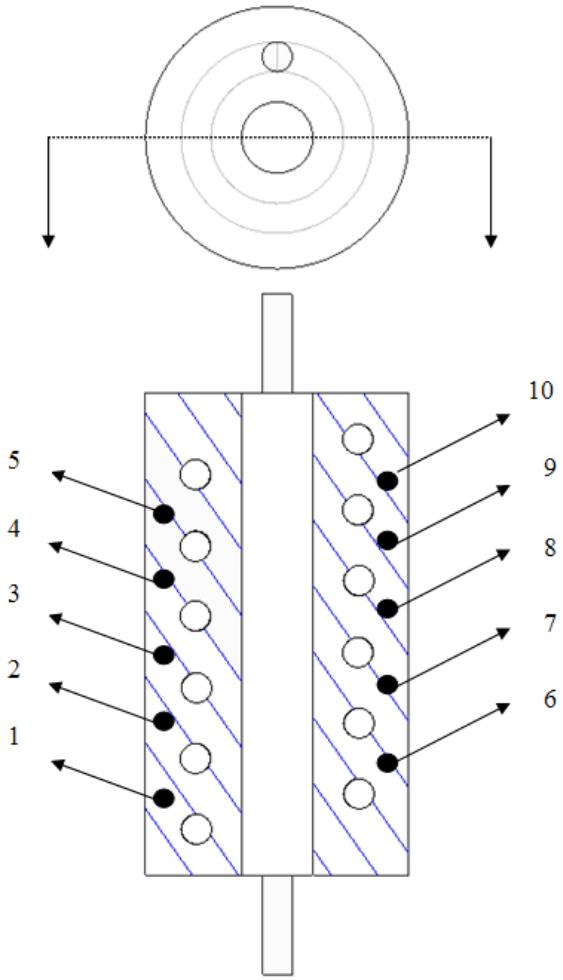

Figure 4.9 The thermocouple placement locations for Bed Design 1 from the crossectional view.

Since bed design is three dimensional without any symmetrical feature, the 10 thermocouples are placed with an angular difference of 180^{o} along the central axis of the cylindrical bed to observe the three dimensional temperature distributions. The

thermocouples are attached to a 1 mm thick brass wire that holds them in place. Measured values for Bed Design 1 will be labeled with the number of the thermocouple given in Figure. The instrumented bed before and after placement into the vacuum chamber can be seen in Figure 4.10

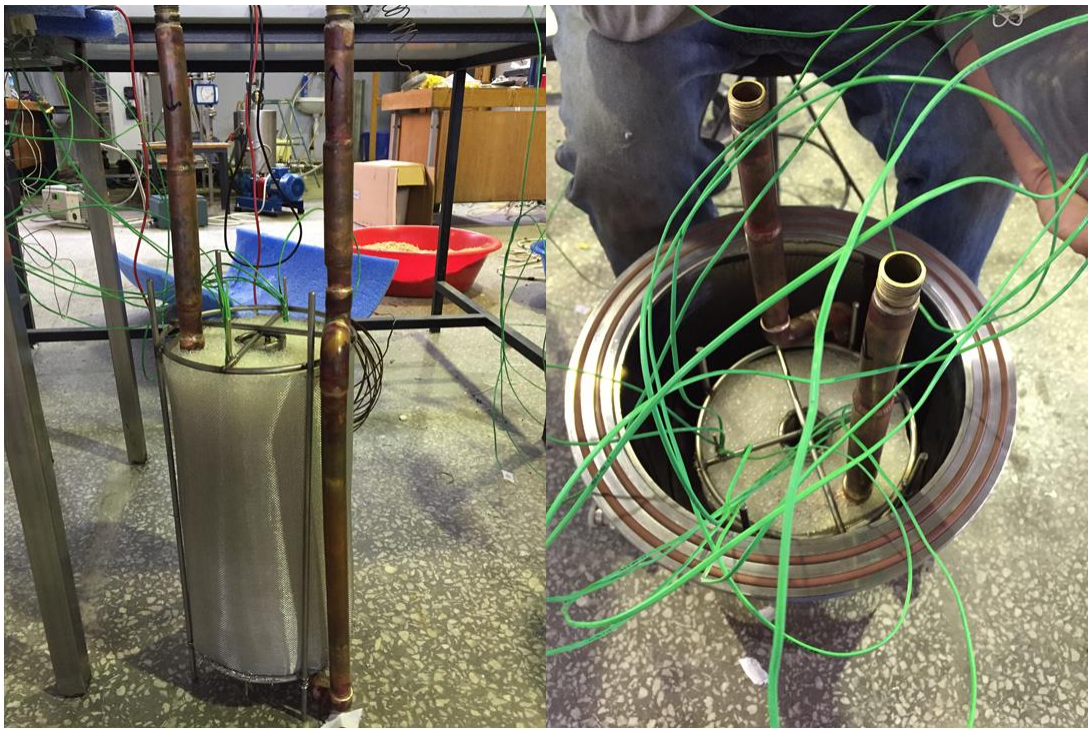

Figure 4.10 The instrumented Bed Design 1 and the placement into vacuum chamber

The dimensions for the Bed Design 1 can be summarized as follows,

- The tube outer diameter is 22 mm , with a wall thickness of 1 mm
- Mean diameter of the helical section is 115 mm
- Pitch of the helical section is 50 mm
- Length of the helical section is 300 mm
- Overall length of the adsorbent bed is 370 mm
- Outer diameter of the frame is 180 mm
- Inner diameter of the frame is 50 mm

- Total amount of adsorbent filled into the frame : 5.79 kg
- Net volume occupied by the adsorbent: 4.56 liters

4.2.1.2.2 Adsorbent Bed Design 2

The design philosophy and the limitations for the Bed Design 2 are also similar with Bed Design 1. Likewise in Bed Design 2 ultimate goal is to improve the heat recovery efficiency. Referring to the design philosophy explained in the previous subsection, the radial heat transfer rate of the adsorbent bed needed to be increased while the axial heat transfer rate is reduced in Bed Design 2 also.

In Bed Design 2 similar to Bed Design 1 the increase of the radial heat exchange rate will be facilitated by the elongation of HTF flow path in the radial direction. The axial advancement rate of the HTF thus the axial heat transfer rate will be decreased by a stair step like HTT pipe design. This design can be described as circular pipe segments in placed concentrically in annulus shaped cylindrical bed slices. The cylindrical bed slices are separate from each other. Since the adsorbent particles are placed into the slices which is not connected, axial heat transfer by conduction among adsorbent particles is eliminated from one slice to another. Additionally all surfaces of the cylindrical slices are open to the vacuum chamber which reduces the mass transfer resistance compared to Bed Design 1. The 3-D CAD model of Bed Design 2 can be seen in Figure 4.11

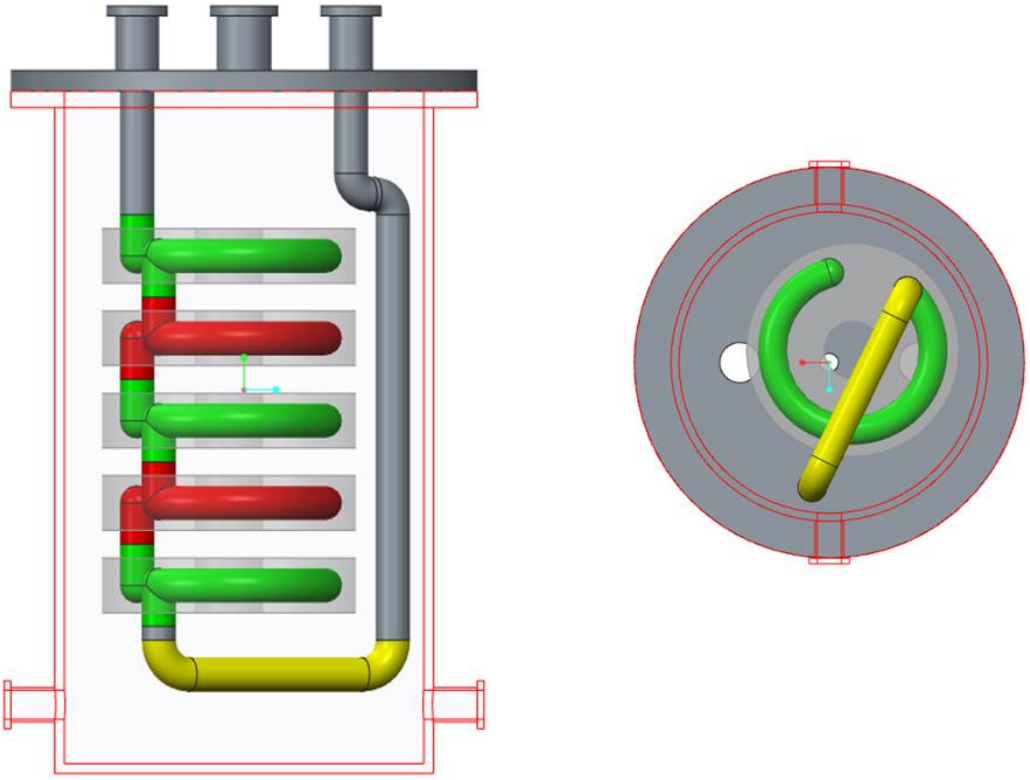

Figure 4.11 3-D CAD model of Bed Design 2 with vacuum chamber, front and bottom views

In the manufacturing process same copper pipe (22 mm outer diameter, 1mm wall thickess) with the Bed Design 1 is used. The circular pipe segments are obtained by winding around a mandrel by the spring manufacturer Deniz Yay A.Ş. The circular pipe segments are connected via elbows and straight pipe sections to form the HTT assembly. Upon completion of the assembling the elbows, pipe sections and the circular pipe segments are brazed together, with silver brazing process. The Bed Design 2 before the brazing process can be seen in Figure 4.12

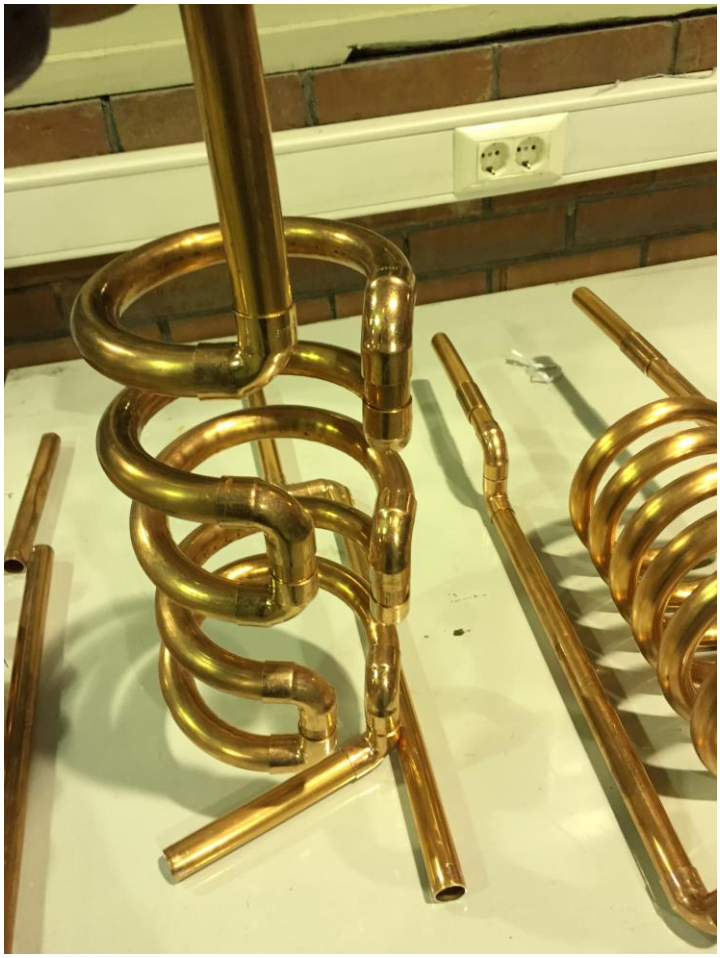

Figure 4.12 The HTT for Bed Design 2 before brazing operation

The Bed Design 2 after the brazing operation can be seen in Figure 4.13. The silver brazing operation is preferred to avoid the possibility of extreme warping of the HTT after welding process.

Figure 4.13 HTT of Bed Design 2 after brazing operation

The bed will be composed of annulus shaped slices which are not connected to each other. Therefore a frame which will carry and support the slices formed from metallic net is manufactured from 6mm stainless steel sticks. Similar to the previous bed construction, the metallic net is stitched with stainless steel wire by hand to form the annulus shaped slices which will be filled with adsorbent particles. The final shape of the stitched metallic net and the frame of the adsorbent bed together with the HTT can be seen in Figure 4.14

Figure 4.14 HTT of Bed Design 2 metallic net forming the annulus shaped slices around the HTT

Similar to the Bed Design 1 here also silica gel produced by Damla Kimya company with an average diameter of 4 mm will be used as adsorbent. The adsorbent will be totally regenerated before being filled into the annular slices formed by the metallic net. The number of thermocouples available for measurements inside the vacuum chamber is 10 due to the available feedthrough connectors. The 10 thermocouples are placed with an angular difference of 180^{o} along the central axis of the annular slices to observe the three dimensional temperature distributions. The thermocouples are inserted into the holes opened in the metallic net, and tied to the net by using stainless steel wire.

The thermocouple locations can be shown on the crossectional view of Bed Design 2 as given in Figure 4.15

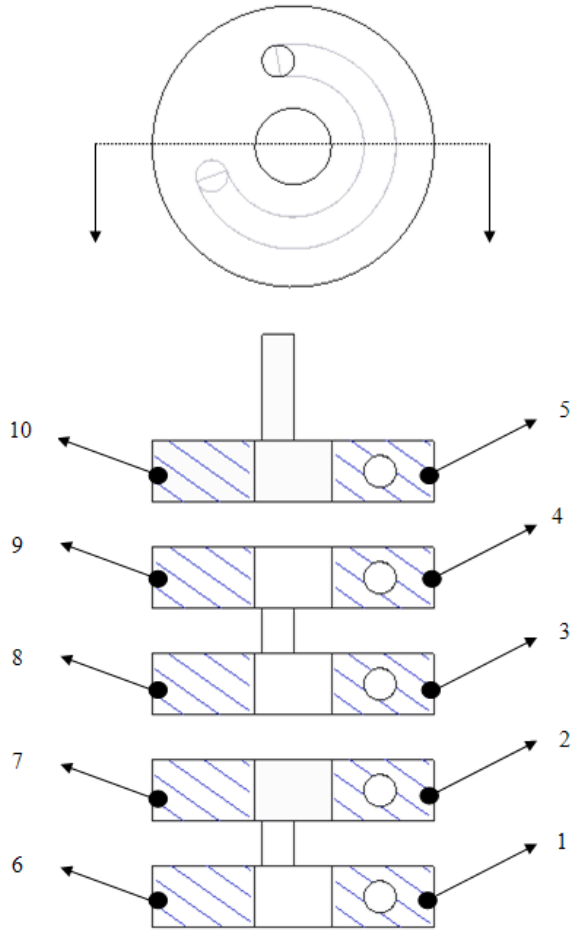

Figure 4.15 The thermocouple locations for Bed Design 2

Measured values for Bed Design 2 will be labeled with the number of the thermocouple given in Figure. The instrumented bed before placement into the vacuum chamber can be seen in Figure 4.16

Figure 4.16 The instrumented Bed Design 2 before placement into the vacuum chamber

The dimensions of the Bed Design 2 can be summarized as,

- The tube outer diameter is 22 mm , with a wall thickness of 1 mm
- Mean diameter of the circular pipe segment is 115 mm
- Angular of the pipe segment is 125^{o}
- Length of the metallic net for each slice is 70 mm but the 40 mm of the slice is filled with adsorbent
- Overall length of the adsorbent bed is 350 mm
- Outer diameter of the annulus is 180 mm

- Inner diameter of the annulus is 50 mm
- Total amount of adsorbent filled into the frame : 3.25 kg evenly distributed to slices
- Net volume occupied by the adsorbent: 2.56 liters

4.2.2 Evaporator

Evaporator is another component of the refrigerant vapor flow line section. The evaporator will be used for receiving the heat from the cooling space by evaporation of the refrigerant. The refrigerant will be water in this study as stated earlier. A simple design which has a low pressure drop will be used as evaporator since it is available from the previous studies [17,14]. However the small pipe diameter and low pressure drop design of the evaporator is suitable for testing of adsorbent beds with small adsorption amounts and rates. Compared to the previous studies the adsorbent beds used in this study have approximately 10 times higher adsorption capacity. When the low cross-sectional area and volume of the evaporator combined with the large adsorption potentials, the water is sucked into the vacuum piping towards the adsorbent bed in liquid form from the condenser. The capillary tube and the throttling valve could not establish the desired pressure drop when used together with the low pressure, low volume evaporator. In the beginning water evaporates as it flows through the capillary tube and evaporator. After some time the water starts to drip into the evaporator from condenser. As the time passes evaporator becomes filled with water and the water proceeds to the bed from vacuum line in liquid form. The liquid water evaporated from the free surface during its travel in the evaporator and the piping but the location of evaporation in the vacuum line changes with time and most of the time evaporation does not take place in the evaporator. These observations are based on the thermocouple readings taken inside the evaporator pipe. Therefore despite the insistent trials, the adsorption experiments could not be performed successfully in a consistent manner and will not be presented in the scope of this study. An evaporator in the form of a cylindrical vessel which contains liquid

refrigerant would be a more proper design for the adsorption experiments. The free surface of the liquid should be higher therefore instead of flowing in liquid form evaporation of refrigerant will be facilitated.

There are three K type thermocouples are placed into the evaporator pipe. One of them is at the bottom, one of them is at the top and the other is at the middle of the evaporator. These thermocouples are connected to a feedthrough connector since they are placed into the vacuum line. The photograph of the evaporator and the feedththrough connector can be seen in Figure 4.17

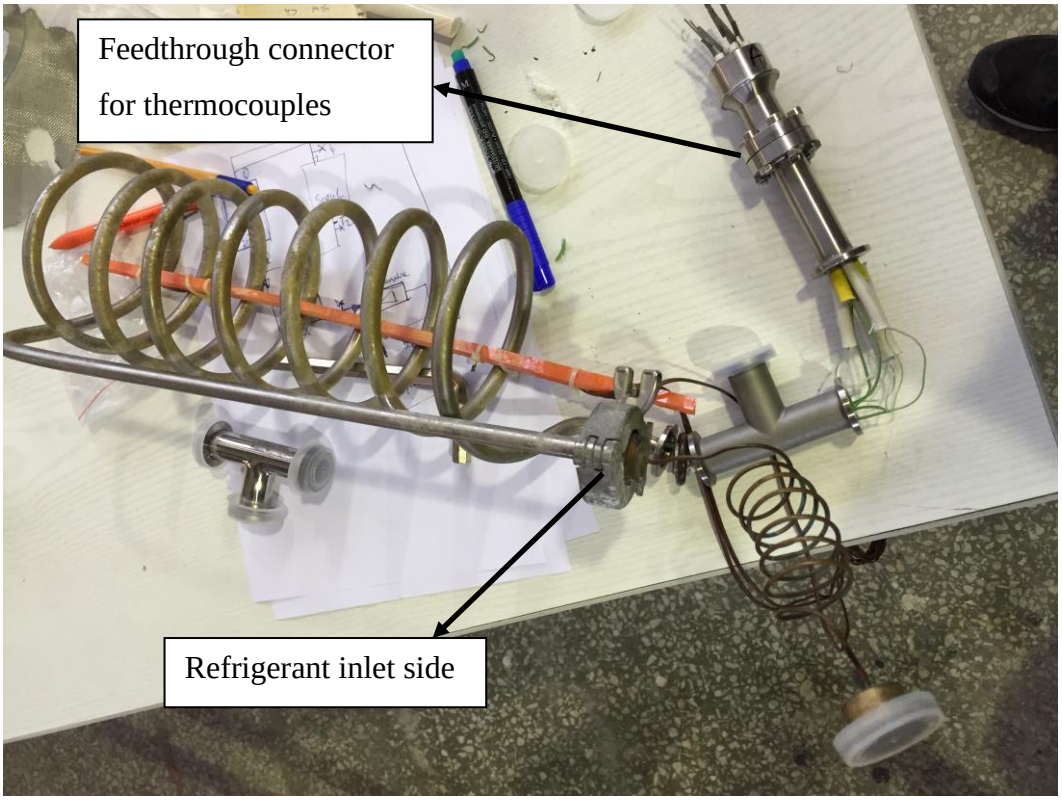

Figure 4.17 The evaporator, feedthrough connector for K type thermocouples

In addition to the thermocouples placed into the evaporator three T type thermocouples are placed into the cooling space in which evaporator will be placed. The cooling space is a 5 liter cylindrical container manufactured from Plexiglas. The

cooling space is filled with water to damp the fluctuations in the temperature of the evaporator and to calculate the cooling power from temperature variations. The cooling space needs to be insulated well to measure the actual cooling power of the bed during adsorption. The evaporator placed into the cooling space before and after application of insulation can be seen in Figure 4.18

Figure 4.18 The evaporator placed in to the cooling space-without and with insulation

4.2.3 Condenser

Condenser is the component in which the refrigerant vapor condenses by releasing heat to the environment. Condenser is also works under vacuum pressure and will be connected to the vacuum chamber during desorption process. To receive the heat rejected at the condenser, condenser is placed into a water bath which is externally cooled and heated to keep the condensation temperature constant during experiments.

The condenser that will be used in the current study had been manufactured and used in the previous studies. There are two main parts in the condenser one of which is condenser tube bundle and other is condenser canister. The condenser tube bundle is consists of stainless steel tube bundles to increase the heat transfer area. The condensation of refrigerant takes places at the tube bundle and then the condensate flows to the canister. The canister is also a stainless steel cylindrical container. For being able to measure the amount of water in the canister a glass window with a scale is installed on to the canister. The photograph of the condenser can be seen in Figure 4.19. Photograph is taken from the study of Solmuş [17] since the condenser is permanently mounted into the water tank and it is not possible to take a photograph.

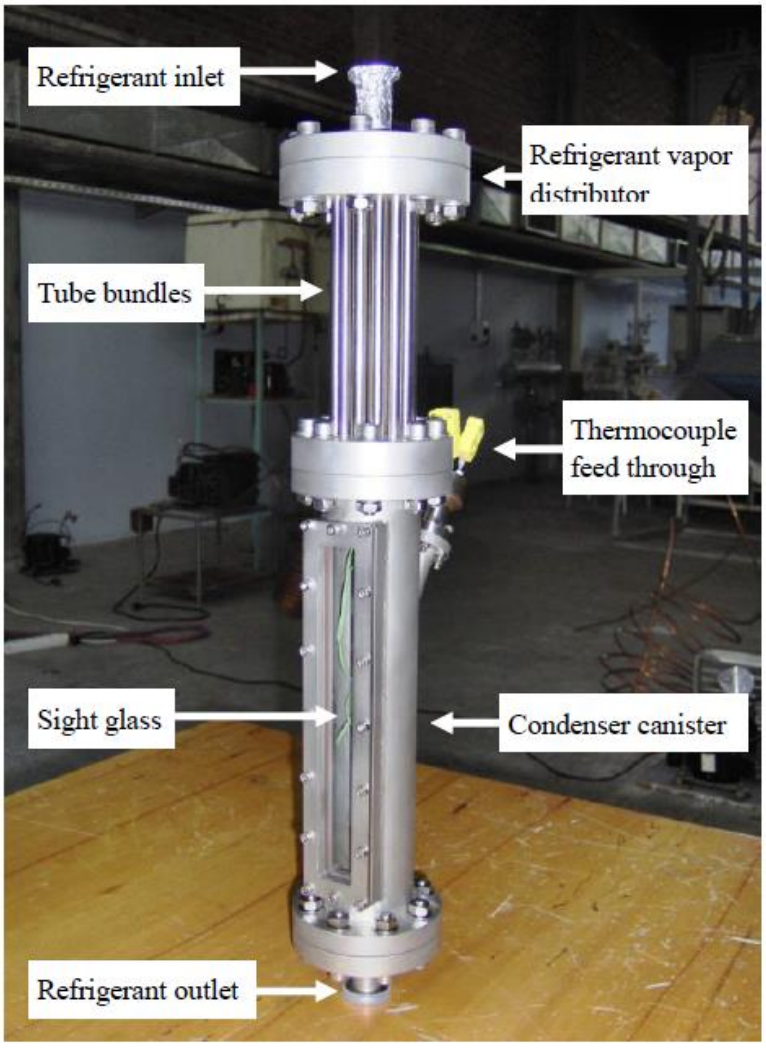

Figure 4.19 Photograph of the condenser [17]

The condenser tube bundles are composed of 22 stainless steel tube with an outer diameter of 8 mm. the length of the tubes in the tube bundle is 135 mm. The canister is constructed by using a 300 mm long tube with an inner diameter of 58 mm.[17] As it had been stated the condenser canister is equipped with a scaled sight glass which can be seen in Figure 4.20

Figure 4.20 The sight glass of the condenser canister

The whole condenser assembly is placed into a temperature controlled water bath. The water bath temperature needed to be controlled since the condensation temperature during the tests will be constant. For this purpose the water bath is equipped with a heater and cooling coil. Additionally a circulation pump is used for circulation and stirring of the water in the tank for homogenization of the water temperature all around the condenser.

However the cooling coil of the vapor compression refrigeration system is found out to be too slow to respond the temperature overshoots resulted from heater. An on-off type controlling procedure is applied to the heater and the cooling system of the tank. A previously installed 1.5 kW heater is used for heating of the water in the tank. The

required fast response cooling system is established by installing a gasketed plate heat exchanger between tap water and the circulating water of the water bath. The tap water flow in the cold side of gasketed plate heat exchanger is also controlled via an on-off type loop and a solenoid valve connected to the tap. The photograph of the gasketed plate heat exchanger used for cooling of the condenser water bath can be seen in Figure 4.21. The tap water temperature was about 20^{o}C (at maximum) during the experiments therefore it had been used for keeping the water bath temperature of the condenser at 30^{o}C when used together with the heater in an on-off operation cycle. A T type thermocouple is placed into the water bath for measuring the temperature of water bath. The measurement taken from this thermocouple is used for controlling the heater and the solenoid valve which controls the flow of tap water into heat exchanger. A sample temperature plot for the condenser water bath for 5 hours of duration can be seen in Figure 4.22. The water bath temperature is set to 30^{o}C and the temperature measured by the thermocouple fluctuates between 29.4^{o}C and 30.4 ^{o}C.

There are also 3 K types thermocouples installed into the upper, lower and middle part of the condenser canister which is connected to a feedthrough connector. However due to corrosion and aging, measurement of temperature inside the canister cannot be performed by using these thermocouples.

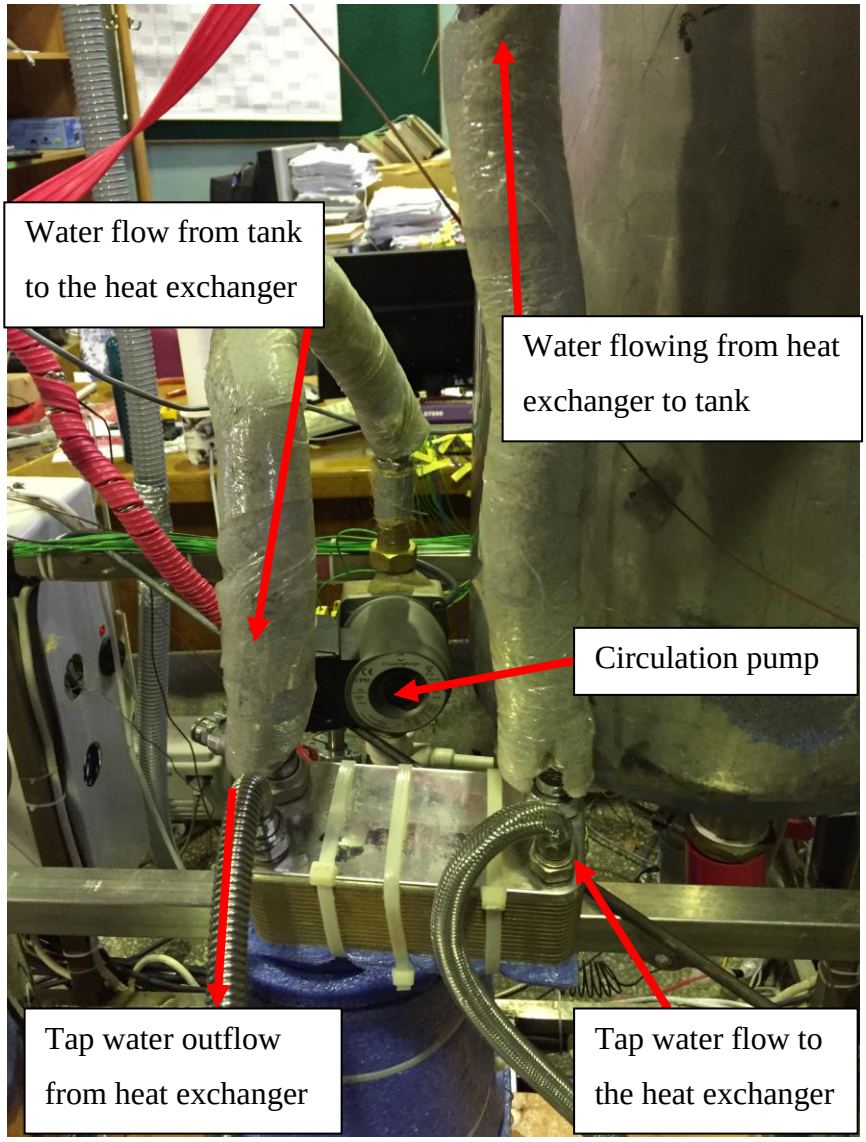

Figure 4.21 Photograph of gasketed plate heat exchanger used for cooling of the condenser water bath

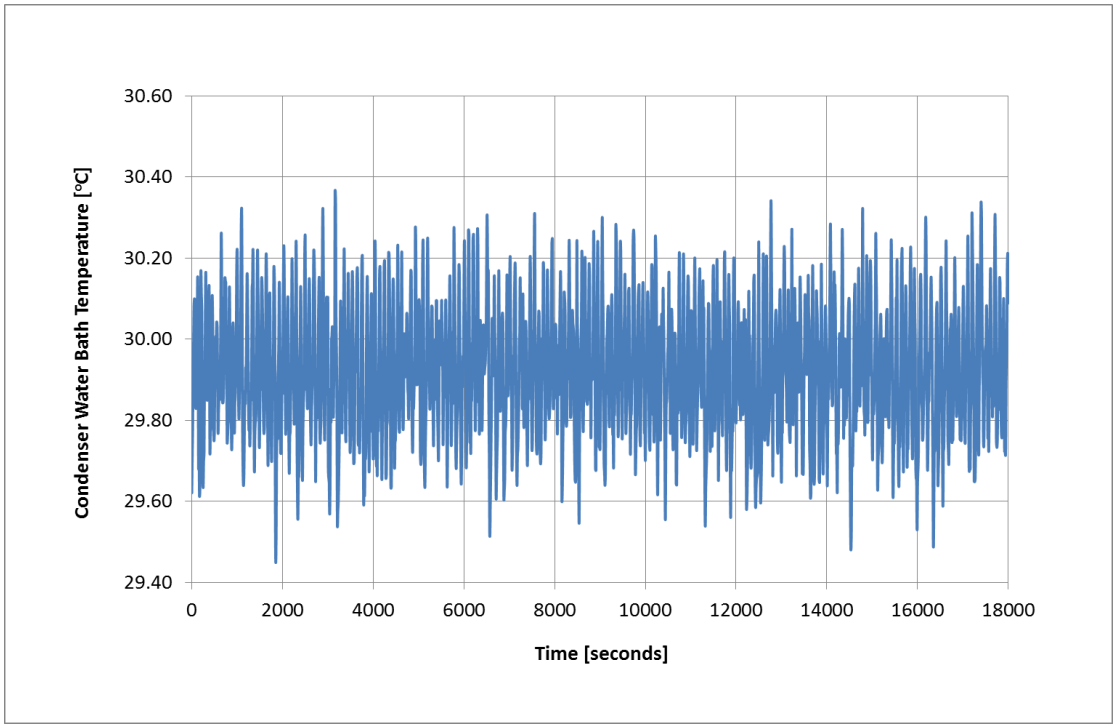

Figure 4.22 Sample condenser water bath temperature variation plot during experiments

4.2.4 Throttling Valve and Capillary Tube

The refrigerant used in the system is stored in the condenser canister and one end of the evaporator is connected to the canister via a throttling valve and a capillary tube. Main function of the throttling valve and capillary tube is to reduce the pressure of the water contained in the canister from condenser pressure to the evaporator pressure. In this system both throttling valve and capillary tube is used together to ensure that the required pressure drop is satisfied. Moreover usage of a throttling valve also adds flexibility for controlling the pressure drop from the condenser canister to evaporator. The photograph of the capillary tube and the throttling valve (BOC-Edwards-LV10K) installed between evaporator and the condenser can be seen in Figure 4.23.

Figure 4.23 Photograph of throttling valve and the capillary tube installed between condenser and evaporator.

Unfortunately this statement of the purpose for using throttling valve and capillary tube could not find its place in the practical application. As explained in detail previously the evaporator design was not proper for performing adsorption experiments. Therefore despite the extensive effort and numerous trials, adsorption tests could not be performed successfully on the available setup. The previous researchers worked on this setup also could not present any adsorption experiment data because of the same reason [14, 17].

4.2.5 Heat Transfer Fluid Loop

The adsorbent bed is heated and cooled by the circulating HTF. The HTF piping is shown in the schematic given in Figure 4 with the red colored lines. There are two by-pass lines exist in the piping. One of the bypass lines is used for adjusting the flow rate of the HTF and therefore starts just after the pump outlet. This bypass line is equipped with a needle valve which enables the fine adjustment of the flow. The second bypass line is installed just before the adsorbent bed HTF inlet. This bypass line is used for circulating oil in a longer loop for heating all the pipes except the adsorbent bed HTF flow path. The oil is circulated through this route for approximately half an hour at stabilized temperature before starting the heating of adsorbent bed. Another needle valve is installed at the downstream of the flowmeter, this valve is used together with the bypass needle valve to adsjust and stabilize the oil flow rate to the adsorbent bed. The whole HTF piping is redesigned and reconstructed since the previous version was not suitable for long duration operation.

4.2.5.1.1 Hot HTF Tank

The hot HTF tank supplies the heated HTF to the system during desorption experiments. The tank is manufactured specific to this study. The previous researchers used open tanks and experienced oil vaporization and odor problem. For this reason closed tanks are designed and manufactured. Unfortunately the odor caused by the heated oil could not be eliminated but contamination due to oil vaporization is prevented with the usage of closed hot HTF tank.

The hot oil tank is equipped with resistive heaters and several ports for oil inlet, oil outflow, resistance heaters and instrumentation. The resistances installed at the bottom face through the sleeves on that face by fastening. Throughout the experiments resistances had been changed for 3 times due to excessive local heating

problems. The hot HTF tank is equipped with four 1kW resistive heaters which are controlled by the data logging device though the relays.

The temperature is measured at the outlet of the tank and the tank outlet temperature is used as the control parameter. The hot HTF tank can be seen before insulation and installation in Figure 4.24

Figure 4.24 Photograph of the hot HTF tank before insulation and installation

4.2.5.1.2 Cold HTF Tank

Similar to the hot HTF tank, cold HTF tank is designed as a closed vessel to prevent the oil vaporization problem. Different than the hot HTF tank cold HTF tank is equipped with a cooling coil. This coil is manufactured from 30 meter stainless steel

pipe. The photograph of the cooling coil that had been installed in the tank can be seen in Figure 4.25.

Figure 4.25 Photograph of the cooling coil placed into the cold HTF tank

For being able to keep the temperature of the HTF, cold HTF tank also equipped with two resistive heaters. The cooling coil is connected to the tap water line and the water flow is controlled by a solenoid valve by the data logger. Similar to the hot HTF tank the temperature measurement location for the cold HTF tank is also at the outlet.

Figure 4.26 Photograph of the cold HTF tank

The hot and cold HTF tanks after installation and insulation can be seen in Figure 4. 27. Gemaoil-Thermoil-32 heat transfer oil, which is available in the laboratory, is used as HTF. The tabulated thermophysical properties of the HTF given by Çağlar [14] can be seen in Table 4.1

Table 4.1 The thermophysical properties of the HTF given by [14]

Gemaoil-Thermoil 32	
Density [kg/m^3]	914
Thermal Conductivity [W/mK]	0.115
Specific Heat [kJ/kgK]	1930

The density value of the HTF changes during operation as a result of contamination and temperature change, therefore density is measured for the operating conditions and this measured value is used in calculations.

Figure 4.27 The insulated and installed HTF tanks and HTF loop

4.2.5.1.3 HTF Pump

In the previous studies a centrifugal oil pump designed to operate at high temperatures is used. During the preliminary experiments, it had been observed that

the nominal flow rate of that pump is relatively high compared to the low flow velocities that are needed. Additionally, instability in pumping head and flow rate with the HTF temperature variations and increased pump temperature becomes a significant problem during 5-6 hours long experiments. Therefore need for pump which has low volumetric flow capacity and good stability characteristics had been raised. There are several positive displacement pumps exist in the market with these qualities however most of these pumps are manufactured specific to hydraulics applications and highest temperature of operation is limited with the 90^{o}C which is the endurance limit of the Viton gaskets used in their construction. After surveying the market and manufacturers, an internal gear type pump, had been ordered to Vimpi Pompa A.Ş. the manufacturer of viscous fluid pumps. Upon the request the original design is modified and all the seals are replaced with high temperature resistant graphite seals for facilitating operation at temperatures over 200^{o}C. The volume of fluid pumped in each revolution is 0.004 liters under ideal conditions, but the volumetric flow rate decreases with decreasing viscosity. However at a constant operating temperature the volumetric flow rate and the head can be kept constant with high stability. The pump is attached to a 2800 rpm 0.55 kW electric motor via a 7 ratio reduction. The pump is unidirectional without a specific direction of rotation, and no check valves need to be installed before the pump since dry operation is not catastrophic. The coupling and alignment of the pump and the motor is also specifically manufactured. The photograph of the pump, reduction and the electric motor can be seen in Figure 4.28.

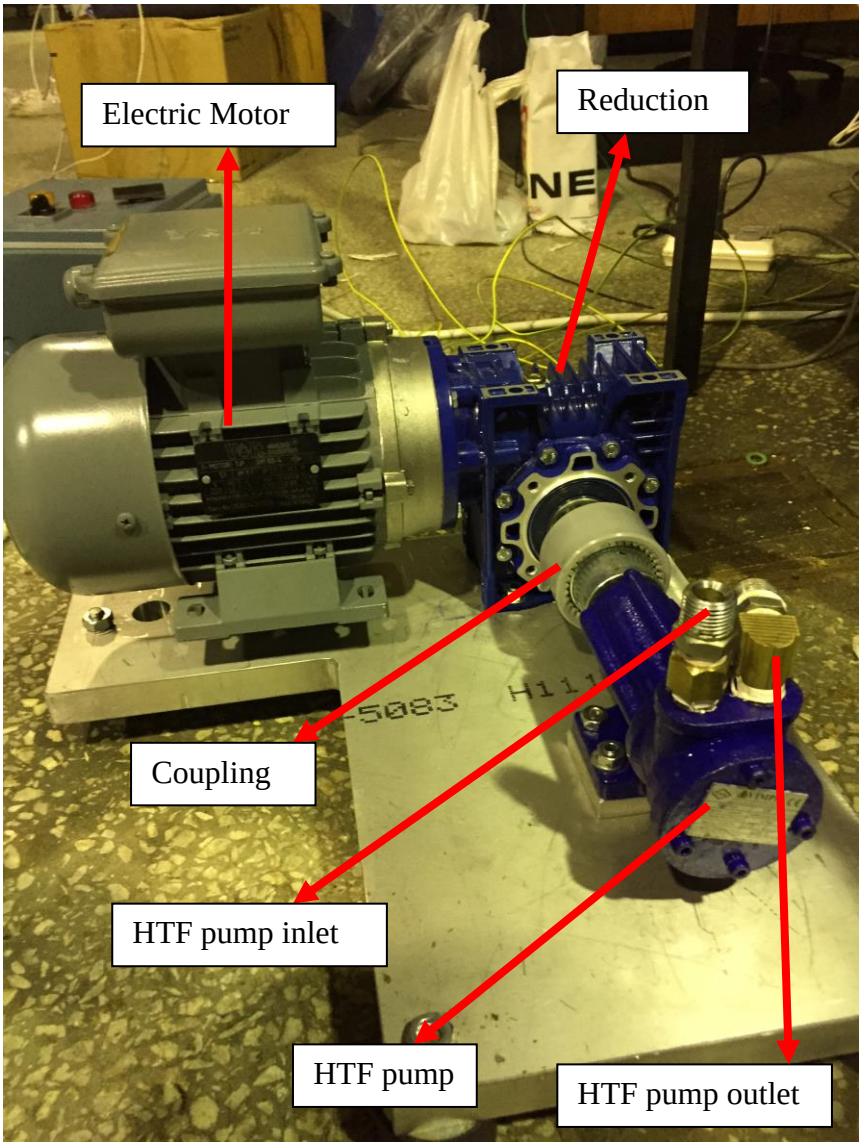

Figure 4.28 The HTF pump assembly, electric motor, reduction and pump

4.2.6 Data Acquisition System and Sensors

The last sub section of the experimental setup is composed of the data acquisition and logging device and sensors. In the experiments the vacuum chamber and vacuum line pressure are measured. In addition to the pressure measurements, the temperature at various locations needed to be measured. Moreover, the flow rate of

the HTF will also be measured during experiments. Therefore the sensors that will be used are mainly,

- Thermocouples
- Pressure transducers
- Flowmeter

In addition to the sensors a data logging device will be used for acquisition and logging the reading of these sensors.

4.2.6.1 Thermocouples

The thermocouples will be used for measuring the temperature at various locations in the experimental setup. The temperature measurement locations and the purpose of measurement could be listed as,

- Hot HTF outlet temperature is measured by a T type thermocouple and used for controlling the temperature of the hot HTF tank.
- Cold HTF outlet temperature is measured by using a T type thermocouple for controlling the temperature of cold HTF tank
- 10 K type thermocouples are used for measuring the temperature within the adsorbent bed
- One T type thermocouple is used for measuring and controllling the condenser water bath temperature
- Three T type thermocouples are used for measuring the top, middle and bottom of the cooling space water temperature
- Three K type thermocouples are used for measuring the refrigerant temperature within the evaporator
- Two T type thermocouples are used for measuring the HTF temperature at the inlet and outlet of adsorbent bed

- One T type thermocouple is used for measuring and controlling the vacuum line heaters and piping.

4.2.6.2 Pressure Transducers

The pressure transducers available in the laboratory was malfunctioning therefore they are replaced with the brand new ones. The pressure transducers are used for measuring the vacuum chamber and condenser pressure. Omega 0-1 bar absolute pressure transducers are used in the experiments. The transducers were factory calibrated therefore did not require any calibration. The output voltage of the transducers is linearly scaled to obtain a pressure value reading. Each sensor is sent with a specific calibration document. The standard mechanical connection is adapted to the vacuum line by manufacturing adapters. The photograph of the pressure transducers that are installed to the condenser and the vacuum chamber can be seen in Figure 4.29.

Figure 4.29 Photograph of the pressure transducer installed to the condenser

4.2.6.3 Flowmeter

As stated earlier the flow rate of the HTF will be measured by using a flowmeter. The flowmeter that will be used in the experimental setup is Khrone H250/M9 flow meter which is also available in the laboratory. This flow meter is a custom made flow meter which can operate at high temperature and low flow rates. The flowmeter is variable section flowmeter and measures the volumetric flow rate of the HTF and will be installed to the outlet of HTF circulation pump. The flow meter reading will be used for controlling the HTF circulation pump and for determining the amount of HTF circulated through the bed during experiments. Since the flow meter is calibrated for 250^{o}C heat transfer oil with a prescribed viscosity, manual measurements performed at different temperature and needle positions to determine the actual flow rate of HTF used in the experiments with respect to corresponding needle positions. The HTF flow rate is adjusted by using the needle valves installed

in the bypass line and at the downstream of the flow meter. The photograph of the flowmeter can be seen in Figure 4.30.

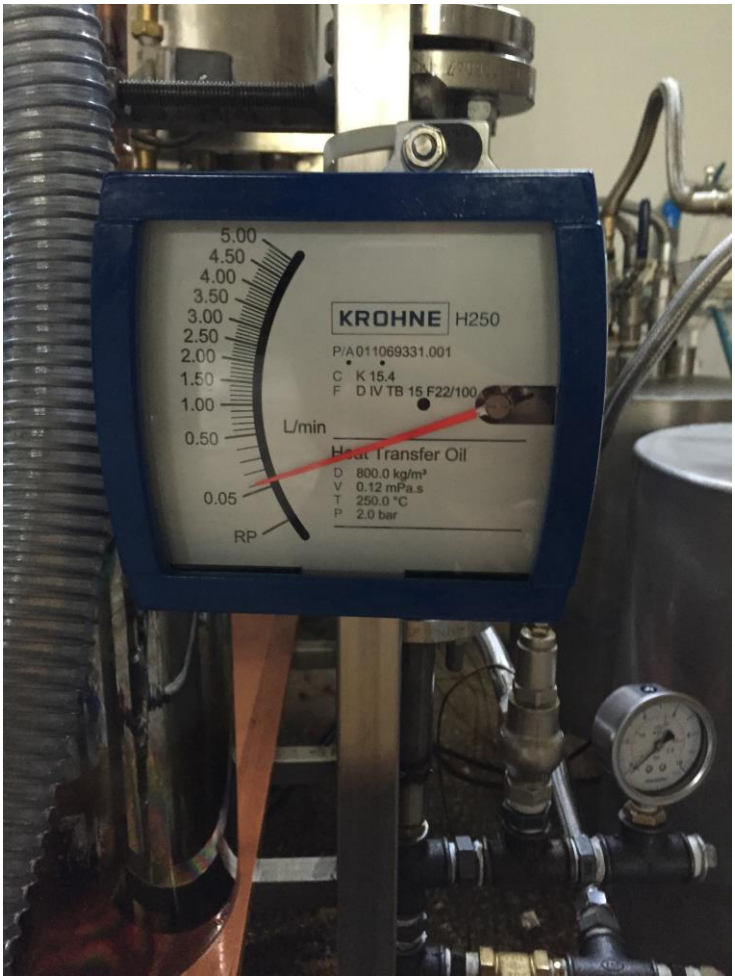

Figure 4.30 Photograph of the HTF flow meter

4.2.6.4 Data Acquisition System

The signals received from sensors will be converted into meaningful values and will be logged by the data acquisition and logging device. For acquiring and logging the sensor readings and controlling the system parameters DT800 type data logger is be used. This device is also available in the inventory of the laboratory. The

thermocouples, pressure transducers will be connected to the analog channels of the data logger. The controllable devices such as heaters and solenoid valves will be controlled through the digital signal output from digital channels. The data logger enables to design on-off type controlling of the relays. The heaters and solenoid vales in the experimental setup is controlled via these relay which are electrified by the output signals produced by the DT800. The photograph of the data logger used in the experiments can be seen in Figure 4.31. The data logger is connected to the PC via RS232 port and the connection is grounded since, any kind of magnetic field affects the operation of data logging and acquisition system. The data logger has an internal memory of 100 MB to store the measurement data this is a limiting factor for the number of channels that can be used and the duration and frequency of measurement.

Figure 4.31 The photograph of the data logger (dataTaker DT800) used in the experiments

Temperature measurement by using different type of thermocouples is an embedded feature of the data logger. Data logger is capable of thermocouple output calibration by measuring the junction temperature with an built-in thermistor. Additionally on-off type control loops can be easily implemented. For example it is possible write a code which opens the heater of the condenser bath when condenser bath temperature is below 30^{o}C and closes the heater and opens the cooling water solenoid valve when it over 30^{o}C. As mentioned heaters and solenoid valves are controlled by using electromechanical relays instrumented on the electric control board. The relays and the electric control board can be seen in Figure 4.32

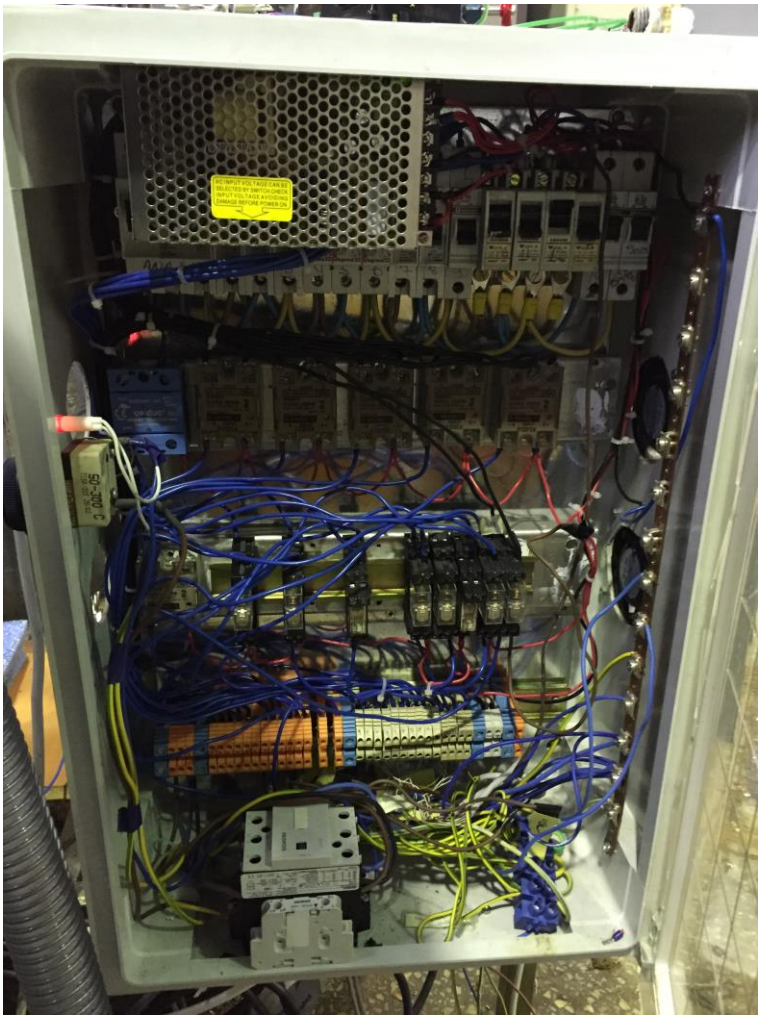

Figure 4.32 Photograph of the electric control board and the relays installed

4.3 Experimental Procedure

Before starting the experiments the packed bed is prepared by placing the HTF tube into the stainless steel frame. Adsorbent material (silica gel) which is completely regenerated in the oven before is filled into the spacing between HTT and the metallic net of the adsorbent bed. 10 K type thermocouples are placed into the predetermined locations of the bed that will be tested. Upon completion of the thermocouple instrumentation, the adsorbent bed is placed into the vacuum chamber and the chamber is sealed. The sealed vacuum chamber containing adsorbent bed is connected to the vacuum line and the HTT of the adsorbent bed connected to the HTF line and parts of the HTT remained outside of the chamber is insulated. Thermocouples that measure the inlet and outlet temperature placed into the measurement locations. After connecting vacuum chamber to the vacuum line, vacuum ball valves between pump and the chamber is opened and the vacuum chamber is evacuated by using the vacuum pump. After the pressure inside the chamber is reduced up to levels of 1-2 mbar, vacuum pump turned off and valves connecting from the vacuum chamber and the pump is are closed. The pressure inside the vacuum chamber is observed for 1-2 hours for any possibility of vacuum leak. If the pressure do not rises it is accepted that no significant leakage into the chamber is observed. The vacuum chamber and adsorbent bed connected to the vacuum and HTF lines can be seen in Figure 4.33

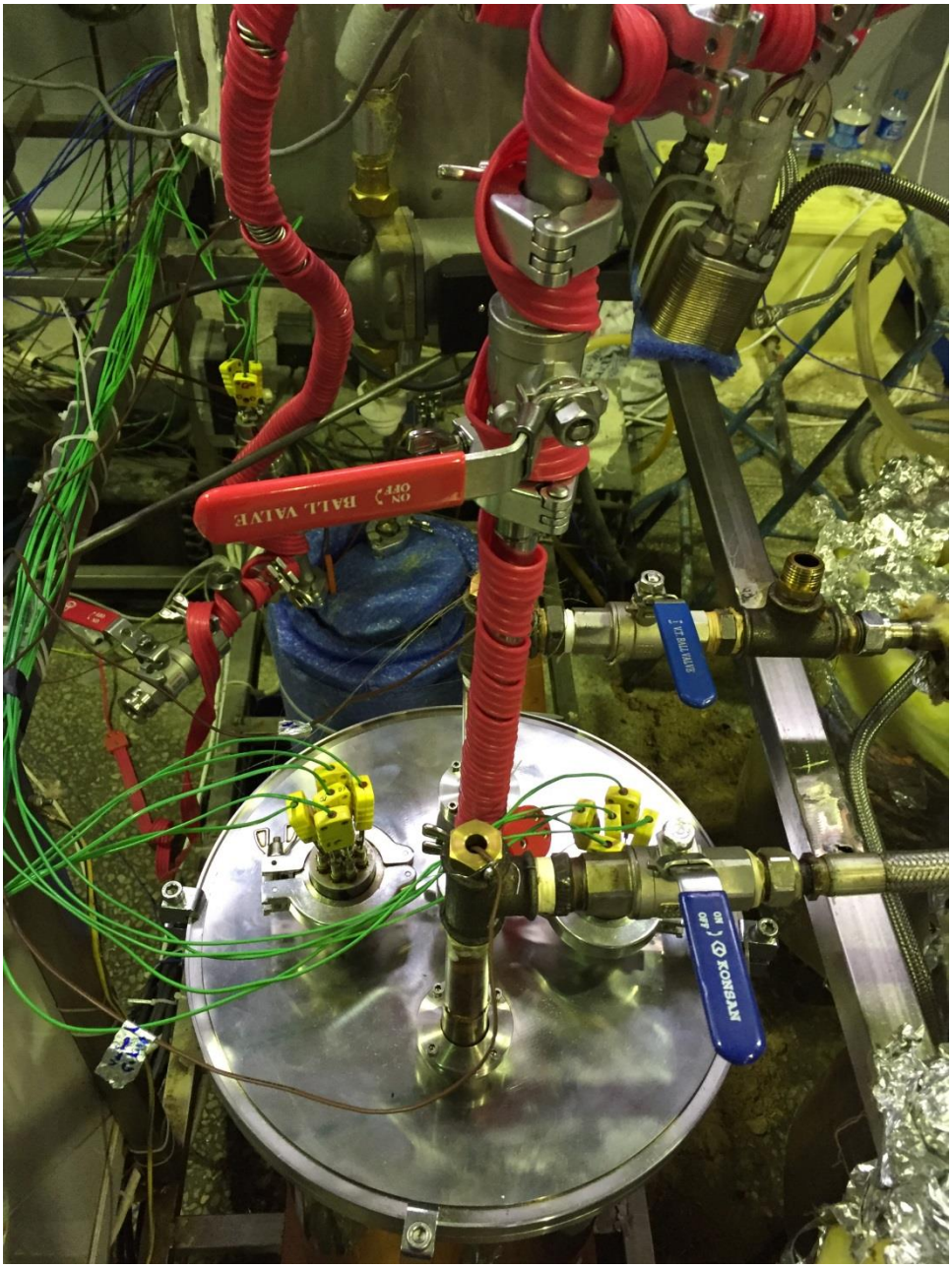

Figure 4.33 Vacuum chamber after being connected to vacuum line and HTF line

The next step is to fill the condenser canister with deionized water. Deionized water is used as the refrigerant in this system since it is free of minerals and particles which may cause fouling and contamination in the vacuum line components. The deionized water is fed from the water feeding line to the system through two ball valves for

controlling the flow. Amount taken into the canister is measured through the view glass and value is recorded. At the same time, the temperature of water bath containing the condenser assembly is set to the desired value and stabilized. In the next step, the valves connecting the vacuum pump and the condenser are opened. The vacuum pump is operated for evacuating the air in the vacuum line between pump and condenser. The condenser pressure is measured and after reaching pressure values below the saturation pressure(42.47 mbar) at the condenser water bath temperature (30^{o}C), the vacuum pump is turned off and the valves in the vacuum line is closed.

The adsorbent was totally regenerated before being filled into the bed therefore the initial step for the experiments will be increasing the adsorbate uptake of the adsorbent up to levels of 0.3. The maximum amount silica-gel used in the experiments can adsorb is %34.6 of its weight [17] therefore adsorbate loadings in the level of 0.3 can be considered as high adsorbate loading value which can be used as an initial condition for the desorption experiments. The valves between condenser and the vacuum chamber are opened for adsorption of the refrigerant to reach the initial adsorbate loading conditions for desorption analyses. The visible part of the volume of the condenser canister from the sight glass is 200 m long which contains to 528 grams of water. The water is adsorbed from condenser since the amount adsorbed need to be recorded. In case of adsorption from evaporator, the liquid water is sucked into the evaporator and the amount adsorbed could not be measured. The Bed Design 1 contains 5.79 kg of adsorbent and the initial adsorption capacity value used in the desorption experiments is equal to 0.33. Required amount of water to reach 0.33 adsorption capacity value is 1.91 kg. Therefore to reach the required adsobate loading, condenser canister is filled 4 times and the vacuum line and condenser is evacuated 4 times. Total process of adsorbing 1.91 kg of water takes 3 days. Similar procedure is also followed for Bed Design 2. This bed contains 3.25 kg of adsorbent and requires adsorbing approximately 1 kg of water to reach the %33 adsorbate loading. After the desired initial adsorbate loading level is reached for the

adsorbent bed the desorption experiments are performed. Before starting an desorption experiment, the hot HTF tank is set to desired temperature and inlet valves and the outlet valve of the hot HTF tank is opened. The HTF pump is started and the HTF started to circulate in the bypass loop without entering the adsorbent bed until the desired temperature is reached and stabilized. The purpose of operating the pump is to achieve the stirring of the HTF in the tank to avoid overheating of the resistance heaters. The vacuum line is wrapped with temperature controlled band heaters. The band heaters that are used for heating the vacuum line piping and therefore they are turned on before starting desorption experiments and set to 80^{o}C which is higher than the condensation temperature to prevent condensation of the refrigerant in vacuum line. After the tank outlet temperature reaches the desired value, the flow rate of the HTF is adjusted by using the needle valves installed downstream of the flow meter and the bypass line of the pump. Approximately in 10 minutes the flow becomes stabilized and ready for heating the adsorbent bed. The data logging starts before hot HTF is fed to the bed. The ball valve at the end of the long bypass loop is closed while the ball valves at the inlet and outlet of the HTT of adsorbent bed are opened to feed the hot HTF into the bed. Initially the bed is at uniform low temperature and low pressure. The first step of the experiment is to increase the vacuum chamber pressure up to condenser pressure. This step is known as pressurization or isosteric heating. During pressurization the valves connecting vacuum chamber and condenser is closed. When the vacuum chamber reaches the condenser pressure the valves connecting the vacuum chamber and condenser is opened and the refrigerant vapor flows through the line and condenses at the tube bundles of the condenser and the condensate flows to the condenser canister. The duration of these desorption experiments are limited with the capacity of the condenser canister and the memory of the data logger. The data logging frequency is set to 10 seconds for reducing the memory requirements. Generally desorption experiments are performed for 5 hours including the isosteric heating duration. It is possible to perform experiments longer than 5 hours however, for re-establishment of the initial conditions, approximately 10 hours are required for being able to perform

a new desorption experiment. Since researcher himself needs to be present at the laboratory throughout desorption experiments and during the re-establishment of initial conditions, a limit for the experiment duration is required to be set. Therefore 5 hours is chosen which seemed to be a reasonable duration for performing experiments.

After completing the desorption process the amount desorbed is recorded, and to reach the initial adsorbate loading for the next experiment the desorbed amount is re-adsorbed. Therefore the valve between condenser and vacuum chamber is left open and the water is adsorbed by the bed. It is possible to accelerate the rate of adsorption between desorption experiments by circulating cold oil in the adsorbent bed. Upon reaching the initial adsorbate loading value the desorption experiment is repeated under different conditions.

Actually there are two different operation modes exists for the experimental setup. The first mode of operation is desorption experiment as described above. Since a successful adsorption experiment could not be conducted in the scope of this study, the mode of operation during adsorption experiments will not be detailed in this text.

4.4 Experimental Results

The experiments performed for the isosteric heating and the desorption phases for a duration of 5 hours due to limitations mentioned. Different bed designs had been experimentally investigated under different, HTF velocities, initial adsorbate loading conditions and HTF inlet temperature values. The bed designs are described in detail in the previous sections. HTF temperature at the adsorbent bed inlet differs much from the hot HTF tank outlet due to low flow rate and relatively long piping. Consistent bed inlet temperature values are tried to be obtained for different beds at different HTF velocities. With trial and error the consistency of inlet temperature at different flow velocity had been established. The HTF inlet and outlet temperature

measurement locations was situated on the HTT at the upstream of the location where HTT enters the vacuum chamber port as can be seen in Figure 4.34. Initially the heat loss in this section is assumed to be negligible, however the results of detailed numerical analyses for this section had been shown that there is a non-negligible heat loss at the HTT section due to contact with the vacuum chamber cap at inlet port and due to natural convection despite the insulation.

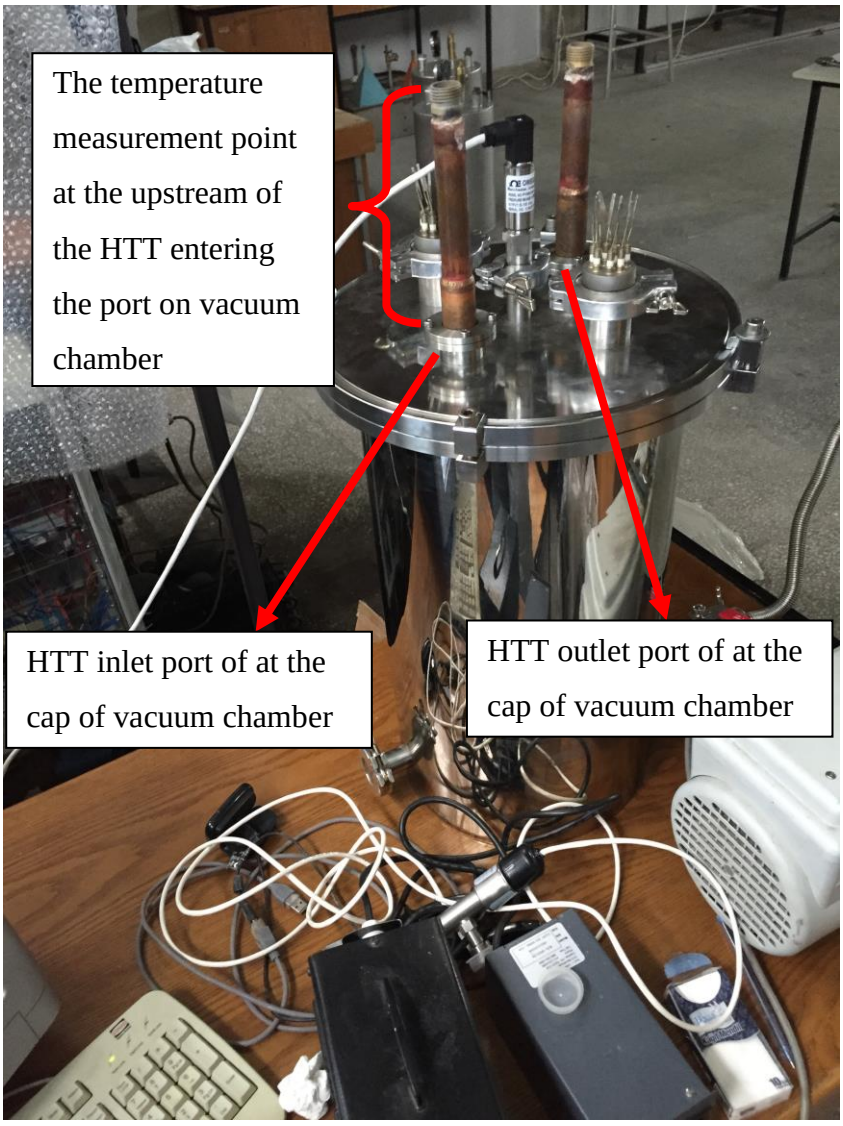

Figure 4.34 The adsorbent bed HTT and the vacuum chamber

The significant part of heat lost through conduction to the vacuum chamber cap where HTT and vacuum chamber is in contact. The hot HTF heats the HTT and then starts to heat the massive stainless steel vacuum chamber cap therefore the temperature of HTF is different from the measured value at the inlet. However the heat loss at the outlet section of the HTT is not significant as the inlet due to low temperature difference between the vacuum chamber cap and the HTF outlet temperatures. Consequently, the inlet and outlet temperatures are measured but some of the heat is used for heating the vacuum chamber through conduction. This heat loss is calculated by the detailed numerical analyses and will be discussed later.

In addition to the inlet and outlet temperature measurements, as stated, temperature measured from the adsorbent bed by using 10 thermocouples. The results will be presented by using temperature measurements in the adsorbent bed under different operating conditions. The locations of the thermocouples for different bed designs are given in the related section.

The initial bed temperature may vary for different experiments since, it is difficult to reach the desired initial temperature since duration required to start experiment may change. Therefore, in the experiments initial temperatures in the range of 300-305 K is tried to be obtained as an initial condition. The adsorbent bed temperature is assumed to be uniform when the temperature values in the bed are in 5 K variation range.

The sampling rate for the temperature measurements is 10s for all of the experiments. Therefore the measured values are discrete in time, however for better graphical presentation, the time variation plots of the experimentally obtained temperature values are plotted as lines. Actually the point plots also results in continuous lines due to sampling frequency and overall duration of experiments.

4.4.1 Experimental Tests of Bed Design 1

The performed desorption experiments on Bed Design 1 can be summarized by the HTF inlet temperature, initial adsorption capacity and HTF velocity as given in Table 4.2.

Table 4.2 The conditions for the experiments of Bed Design 1

Bed Design 1	HTF Inlet Temperature [K]	HTF Inlet Velocity [m/s]	Initial Adsorption Capacity [$kg_{water}/kg_{adsorbent}$]
Experiment 1	397.00	0.0012	0.332
Experiment 2	397.00	0.0020	0.330
Experiment 3	370.00	0.0020	0.330
Experiment 4	394.00	0.0020	0.320

Four different experiments performed with Bed Design 1, Experiment 1 is performed with low HTF velocity, high HTF inlet temperature and high initial adsorption capacity. In Experiment 2 HTF inlet temperature, HTF velocity and the initial adsorption capacity of the adsorbent bed is high. In Experiment 3 the HTF inlet temperature is lowered keeping the HTF velocity and the initial adsorption capacity high. In Experiment 4 the initial adsorption capacity of the adsorbent bed is lowered to 0.32 while HTF inlet velocity and temperature is kept high.

At high HTF inlet velocity values, heat exchange between HTF and the bed reduces due to low heat transfer rate within the bed. The HTF inlet velocity values used in the experiments are chosen to be at very low levels to improve the heat exchange in the directions perpendicular to HTT surfaces. Therefore as HTF inlet velocity value 0.0012 and 0.002 m/s are used in the experiments based on the preliminary tests and the previous studies [14, 23].

The measured HTF inlet temperature is given in the table, however as stated above the temperature at the position where HTT enters the vacuum chamber is different from the measured value. The tabulated values are the mean value of the measured temperature during 18000 seconds.

The initial adsorption capacity is determined by using the adsorbed amount at the beginning of experiments. Also it is possible to calculate the adsorption capacity from Dubinin-Ashtakov relation given previously by using the temperature and the pressure of the adsorbent bed.

It is difficult to obtain exactly the same inlet temperature values in different experiments due to changes in ambient temperature and wearing of the insulation. Additionally the adsorbed amount could not be adjusted precisely to obtain the same adsorption capacity in Experiment 1, 2 and 3. The initial adsorption capacity intentionally lowered for Experiment 4 to see the effect of reduced initial adsorption capacity.

The temperature measurement points are placed in Bed Design 1 at 10 different locations. Five of the thermocouples (from 1 to 5) are located on the right hand side of the crossectional view shown in Figure 4. The other five (from 6 to 10) is located on the left hand side of the crossectional view. The thermocouple numbers and the placement on the crossection shown is given in the Figure 4.35. These numbers will be used for the presentation of bed temperature variations plots.

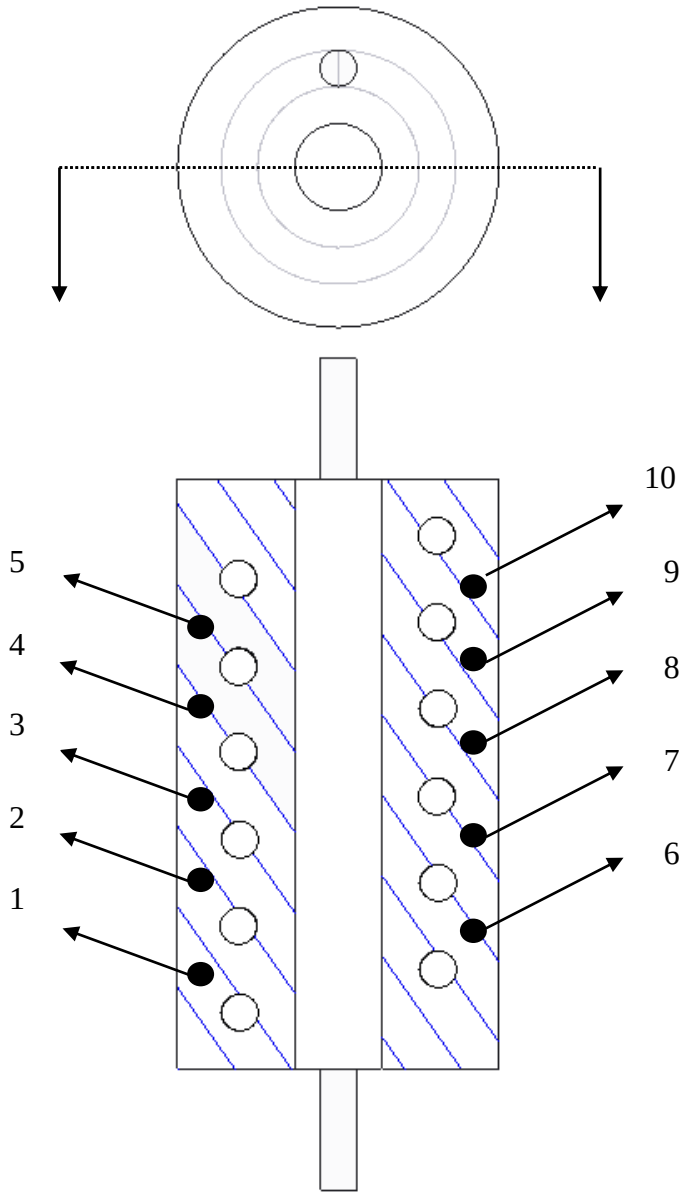

Figure 4.35 The thermocouple placement locations shown on the crossectional view of the packed bed.

The results of the experiments will be presented in terms of time variation of the measured bed temperatures, and the temperature distribution along the bed axial position measured from right hand side and the left hand side of the bed as shown in the figures below. The measurements taken from thermocouples 6 to 10 will be

named as temperature measurements on right axis values, while the measurement of thermocouples from 1 to 5 will be named as left axis values. The axial temperature variations in the bed will be taken from 300, 1200, 4800, 9600, 12000 and 18000 seconds of the experiments.

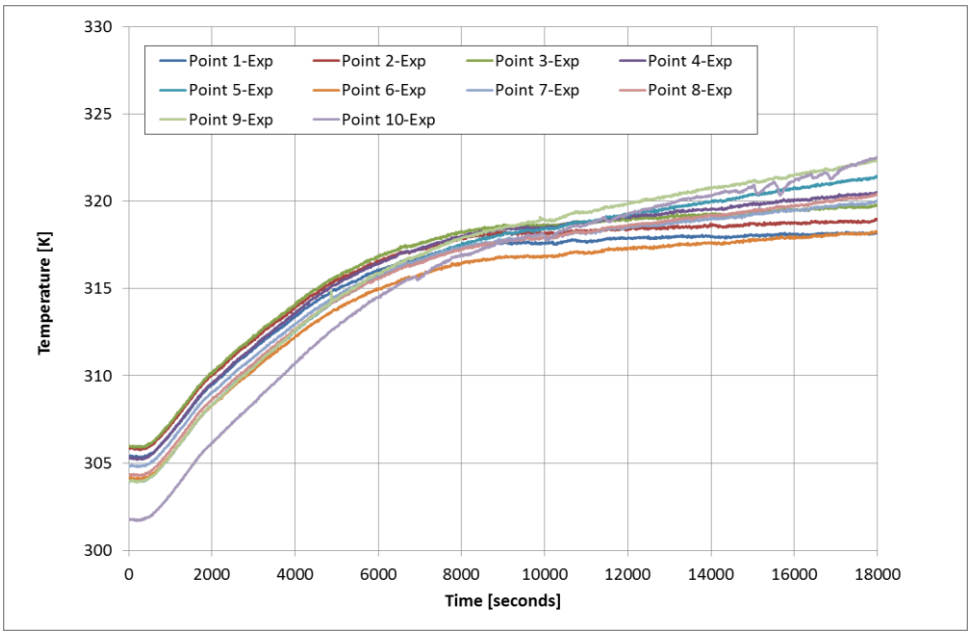

Figure 4.36 Bed temperature variations with time for Bed Design 1 in Experiment 1

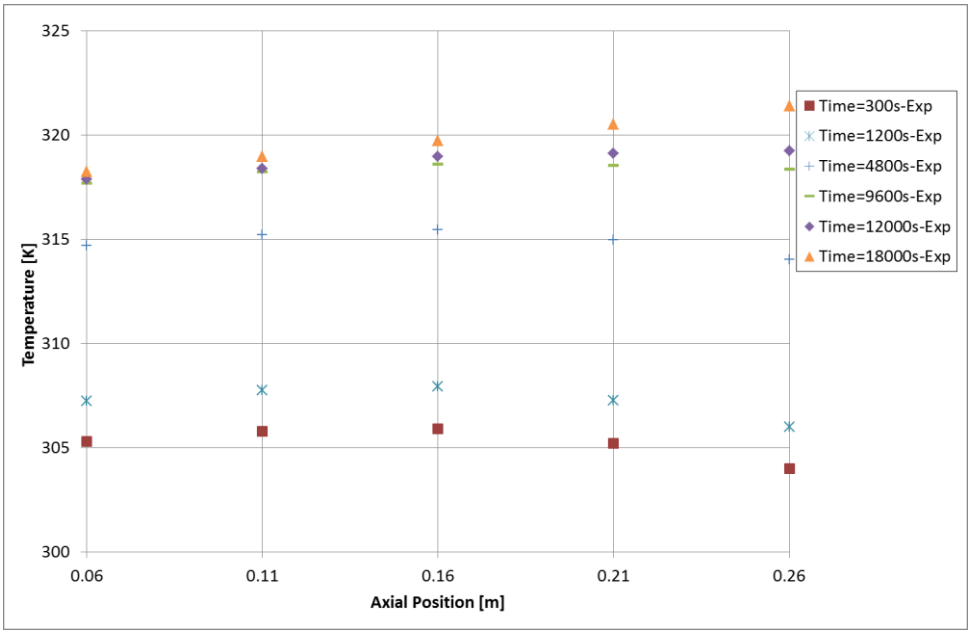

Figure 4.37 The axial temperature variations of Bed Design 1 in Experiment 1-Left axis

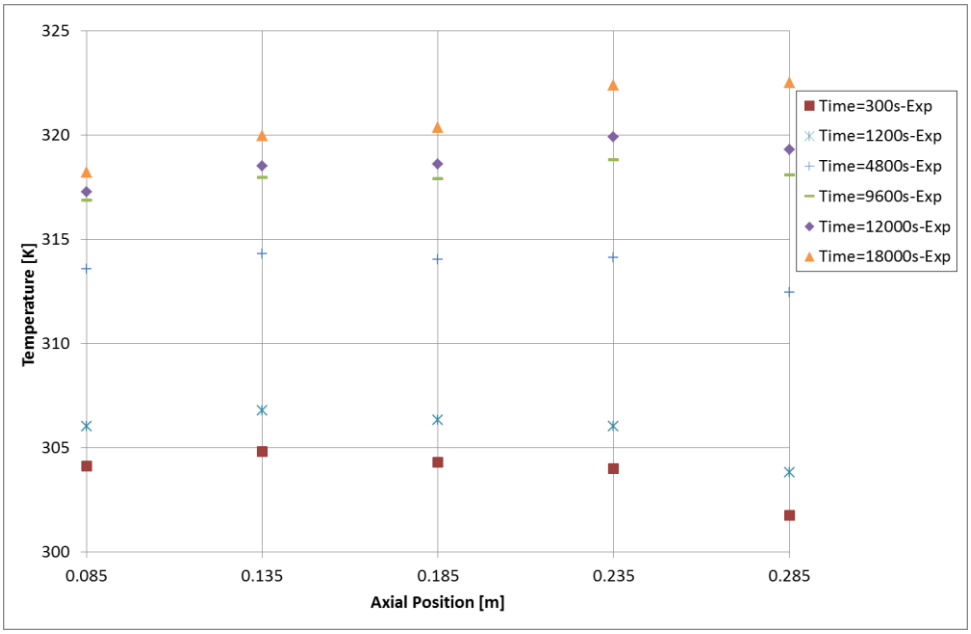

Figure 4.38 The axial temperature variations of Bed Design 1 in Experiment 1-Right axis

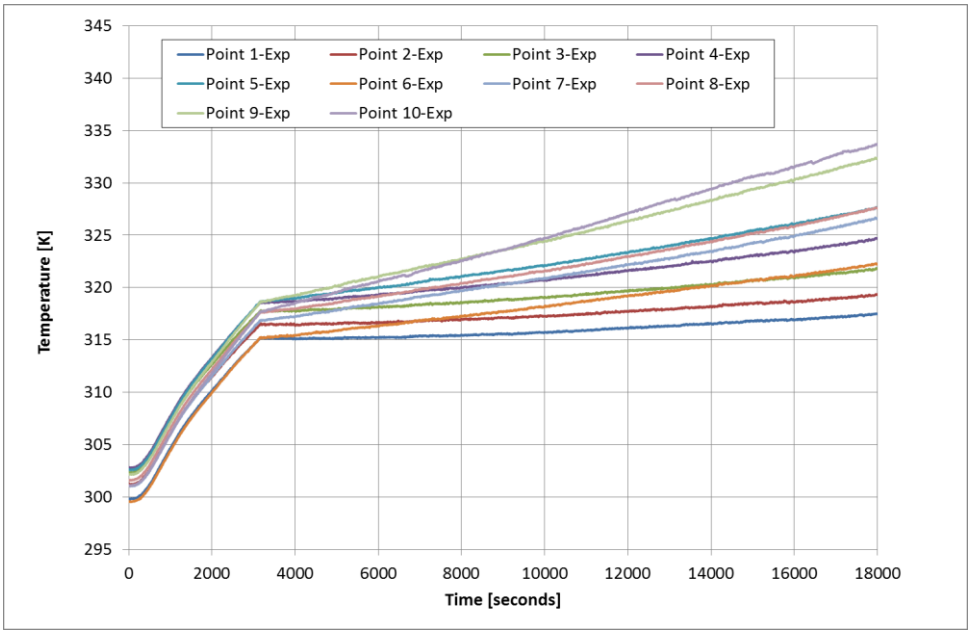

Figure 4.39 Bed temperature variations with time for Bed Design 1 in Experiment 2

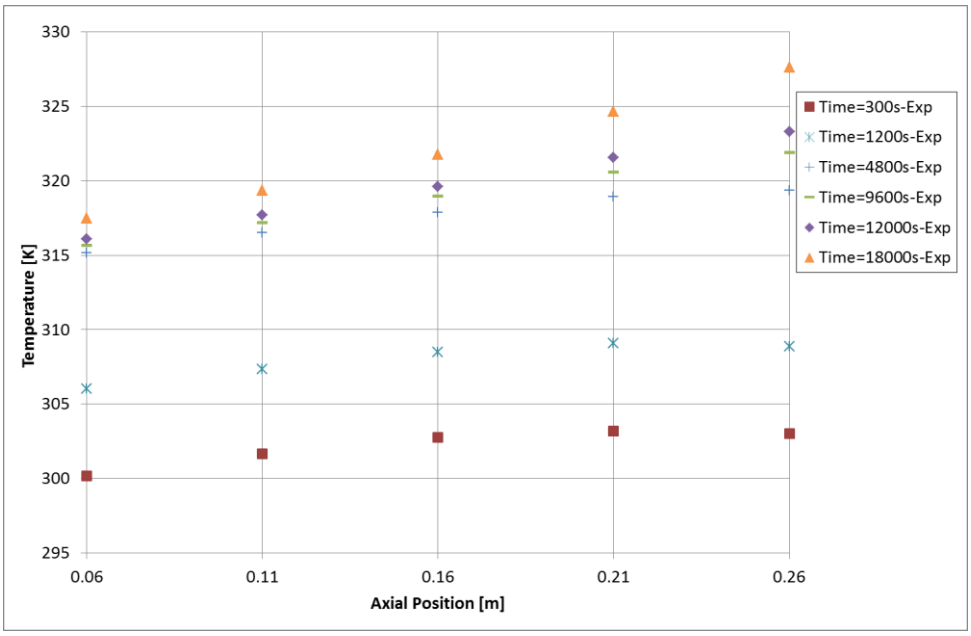

Figure 4.40 The axial temperature variations of Bed Design 1 in Experiment 2-Left axis

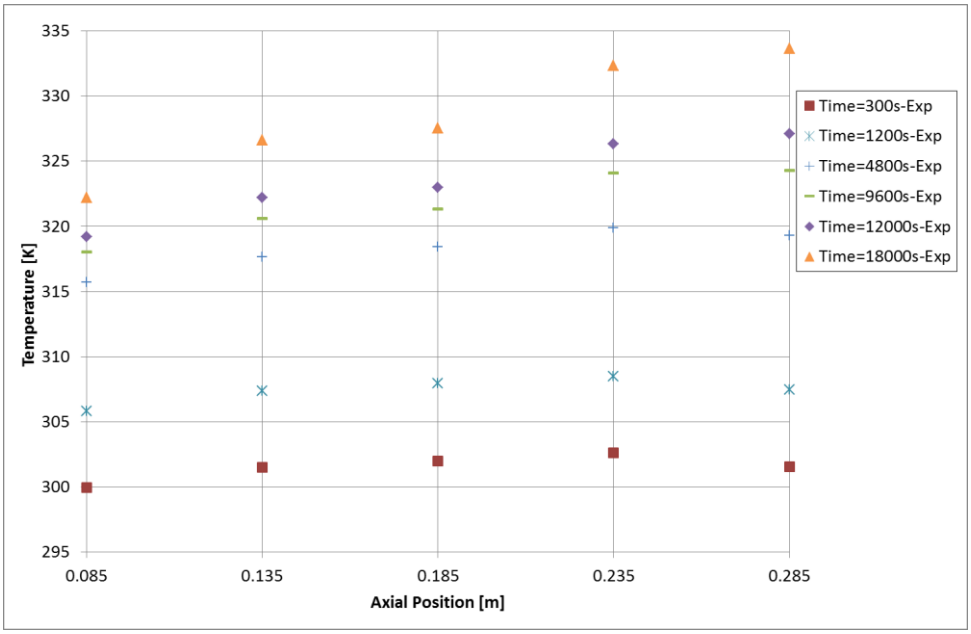

Figure 4.41 The axial temperature variations of Bed Design 1 in Experiment 2-Right axis

The difference between Experiment 1 and Experiment 2 is the HTF flow velocity values used. In Experiment 1 HTF flow velocity is 0.0012 m/s while in Experiment 2 HTF flow velocity is 0.002. In all of the experiments bed is initially at low temperature, the hot HTF flows into the bed and until the pressure of the vacuum chamber reaches the condenser pressure at 30^{o}C, valve between vacuum chamber and condenser is closed. The valve is opened manually when the pressure of the vacuum chamber reaches approximately equal to 42 mbar. After being connected to the condenser, the bed starts to desorb refrigerant. The desorbed refrigerant condenses and the condensate is accumulated in the condenser canister. During isosteric heating (pressurization) phase of the experiment, the temperature of the bed rapidly increases compared to the desorption phase. Since bed does not desorb any refrigerant in the isosteric heating phase, (the total adosbate amount in the vacuum chamber does not change while the valve of the chamber is closed), heat added to the system only increases the temperature and pressure of the bed. The heat added to the system during pressurization is called as sensible heat. The slope of the time

variation of temperature curves is steeper in the isosteric heating phase of the experiment which means temperature rise is faster. After the valve is opened desorption starts. The desorbed adsorbate leaves the bed and flows to the condenser. Some amount of heat is transfered from regions close to HTT towards the boundaries of adsorbent bed by convection via flow of refrigerant vapor. The rest of the heat added to the system is the portion required for desorption to take place. The isosteric heat of adsorption is on the order of 2000 kJ/kg for water silica gel pair. Which means, to desorb 1 kg of water, 2000 kJ energy is required. Therefore major part of the heat added to the system is spent for desorption after the valve of chamber is opened. The adsorbate loading starts to decrease with time as the desorption takes place and in the regions where adsorbate loading is lowered, the temperature starts to increase. As demonstrated in the Clapeyron diagrams, under constant pressure conditions, the desorption takes place at higher temperatures for decreasing adsorbate loading (adsorption capacity). Therefore in the upper regions of the bed which is close to the HTF inlet, the adsorption capacity is lowered due to the desorption and further heat addition resulted in temperature increase in these regions during process. The HTF temperature decreases as it advances towards the end of the bed, and heat addition at these regions was not even enough for providing the required amount for desorption. Therefore the temperature at the lower parts of the bed does not increase as fast as the upper parts. It is possible to see this kind of distribution for all of the experiments and all bed designs. Here the main difference between Experiment 1 and Experiment 2 is the heat input rate due to the HTF flow velocity. The increased heat input in Experiment 2 results in shorter isosteric heating period and higher maximum temperatures within the bed. Additionally when the axial temperature variation plots are examined, higher velocity also resulted in higher axial temperature gradients. As the heat added to the system during 18000 second duration is higher, the desorbed amount is also higher when the HTF inlet velocity is 0.002.

In Experiment 3 the HTF inlet temperature is lowered to 370 K while velocity is 0.002 and the initial adsorbate loading is 0.33.

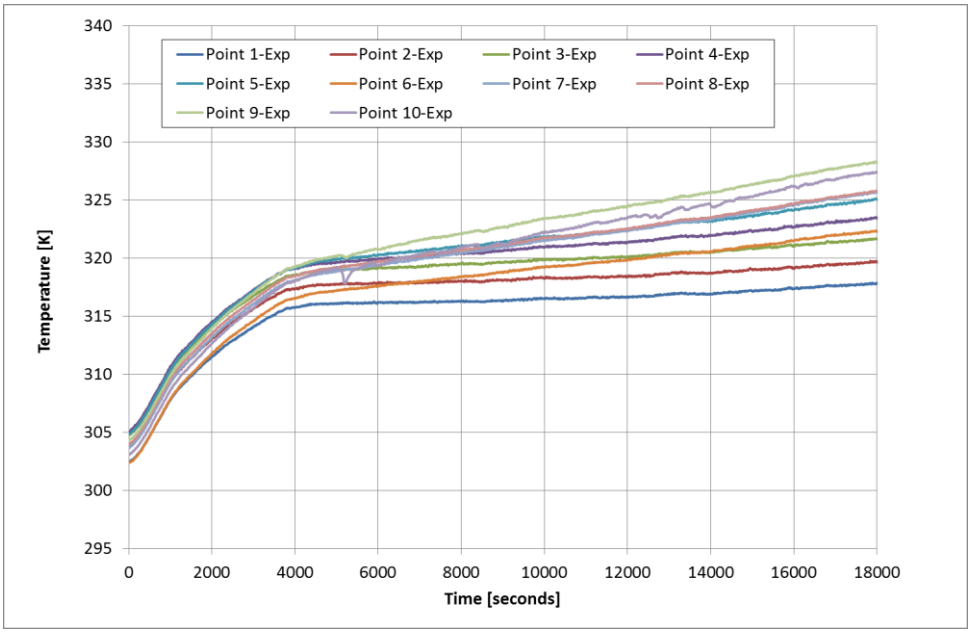

Figure 4.42 Bed temperature variations with time for Bed Design 1 in Experiment 3

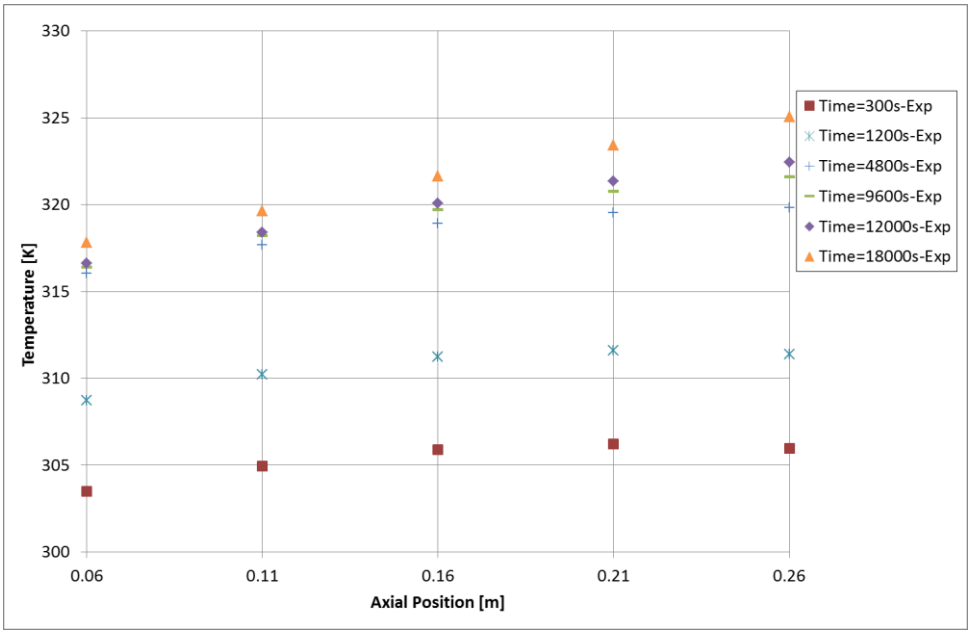

Figure 4.43 The axial temperature variations of Bed Design 1 in Experiment 3-Left axis

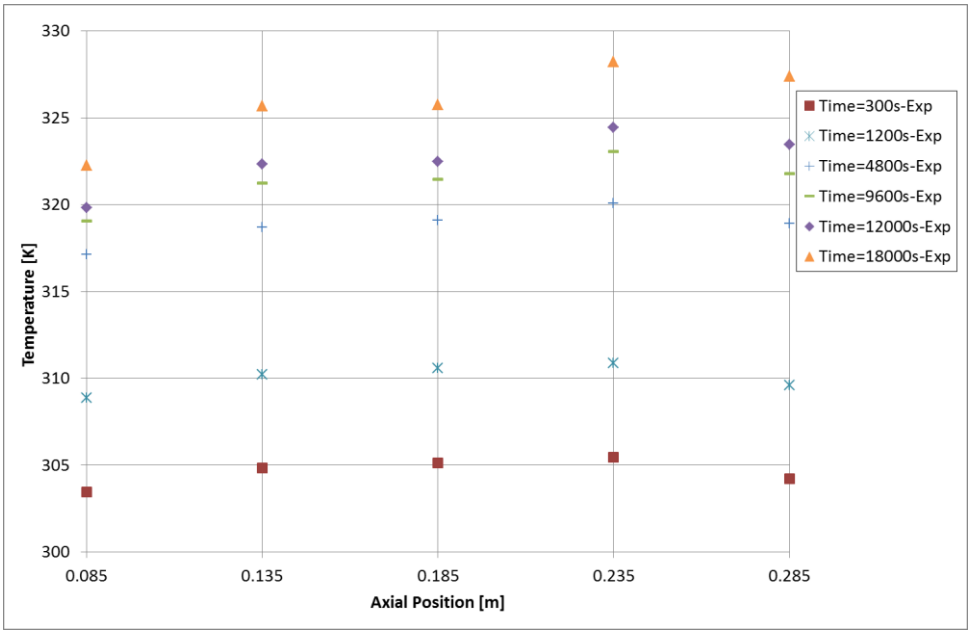

Figure 4.44 The axial temperature variations of Bed Design 1 in Experiment 3- Right axis

Compared to the values of Experiment 2 the low HTF inlet temperature increases the isosteric heating duration as a result of lowered rate of heat addition to the system. Since the temperature difference between HTF and the bed is lowered in Experiment 3 compared to Experiment 2, the slope of the temperature curves plotted against time is also decreased. Additionally the reduced inlet temperature also resulted in lowered axial temperature gradients with lowered maximum temperature values.

In Experiment 4 the initial adsorption capacity of the bed is lowered compared to other three experiments, the HTF inlet temperature was set to the same value with Experiment 2 however, the results yielded was 5 K low probably as a result of flow rate variation or the change in the ambient temperature. The adsorbate loading value for Experiment 4 is 0.32.

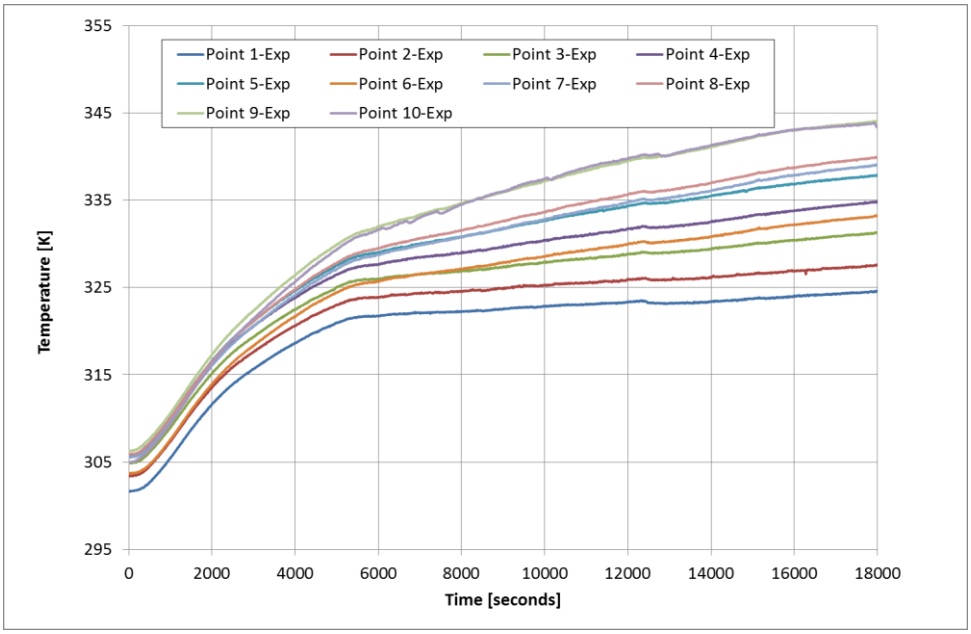

Figure 4.45 Bed temperature variations with time for Bed Design 1 in Experiment 4

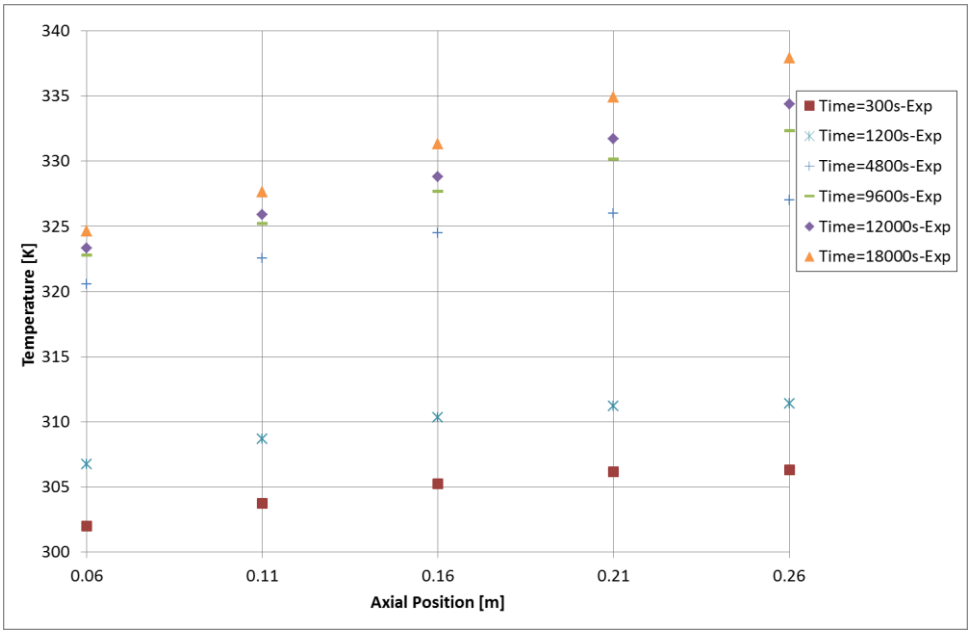

Figure 4.46 The axial temperature variations of Bed Design 1 in Experiment 4-Left axis

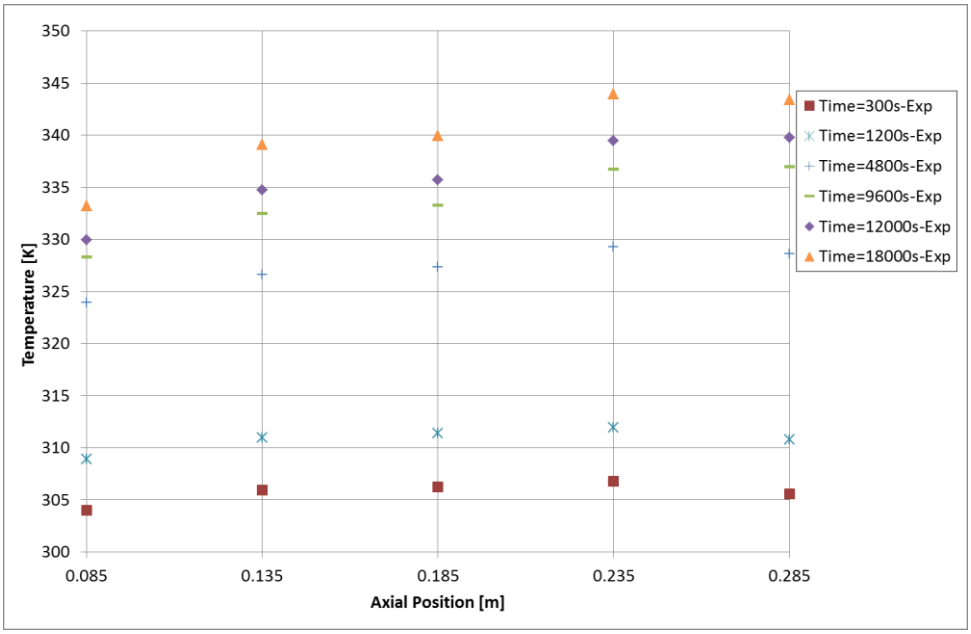

Figure 4.47 The axial temperature variations of Bed Design 1 in Experiment 4-Right axis

The initial adsorption capacity of the bed was 0.32 which is 0.01 lower compared to the Experiment 2. The difference is equals to 60 grams of water for 5.71 kg of adsorbent in the Bed Design 1. The reduced initial adsorption capacity results in reduced sensible heat load. Additionally the initial pressure of the bed is lowered due to low adsorbate loading. Due to low initial pressure isosteric heating duration is longer for Experiment 4 compared to Experiment 2. The slope of the time vartiation of bed temperature in the isosteric heating phase is lower in Experiment 4 compared to Experiment 2. In addition to duration, the temperature of the adsorbent bed at the end of isosteric heating phase is higher than the Experiment 2 since for a lower adsorption capacity value, same pressure can be reached at higher temperature. When the desorption phase temperature change rates of Experiment 2 and Experiment 4 is compared, both have similar variations. Despite the lowered sensible heat load in Experiment 4, the heat exchange rate with the HTF is also lowered since desorption takes place at a relatively high temperature. As the temperature change rates are similar, also the axial gradient magnitudes of Experiment 2 and 4 are close to each

other. However the maximum temperature values of Experiment 4 is higher compared to Experiment 2. The maximum temperature values are affected from the temperature values of the bed at the end of isosteric heating process. Therefore, when the adsorbate loading is lowered, the condensation pressure is reached at a higher temperature thus the maximum temperature values observed at the end of experiment is higher compared the other experiments.

4.4.2 Experimental Tests of Bed Design 2

The experiments for the Bed Design 2 is tried to be performed by using the same conditions with the experiments of Bed Design 1. However these two set of experiments are performed 2 months apart from each other. During that period, HTF line insulation is renewed; the flow meter is disassembled and cleaned due to clogging problems a HTF filter is installed to the system. Therefore extensive effort spent on obtaining the same conditions with the Bed Design 1 experiments however, some variations exist between experiments of Bed Design 1 and Bed Design 2.

The HTF inlet temperature, HTF velocity and the initial adsorption capacity values that had been used in experiments of the Bed Design 2 can be seen in Table 4.3.

Table 4.3 The conditions for the experiments of Bed Design 2

Bed Design 2	HTF Inlet Temperature [K]	HTF Inlet Velocity [m/s]	Initial Adsorption Capacity [$kg_{water}/kg_{adsorbent}$]
Experiment 1	397.00	0.0012	0.335
Experiment 2	390.00	0.0020	0.335
Experiment 3	370.00	0.0020	0.335
Experiment 4	390.00	0.0020	0.324

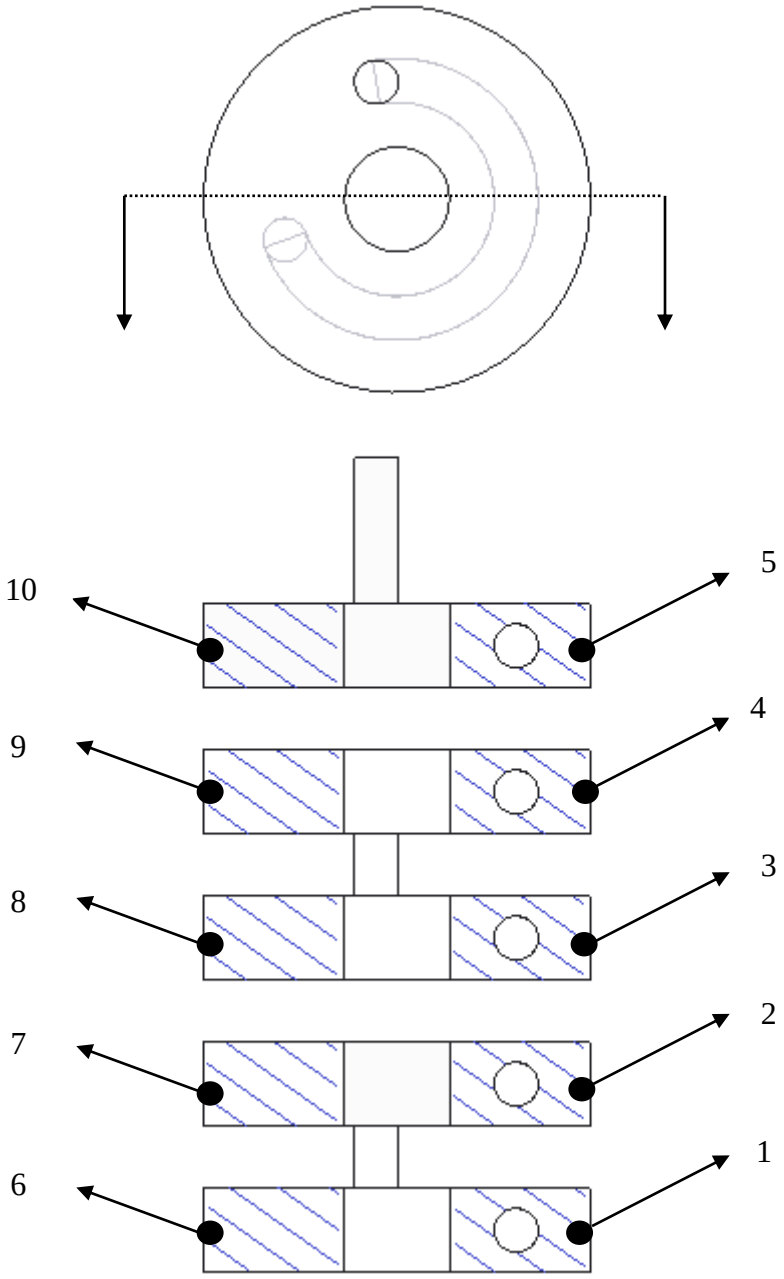

Figure 4.48 The thermocouple placement locations shown on the crossectional view of the packed bed.

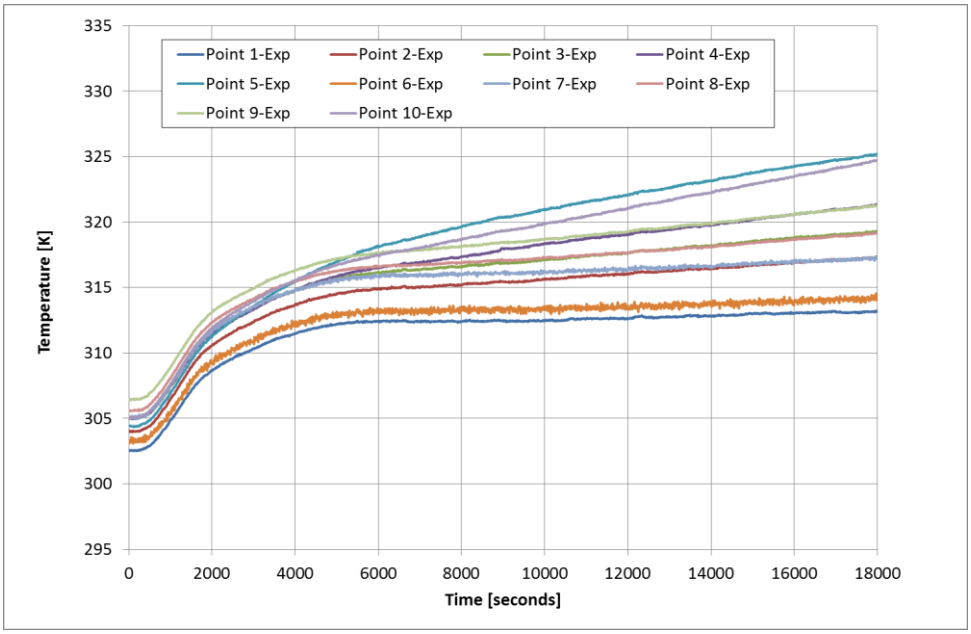

Figure 4.49 Bed temperature variations with time for Bed Design 2 in Experiment 1

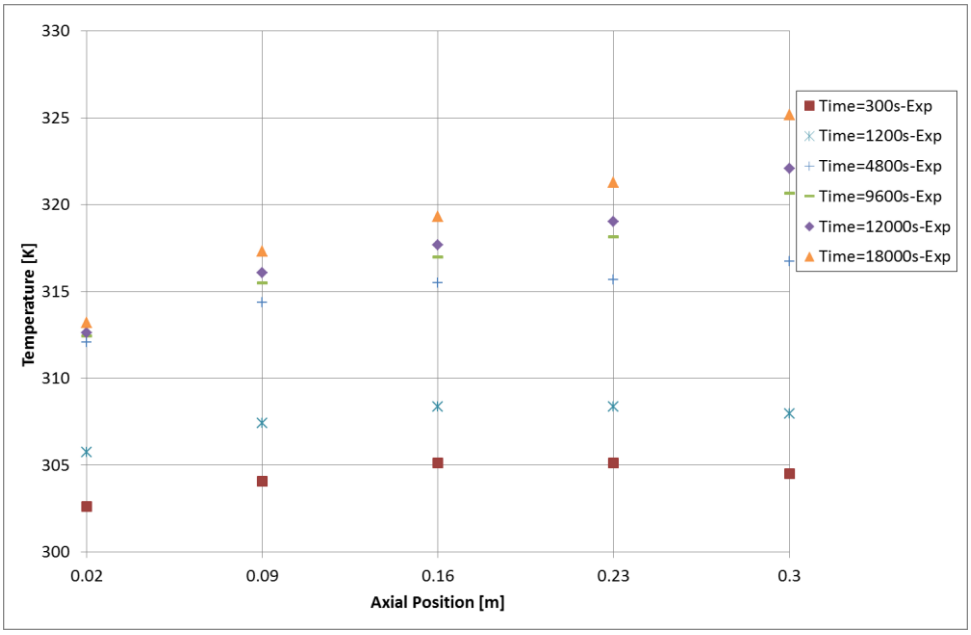

Figure 4.50 The axial temperature variations of Bed Design 2 in Experiment 1-Right axis

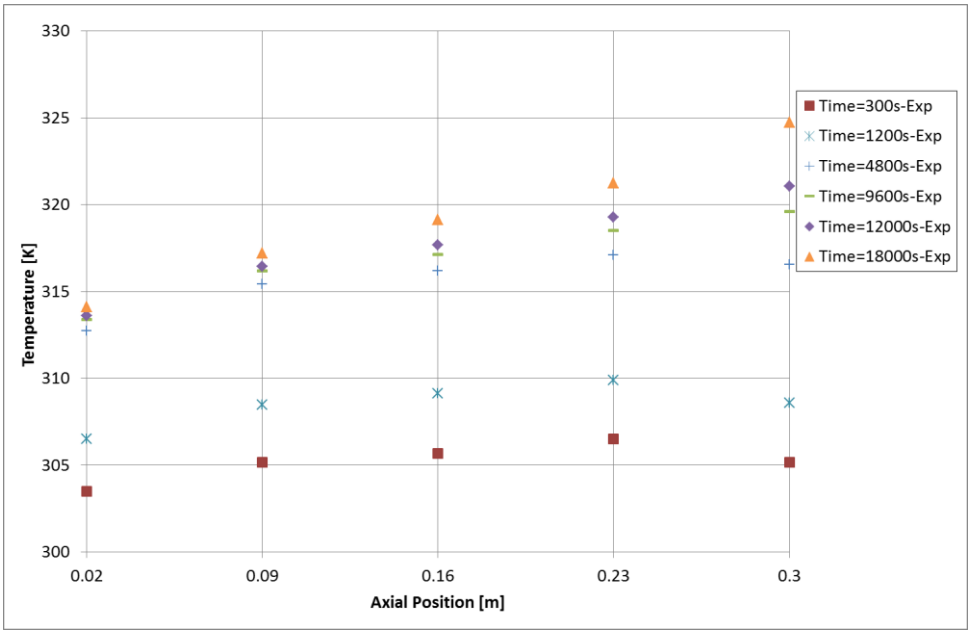

Figure 4.51 The axial temperature variations of Bed Design 2 in Experiment 1-Left axis

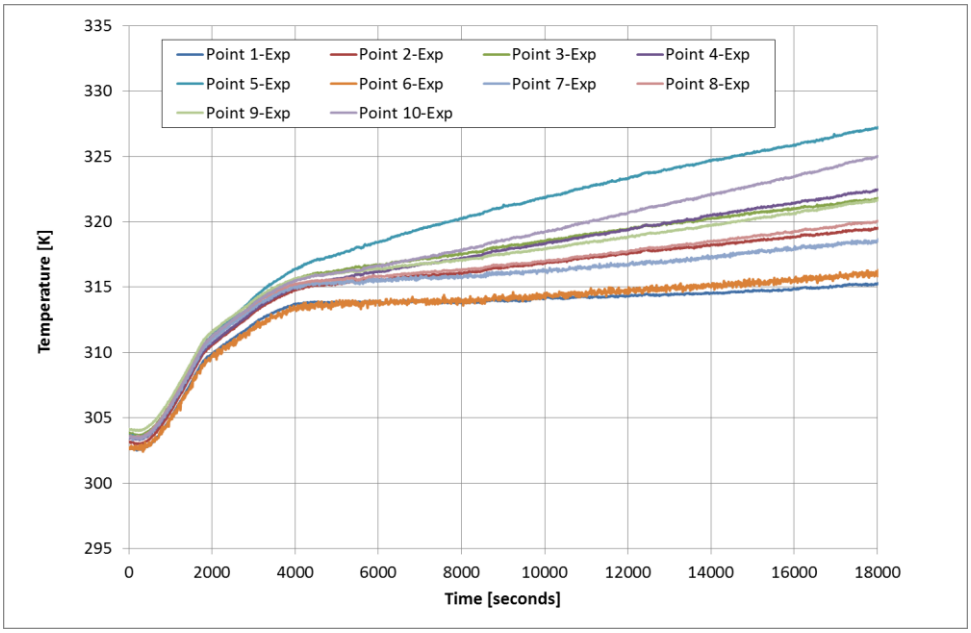

Figure 4.52 Bed temperature variations with time for Bed Design 2 in Experiment 2

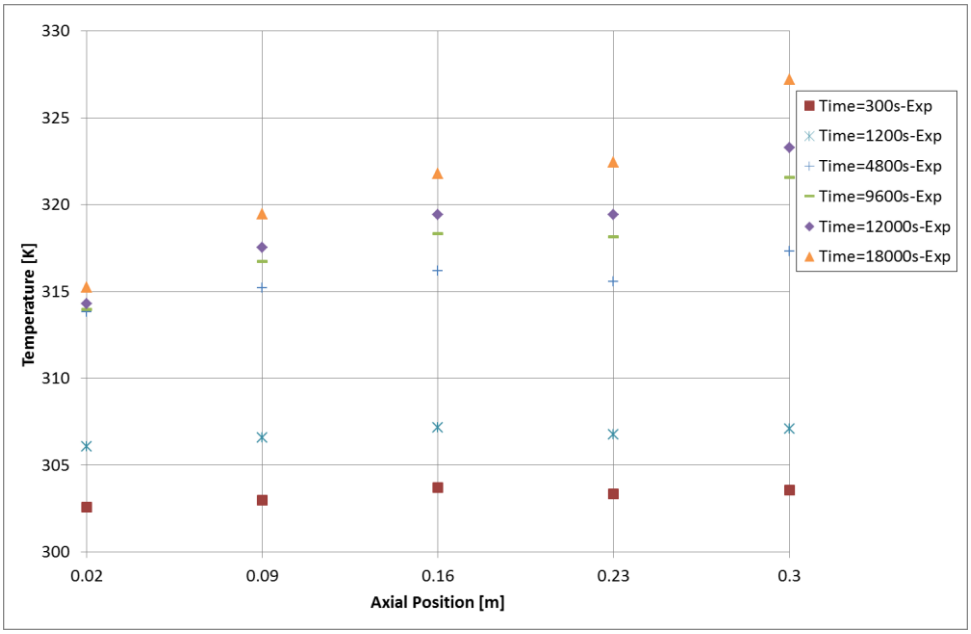

Figure 4.53 The axial temperature variations of Bed Design 2 in Experiment 2-Right axis

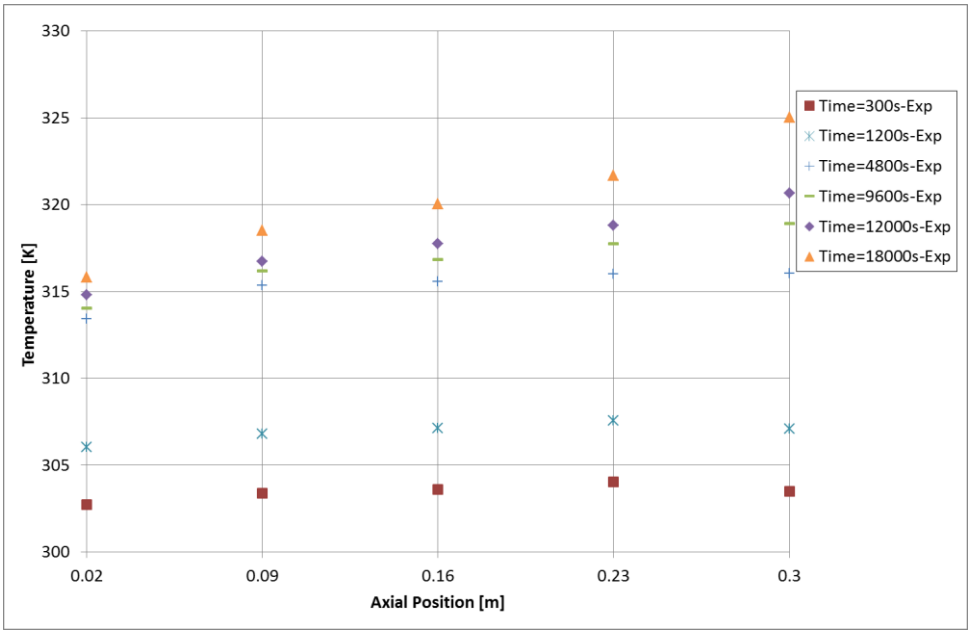

Figure 4.54 The axial temperature variations of Bed Design 2 in Experiment 2-Left axis

When the Experiment 1 and Experiment 2 for Bed Design 2 considered, it can be said that the temperature variation plots are similar. However, the initial temperature of the bed and the maximum values at the end of the experiment are different. The HTF velocity and the heat transfer rate to the bed is higher for the Experiment 2 compared to Experiment 1 and as expected the temperature change for Experiment 2 is higher than Experiment 1. On the other hand, the temperature gradients in the axial direction do not significantly differ. Due to the shape of the HTT, the HTF flows in the clockwise direction while looking from the top. As a result the temperature values measured at the right axis is higher compared to measured values on the left axis. However, the differences are relatively small which suggests that the temperature variation along the angular direction is not significant.

In Experiment 3, the HTF inlet temperature is reduced to observe the effect of inlet temperature on temperature distribution. When the results of Experiment 3 compared with Experiment 2 the effect of HTF inlet temperature could be understood for Bed Design 2.

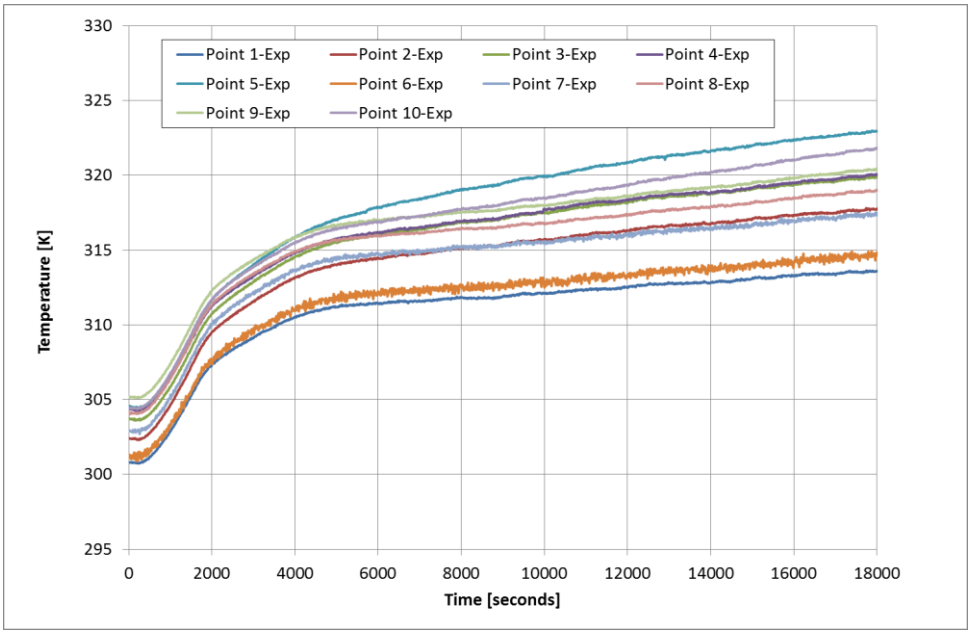

Figure 4.55 Bed temperature variations with time for Bed Design 2 in Experiment 3

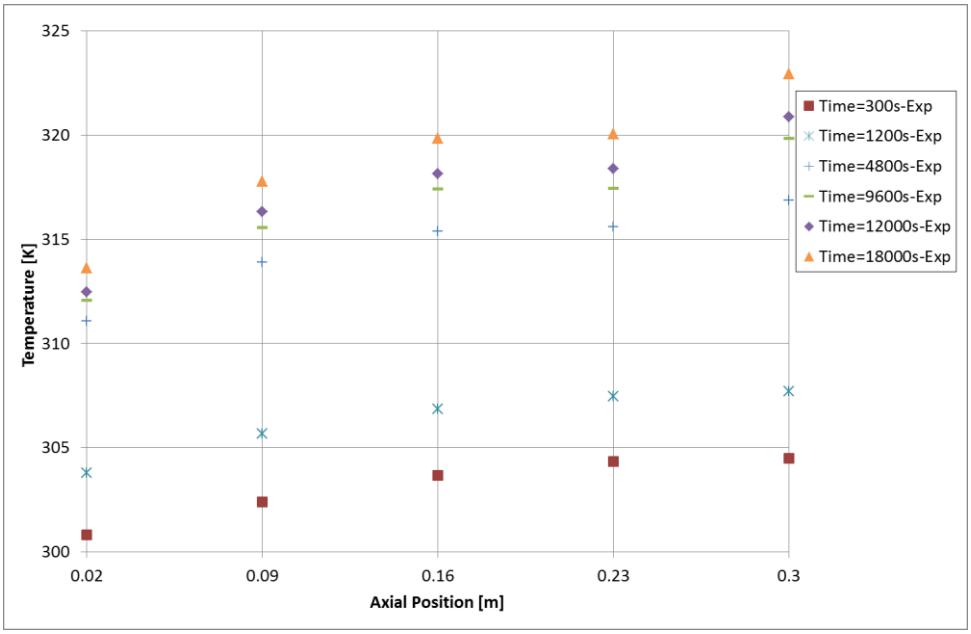

Figure 4.56 The axial temperature variations of Bed Design 2 in Experiment 3-Right axis

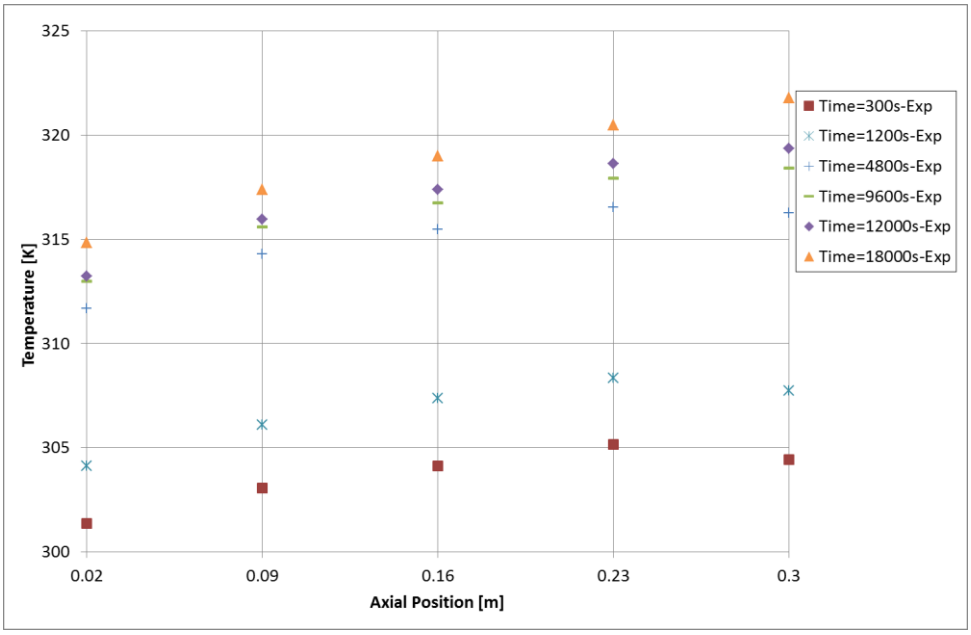

Figure 4.57 The axial temperature variations of Bed Design 2 in Experiment 3-Left axis

The reduced HTF results in reduced axial temperature gradients and reduced maximum temperature values within the bed at the end of experiment. When compared with the Experiment 2 the slope of the temperature variation plot in desorption phase, is low due to reduced heat transfer.

The Experiment 4 initial adsorbate loading is chosen to demonstrate the effect of reduced initial adsorption capacity of the bed.

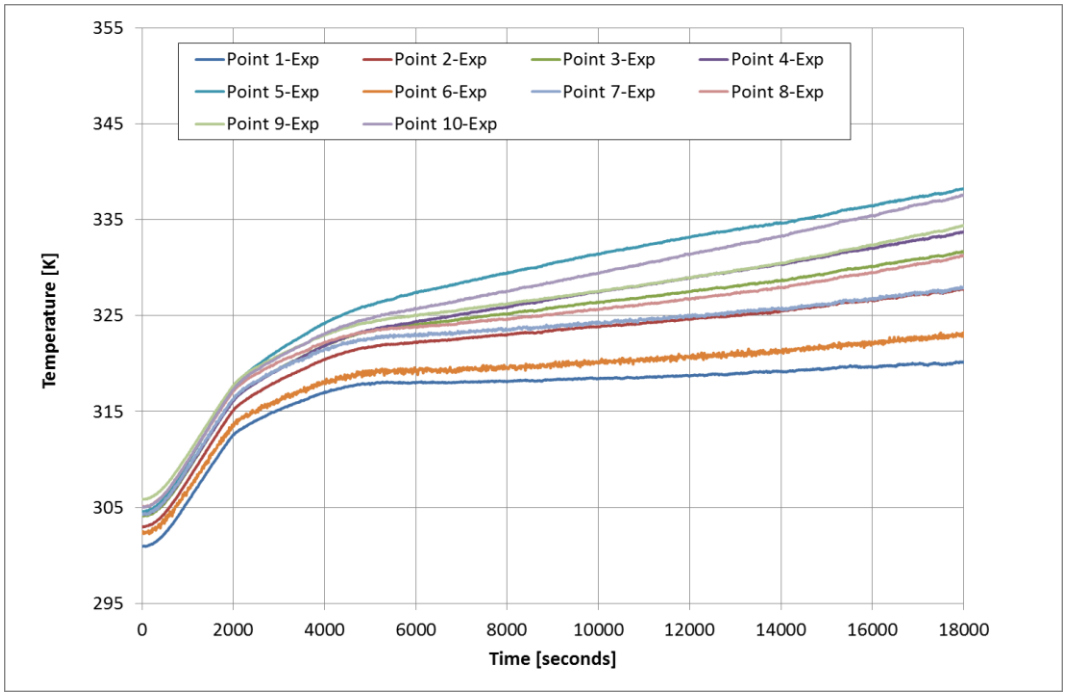

Figure 4.58 Bed temperature variations with time for Bed Design 2 in Experiment 4

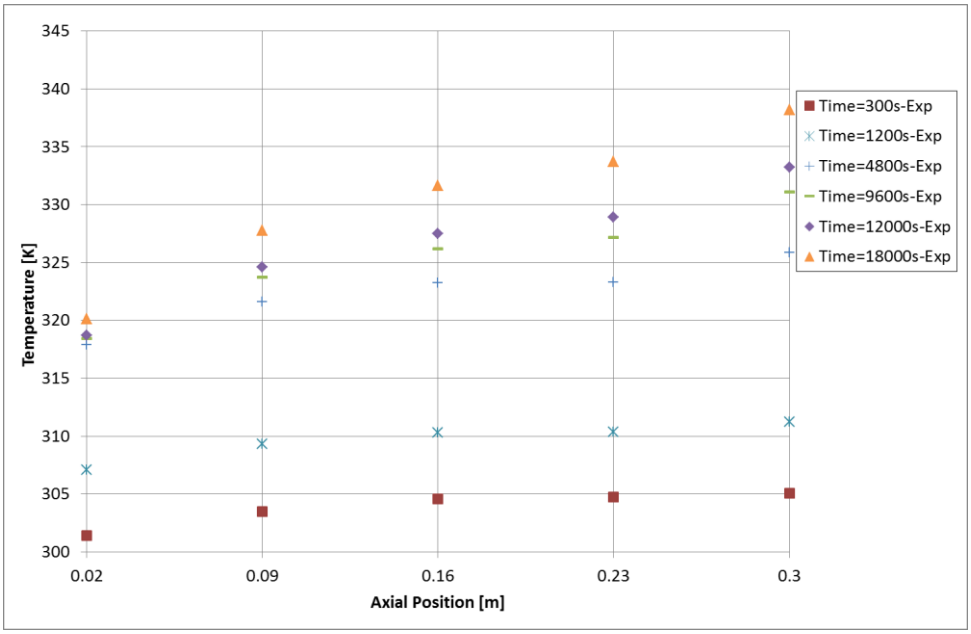

Figure 4.59 The axial temperature variations of Bed Design 2 in Experiment 3-Right axis

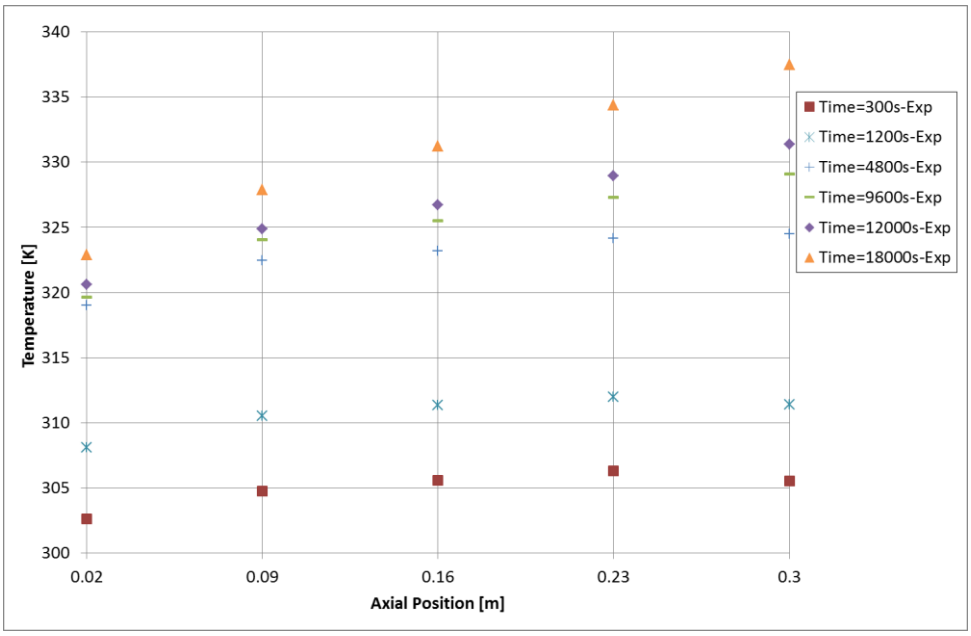

Figure 4.60 The axial temperature variations of Bed Design 2 in Experiment 3-Left axis

The reduced initial adsorbate loading results in low initial vacuum chamber pressure at a fixed temperature. Similar to the Bed Design 1 Experiment 4, the reduced adsorbate loading results in increased isosteric heating duration to reach the condenser pressure. The slope of the temperature variation plots in Experiment 4 are almost same with the Experiment 2, however the maximum temperature value and the axial temperature gradients are highest among the experiments. The higher axial temperature gradients within the bed is desired for approximating the heat recovery efficiency of an idealized thermal wave adsorption cycle. Therefore in the evaluations axial temperature gradient values will be used as a measure of heat recovery efficiency. The maximum value of the temperature gradients calculated based on the top and bottom thermocouple readings for both beds is be given in Table 4.4

Table 4.4 The maximum value of the axial temperature gradient along the adsorbent bed obtained from experimental measurements

	Maximum Axial Temperature Gradient [K/m]	
	Bed Design 1	Bed Design 2
Experiment 1	21.6	42.7
Experiment 2	57.1	42.7
Experiment 3	36.2	33.3
Experiment 4	66.5	64.6

The experiments for Bed Design 2 are tried to be performed under the same initial and boundary conditions with Bed Design 1. The adsorbent amount in Bed Design 1 is 5.71 kg which is 75 % higher than Bed Design 2. Regarding the tabulated data, the maximum axial temperature gradient values are observed at low initial adsorption capacity experiments for both of the beds. The main reason for observed higher axial temperature gradients in Experiment 4 could be the low sensible heat requirement due to reduced adsobate loading. Furthermore based on the obtained results, it could

be stated that the HTF inlet temperature affects the magnitude of the axial temperature gradients in beds. Axial temperature gradients observed in Experiment 3 are low compared to Experiment 2 for both of the beds, where only difference is the reduced HTF inlet temperature. The reduced HTF velocity had also reduced the temperature gradients in Bed Design 1 however, the maximum value for the axial gradients do not change for Bed Design 2 in Experiment 1 and Experiment 2. The temperature variation within the adsorbent bed is also related with the mass transfer characteristics of the bed, besides the thermal conductivity of the bed. Desorption rate would be reduced with the increasing mass transfer resistance of the bed under constant heat input conditions. The maximum temperature within the bed is expected to be increased with the increased mass transfer resistance for the same amount of heat input and same bed thermal conductivity. Additionally the low heat diffusion rate within the classical packed bed type adsorbent beds is another limiting phenomena for the desorption or adsorption rate in general.

The mass transfer resistance of the Bed Design 2 is relatively low due to higher mass transfer surface area and less amount of adsorbent surrounding the HTT. The mass transfer rate under same conditions would be higher for the Bed Design 2 compared to Bed Design 1. Therefore in Bed Design 2, which has lower mass transfer resistance, increasing the HTF velocity do not results in higher temperatures and higher axial temperature gradients since increased heat transfer rate do not further increase the desorption rate under the conditions of Experiment 1 and 2. Additionally the heat transfer rate is limited by the heat diffusion within the adsorbent particles. Since the packing density for Bed Design 2 is lower compared to Bed Design 1 heat diffusion within the bed is another limiting factor that affects temperature distributions. Additionally the Bed Design 2 has lower HTT surface area in contact with adsorbent particles compared to Bed Design 1. Therefore increased HTF velocity does not significantly changed the temperature distribution and the maximum value of the axial temperature gradient. Resultantly similar temperature

profiles and axial temperature gradients observed in Experiment 1 and Experiment 2 of the Bed Design 2.

On the other hand, in Bed Design 1 due to relatively higher mass transfer resistances temperature and pressure distribution is more related with the heat transfer rate and HTF velocity. Since the higher mass transfer resistance of Bed Design 1 is imposing a limit on the desorption rate, therefore the temperature and pressure distribution within the bed would be altered with increased heat transfer rate. Moreover in Bed Design 1 heat exchange surface area between HTT and the adsorbent particles is relatively high thus, increased HTF velocity effect may be more emphasized on the temperature distribution in Bed Design 1.Resultantly increased HTF velocity and increased heat transfer between HTF and the adsorbent particles results in higher axial temperature gradients and higher temperature values in Bed Design 1 referring to the results of Experiment 1 and Experiment 2.

The higher adsorbent temperature reduces the heat transfer rate between HTF and adsorbent particles. Since the temperature difference between HTT and the adsorbent particles is reduced the heat transfer rate is reduced. As a result of this reduction, the limiting effect of mass transfer rate on the bed temperature distribution had not been observed. Therefore, the maximum values of the axial temperature gradients in both bed designs are reached the same values regardless of the mass transfer characteristics in Experiment 4. Consequently, it could be stated that, when the desorption process is not constrained by the mass transfer rate, heat transfer characteristics and the axial temperature gradients depends on the heat transfer rate between HTF and the bed. The heat transfer rate between HTF and the bed is limited by the heat diffusion rate within the bed.

Higher maximum temperature values observed in the Bed Design 1 compared to Bed Design 2 in all experiments. The higher maximum temperature values could be reasoned from the higher mass transfer resistance of the Bed Design 1. As stated

earlier with the increased mass transfer resistance, higher adsorbent temperature and pressures are required for desorption to take place. The vapor pressure needs to be higher at the desorbing regions of the bed to overcome the resistance inside bed to flow out of the boundaries. In the current designs beds are heated from inner regions by the HTF and the particles in the regions close to HTT start to desorb earlier than the particles in the outer regions. Therefore the temperature distributions within the bed closely coupled with the pressure distribution within the bed which is the driving force for the flow of refrigerant vapor towards the boundaries.

In the experiments higher maximum temperature values and axial temperature gradients are observed for Bed Design 1 despite its high dead mass compared to Bed Design 2. Moreover, the axially discontinuous structure of Bed Design 2 had not significantly changed the temperature gradients in the axial direction and improved the heat recovery efficiency of the bed.

These results may suggest that the conductive heat transfer in the axial direction within the bed is not significant compared to the advancement rate of the HTF in axial direction. Moreover, the bed dead mass does not significantly change the heat recovery efficiency of the adsorbent bed regarding the evaluation based on the maximum values of axial temperature gradients within the bed. Under the conditions investigated lower initial adsorption capacity values may yield higher heat recovery efficiency of the adsorbent bed during desorption. Additionally the effect of HTF velocity also depends on the mass transfer characteristics of the bed. The heat recovery efficiency indicated by the maximum value of axial temperature gradients, could be increased by the increased HTF velocity if the desorption rate is limited by the mass transfer resistance. On the other hand HTF velocity increase may not affect the heat recovery efficiency significantly when mass transfer resistance of the bed is not limiting the desorption rate. All of the observation and conclusions are derived based on the results of experimental investigations of bed designs under the specified

conditions. The uncertainty quantification for the experimental investigation can be seen in Appendix E.

4.5 Three Dimensional Numerical Analyses of Adsorbent Beds

In addition to the experimental tests performed, the designed beds subjected to investigation are also numerically analyzed by using the commercial finite element solver COMSOL Multiphysics. The mathematical models used in the analyses are LTE and LTNE based models. The details of the mathematical modeling and the governing equations used were given in the previous chapter. In this chapter the three dimensional full scale analyses results will be given in comparison with the experimental data. The boundary conditions and operating conditions are defined to be identical with the experimental conditions for being able to make a comparison with the experimental data. The difficulty of making three dimensional analyses with all of the governing equations solved in a coupled manner requires extremely high amounts of computer resources (memory and cpu) and run times. Therefore to reduce the overall size of the computational domain,3-D models used in the analyses represent the part of the bed which is inside the vacuum chamber. The numerically modeled part of the adsorbent bed in the vacuum chamber for different bed designs can be seen in Figure 4.61.

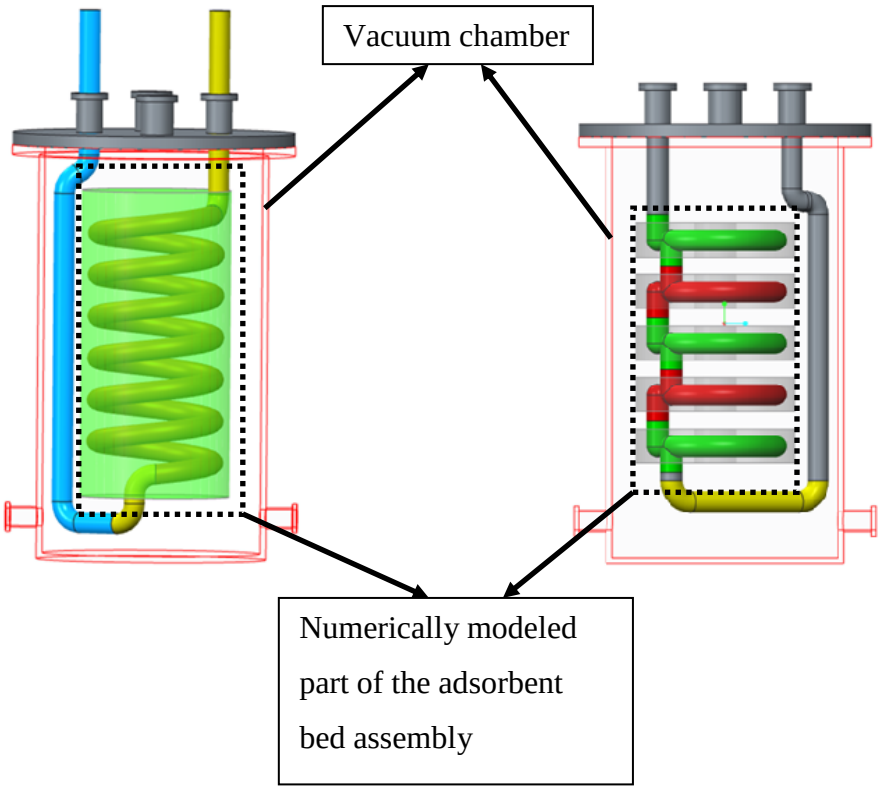

Figure 4.61 Numerically modeled part of the adsorbent bed assembly in the vacuum chamber

Additionally, the vacuum chamber and had not been modeled which would increase the memory requirements and the run time. Instead the conditions imposed on the adsorbent bed by the vacuum chamber tried to be defined on the adsorbent bed domain boundaries. All other assumptions presented in Chapter 3 are also used in the modeling.

The 3-D CAD data of the Bed Design 1 had been imported into the analysis software and the spatial discretization applied by meshing the geometry. After completing the mesh generation process, the governing equations and parameter definitions for two different modeling approaches had been made. The governing equations for the HTF

and HTT is identical for both LTE and LTNE based models, these equations can be listed as,

Mass, momentum and energy conservation equations for the HTF

$$\rho_f \nabla . \mathbf{V_f} = 0 \tag{4.1}$$

$$\frac{D\mathbf{V_f}}{Dt} = -\frac{1}{\rho_f}\nabla p_f + \frac{\mu_f}{\rho_f}\nabla^2 \mathbf{V_f} \tag{4.2}$$

As mentioned earlier, the effect of body forces is assumed to be negligibly small. In the circular flow path shapes, body forces can also be resulted by centrifugal acceleration in addition to gravitational acceleration. However due to low flow velocity values, the effect of body forces caused by centrifugal acceleration will also be neglected in the calculations.

$$\rho_f c_f \frac{DT_f}{Dt} = k_f \nabla^2 T_f \tag{4.3}$$

Since HTT is immobile only energy conservation equation had been solved.

$$\rho_t c_t \frac{\partial T_t}{\partial t} = k_t \nabla^2 T_t \tag{4.4}$$

The set of governing equations used in the LTE analyses for modeling the adsorbent bed can be listed as follows,

Conservation equations for the adsorbent bed

Mass conservation equation for the gas phase:

$$\varepsilon_t \frac{\partial \rho_g}{\partial t} + (1-\varepsilon_g)\rho_s \frac{\partial X}{\partial t} + \boldsymbol{\nabla}.\mathbf{V_g} = 0 \tag{4.5}$$

Momentum conservation equation for the gas phase,

$$\mathbf{V_g} = -\frac{\kappa_g}{\mu}\boldsymbol{\nabla} p_g \tag{4.6}$$

Energy conservation equation for solid, gas and adsorbed phases,

$$\varepsilon_t \rho_g c_{pg} \frac{\partial T_{gs}}{\partial t} - \varepsilon_g \frac{\partial p_g}{\partial t} + (1-\varepsilon_t)\rho_s c_{ps} \frac{\partial T_{gs}}{\partial t} + (1-\varepsilon_t)\rho_s X c_{pl} \frac{\partial T_{gs}}{\partial t}$$
$$= \nabla\left(k_{eq} \nabla T_{gs}\right) + (1-\varepsilon_t)\rho_s \frac{\partial X}{\partial t} \Delta H_{ad} - \rho_g \mathbf{V_g} c_{pg} \boldsymbol{\nabla}. T_{gs} \tag{4.7}$$

Adsorption-desorption rate equation (based on LDF model)

$$\frac{\partial X}{\partial t} = k_m\left(X_{eq} - X\right) \tag{4.8}$$

As an equation of state for the gas phase the ideal gas equation will be used to solve the system of equations by using numerical methods.

$$p_g = \rho_g R_g T_{gs} \tag{4.9}$$

As mentioned previously for the analyses based on the LTNE assumption, there are two different energy conservation equations exists, one of which is for the gas phase the other is for the solid phase. The set of governing equations used in the LTNE based analyses can be given as,

Mass conservation equation for the gas phase:

$$\varepsilon_t \frac{\partial \rho_g}{\partial t} + (1 - \varepsilon_g)\rho_s \frac{\partial X}{\partial t} + \boldsymbol{\nabla}.\mathbf{V_g} = 0 \tag{4.10}$$

Momentum conservation equation for the gas phase,

$$\mathbf{V_g} = -\frac{\kappa_g}{\mu}\boldsymbol{\nabla} p_g \tag{4.11}$$

Energy conservation equation for solid phase,

$$\begin{aligned}&(1 - \varepsilon_t)\rho_s(c_{ps} + X c_{pl})\frac{\partial T_s}{\partial t} + \\ &= \boldsymbol{\nabla}(K_{seq}\boldsymbol{\nabla} T_s) + a_{gs}h_{gs}(T_g - T_s) + (1 - \varepsilon_t)\rho_s \frac{\partial X}{\partial t}\Delta H_{ad}\end{aligned} \tag{4.12}$$

Energy conservation equation for gas phase,

$$\begin{aligned}&\varepsilon_t \rho_g \frac{\partial(c_{pg}T_g)}{\partial t} + \rho_g \mathbf{V_g}.\boldsymbol{\nabla}(c_{pg}T_g) + c_{pg}(T_s - T_g)(1 - \varepsilon_t)\rho_s \frac{\partial X}{\partial t} \\ &= \boldsymbol{\nabla}(K_{geq}.\boldsymbol{\nabla}\langle T_g\rangle_g) - a_{gs}h_{gs}(T_g - T_s)\end{aligned} \tag{4.13}$$

Adsorption-desorption rate equation,

$$\frac{\partial X}{\partial t} = k_m(X_{eq} - X) \tag{4.14}$$

As an equation of state for the gas phase the ideal gas equation will be used.

$$p_g = \rho_g R_g T_{gs} \tag{4.15}$$

The mesh generated on both bed designs are based on similar procedures. The main aim is to intensify the mesh around the locations where higher gradients may exist.

Additionally for being able to accurately solve the HTF low in HTT, boundary layer elements are used for meshing the HTF domain. The HTT is a relatively complex geometry. The curvature and the possible high gradients in the proximity, the HTF domain is meshed by using smaller elements. The size functions are applied to facilitate slow growth of mesh size from the high mesh density regions. The HTT domain is not physically modeled since it has a thickness of 1 mm and creating mesh elements on thin walls will increase the mesh element number of the model dramatically. Therefore HTT is modeled by using thin conductive layer feature which is a built in module in the software. The thin layer feature imposes conductive effect of the HTT in energy equations by employing conduction equation solution on the shell type mesh elements. Thin layer feature also accounts for the heat capacity and the mass of the HTT. More details on the feature can be found in [151]. The meshes used in the computations are dominantly composed of unstructured tetrahedral elements. Additionally there are prismatic elements used in the HTF domain in the proximity of the HTT walls. The mesh used for analysis of Bed Design 1 and Bed Design 2 can be seen in Figure 4.62 and Figure 4.63 respectively.

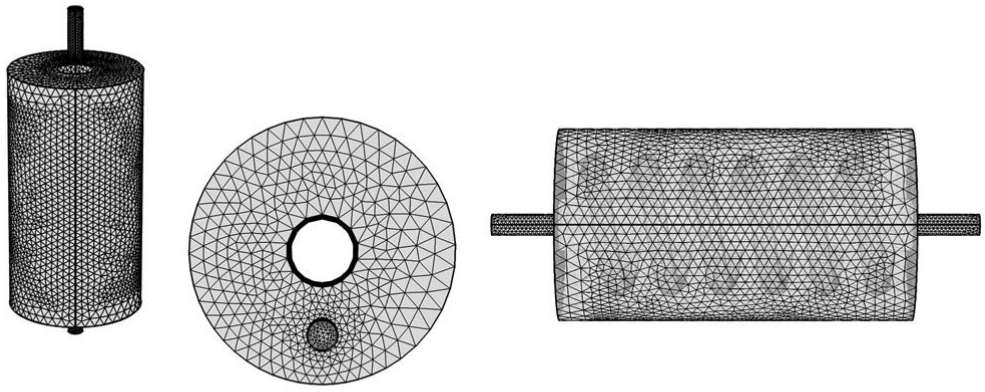

Figure 4.62 General, top and side view of the mesh structure used for analyses of Bed Design 1

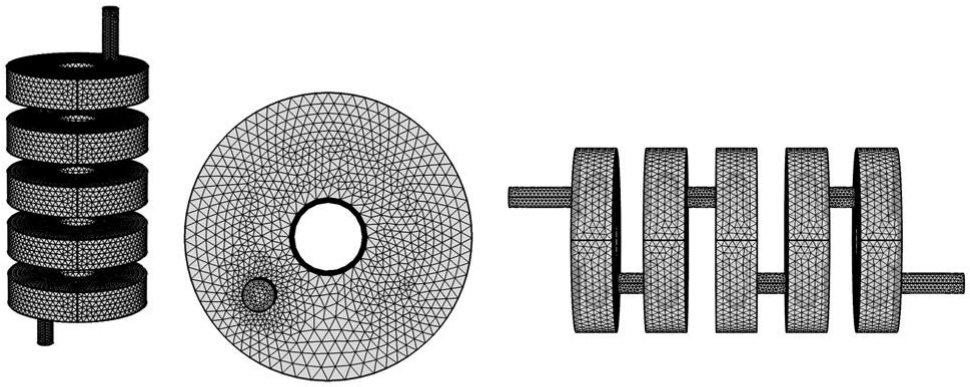

Figure 4.63 General, top and side view of the mesh structure used for analyses of Bed Design 2

The number of mesh elements used in the LTE based analyses of Bed Design 1 is 659429 and the number elements used in the LTNE based analyses is 1195842. The number of elements used in the LTE based analyses of Bed Design 2 is 585256 while the number of mesh element used for LTNE based analyses is 1065634. The grid independence of the solutions are checked by using higher number of mesh elements, the results of the grid independence study can be found in Appendix D. The performed analyses required approximately, 38 GB of memory during the solutions of normal sized mesh and a typical analysis takes 5 hours to be completed by using 16 core CPU. The size of the results file for a single case is 18 GB but file size can be as high as 67 GB depending on the modeling approach and mesh size.

4.5.1 Boundary and Initial Conditions Used in Three Dimensional Analyses

The computational domain is mainly composed of physical domains. One of them is the HTF domain. The HTF supposed to be surrounded by the HTT however, as a model simplification, HTT is not physically modeled. As mentioned the thickness of the HTT is relatively small and direct modeling of HTT will result in dramatic increase in the mesh element number. Therefore thickness and thermophysical properties of the HTT are defined in the thin layer feature of the software. The thin layer module accounts for the conductance and thermal impedance of the HTT by assigning these properties on surface elements. The thin layer surface is defined as the outer surfaces of the HTF domain. The second physical domain is the volumes that are filled with adsorbent particles. These volumes are also physically modeled and meshed. The HTF domain for Bed Design 1 and Bed Design 2 can be seen in Figure 4.64.

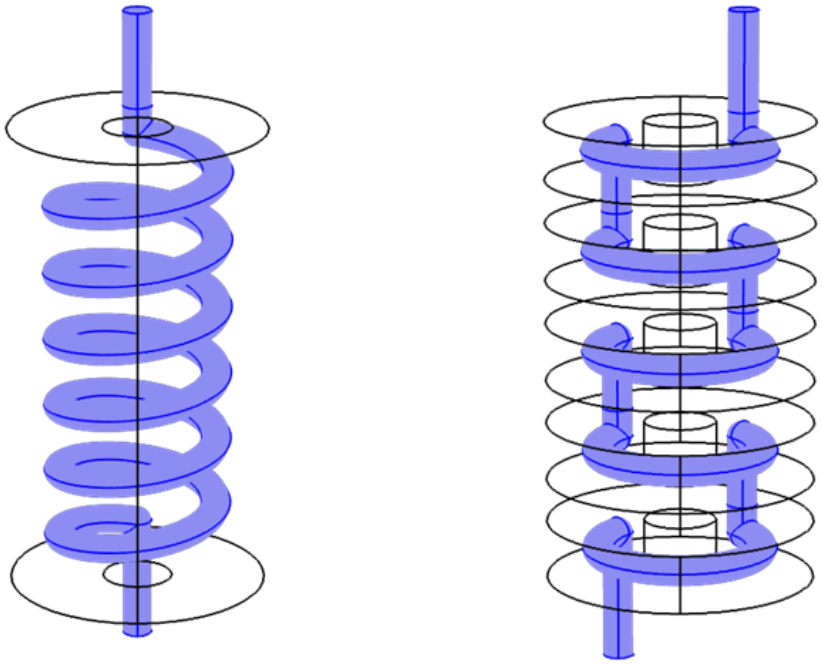

Figure 4.64 HTF domains for Bed Design 1 (Left) and Bed Design 2 (Right) analysis models

The mass and momentum conservation equations for the HTF are solved in these domains. The colored surfaces are defined as no-slip wall boundary during the solution of momentum conservation equation. The surfaces which are defined as inlet and outlet for the HTF domain can be seen in Figure 4. 65.

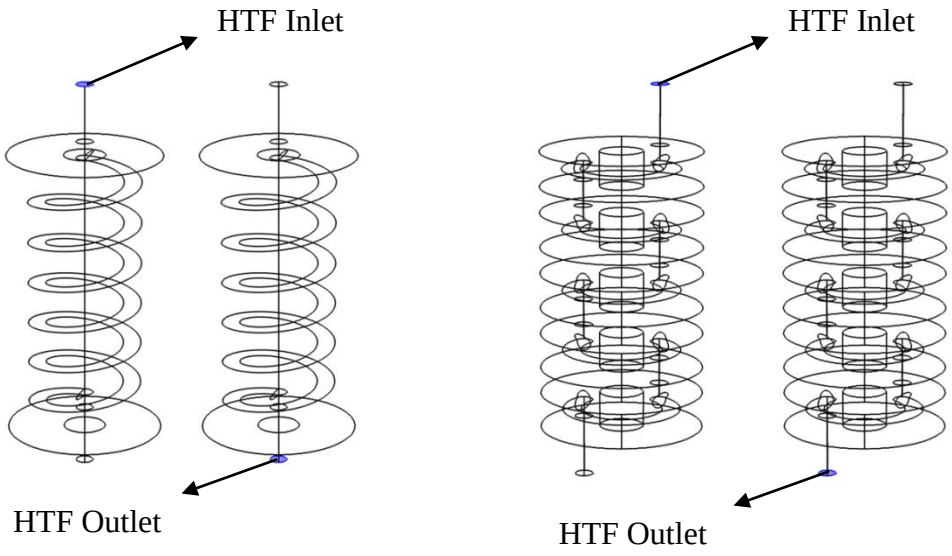

Figure 4.65 Inlet and outlet boundaries for the HTF domain in Bed Design 1(Left) and Bed Design 2 (Right)

The velocity value is specified at the inlet boundary in numerical analyses. The outlet boundary for the HTF is defined to be pressure outlet boundary, which imposes a pressure value at the outlet section. In computational methods this type of boundary definition is commonly used when the domain is open to atmospheric pressure. In the analyses, the HTF velocity values measured are directly used.

As stated earlier the numerical models are constructed by using the part of the adsorbent bed which remains within the vacuum chamber. However, the temperature of the HTF inlet and outlet had been measured from a different location than they had been defined in the numerical model. Additionally, the HTT is in contact with the massive vacuum chamber cap which could cause the variation of temperature of HTF as it flows from the measured location to the HTF inlet location defined in the numerical analysis model. As a result, to impose more accurate HTF inlet temperature values to the numerical analysis models, the part of the system remaining between the analysis model and the HTF inlet temperature measurement location and the cap of the vacuum chamber is also numerically analyzed by using a

separate model. In this model the measured HTF inlet temperature is used for calculating the HTF temperature at the HTF inlet boundary which is used in the numerical analyses. The details of this numerical sub-model can be found in Appendix F. In the numerical analyses of the adsorbent bed the HTF inlet temperatures obtained from the sub-model analyses of the vacuum chamber cap and HTT section remaining outside the vacuum chamber is used. The HTF inlet temperatures used in the numerical analyses are given in Table 4.5 together with the experimentally measured values.

Table 4.5 The boundary conditions used for the HTF domain in numerical analyses

		HTF Inlet Temperature [K]	HTF Inlet Velocity [m/s]	HTF Inlet Temperature Used in The Analysis [K]
Bed Design 1	Experiment 1	397	0.0012	384
	Experiment 2	397	0.002	388
	Experiment 3	370	0.002	364
	Experiment 4	394	0.002	385
Bed Design 2	Experiment 1	397	0.0012	384
	Experiment 2	390	0.002	381
	Experiment 3	370	0.002	364
	Experiment 4	390	0.002	381

A similar situation exists for the outlet of the HTF however; it is not possible to determine the difference between measured value and the values obtained from analyses since outlet temperature varies with time. Therefore the outlet temperature obtained from the analyses will not be presented.

In the full scale numerical analyses of the adsorbent bed the HTT is defined on the surface of the HTF domains shown in Figure by using the thin layer feature. The thickness of the HTT is 1 mm and the material for HTT is copper. The outer surface of the HTT is in contact with the adsorbent particles. As previously stated an explicit

heat transfer coefficient is defined at this boundary to simulate the effect of thermal resistance between HTT and the adsorbent particles. There are various different values available in the literature. The method that had been used in this study is explained in Chapter 3. Therefore heat transfer coefficient of 40W/m^{2}K is defined at the HTT adsorbent particle interface. The surfaces at which this thermal resistance is defined can be seen in Figure 4. 66 for Bed Design 1 and Bed Design 2.

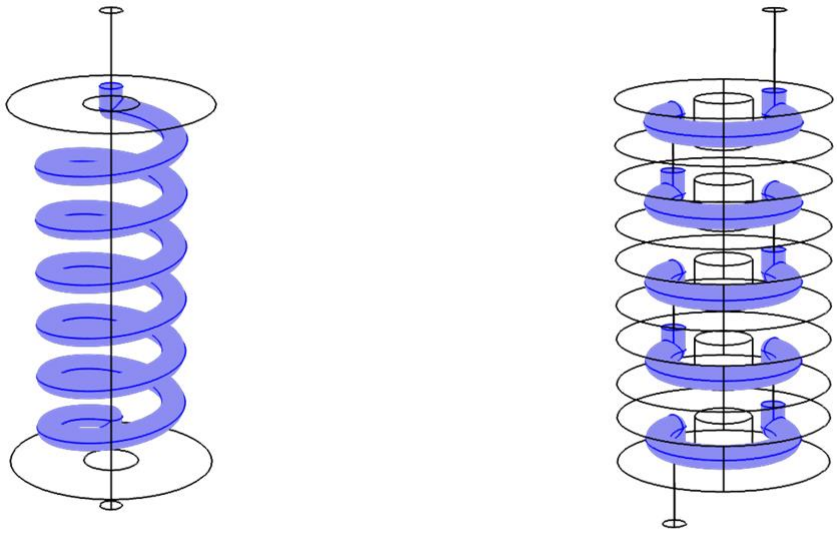

Figure 4.66 The surfaces contact surface between HTT and the adsorbent particles, in numerical analysis model for Bed Design 1 (Left) and Bed Design 2 (Right)

The surfaces in contact with the adsorbent particles are defined to be no flow boundaries for the solution of the Darcy's equation. The remaining parts of the HTT are exposed to the vacuum chamber. According to the assumptions that had been made, the effect of radiative heat transfer is neglected, and therefore the remaining surfaces of the HTT are defined as insulated boundary. The surfaces of the HTT defined as the insulated boundary in Bed Design 1 and Bed Design 2 can be seen in Figure 4.66.

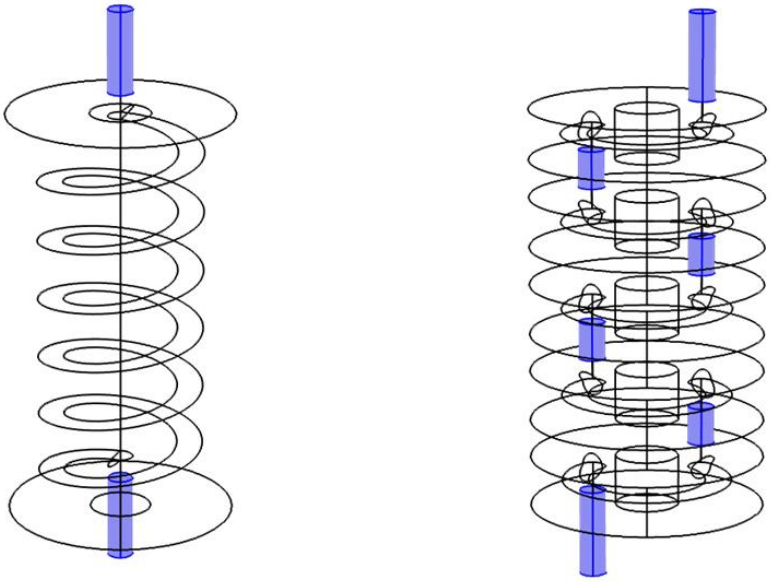

Figure 4.67 The surfaces of the HTT facing the vacuum chamber and defined as insulated

The outer surfaces of the adsorbent bed facing to the vacuum chamber are defined as constant pressure boundary. The pressure at the outer faces of the adsorbent beds is defined as equal to the vacuum chamber pressure. These same boundaries also defined as zero heat flux boundaries. These surfaces are the interface of adsorbent bed with the vacuum chamber and no heat flows through these boundaries. Therefore zero heat flux boundary condition is defined at these boundaries.

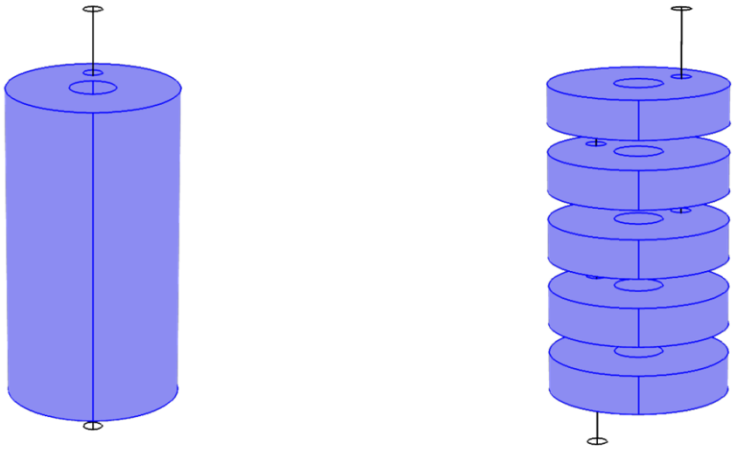

Figure 4.68 Boundaries of Bed Design 1(Left) and Bed Design 2 (Right) that are interfacing with the vacuum chamber.

In addition to the definition of the boundary conditions initial condition also need to be defined for the analyses. The whole domain including HTF, HTT and adsorbent particles is assumed to have same initial temperature condition. The temperature of the domain is assumed to be uniform initially; however it was not the case for the experiments. The initial adsorption capacity distribution within the adsorbent bed is assumed to be uniform also. The initial adsorption capacity values are taken from the experimental tests. The initial temperature values are calculated by taking the average of the initial thermocouple readings inside the bed. The initial pressure value used in the analyses is also taken from the experimental measurements. The pressure is assumed to be linearly increasing from initial value to condenser pressure, during isosteric heating of the bed based on the observations during experiments. Measured initial pressure values and the recorded isoteric heating duration of bed are used together for the definition of the vacuum chamber pressure in the analyses. The initial temperature, pressure values and the isosteric heating duration can be seen in Table 4.6 for each numerical analysis simulating each of the experiment. In the

numerical analyses, condenser pressure is taken as constant and equal to 42.47 mbar for the 30^{o}C condenser temperature.

Table 4.6 Initial temperature and pressure values and isosteric heating durations used as an input to the analyses

		Initial Temperature [K]	Initial Pressure [mbar]	Isosteric Heating Duration[s]
Bed Design 1	Experiment 1	304.6	20.4	7000
	Experiment 2	301.4	16.5	3100
	Experiment 3	303.8	18	4000
	Experiment 4	304.8	14	5300
Bed Design 2	Experiment 1	304.7	23	5000
	Experiment 2	303.4	21	3800
	Experiment 3	303.4	21	5000
	Experiment 4	304	15	5000

In the numerical analyses, the laminar flow of the HTF is solved by using a stationary solver. The velocity field of the HTF is assumed to be not affected by the temperature. Except the mass and momentum conservation equations of the HTF all other governing equations are solved by using transient formulation. The steady solution of the HTF velocity field is performed by using a coupled solver. Since the domain size of the HTF is relatively small required memory could be provided by the available computer source. The coupled solver convergence rate is relatively high compared to the segregated solver therefore to reduce the run time, the steady solution for the HTF velocity field is performed by using coupled solver. On the other hand, as a result of complexity of the numerical scheme in heat and mass transfer equations, transient part of the analyses performed by using a segregated solver. Compared to fully coupled solvers, memory requirement of segregated solvers are at more reasonable levels. However, the cost of reduced memory requirements results in high run times. Segregated solvers, solve each equation separately in a sequential manner within a time step. In a single time step, segregated

solver performs inner iterations until a converged solution for the system of equations are obtained. More details on the solver settings of the software can be found in [151]. The constants used in the analyses for analyses can be seen in Table 4.7

Table 4.7 The constants used in the 3-D analyses of Bed Designs

Parameter	Value	Unit	Definition and Reference
ε_b	0.37		Bed porosity [17,10]
ε_p	0.42		Particle porosity [17,10]
d_p	4.00E-03	m	Adsorbent particle diameter
μ_v	1.00E-05	kg/m.s	Dynamic viscosity of water vapor [162]
k_v	0.024	W/mK	Thermal conductivity of water vapor [161]
c_{pv}	1880	J/kgK	Specific heat of water vapor [161]
ρ_s	2000	kg/m^3	Density of the adsorbent particles [17]
k_s	0.198	W/m.K	Thermal conductivity of adsorbent particles [17]
c_{ps}	880	J/kg.K	Specific heat of adsorbent particles [17,14]
ρ_{HTF}	780	kg/m^3	Density of HTF
k_{HTF}	0.115	W/m.K	Thermal conductivity of HTF
c_{HTF}	2000	J/kg.K	Specific heat of HTF [14]
μ_{HTF}	4.00E-04	kg/m.s	Dynamic viscosity of HTF [14]
ρ_t	8700	kg/m^3	Density of HTT [162]
k_t	400	W/m.K	Thermal conductivity of HTT [162]
c_t	385	J/kg.K	Specific heat of HTT [161]
E_a	4.20E+04	J/mol	Surface diffusion activation energy [17,10]
D_0	2.54E-04	m^2/s	Reference diffusivity [17,23]
h_{tg}	40	W/m^2	Convective heat transfer coefficient between packed bed and HTT [132]
Q_{ad}	2510	kJ/kg	Heat of adsorption [164]

4.5.2 Results of Numerical Analyses of Bed Design 1

The analyses performed for Bed Design 1 are based on two different approaches as mentioned earlier. The LTE and LTNE based analyses are given in comparison with the experimental results for each experiment separately. The comparison is mainly based on the temperature measurements taken from the adsorbent bed. The experimental time variation of temperature within the adsorbent bed is compared with the results of the numerical analyses. Additionally plots representing the axial temperature variation also used for comparison. Solid phase temperatures are considered while the temperature results are presented for the LTNE based models. The sampling frequency for the time variation of temperature plots is 30 seconds for the numerical results. The data set obtained from numerical analyses is composed of discrete values of temperature in time, however for better graphical visualization, both experimentally obtained and numerically obtained data is plotted as continuous lines. When the sampling frequency and overall duration is compared, graphical representation of the data by using points will also look like continuous lines.

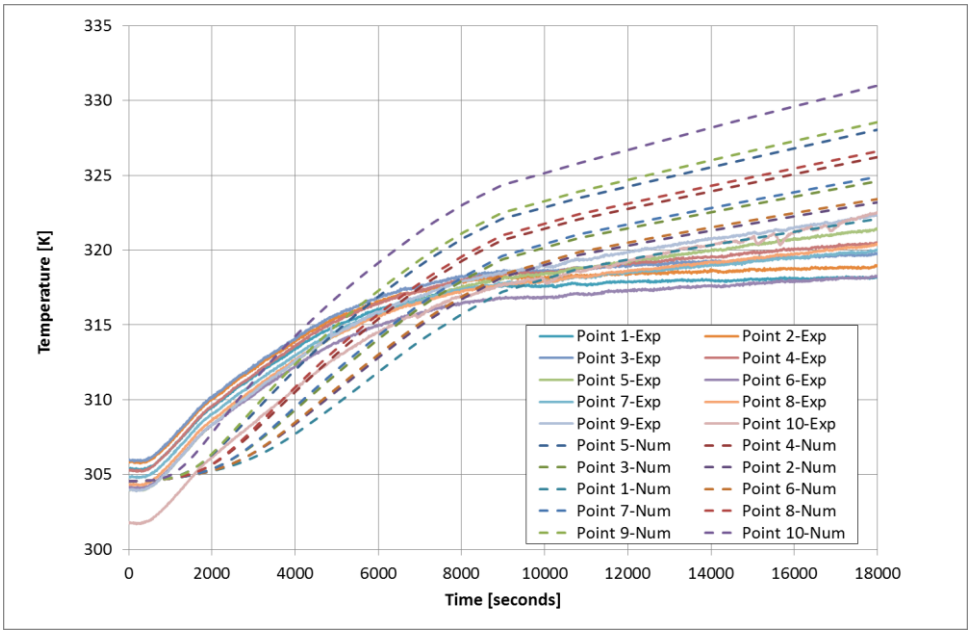

Figure 4.69 Bed temperature variations with time for Bed Design 1 in Experiment 1 vs results obtained from LTE based numerical analysis

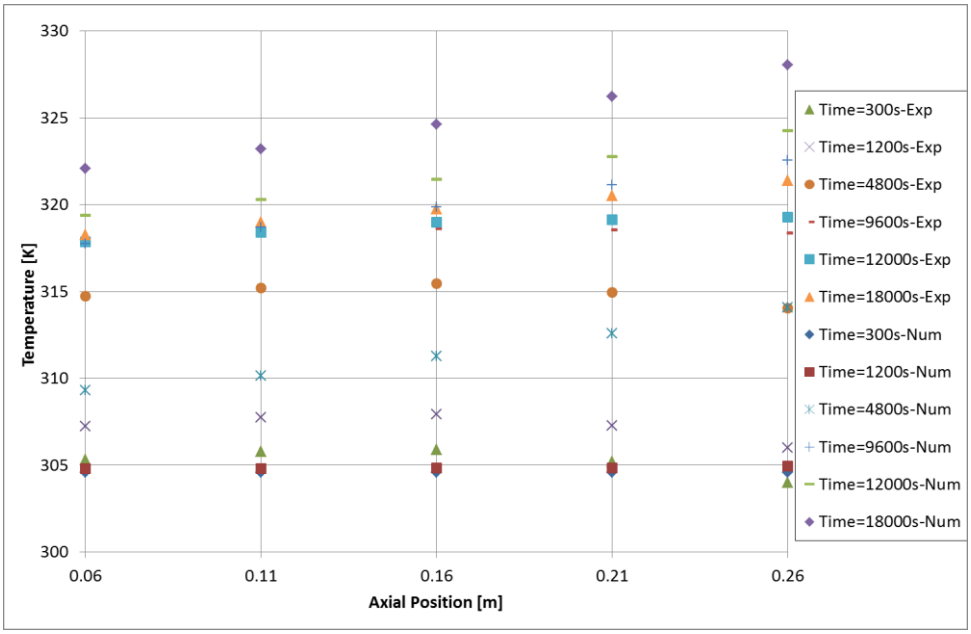

Figure 4.70 The axial temperature variations of Bed Design 1 in Experiment 1-Left axis vs results obtained from LTE based numerical analysis

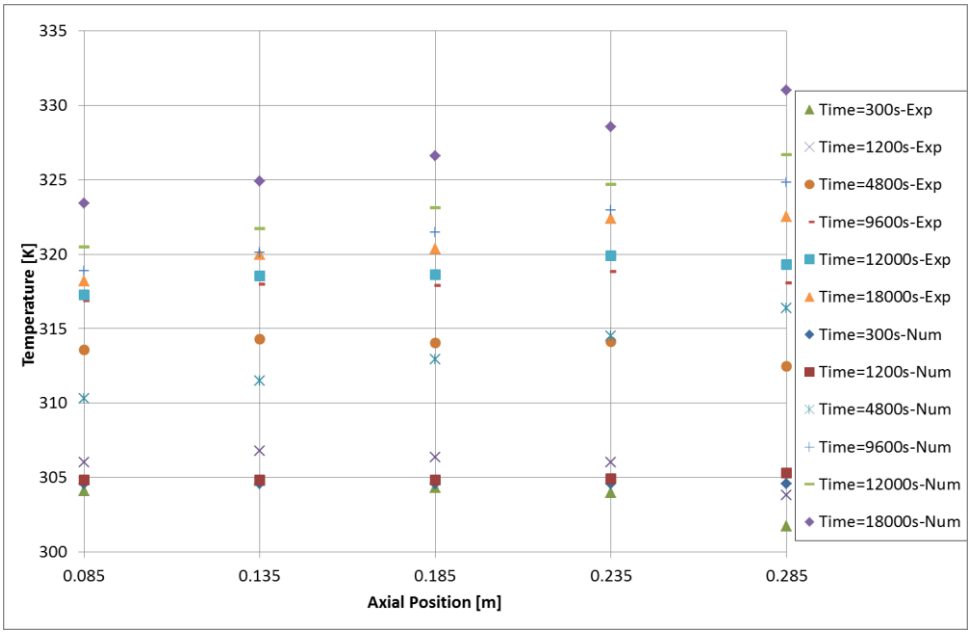

Figure 4.71 The axial temperature variations of Bed Design 1 in Experiment 1-Right axis vs results obtained from LTE based numerical analysis

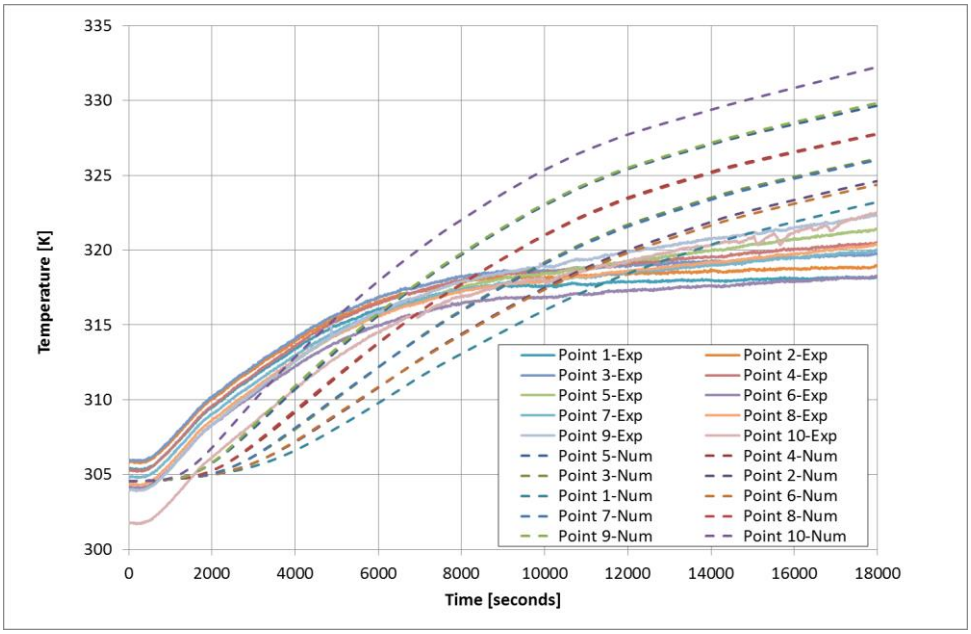

Figure 4.72 Bed temperature variations with time for Bed Design 1 in Experiment 1 vs results obtained from LTNE based numerical analysis

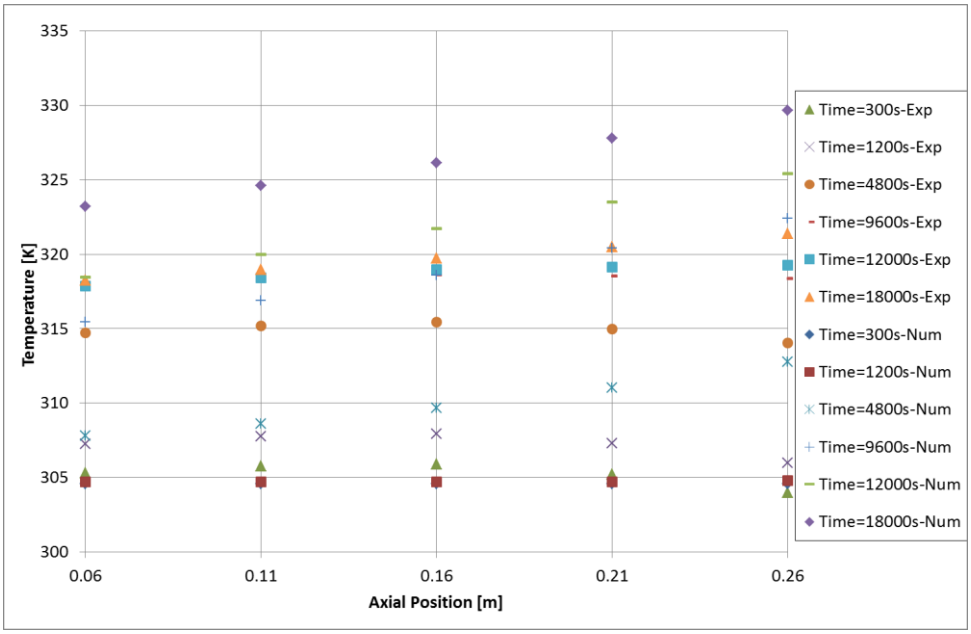

Figure 4.73 The axial temperature variations of Bed Design 1 in Experiment 1-Left axis vs results obtained from LTNE based numerical analysis

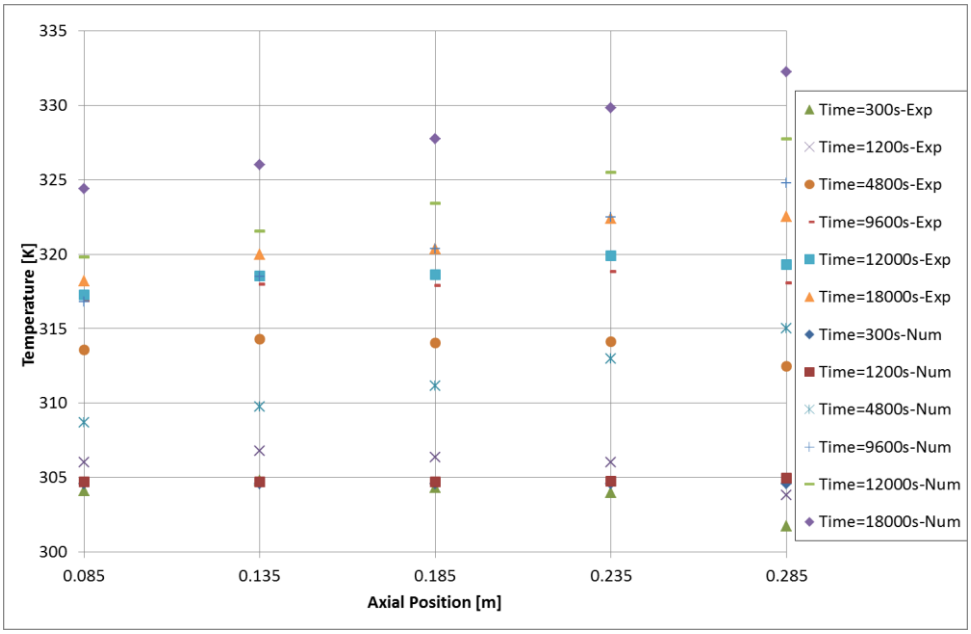

Figure 4.74 The axial temperature variations of Bed Design 1 in Experiment 1-Right axis vs results obtained from LTNE based numerical analysis

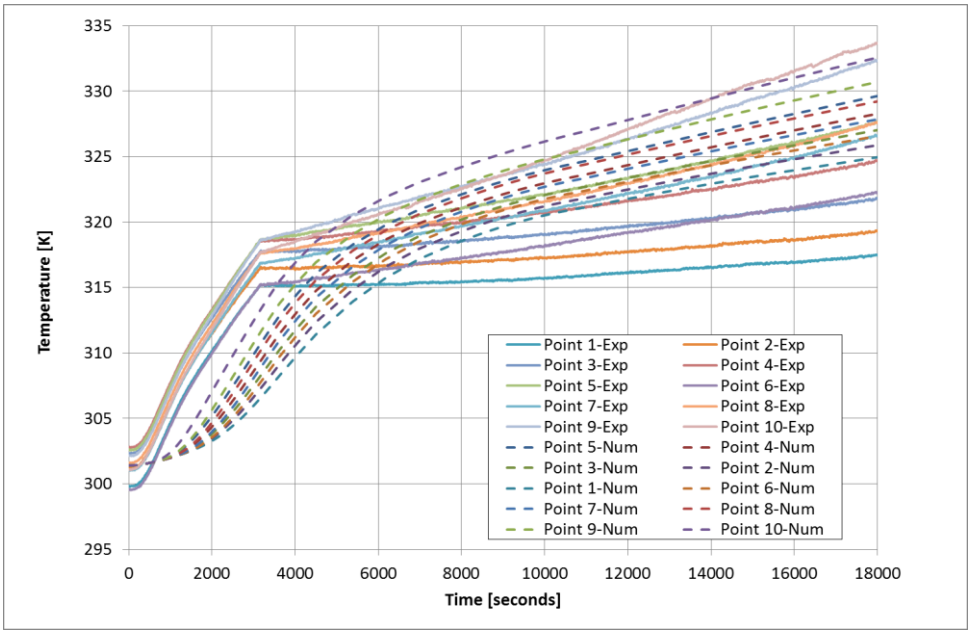

Figure 4.75 Bed temperature variations with time for Bed Design 1 in Experiment 2 vs results obtained from LTE based numerical analysis

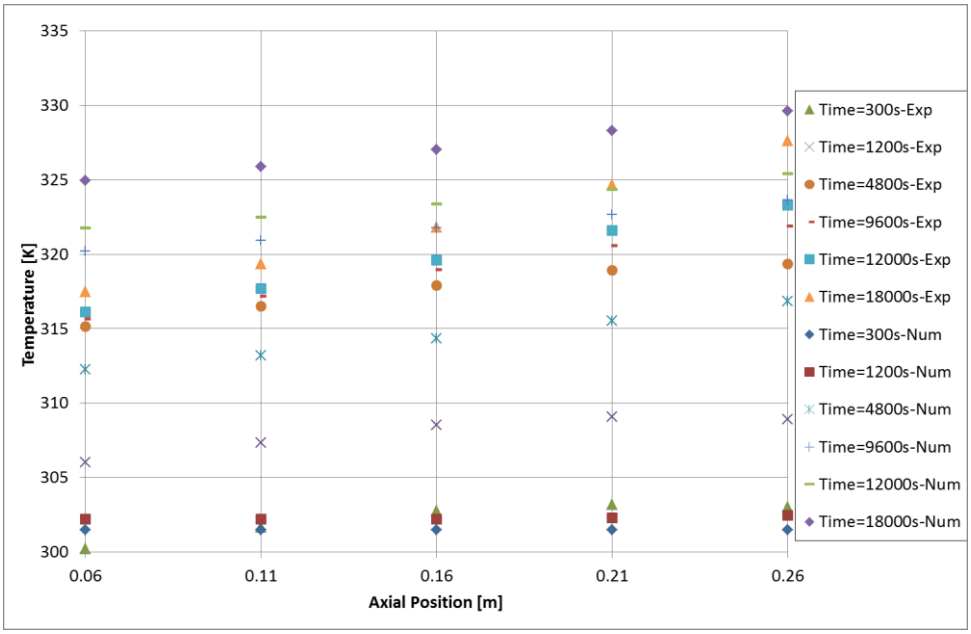

Figure 4.76 The axial temperature variations of Bed Design 1 in Experiment 2-Left axis vs results obtained from LTE based numerical analysis

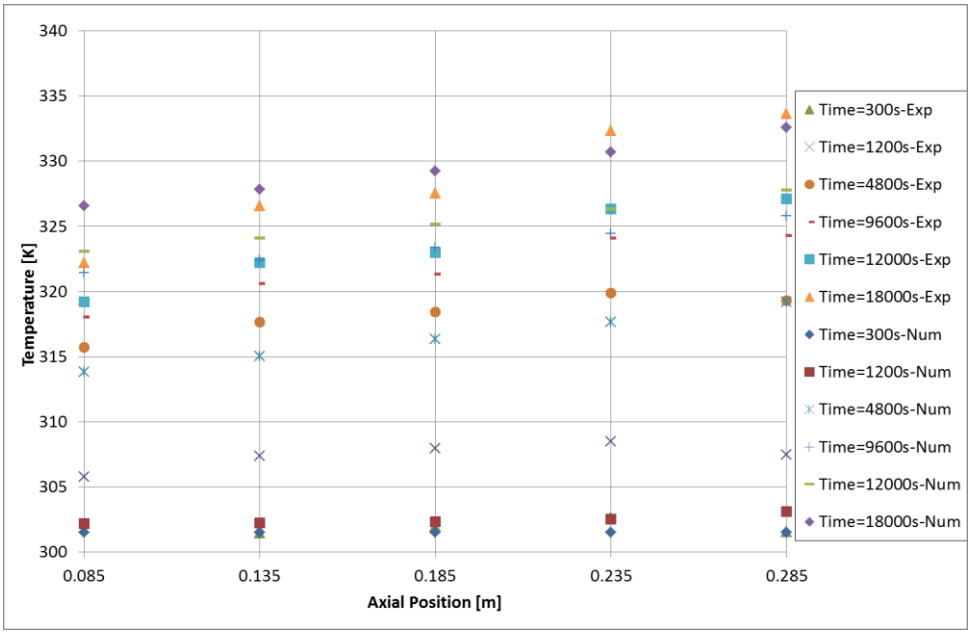

Figure 4.77 The axial temperature variations of Bed Design 1 in Experiment 2-Right axis vs results obtained from LTE based numerical analysis

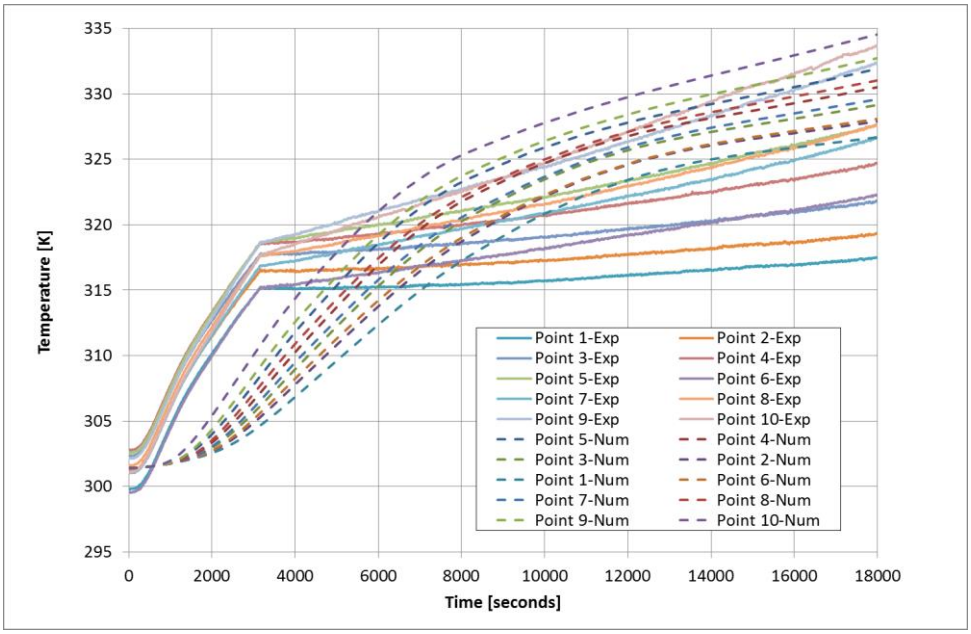

Figure 4.78 Bed temperature variations with time for Bed Design 1 in Experiment 2 vs results obtained from LTNE based numerical analysis

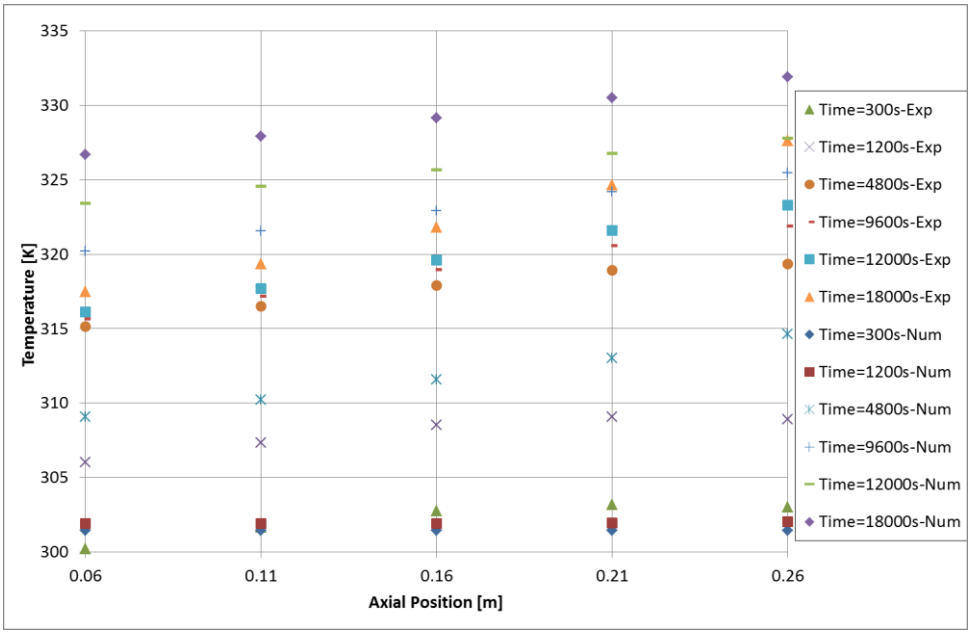

Figure 4.79 The axial temperature variations of Bed Design 1 in Experiment 2-Left axis vs results obtained from LTNE based numerical analysis

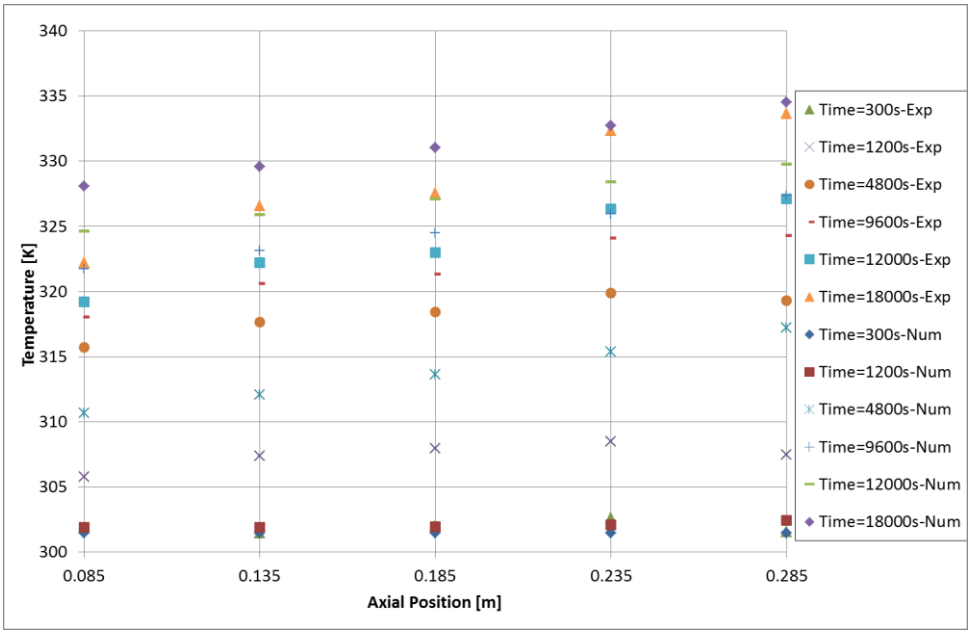

Figure 4.80 The axial temperature variations of Bed Design 1 in Experiment 2-Right axis vs results obtained from LTNE based numerical analysis

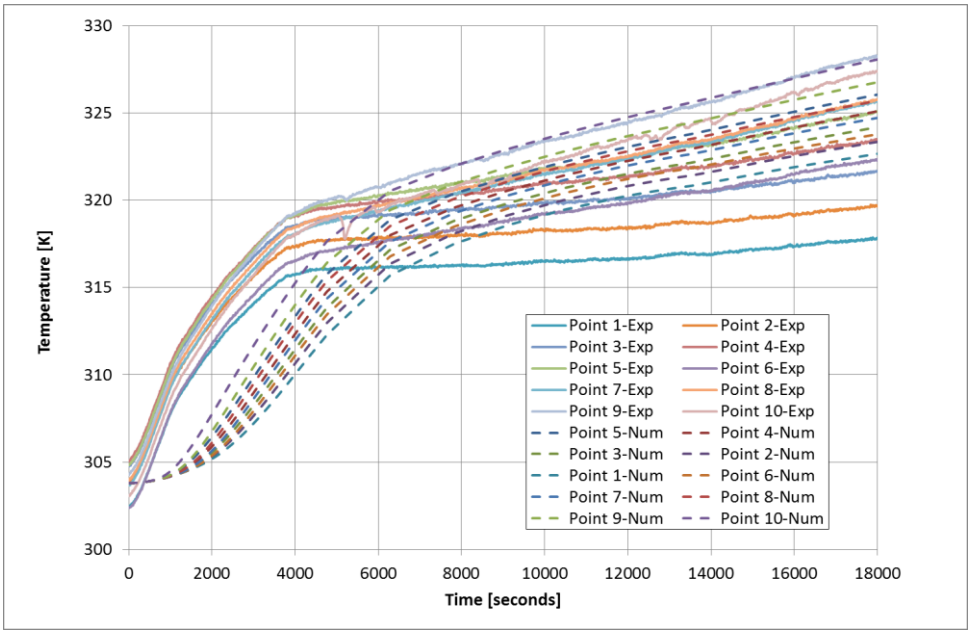

Figure 4.81 Bed temperature variations with time for Bed Design 1 in Experiment 3 vs results obtained from LTE based numerical analysis

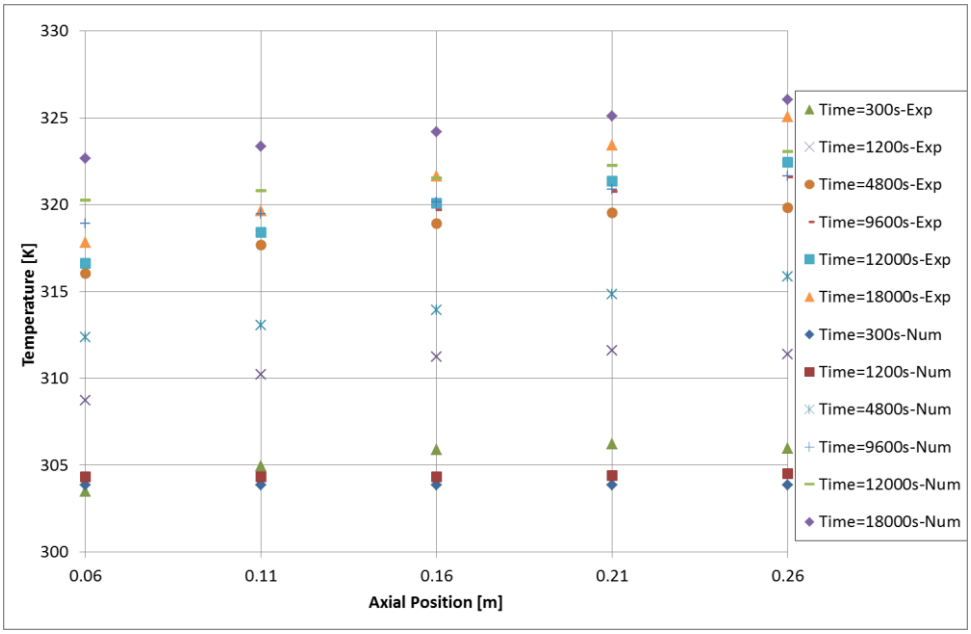

Figure 4.82 The axial temperature variations of Bed Design 1 in Experiment 3-Left axis vs results obtained from LTE based numerical analysis

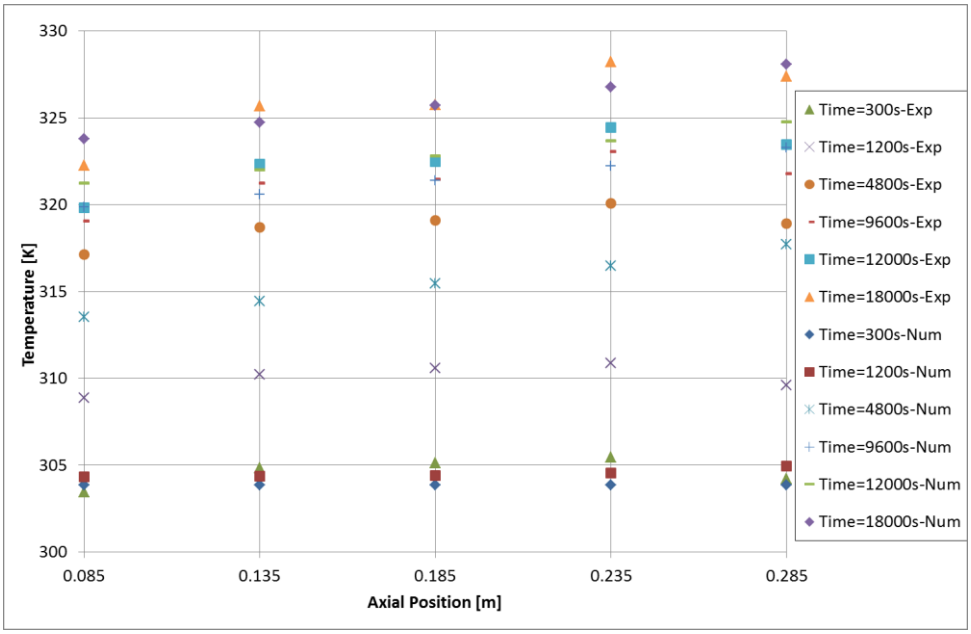

Figure 4.83 The axial temperature variations of Bed Design 1 in Experiment 3-Right axis vs results obtained from LTE based numerical analysis

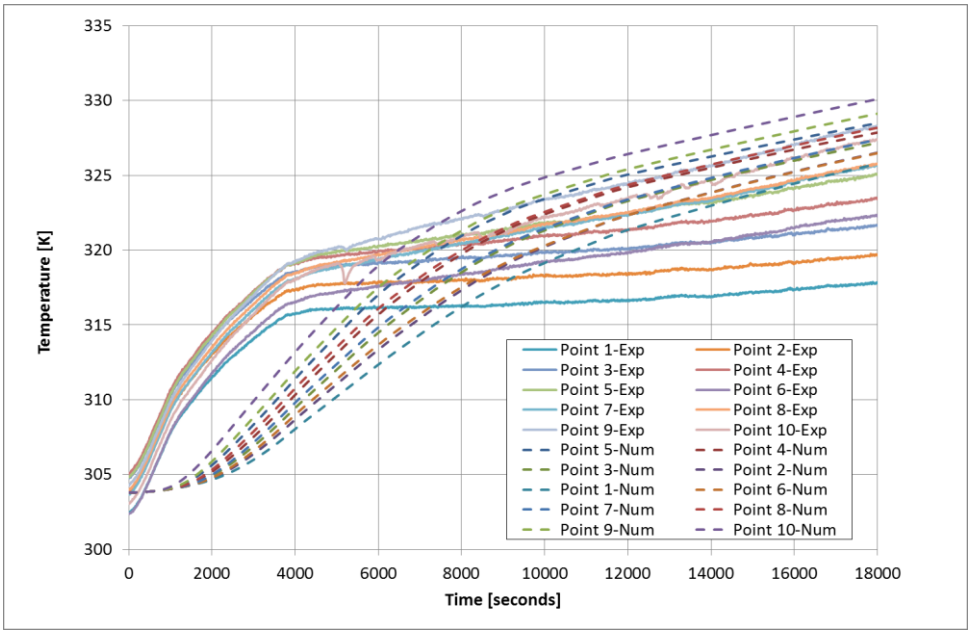

Figure 4.84 Bed temperature variations with time for Bed Design 1 in Experiment 3 vs results obtained from LTNE based numerical analysis

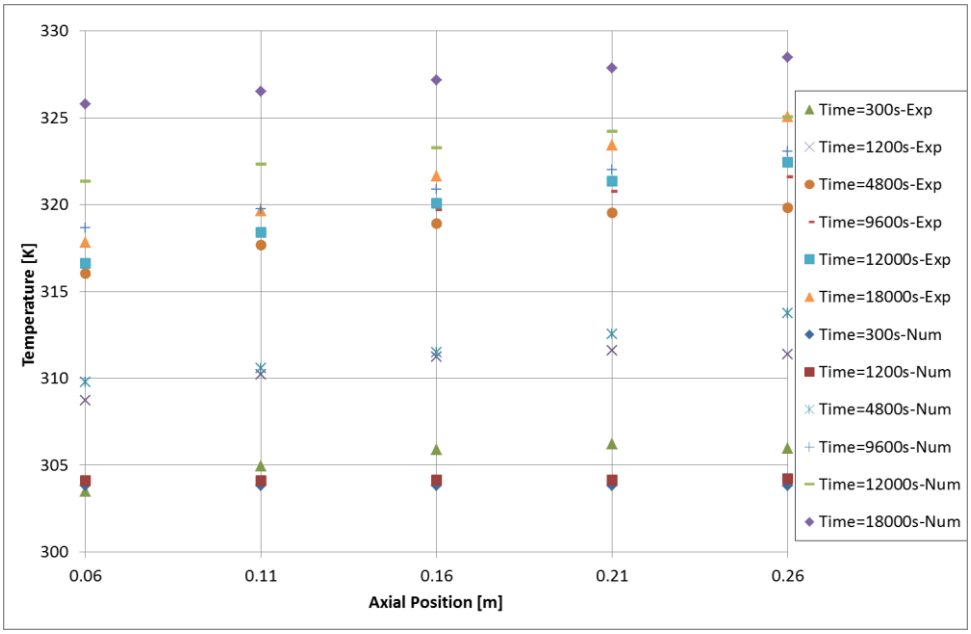

Figure 4.85 The axial temperature variations of Bed Design 1 in Experiment 3-Left axis vs results obtained from LTNE based numerical analysis

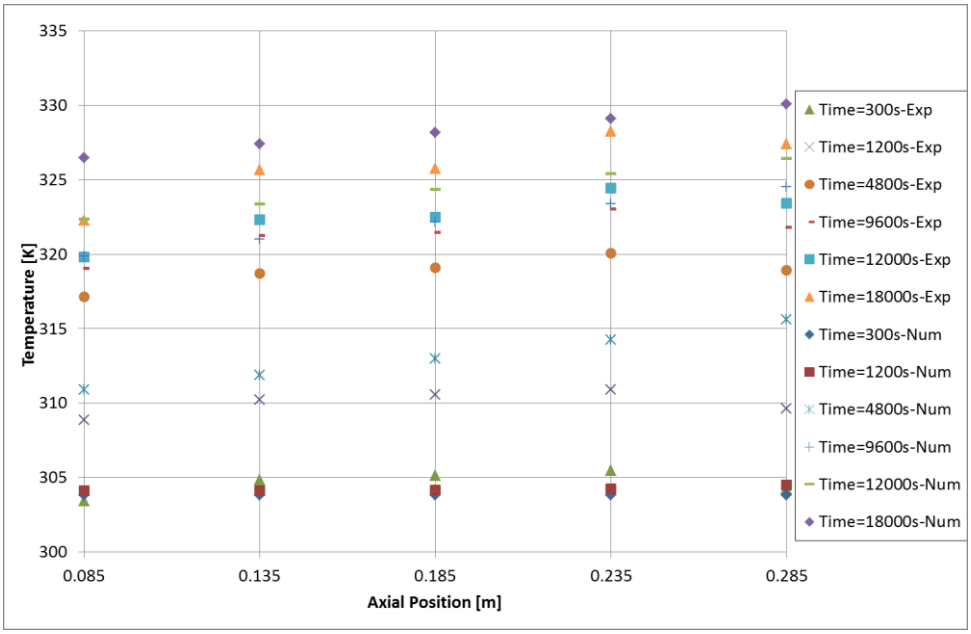

Figure 4.86 The axial temperature variations of Bed Design 1 in Experiment 3-Right axis vs. results obtained from LTNE based numerical analysis

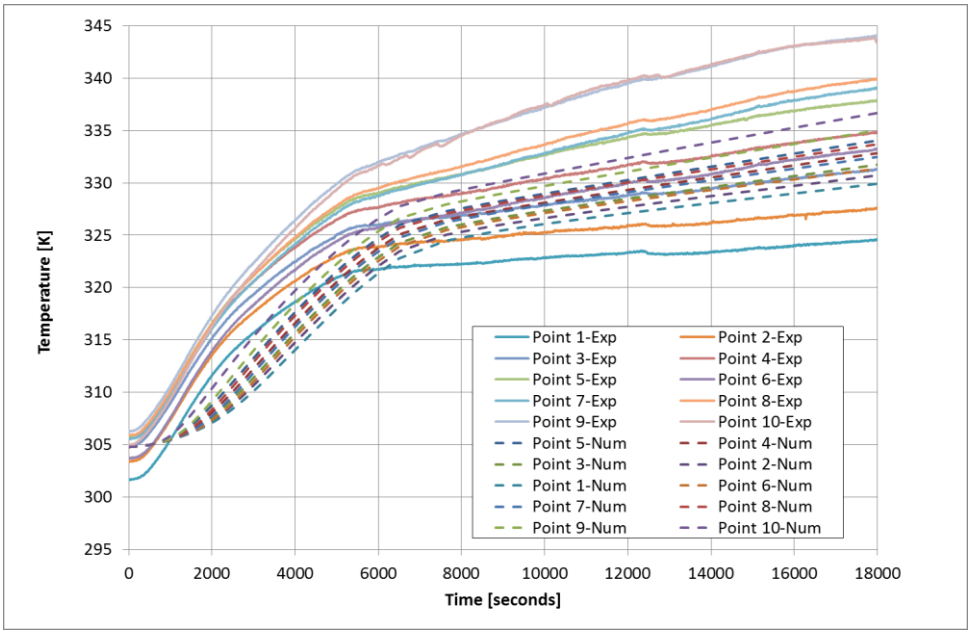

Figure 4.87 Bed temperature variations with time for Bed Design 1 in Experiment 4 vs. results obtained from LTE based numerical analysis

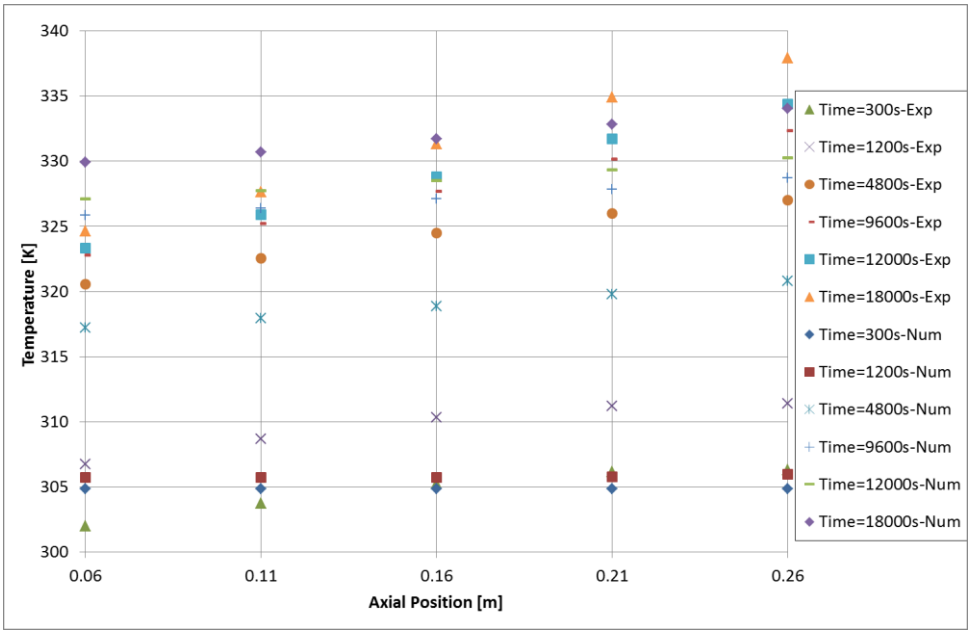

Figure 4.88 The axial temperature variations of Bed Design 1 in Experiment 4-Left axis vs results obtained from LTE based numerical analysis

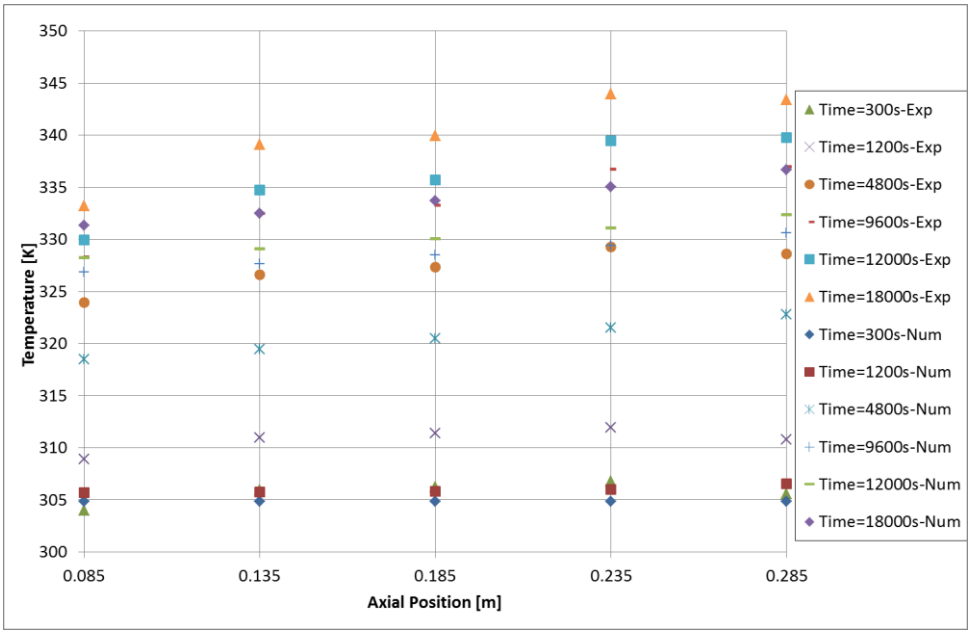

Figure 4.89 The axial temperature variations of Bed Design 1 in Experiment 4-Right axis vs results obtained from LTE based numerical analysis

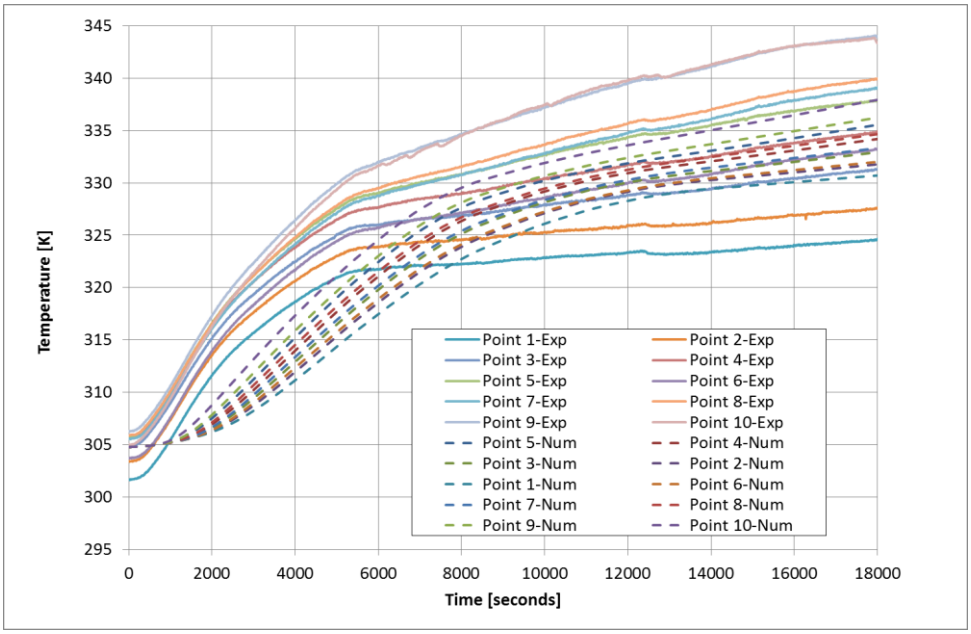

Figure 4.90 Bed temperature variations with time for Bed Design 1 in Experiment 4 vs results obtained from LTNE based numerical analysis

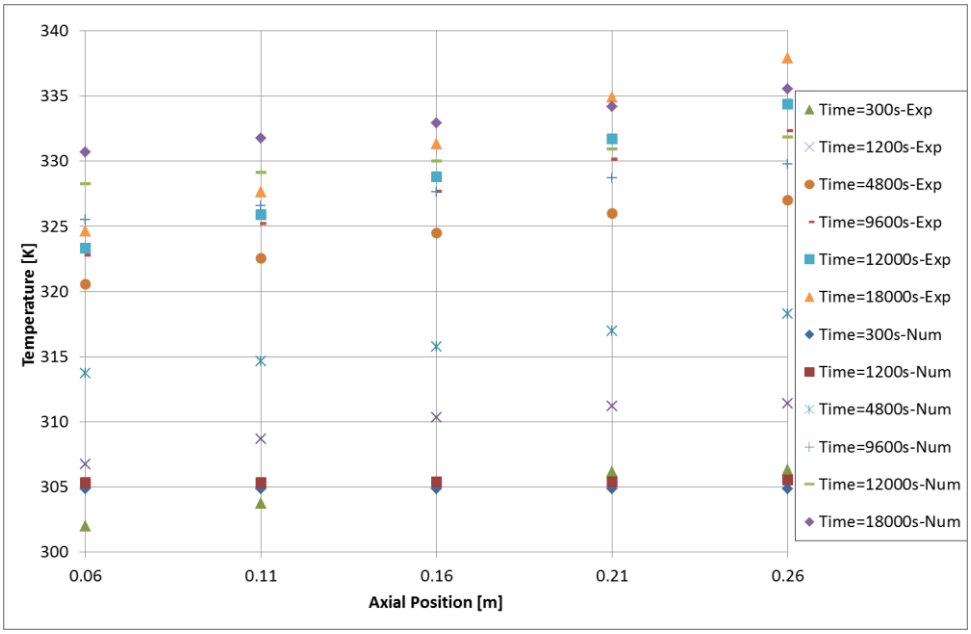

Figure 4.91 The axial temperature variations of Bed Design 1 in Experiment 4-Left axis vs results obtained from LTNE based numerical analysis

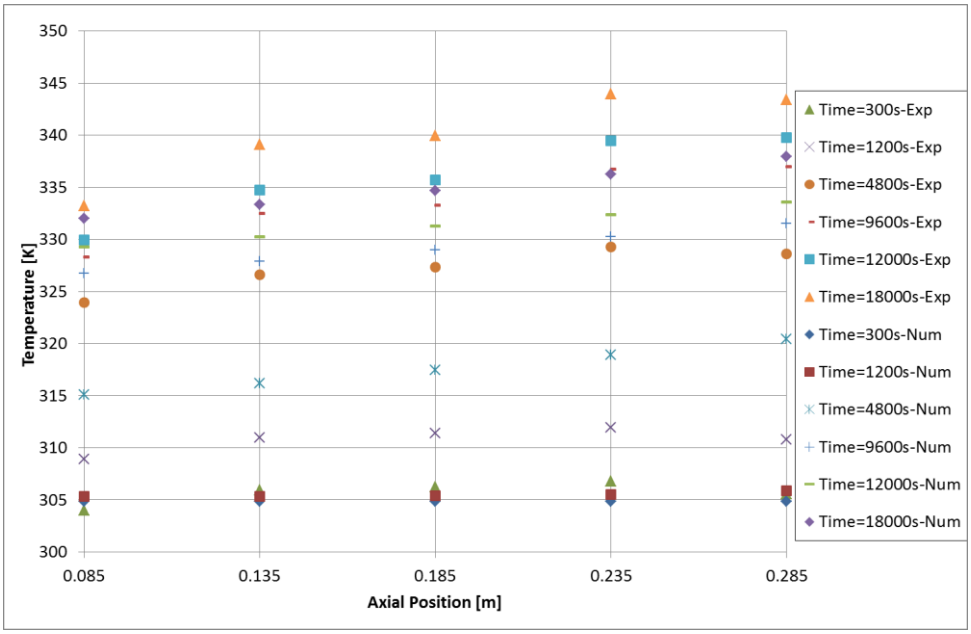

Figure 4.92 The axial temperature variations of Bed Design 1 in Experiment 4-Right axis vs results obtained from LTNE based numerical analysis

The temperature of the Bed Design 1 under conditions of Experiment 1 is more closely predicted by the LTE based numerical model compared to the LTNE based one. However both LTE and LTNE based numerical models overestimated the temperature increase rate of the bed for the low HTF velocity conditions of the Experiment 1.

In general there is a delay in the time variation of temperature curves obtained from numerical analyses. This delay mainly observed in the isosteric heating part of the process. The delay also affects the differences in the desorption phase. The delay in the temperature rise in isosteric heating period observed in the numerical analysis data is higher in the LTNE based models. However the difference between LTE and LTNE based temperature predictions are less for the Experiment 3 and Experiment 4 conditions. Regarding this information it could be suggested that the temperature difference between solid and vapor phases is less under low initial adsorbate loading and low HTF inlet temperatures.

As a general observation, LTE and LTNE based numerical models predict the inclination change in temperature curve after the isosteric heating phase, due to desorption. In part of the process in which vacuum chamber is connected to the condenser and heat received by the bed mainly drives the desorption of the adsorbed phase therefore the temperature rise in this region is relatively slow compared to isosteric heating process where no phase change is involved.

The temperature variation predicted by LTE based numerical model more closely follows the experimental data of Experiment 2; however the temperature of the points which are positioned in the lower portion of the bed is overestimated by the numerical model. Similar to the LTE based model also LTNE based numerical model predicts higher temperatures for the lower portion of the bed. Additionally for the numerical analyses of the Bed Design 1 under conditions of Experiment 1 and Experiment 2, the axial temperature gradients and the temperatures predicted by the

LTNE model is relatively higher compared to the LTE based numerical model and the experimental data. Regarding this observation, under conditions of Experiment 1 and Experiment 2, the difference between solid and vapor phase temperatures in the adsorbent bed could be high and therefore, the LTE based approach gives different results compared to the LTNE based one. However, as the trend of temperature change within the bed is considered, the LTE based model predicts the trend of variation of the experimental data closer than the LTNE based model under conditions of Experiment 2.

Based on the numerical analysis results of the Bed Design 1 the main points of the observations about the numerical analysis results can be summarized as follows,

- The LTNE and LTE based models predicted the temperature variation with time in isosteric heating pediod with a delay compared to the experimental data
- The delay observed in the results of LTE based analysis is less compared to the results of LTNE based analysis
- Under low initial adsorbate loading conditions (Experiment 4) the differences between temperature values obtained from LTE and LTNE based numerical models is less compared to high HTF inlet temperature conditions.
- The temperature differences within the bed obtained from LTNE based numerical analyses are relatively higher, however the numerically obtained temperature differences within the bed is low compared to the experimental data.

In addition to the point temperatures also, the spatial distribution of adsorption capacity and temperature could be obtained by the analyses. These results can be utilized in the evaluation of the geometric design of the bed. The temperature variations taken from the crossection used in the experimental measurements for Bed Design 1 under conditions of Experiment 2 could be seen in Figure 4.92 And figure

4.93. The adsorption capacity variation at the same crossections also can be seen in Figure 4.94 and Figure 4.95 obtained from LTE and LTNE based numerical analyses for the conditions of Experiment 2.

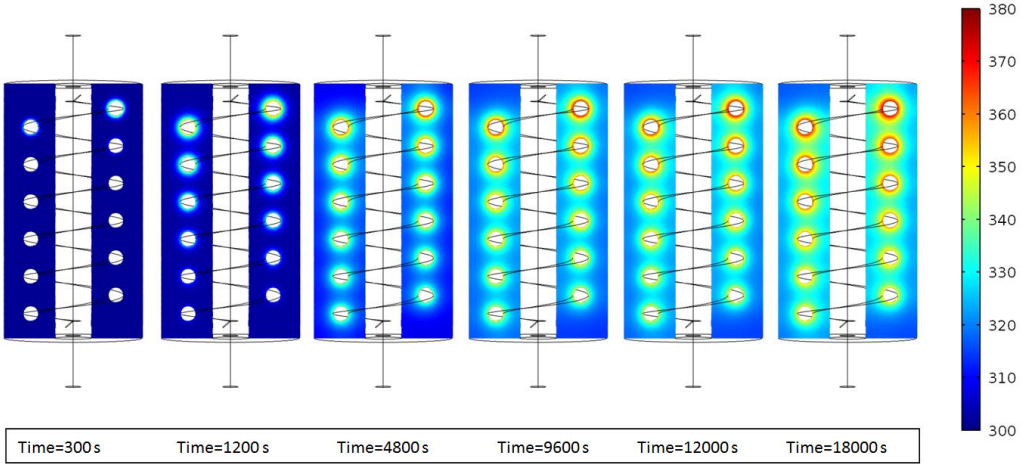

Figure 4.93 Temperature distribution contour plots taken from a planar crossection, obtained from LTE based numerical analysis of Bed Design 1

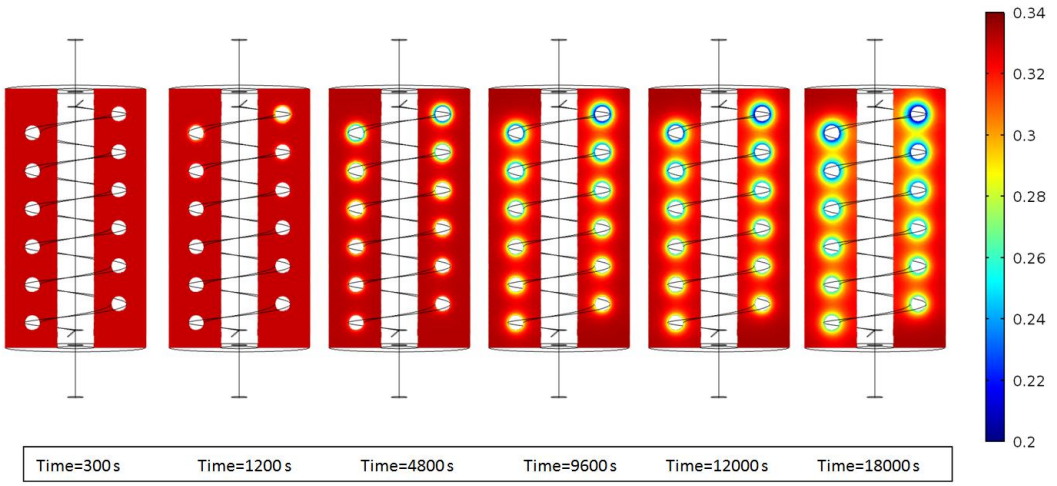

Figure 4.94 Adsorption capacity (X) distribution contour plots taken from a planar crossection, obtained from LTE based numerical analysis of Bed Design 1.

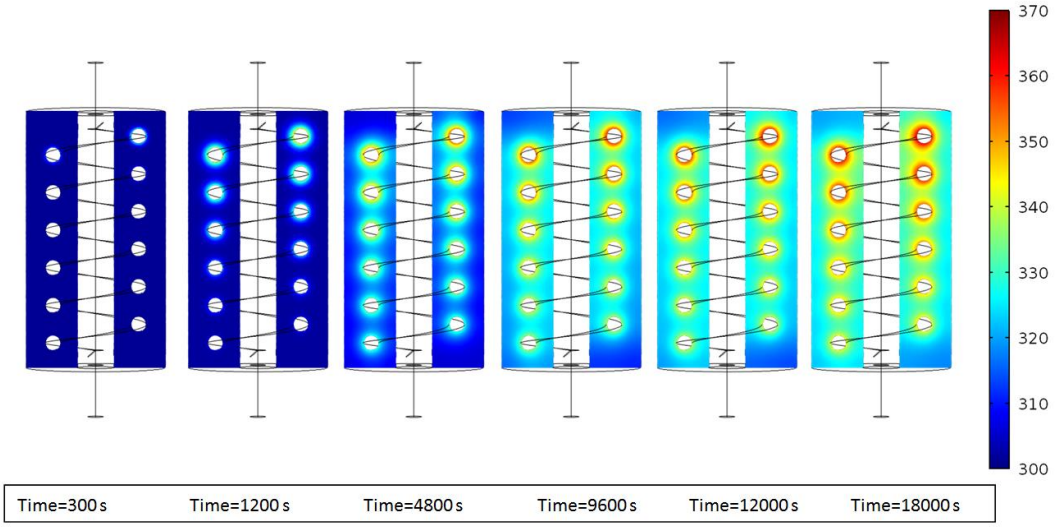

Figure 4.95 Temperature distribution contour plots taken from a planar crossection, obtained from LTNE based numerical analysis of Bed Design 1.

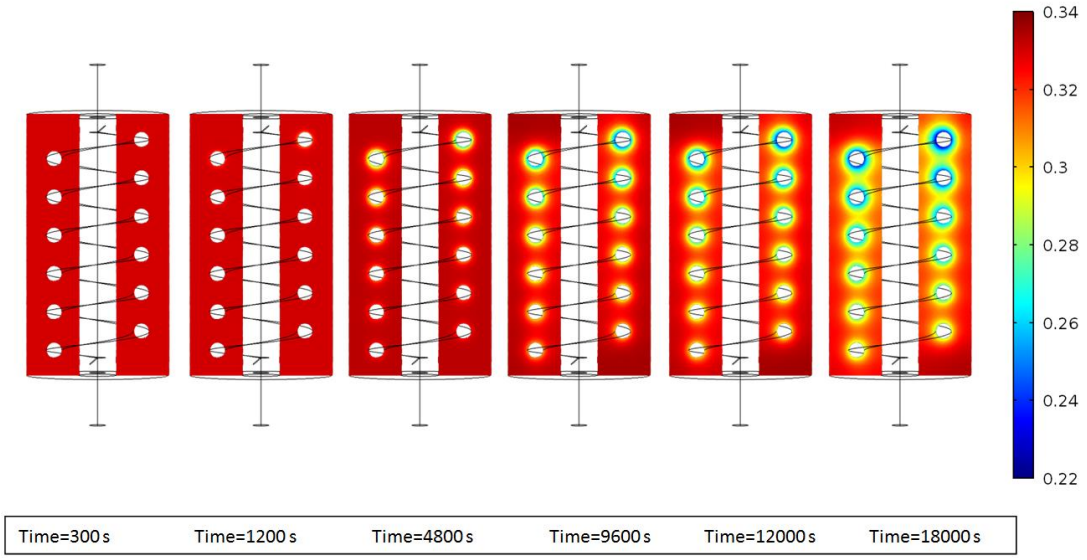

Figure 4.96 Adsorption capacity (X) distribution contour plots taken from a planar crossection, obtained from LTNE based numerical analysis of Bed Design 1.

4.5.3 Results of Numerical Analyses of Bed Design 2

Similar to the numerical analyses results of the Bed Design 1, the results obtained for Bed Design 2 will also be presented in form of time variation plots and axial temperature plots.

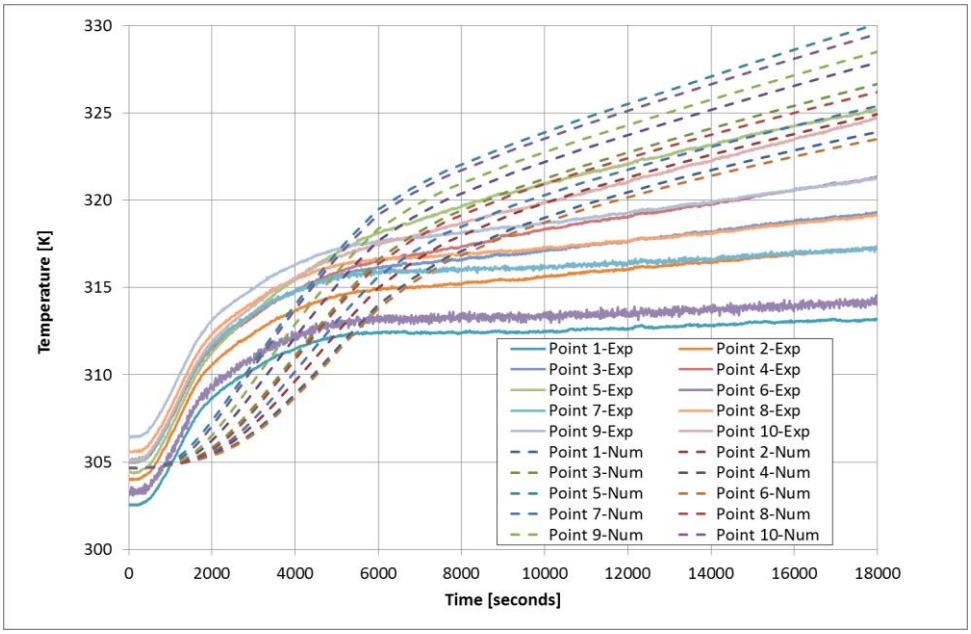

Figure 4.97 Bed temperature variations with time for Bed Design 2 in Experiment 1 vs results obtained from LTE based numerical analysis

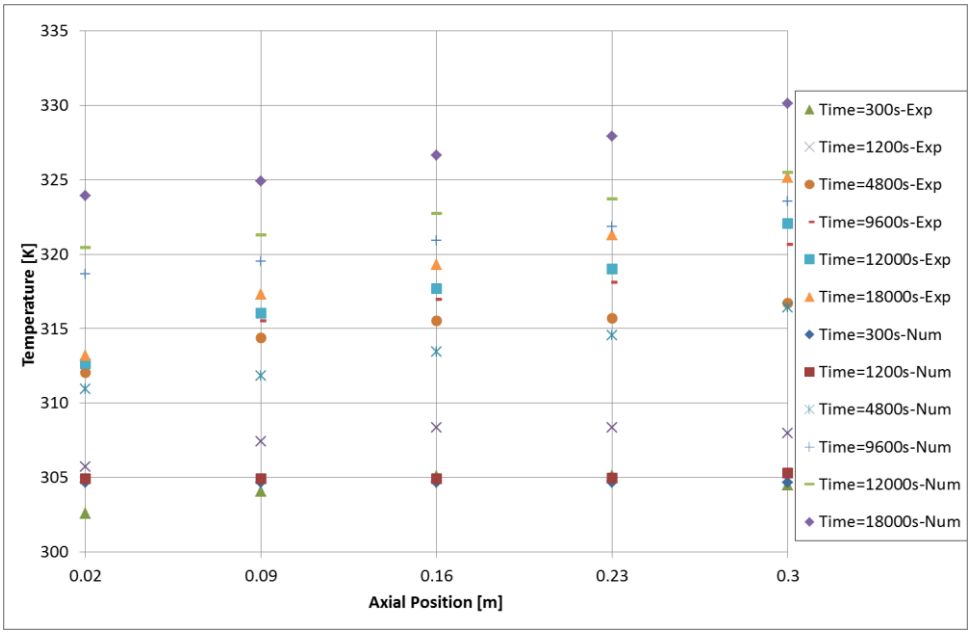

Figure 4.98 The axial temperature variations of Bed Design 2 in Experiment 1-Right axis vs results obtained from LTE based numerical analysis

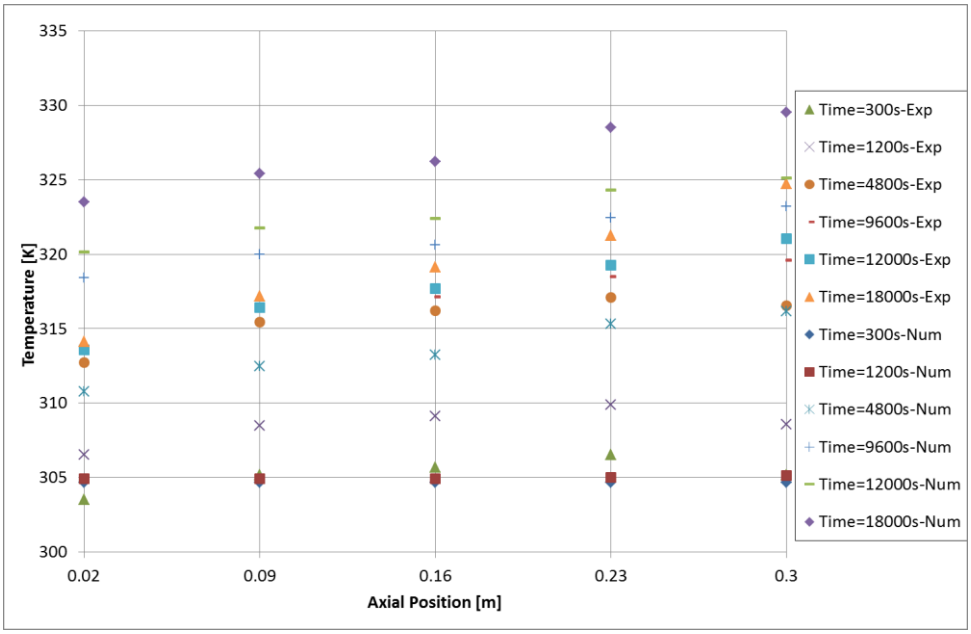

Figure 4.99 The axial temperature variations of Bed Design 2 in Experiment 1-Left axis vs results obtained from LTE based numerical analysis

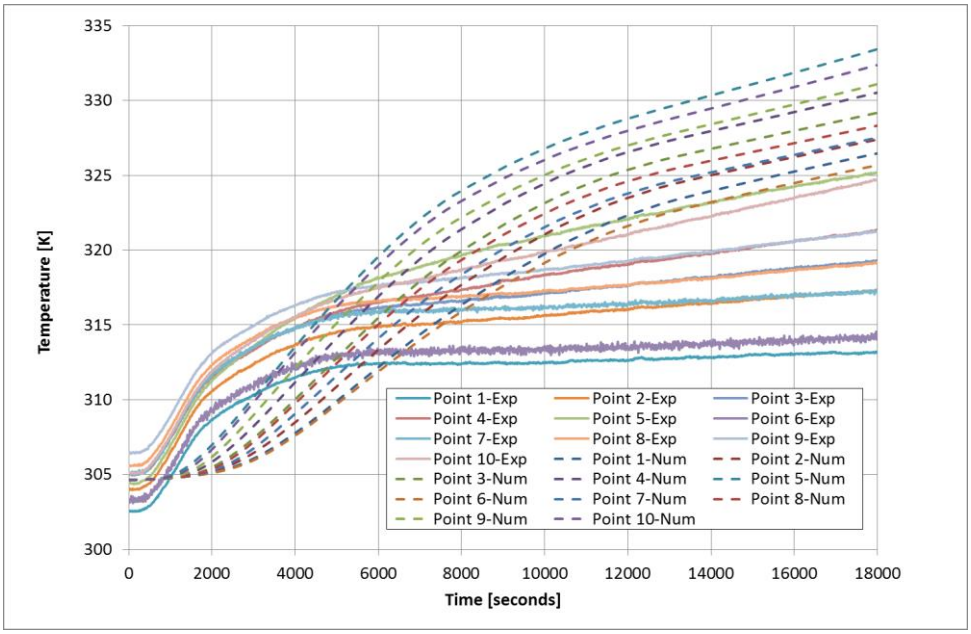

Figure 4.100 Bed temperature variations with time for Bed Design 2 in Experiment 1 vs results obtained from LTNE based numerical analysis

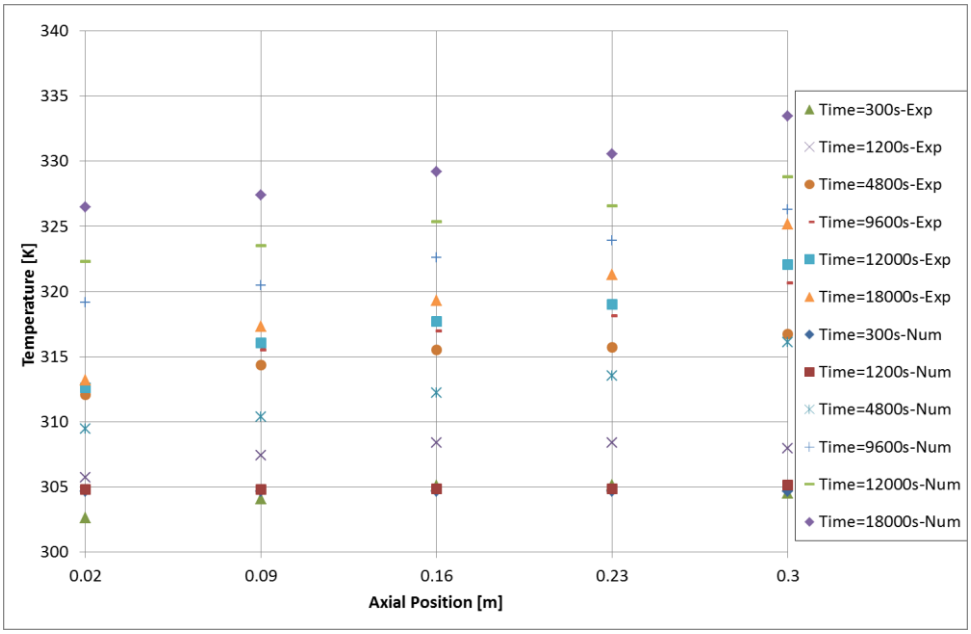

Figure 4.101 The axial temperature variations of Bed Design 2 in Experiment 1-Right axis vs results obtained from LTNE based numerical analysis

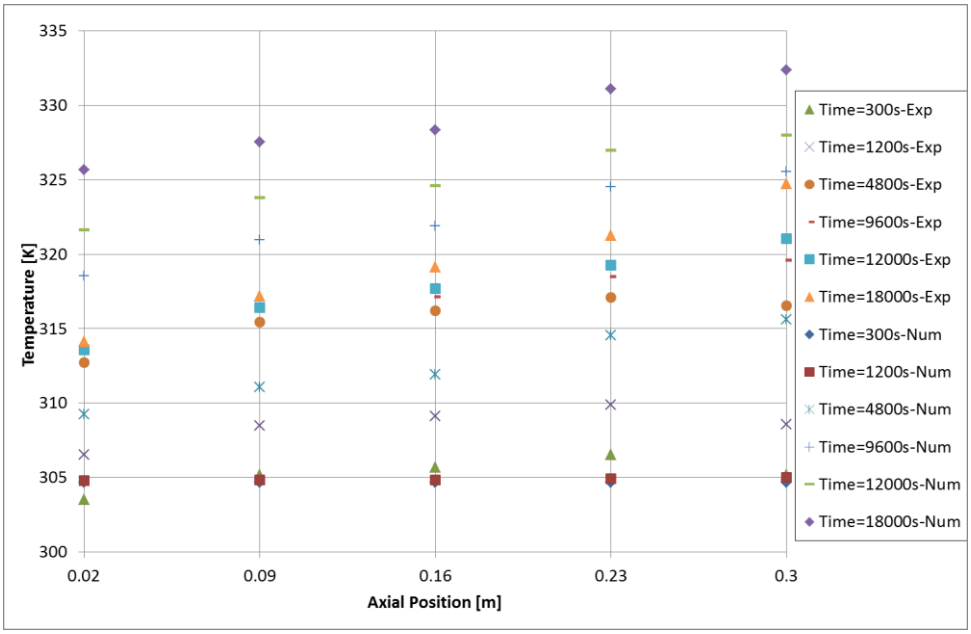

Figure 4.102 The axial temperature variations of Bed Design 2 in Experiment 1-Left axis vs results obtained from LTNE based numerical analysis

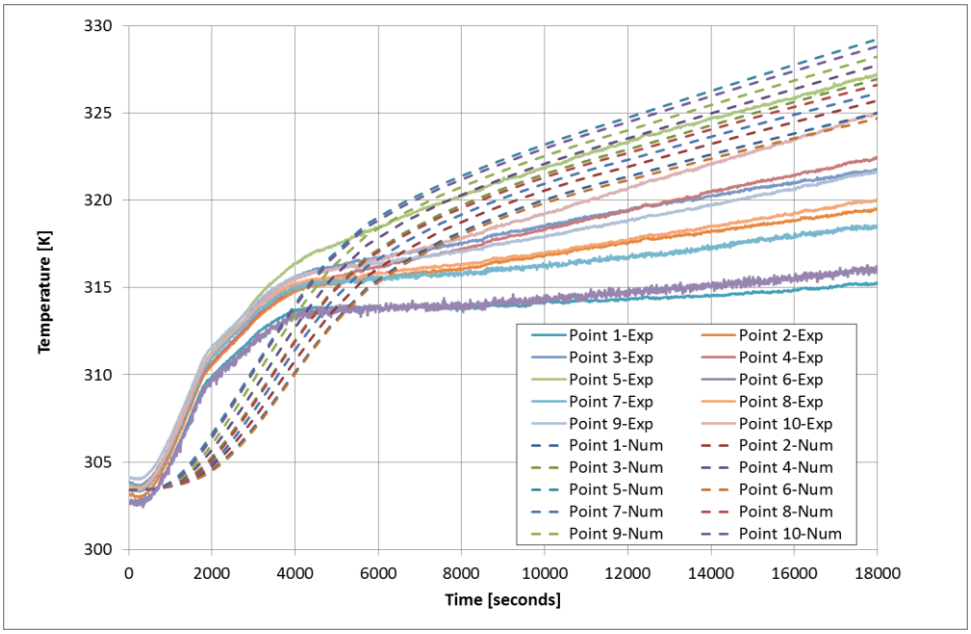

Figure 4.103 Bed temperature variations with time for Bed Design 2 in Experiment 2 vs results obtained from LTE based numerical analysis

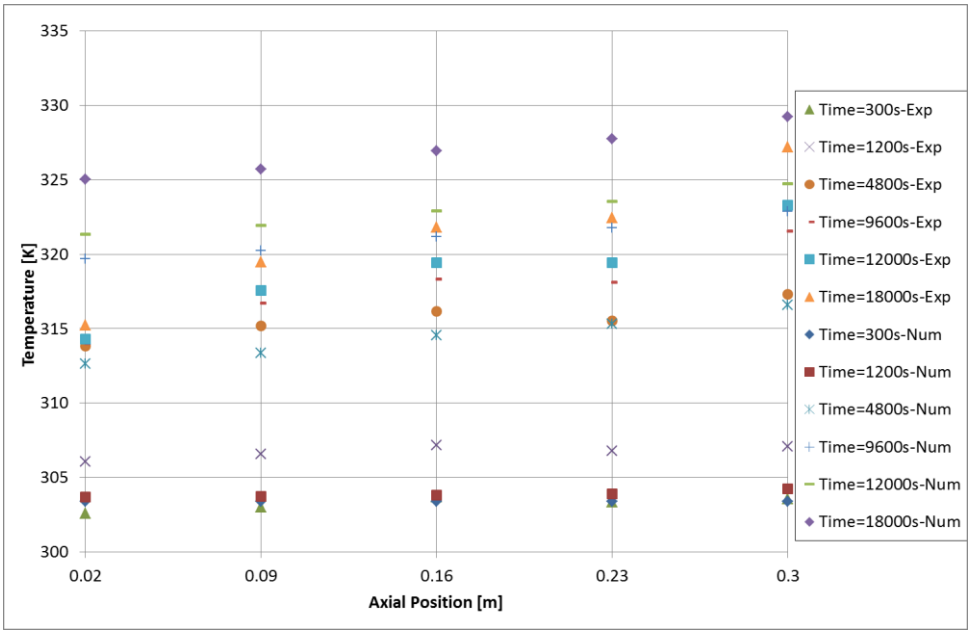

Figure 4.104 The axial temperature variations of Bed Design 2 in Experiment 2-Right axis vs results obtained from LTE based numerical analysis

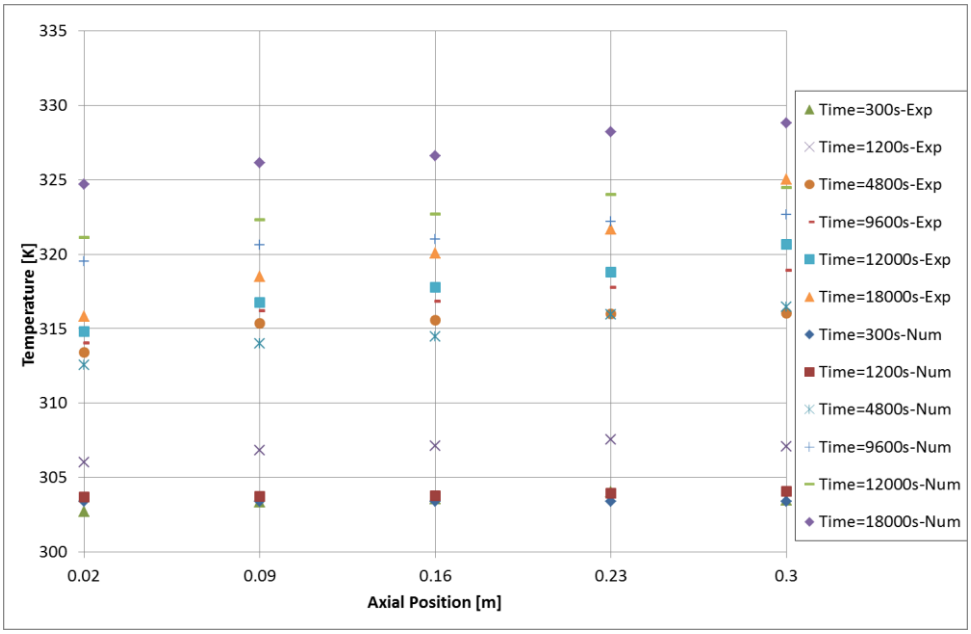

Figure 4.105 The axial temperature variations of Bed Design 2 in Experiment 2-Left axis vs results obtained from LTE based numerical analysis

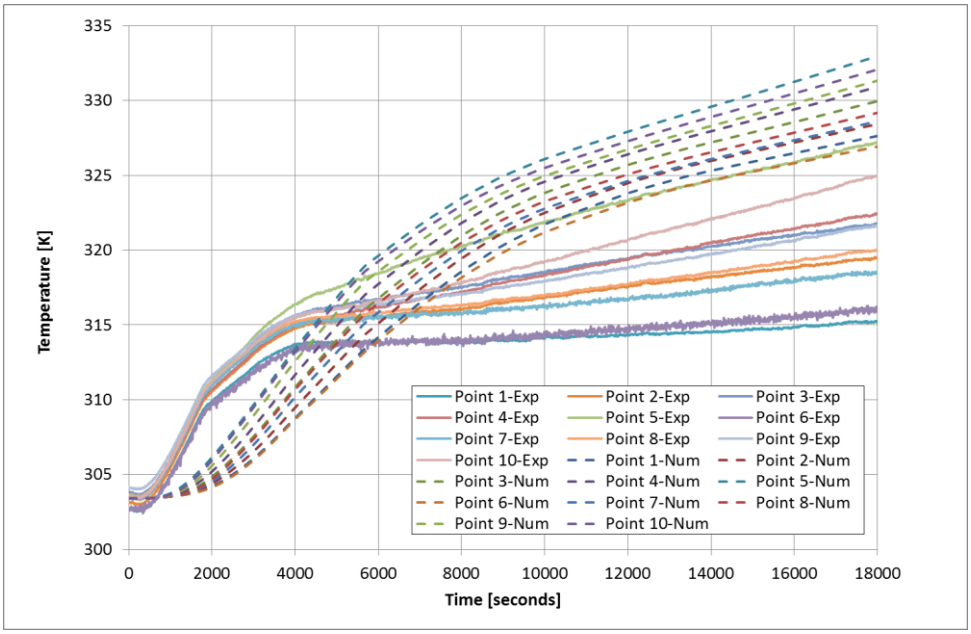

Figure 4.106 Bed temperature variations with time for Bed Design 2 in Experiment 2 vs results obtained from LTNE based numerical analysis

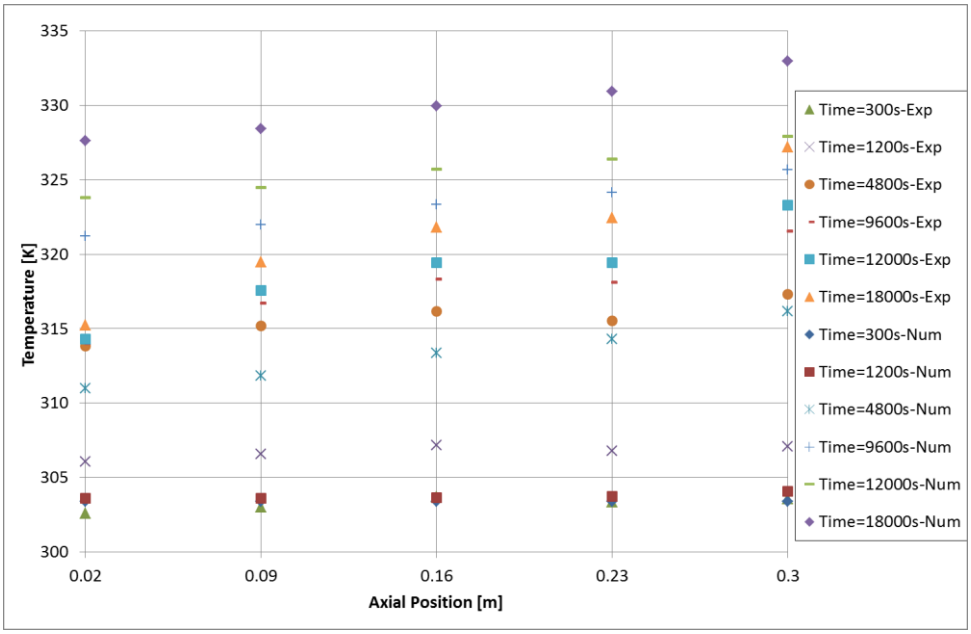

Figure 4.107 The axial temperature variations of Bed Design 2 in Experiment 2-Right axis vs results obtained from LTNE based numerical analysis

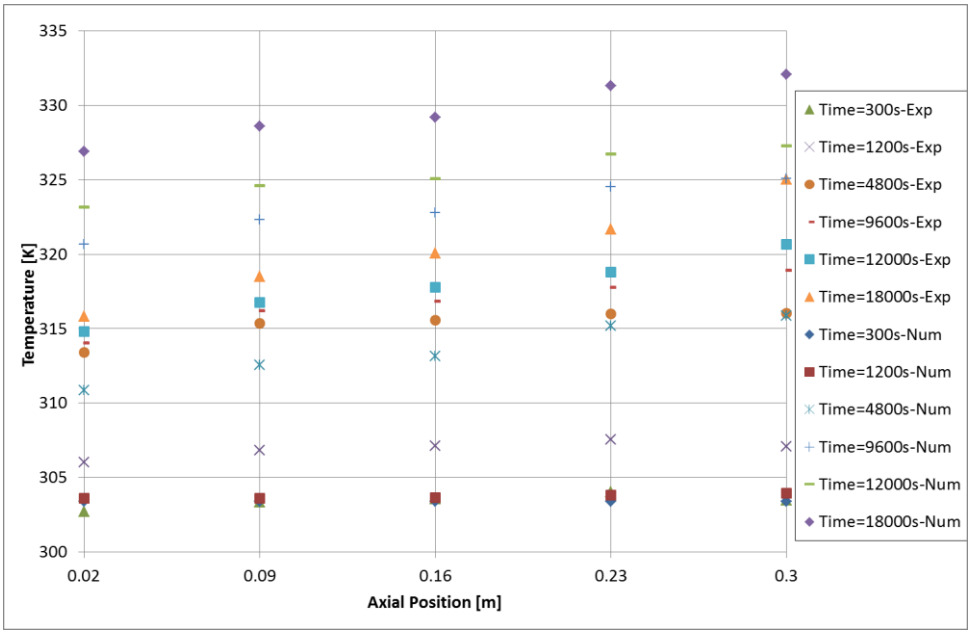

Figure 4.108 The axial temperature variations of Bed Design 2 in Experiment 2-Left axis vs results obtained from LTNE based numerical analysis

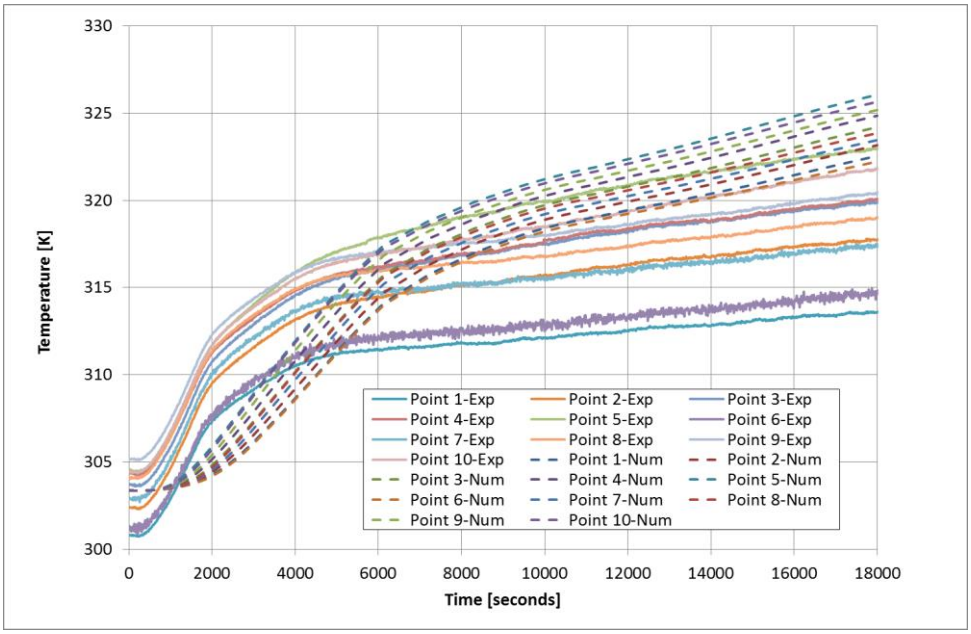

Figure 4.109 Bed temperature variations with time for Bed Design 2 in Experiment 3 vs results obtained from LTE based numerical analysis

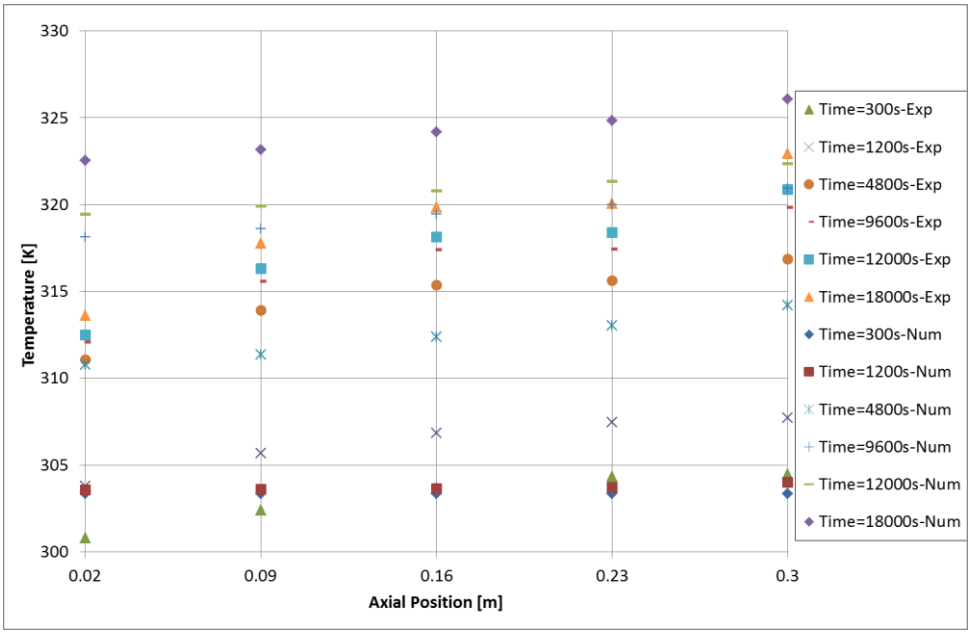

Figure 4.110 The axial temperature variations of Bed Design 2 in Experiment 3-Right axis vs results obtained from LTE based numerical analysis

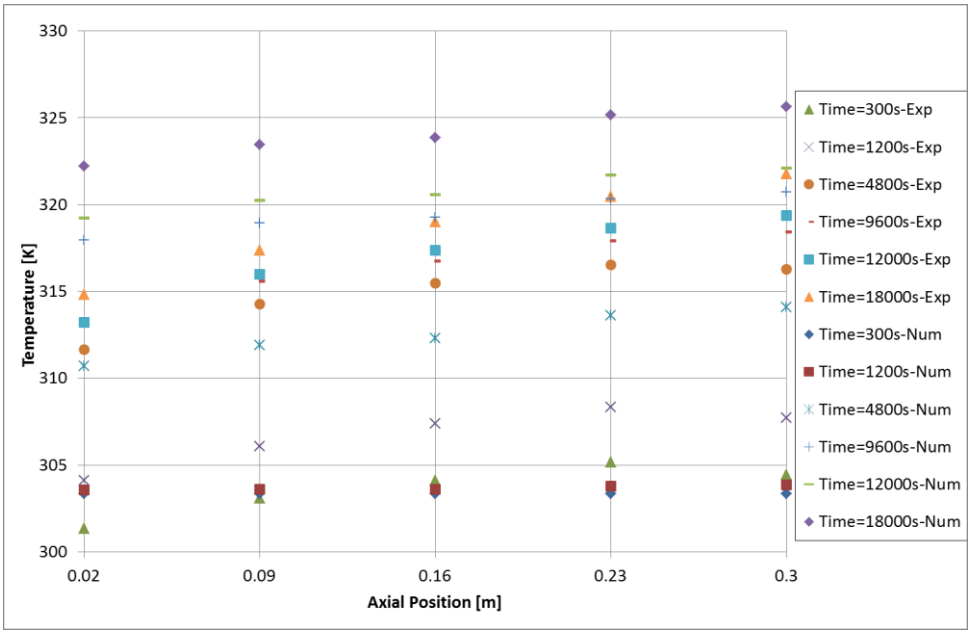

Figure 4.111 The axial temperature variations of Bed Design 2 in Experiment 3-Left axis vs results obtained from LTE based numerical analysis

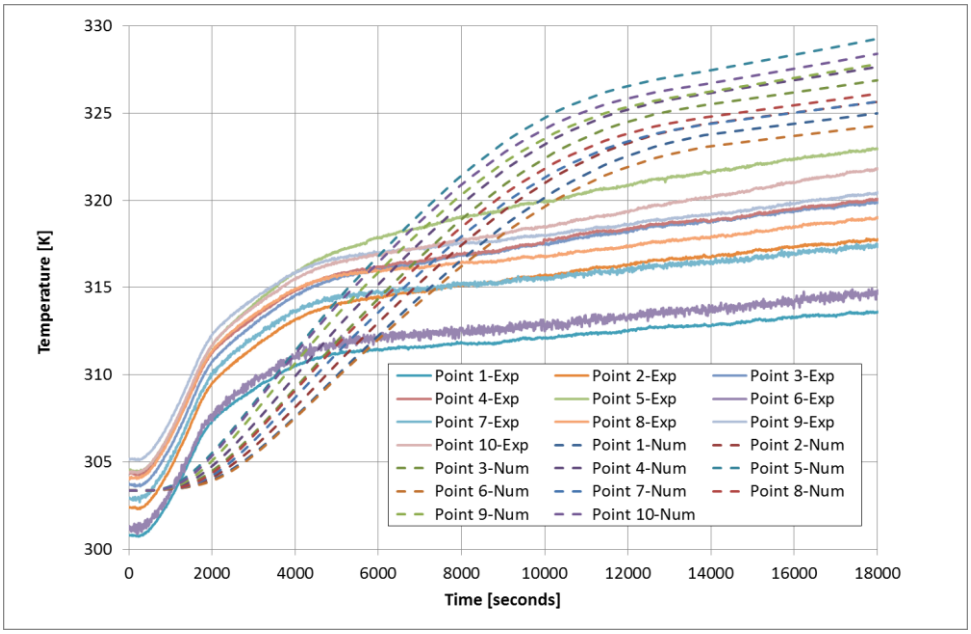

Figure 4.112 Bed temperature variations with time for Bed Design 2 in Experiment 3 vs results obtained from LTNE based numerical analysis

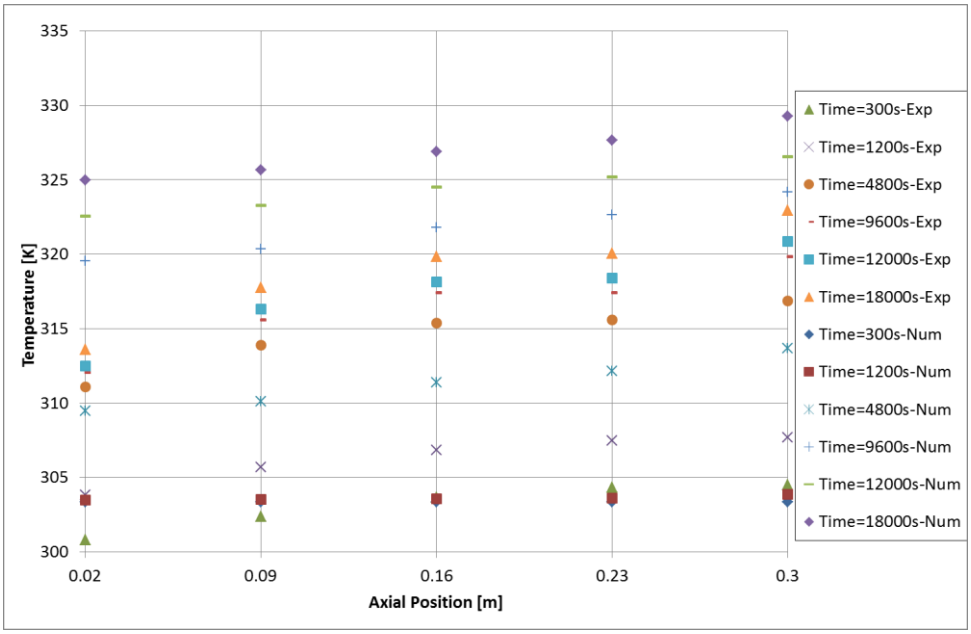

Figure 4.113 The axial temperature variations of Bed Design 2 in Experiment 3-Right axis vs results obtained from LTNE based numerical analysis

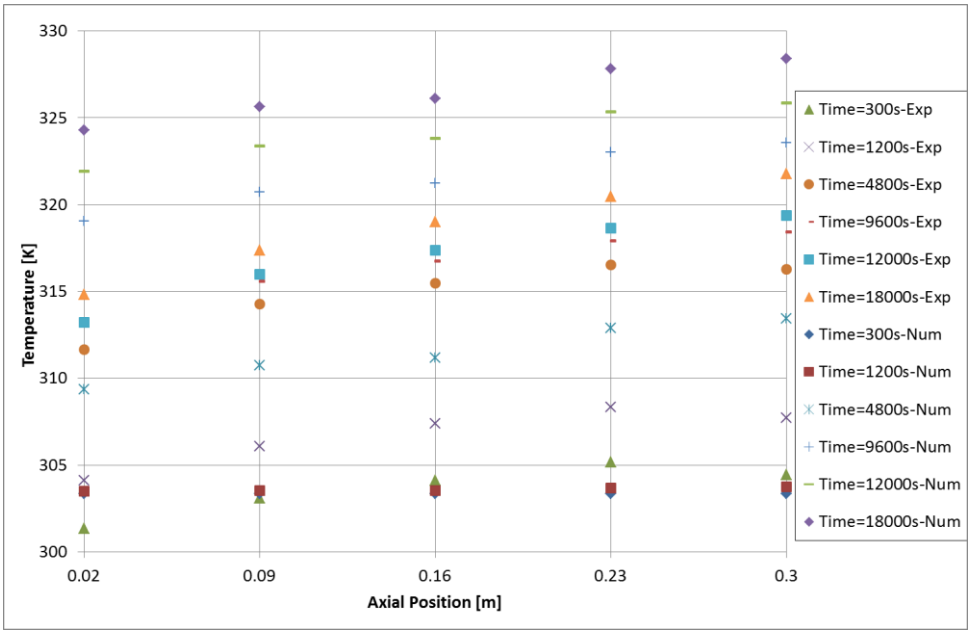

Figure 4.114 The axial temperature variations of Bed Design 2 in Experiment 3-Left axis vs results obtained from LTNE based numerical analysis

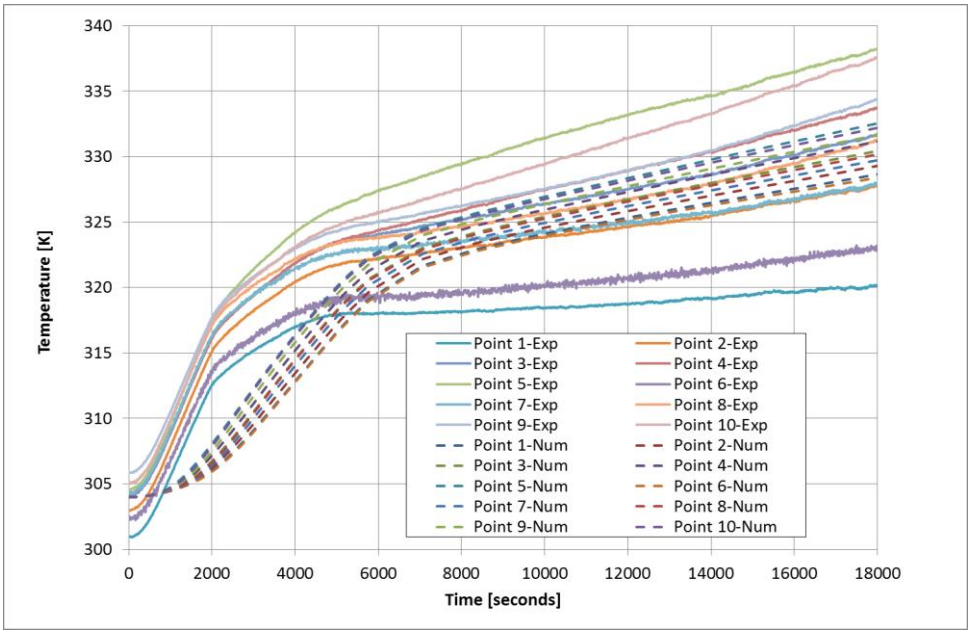

Figure 4.115 Bed temperature variations with time for Bed Design 2 in Experiment 4 vs results obtained from LTE based numerical analysis

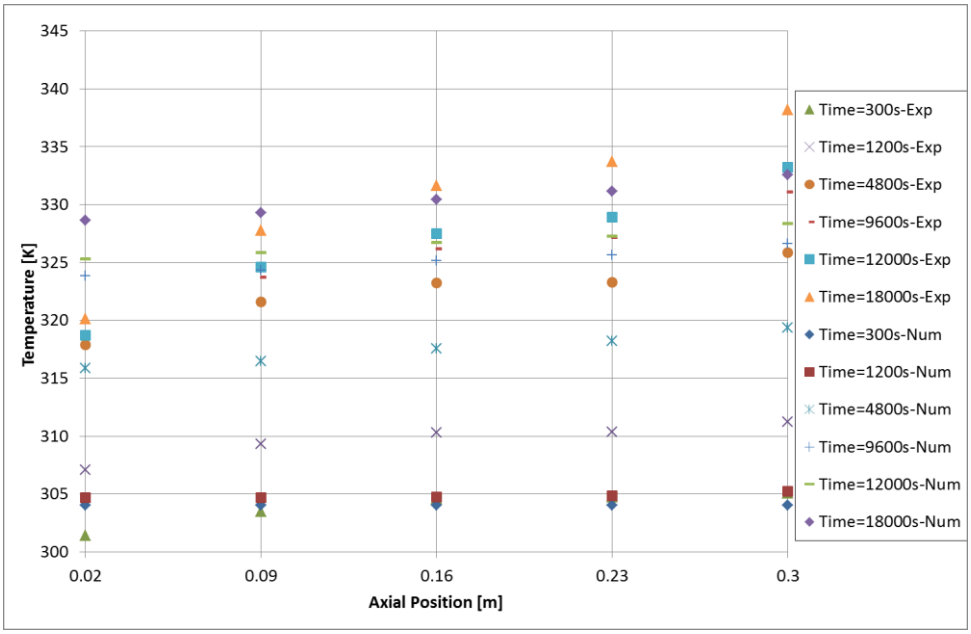

Figure 4.116 The axial temperature variations of Bed Design 2 in Experiment 4-Right axis vs results obtained from LTE based numerical analysis

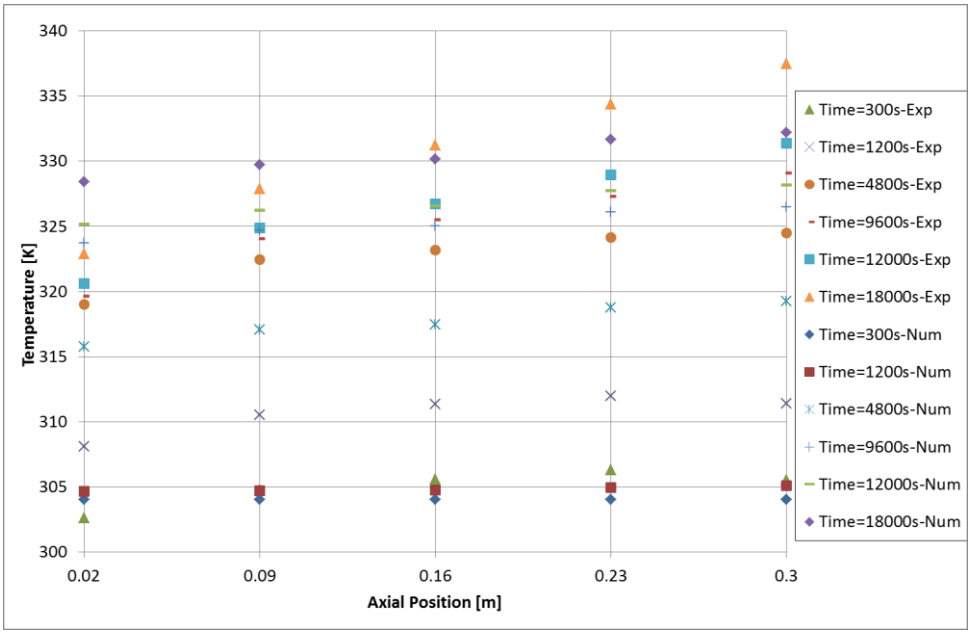

Figure 4.117 The axial temperature variations of Bed Design 2 in Experiment 4-Left axis vs results obtained from LTE based numerical analysis

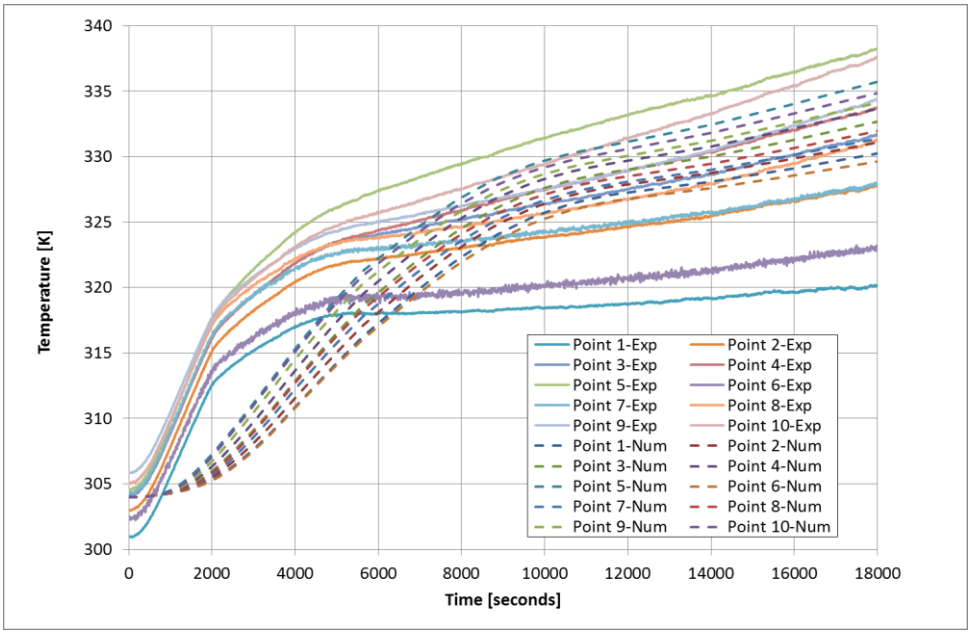

Figure 4.118 Bed temperature variations with time for Bed Design 2 in Experiment 4 vs results obtained from LTNE based numerical analysis

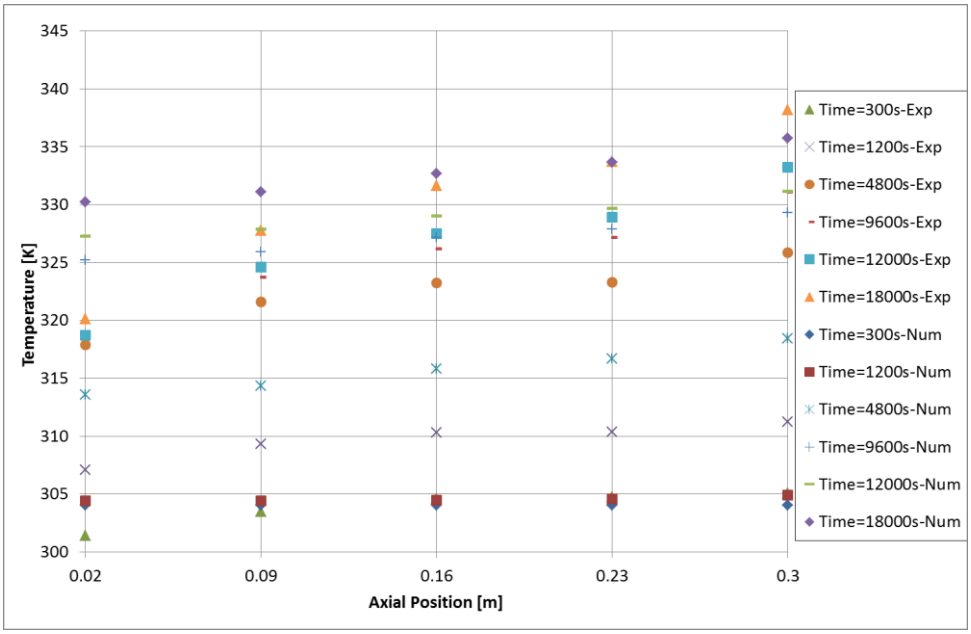

Figure 4.119 The axial temperature variations of Bed Design 2 in Experiment 4-Right axis vs results obtained from LTNE based numerical analysis

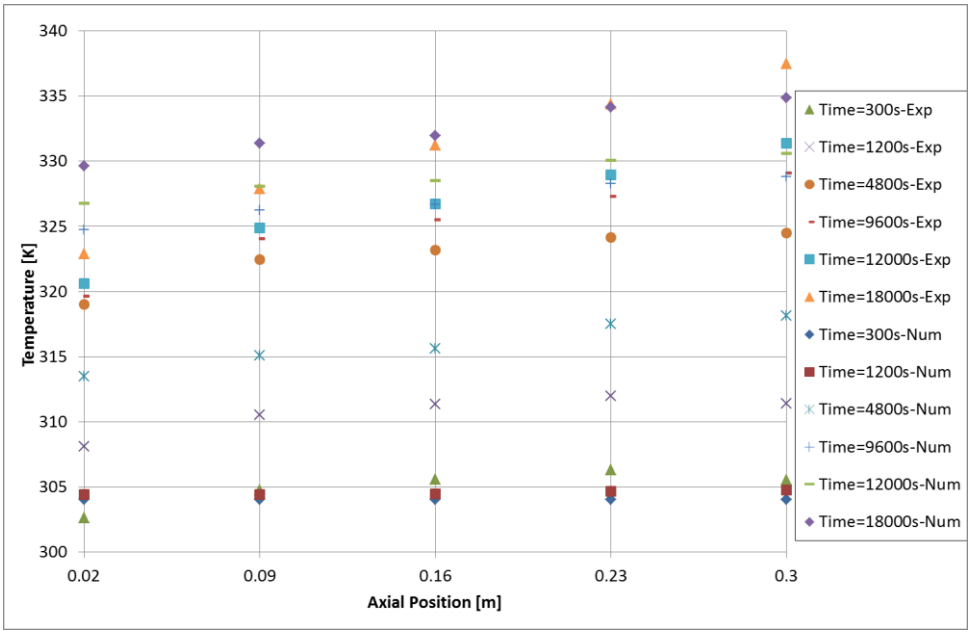

Figure 4.120 The axial temperature variations of Bed Design 2 in Experiment 4-Left axis vs results obtained from LTNE based numerical analysis

The temperature of the Bed Design 2 under conditions of Experiment 1 is more closely predicted by the LTE based numerical model compared to the LTNE based one. The LTE based numerical model predicts the temperature rise in the lower temperature higher than the experimental data however LTNE based numerical models overestimated the temperature of all points especially in the desorption phase under conditions of the Experiment 1.

Similar to the observations of the Bed Design 1, in Bed Design 2 also there is a delay in the time variation of temperature curves obtained from numerical analyses. This delay mainly observed in the isosteric heating part of the process. The delay also affects the differences in the desorption phase. The delay in the temperature rise in isosteric heating period observed in the numerical analysis data is higher in the LTNE based models. Compared to the numerical analysis results of Bed Design 1, the differences between results obtained from LTE based and LTNE based numerical models are higher for Bed Design 2.

The temperature variation predicted by LTE based numerical model more closely follows the experimental data of Experiment 2; however the temperature of the points which are positioned in the lower portion of the bed is overestimated by the numerical model. The LTNE based numerical model predicts higher temperatures for the bed during desorption phase. Also the decrease in the slope of time variation of bed temperatures started later compared to the results of LTE based numerical models.

The temperature variation trends and the slope of temperature curves predicted by the LTE and LTNE based numerical models are more similar under the conditions Experiment 4 compared to the other analysis conditions.

Based on the numerical analysis results of the Bed Design 2 the main points of the observations about the numerical analysis results can be summarized as follows,

- The LTNE and LTE based models predicted the temperature variation with time in isosteric heating period with a delay compared to the experimental data
- The delay observed in the results of LTE based analysis is less compared to the results of LTNE based analysis
- Under low initial adsorbate loading conditions (Experiment 4) the differences between time variation of temperature curves obtained from LTE and LTNE based numerical models is less compared to the other analysis conditions.
- The delayed inclination of the temperature variation plots and higher temperatures obtained from the LTNE based analyses may indicate that the heat transfer resistance could be predicted lower and therefore increased rate of desorption decreases the slope of the temperature variation with time curves.
- Similar to the analysis results of Bed Design 1, the LTNE based analyses also predicts higher temperature differences within the bed compared to LTE based numerical models.
- The axial temperature gradients and the temperatures predicted by the LTNE model is relatively higher compared to the LTE based numerical model.

The temperature variations taken from the crossection used in the experimental measurements for Bed Design 2 under conditions of Experiment 2 could be seen in Figure 4.120 And figure 4.121 The adsorption capacity variation at the same crossections also can be seen in Figure 4.122 and Figure 4.123 obtained from LTE and LTNE based numerical analyses for the conditions of Experiment 2.

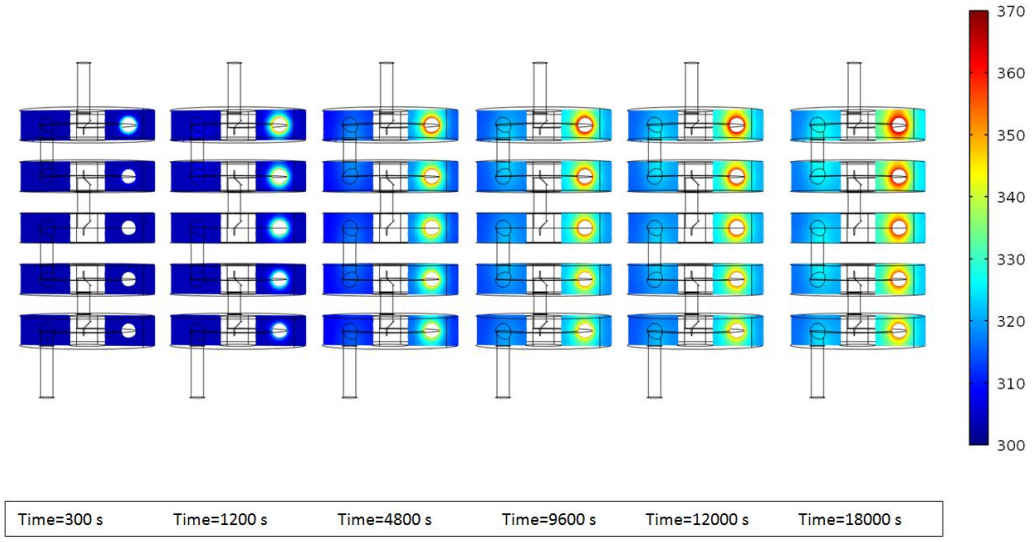

Figure 4.121 Temperature distribution contour plots taken from a planar crossection, obtained from LTE based numerical analysis of Bed Design 2.

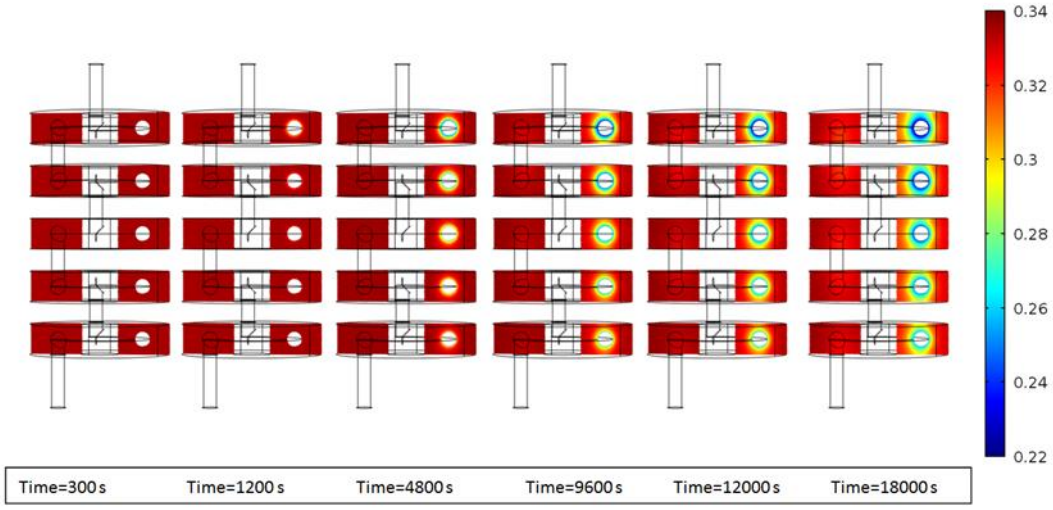

Figure 4.122 Adsorption capacity (X) distribution contour plots taken from a planar crossection, obtained from LTE based numerical analysis of Bed Design 2.

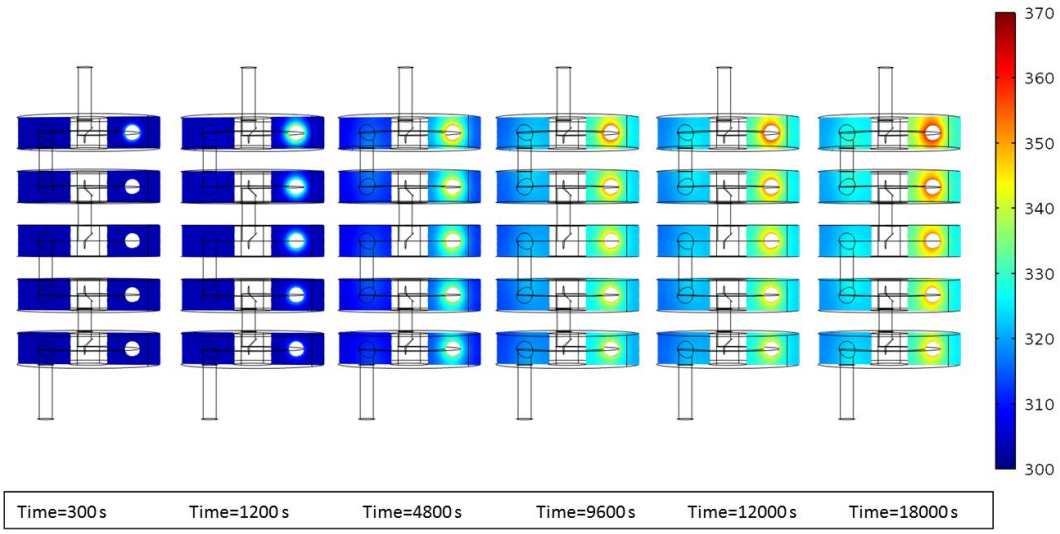

Figure 4.123 Temperature distribution contour plots taken from a planar crossection, obtained from LTNE based numerical analysis of Bed Design 2.

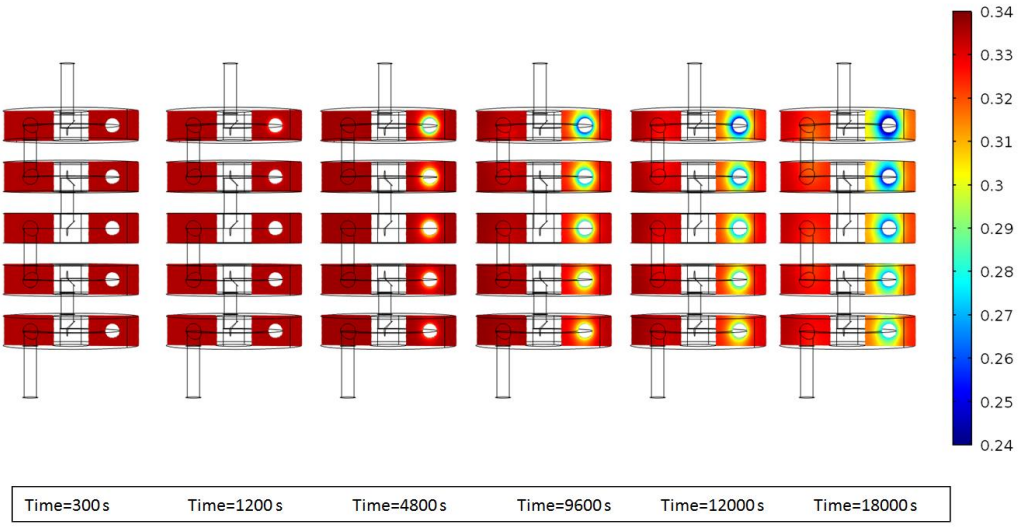

Figure 4.124 Adsorption capacity (X) distribution contour plots taken from a planar crossection, obtained from LTNE based numerical analysis of Bed Design 2.

The general observations for the numerical analyses of both bed designs based on LTE and LTNE approach can be listed as follows,

- The time variation of point temperatures predicted by both LTE and LTNE based numerical analyses; exhibit a delayed rise in the isosteric heating period. This delay affects the compared axial temperature distributions also.
- The temperature variation rate in the isosteric heating and the desorption phases of the process are generally approximated closely by the results obtained from LTE based numerical models.
- LTNE based numerical models generally predicts higher temperature values compared to the LTE based numerical values.
- The difference between LTE and LTNE based numerical models are less for under low initial adsorbate loading conditions compared to the other analysis conditions.
- Except the differences in the delay, both LTE and LTNE based numerical analyses predicted similar temperature variation trends with the experiments.
- The slow increase observed for temperature measurement points situated in the lower portions of the bed (points 1, 2, 6 and 7) could not be approximated well by the analysis models.
- Predicted temperature values by the LTE based numerical models in desorption period, are generally lies between the maximum and minimum values measured experimentally. Additionally the slope of the lower and upper point temperature variation curves obtained from LTE based analyses differing in a range which resembles the experimentally obtained temperature distribution. However the temperature differences within the bed could not be approximated closely by the LTE based numerical models since the numerically obtained temperature differences within the bed and the axial temperature gradients are lower than the experimentally obtained values.
- The slope of the time variation plots after the inclination due to desorption taking place is close to each other for all the temperature points in LTNE

based numerical analysis results. The slope of the time variation curves of the points is lower than the experimental results of the top measurement point and higher than the bottom measurement point in the results of LTNE based numerical models.

- Compared to the results of the LTE based numerical models the axial temperature gradients predicted by LTNE based numerical models are more close to the experimentally measured values however still a total agreement not exists.

The axial temperature gradients also can be used as a measure for evaluating the heat recovery efficiency as it had been stated previously. Therefore in addition to the time variation plots of temperatures obtained for bed designs also the maximum axial temperature gradients obtained from the analyses are compared with the experimental results. The maximum axial temperature gradients obtained from analyses are given in comparison with the experimentally obtained values in Table 4.7.

Table 4.8 The maximum axial temperature gradients observed during operation, the results of numerical analyses and experimental values

		Maximum Axial Gradient [K/m]		
		Experimental Result	Numerical Result-LTE	Numerical Result-LTNE
Bed Design 1	Experiment 1	21.6	37.9	39.8
	Experiment 2	57.1	30.0	32.6
	Experiment 3	36.2	21.4	23.6
	Experiment 4	66.5	26.6	29.6
Bed Design 2	Experiment 1	42.7	22.1	25.6
	Experiment 2	42.7	15.1	19.1
	Experiment 3	33.3	12.5	16.6
	Experiment 4	64.6	13.9	19.6

Based on the maximum axial temperature gradients, it could be said that the numerically predicted values are lower than the experimentally obtained values in all of the cases except the Bed Design 1-Experiment 1. As it had been observed previously the LTNE based analysis models predicts higher axial temperature gradients compared to LTE based analysis models for all of the analysis cases. Disregarding the Experiment 1, the values calculated from numerical analyses can be used as a measure for evaluating the heat recovery efficiency of Bed Design 1 since; variation trends are similar with the experimentally obtained values. However the variation of the maximum axial temperature gradients predicted by numerical results could not be used as a guide to evaluate the heat recovery efficiency of the Bed Design 2 under the analyzed conditions.

The source of differences between the LTE and LTNE models could be the difference between thermal conductivity definitions of the bed. Additionally, the differences in temperature of the solid and vapor phases within the adsorbent bed could be a reason for the difference between LTE and LTNE models, however regarding the temperature variation results, the LTE based models predicts the temperature variation trends of the bed better than the LTNE based models.

Another source of difference between experiments and the numerical analyses could be the definition of the heat transfer coefficient at the HTT and adsorbent particle interface. In the analyses a constant value defined to this interface however, the contact resistance varies with the pressure applied, therefore, the contact resistance could be low at the lower portions of the Bed Design 1 and would be much higher for the Bed Design 2 which is loosely packed. Unfortunately the exact value of the contact resistance between particles and HTT and the variation with the pressure is not known.

Additionally the effect of refrigerant vapor flow and the radiative heat transfer had not been included in the analysis models which may lead to differences also.

Therefore, more detailed analyses should be made to understand the effect of neglected or underestimated parameters which affects the characteristics of the experimental prototypes and cannot be predicted by the available numerical modeling approaches.

The main aim of presenting the results of LTE and LTNE based numerical analysis models together with the experiments is to demonstrate the effectiveness of the analysis tools for predicting the heat recovery performance of realistically designed three dimensional adsorbent beds. However the results had shown that the design of adsorbent beds is a complicated process which could not be solely based on the analysis tools. The results obtained from the analyses can be used for shaping the geometric design features but the results of presented numerical analyses are not a suitable tool for the performance evaluation of the beds, since the results may mislead even for the relative comparisons. Moreover, using the maximum axial temperature gradient as the single measure for evaluating the heat recovery efficiency may also be misleading. Additional analyses and experiments would be helpful to develop our understanding on the relation between axial temperature gradients and heat recovery efficiency.

CHAPTER 5

SUMMARY AND CONCLUSION

In this thesis study cylindrical adsorbent beds with circular heat exchange coils are theoretically and experimentally investigated. In the first part of the investigation the governing equations which identify the adsorption phenomena is derived. Two different numerical models are presented which are based on different assumptions. Additionally the governing equations for simulating the effect of non-adsorbing gas existence in the bed are also derived. Numerical analyses performed on the simple geometry with the proposed numerical models to demonstrate the effect of, modeling assumptions and the non-adsorbing gas existence within the adsorbent bed during adsorption and desorption processes. Thirdly two different beds are designed. The designed adsorbent beds are manufactured, analyzed and experimentally tested. The results of the theoretical and experimental analyses are discussed in comparison. The conclusions derived from different parts of the study are given in detail in the following part.

In the theoretical investigation part, numerical models based on the Local Thermal Equilibrium (LTE) and Local Thermal Non-Equilibrium (LTNE) assumptions are derived. The LTE based equations are derived using the control volume approach while the governing equations for based on LTNE assumption is derived by volume averaging approach. In addition to the LTE and LTNE assumptions, governing equation set for simulating the effect of a non-adsorbing gas existence is also derived. The analyses performed on a simple two dimensional axisymmetrical geometry by using different numerical models showed that the LTE based numerical model predicts lower heat exchange rates with the heat transfer fluid compared to the

LTNE based models. Additionally, the results of the analyses performed to investigate the effect of non-adsorbing gas existence in the system had shown that the even small amounts of air existence may affect the heat and mass transfer characteristics of bed significantly during adsorption process. On the other hand the analysis results showed that existence of a non-adsorbing gas is less effective on heat and mass transfer characteristics of the adsorbent bed during desorption process.

In the second part of the study two different cylindrical adsorbent beds are designed. The design philosophy aims to increase the heat transfer rate in radial direction while reducing the axial heat transfer rate. Regarding this design philosophy, two different designs utilizing circular shaped HTT are proposed. The Bed Design 1 is an annular cylinder equipped with a spiral shaped HTT. The HTT in Bed Design 2 is composed concentrically positioned circular arcs arranged in a row in the axial direction. There are five circular arcs placed into annular adsorbent bed slices in Bed Design 2. In both of the designs, the HTF flow path is elongated in the radial direction to increase the heat transfer surface area in the radial direction while retarding the flow velocity of HTF in the axial direction.

The idea behind these designs is to improve the heat recovery efficiency of the adsorbent bed by obtaining a thermal wave like temperature distribution within the bed and the HTF during operation. Since it is difficult to obtain an exact thermal wave type distribution the heat recovery efficiency of the design is evaluated based on the magnitude of the axial temperature gradients. The designed beds are manufactured for experimental investigation in the test setup available in the laboratory. The test setup is upgraded and various components are replaced since they were malfunctioning and not suitable for performing long duration experiments. Still further modifications are required in the test setup for improving the stability and repeatability of the experimental conditions.

The evaluation of the designed beds are mainly based on the experimental investigations performed under desorption conditions. As stated earlier the magnitude of the maximum axial temperature gradient observed is used as an evaluation criterion. The experiments for both beds are performed under four different conditions. First of the conditions is the low HTF velocity condition, 0.0012 m/s is chosen as the HTF velocity for these experiments while the HTF inlet temperature is kept constant at 397 K. The second experimental condition is the high HTF inlet temperature and high HTF velocity. The HTF inlet temperature is tried to be kept at 397 K for this experiments while the HTF velocity is tried to be kept equal to 0.002 m/s. The third experimental condition is defined for determining the effect of low HTF inlet temperature therefore inlet temperature is set to 370 K in these experiments while the HTF velocity is equal to 0.002 m/s. The last experimental condition is chosen for demonstrating the effect of low initial adsorbate loading therefore the initial adsorbate capacity of the bed is adjusted to be 0.01 lower than the other three experimental conditions. Significant results derived from the experimental investigation of the proposed bed designs could be summarized as follows,

- The maximum values of the axial temperature gradients thus the heat recovery efficiency of the bed is related with the initial adsorption capacity of the bed. The maximum value of the axial temperature gradients increases with the reduced initial adsorption capacity value for both of the bed designs.
- Based on the mentioned design philosophy the conductive heat transfer rate in the axial direction within the bed, does not significantly affect the axial temperature gradients under the investigated operating conditions. Therefore regarding the investigated designs, features that reduce the axial heat transfer rate seemed to be unnecesarry.
- When the desorption process is not constrained by the mass transfer rate, heat transfer characteristics and the axial temperature gradients may depend on the

heat transfer rate between HTF and the bed until this heat transfer rate exceeds the heat diffusion rate within the bed.

- The heat recovery efficiency indicated by the maximum value of axial temperature gradients, could be increased by the increased HTF velocity if the desorption rate is limited by the mass transfer resistance.

In addition to experimental evaluation of the adsorbent bed designs, also numerical analyses on full scale models had been performed by using both LTE and LTNE based numerical modeling approaches. One of the main aims in performing the numerical analyses is to compare the results obtained with the experimental results and understand the effectiveness of the numerical models in performance predictions and design evaluation. Therefore the numerical models are prepared by using as much as details to obtain close results with the experiment. However the limitations imposed by the software and computer resources leads to simplifications in the numerical analysis models. In the numerical models, the vacuum chamber and the flow inside the chamber had not been modeled for reducing the computational domain size. The conditions inside the vacuum chamber are assigned to boundaries of the adsorbent bed domain. The important conclusions drawn from the comparison of the numerical analysis results can be summarized as follows,

- The time variation of point temperatures predicted by both LTE and LTNE based numerical analyses; exhibit a delayed rise in the isosteric heating period. This delay affects the compared axial temperature distributions also.
- Except the differences in the delay, both LTE and LTNE based numerical analyses predicted similar temperature variation trends with the experiments
- The temperature variation rate in the isosteric heating and the desorption phases of the process are approximated closely by the results obtained from LTE based numerical models compared to the LTNE based models in all of the analysis conditions.

- LTNE based numerical models generally predicts higher temperature values compared to the LTE based numerical values as it had been observed in the analyses performed on simple model.
- The difference between LTE and LTNE based numerical models are less for under low initial adsorbate loading conditions compared to the other analysis conditions for both bed designs.
- The slow increase observed for temperature measurement points situated in the lower portions of the bed could not be approximated well by both analysis models.
- Predicted temperature values by the LTE based numerical models in desorption period, are generally lies between the maximum and minimum values measured experimentally. Additionally the slope of the lower and upper point temperature variation curves obtained from LTE based analyses differing in a range and resembles the experimentally obtained temperature distribution. However the temperature differences within the bed could not be approximated closely even by the LTE based numerical models. The numerically obtained temperature differences within the bed and the axial temperature gradients are lower than the experimentally obtained values
- The slope of the time variation plots after the inclination due to desorption taking place is close to each other for all the temperature points in LTNE based numerical analysis results. The slope of the time variation curves of the points obtained from LTNE based numerical models is lower than the slope of experimental temperature variation at top measurement point and higher than curve of the bottom measurement point in.
- Compared to the results of the LTE based numerical models the axial temperature gradients predicted by LTNE based numerical models are more close to the experimentally measured values however still a good agreement does not exist.

- The maximum axial temperature gradients are underestimated by both numerical models except the results obtained for Experiment 1 of Bed Design 1.
- Since the trend in variation for the axial temperature gradient values obtained from numerical results does not match with the experimentally obtained gradient values consistently, the numerical analysis results could not be used as a tool for evaluating the heat recovery efficiency of the bed designs.

There could be various causes for the differences between analysis results and the experimental results. Some of the possible reasons of the differences between experimental and numerical analyses could be, effective thermal conductivity definition in LTE based models, heat transfer resistance definition at the HTT adsorbent particle interface, effect of variation of thermophysical properties with temperature, radiative heat transfer, and vapor flow in the vacuum chamber. However it is difficult to predict the combined effect of all these parameters on the results. Therefore, more detailed analyses should be made to understand the effect of neglected or underestimated parameters which affects the characteristics of the experimental prototypes and cannot be predicted by the performed numerical analyses.

In the light of experience gained in this study some of the recommendations for the future research activities could be listed as,

- In the current study, HTF inlet temperature is altered by the thermal inertia of the thick walled, general purpose vacuum chamber. Additionally the large volume of the vacuum space thought to affect the adsorption capacity and temperature distributions of the adsorbent bed due to vapor flow inside the chamber. Therefore in the future studies instead of using a general purpose test chamber, vacuum chamber should designed to have minimum impact on the heat and mass transfer within the bed and between bed and HTF.

- The high amount of adsorbent and the low HTF velocities used in the experiments, resulted in long desorption durations. It is difficult to keep the HTF flow rate and the inlet temperature constant throughout the long duration. Thus, for conducting each experiment with consistent values successive trials and very long period time is spent. Therefore, while designing the experiments, HTF velocity, adsorbent amount, regeneration temperatures need to be considered to have reasonable duration for experiments.
- As mentioned earlier to be able to measure the desorbed amount from the adsorbent bed more accurately the effect of vacuum space volume need to be reduced by reducing the size of the vacuum chamber.
- The refrigerant level in the condenser canister is measured by using a sight glass which makes the measurements more difficult and less accurate; therefore in the future research activities to measure the refrigerant amount in the condenser canister a digital levelmeter could be used.
- The HTF flow rate in the current experimental setup is adjusted by two needle valves. One of the valves is on the bypass line and the other is at the downstream of the bypass junction. However it is difficult to stabilize the flow rate at low values such as 0.1 liter per minute. Therefore a precise flow rate control system would be useful to accurately control and measure the HTF flow rate.
- In the current study adsorption experiments could not be performed due to improper evaporator design of the available experimental setup. In the future research activities a new evaporator need to be designed and manufactured with a large free surface area for.
- Due to long durations and experimental difficulties, the results could not be evaluated from point of repeatability. In the future research activities, repeatability of the experiments also need to be checked.
- In the adsorbent bed design, in addition to elongating the HTF flow path also use of extended surfaces will improve the heat transfer characteristics of the

bed. Moreover, reduced adsorbent layer thickness around the HTT would reduce the mass transfer resistances and improve the overall adsorption/desorption performance of the bed. Therefore the performance enhancements can be achieved through geometric design of the bed. Numerical analyses would be a proper tool for evaluating and improving the design of the adsorbent bed.

Consequently, the numerical and experimental investigations in the scope of this study aimed to develop concepts which could help understanding and evaluation of the adsorbent bed designs from the heat recovery efficiency aspect. For this purpose the axial temperature gradient value is used as a measure. Additionally the link between numerical and the experimental analyses tried to be established; however the detail level of the analyses performed is not mature enough to be solely used for the evaluation purposes. Resultantly, still more efforts need to be spent for understanding the differences between numerical models and the actual adsorption systems.

REFERENCES

[1] Sumathy K.,Yeung K.H., Yong L. "Technology development in the solar adsorption refrigeration systems" Progress in Energy and Combustion Science, 29, pp 301-307, 2003.

[2] Taylan O., Baker D.K., Kaftanoğlu B., "COP trends for ideal thermal wave cooling cycles with enhancements", International Journal of Refrigeration, 35, pp 562-570,2012

[3] Baker D.K., "Thermodynamic limits to thermal regeneration in adsorption cooling cycles", International Journal of Refrigeration, 31, pp 55-64, 2008.

[4] Taylan O., Baker D.K., Kaftanoğlu B., "Limits to the thermodynamic zhengance of a thermal wave adsorption cooling cycle.", Procedings of 5th International Conference on Heat Transfer, Fluid Dynamics and Thermodynamics, HEFAT 2007, 1-4.07.2007, Sun City, South Africa.

[5] Shelton S.V., "Solid adsorbent heat pump system", United States Patent, Patent number: 4,610,148, 1986.

[6] Sun M., Ben Amar N., Meunier F., "Numerical study on coupled heat and mass transfer in an adsorber with external fluid heating", Heat Recovery Systems & CHP, 15, pp 19-29, 1995.

[7] Ben Amar N., Sun M.L., Meunier F., "Numerical analysis of adsorptive temperature wave regenerative heat pump", Applied Thermal Engineering, 16, pp 405-418, 1996.

[8] Sward B.K., LeVan D., Meunier F., "Adsorption heat pump modeling:thermal wave process with local equilibrium", Applied Thermal Engineering, 20, pp 759-780, 2000.

[9] Sakoda A., Suzuki M., Fundamental study on solar power adsorption cooling system, Journal of Chemical Engineering of Japan 17 (1984) 52–57.

[10] Solmuş İ., Andrew D., Rees S., Yamali C., Baker D., Kaftanoğlu B., "Numerical investigation of coupled heat and mass transfer inside the adsorbent bed of an adsorption cooling unit", Int. Journal of Refrigeration, 35, pp 652-662, 2012.

[11] Zhang L.Z., “A three dimensional non-equilibrium model for an intermittent adsorption cooling system”, Solar Energy, 69, pp 27-35, 2000.

[12] Di J., Wu J., Xia Z.Z., Wang R.Z.,”Theoretical and experimental study on characteristics of a novel silica gel-water chiller under the conditions of variable heat source temperature” Int. Journal of Refrigeration, pp 515-526, 2007.

[13] Chen Z., Huan G., Ma Y., “Computational methods for multiphase flows in porous media”, SIAM Computation Science & Engineering, 2006.

[14] A. Çağlar, “Design and Experimental Testing of an adsorbent bed for a thermal wave adsorption cooling cycle,” PhD Thesis, Middle East Technical University, Ankara, Turkey, September 2012.

[15] Wang L.W., Wang R.Z., Oliviera R.G., “A review on adsorption working pairs for refrigeration”, Renewable and Sustainable Energy Reviews,13, pp 518-534, 2009.

[16] Yong L., Sumathy K., “Comparison between heat transfer and heat mass transfer models for transportation process in an adsorbent bed”, International Journal of Heat and Mass Transfer, 47, pp 1587-1598, 2004.

[17] Solmuş İ.,” An Experimental Study on the Performance of an Adsorption Cooling System and the Numerical Analysis of its Adsorbent Bed”, PhD Thesis, Middle East Technical University, Ankara, Turkey, December 2011.

[18] Wikipedia, http://en.wikipedia.org/wiki, Last visited May 2012.

[19] Suzuki M. “Adsorption for energy transport”, Adsorption Engineering, Elsevier, Vol25, 1990.

[20] Askalany A., Salem M., Ismail I.M., Ali A.H.H., Morsy M.G., “A review of adsorption cooling systems with adsorbent carbon” Renewable and Sustainable Energy Reviews, 16, pp 493-500, 2012.

[21] Lemmini F., Errougani A., “Technical note: experimentation of a solar adsorption Refrigerator in Morocco”, Renew Energy, 32, pp 2629–41, 2007.

[22] Wang R.Z. “Performance improvement of adsorption cooling by heat and mass recovery operation”, International Journal of Refrigeration, 24, pp 602–11, 2001.

[23] Çağlar A. Yamalı C.,Baker D.K., “Two dimensional transient coupled analysis of a finned tube adsorbent bed for a thermal wave cycle”, International Journal of Thermal Sciences, 73, pp 58-68, 2013.

[24] Critoph R.E.," Forced convection adsorption cycles", Applied Thermal Engineering, 18, pp799–807, 1998.

[25] Anyanwu E.E., "Review of solid adsorption solar refrigeration II: An overview of the principles and theory", Energy Conversion and Management, 45, pp 1279-1295, 2004.

[26] Best R, Ortega N., "Solar refrigeration and cooling" Renewable Energy, 16, pp685–90. 1999.

[27] Critoph R.E., "An ammonia carbon solar refrigerator for vaccine cooling" Renewable Energy, 5, pp502-8,1994.

[28] Boubakri A., Arsalane M., Yous B., Ali-Moussa L., Pons M., Meunier F., "Experimental study of adsorptive solar-powered ice makers in Agadir (Morocco):Performance on actual site" Renewable Energy 2, pp 7–13, 1992.

[29] Grenier P.H., Guilleminot J.J., Meunier F., Pons M.,"Solar powered solid adsorption cold store", Journal of Solar Energy Engieneering, 110, pp 192–7, 1998.

[30] Sakoda A., Suzuki M., "Simultaneous transport of heat and adsorbate in closed type adsorption cooling system utilizing solar heat", Journal of Solar Energy Engineering, 108, pp 239–49, 1986.

[31] Critoph R.E.,"Performance limitations of adsorption cycles for solar cooling", Solar Energy, 41, pp23-31, 1988.

[32] Tatlıer M., Ersolmaz-Tantekin B., Şenatalar-Erdem A., "A novel approach to enhance heat and mass transfer in adsorption heat pumps using the zeolite-water pair", Microporous and Mesoporous Materials, 27, pp 1-10, 1999.

[33] Leong K.C., Liu Y., " Numerical modeling of combined heat and mass transfer in the adsorbent bed of a zeolite/water cooling system", Applied Thermal Engineering, 24, pp 2359-2374,2004.

[34] C.T. Hsu, P. Cheng, K.W. Wong, "A lumped parameter model for stagnant thermal conductivity of spatially periodic porous media", International Journal of Heat and Mass Transfer 37, 2751–2759, 1995.

[35] Liu Y., Leong K.C., "Numerical modeling of a zeolite/water adsorption cooling system with non-constant condensing pressure", International Communications in Heat and Mass Transfer 35, pp 618-622, 2008.

[36] Maggio G., Freni A., Restuccia G., "A dynamic model of heat and mass transfer in a double-bed adsorption machine with internal heat recovery" International Journal of Refrigeration, 29, pp-589-600, 2006.

[37] Demir H., Mobedi M., Ülkü S., "Effects of porosity and mass transfer in granular adsorbent bed" Int. Communications in Heat and Mass Transfer 36, pp 372-377, 2008.

[38] Marletta L., Maggio G., Freni A., Ingrasciotta M., Restuccia G., " A non-uniform pressure dynamic model of heat and mass transfer in compact adsorbent beds" Int. Journal of Heat and Mass Trasnfer, 45, pp 3321-3330, 2002.

[39] Mhimid A., "Theoretical study of heat and mass transfer in a zeolite bed during water desorption: validity of local thermal equilibrium assumption" Int. Journal of Heat and Mass Transfer, 41, pp 2967-2977, 1998.

[40] Li M., Wang R.Z., "Heat and mass transfer in a flat plate solar solid adsorption refrigeration ice maker", Renewable Energy 28, pp 613-622, 2003.

[41] Mei N., Xie Y., Xu Z., Su J., "Experimental investigation and mathematical modeling of a solid adsorption refrigeration system", International communications in Heat and Mass Transfer 32 , pp 349-359, 2005.

[42] Solmuş İ., Yamalı C., Kaftanoğlu B., Baker D., Çağlar A., "Adsorption properties of a natural zeolite-water pair for use in adsorption cooling cycles", Applied Energy 87, pp 2062-2067, 2010.

[43] Solmuş İ., Yamalı C., Kaftanoğlu B., Baker D., "Experimental investigation of natural zeolite-water adsorption cooling unit", Applied Energy 88, pp 4206-4213,2010.

[44] Nizamand H., Dabzadeh I. "Numerical simulation of heat and mass transfer in adsorbent beds with annular fins", International Journal of Refrigeration,35, pp581-593, 2010.

[45] Duval F.,Fichot F., Quintard M., "A local thermal non-equilibrium model for two-phase flows with phase-change in porous media", International Journal of Heat and Mass Transfer, 47,pp 613-639, 2004.

[46] Leong K.C., Liu Y., "Numerical study of a combined heat and mass recovery adsorption cooling cycle", International Journal of Heat and Mass Transfer, 47,pp 4761-4770, 2004.

[47] Yong L., Sumathy K., "Review of mathematical investigation on the closed adsorption heat pump and cooling systems", Renewable and Sustainable Energy Reviews, 6, pp 305-337, 2002.

[48] Sun L.M., Feng Y., Pons M., "Numerical investigation of adsorptive heat pump systems with thermal wave heat regeneration under uniform-pressure conditions", International Journal Heat Mass Transfer,40,pp 281-293, 1997.

[49] El-Sharkawy I.I., Hassan M., Saha B.B., Koyama S.,Nasr M.M., "Study on adsorption of methanol onto carbon based adsorbents", International Journal of Refrigeration, 32, pp 1579-1586, 2009.

[50] Meunier F., "Adsorption heat powered heat pumps", Applied Thermal Engineering,Article in Press , 2013.

[51] Wang R.Z., "Adsorption refrigeration research in Shanghai Jiao Tong University", Renewable and Sustainable Energy Reviews,5, pp 1-37, 2001.

[52] Wang D.C., Li Y.H., Li D., Xia Y.Z., Zhang J.P.,"A review on adsorption refrigeration technology and adsorption deterioration in physical adsorption systems", Renewable and Sustainable Energy Reviews,14, pp 344-353, 2010.

[53] Lambert M.A., "Design of solar powered adsorption heat pump with ice storage", Applied Thermal Engineering,27, pp1612-1628, 2007.

[54] Saar O. M., "The Relationship between permeability, porosity and microstructure in vesicular basalts", MSc Thesis, University of Oregon, Oregon, USA, June 1998.

[55] Zou Q., "A CFD Modeling system for air flow and heat transfer in ventilated packing systems during forced air cooling of fresh produce", PhD Thesis, Massey University, USA, 2002.

[56] Civan F., "Porous Media Transport Phenomena", John Wiley and Sons Inc. Publication, Oklahoma, 2011.

[57] Whitaker S., "The Method of Volume Averaging" Kluwer Academic Publishers, Boston, 1999.

[58] Brown G.O., Hsieh H.T. , Lucero , D.A.. "Evaluation of laboratory dolomite core sample size using representative elementary volume concept" Water Resources Research, 36 (6), pp. 1199-1207, 2000.

[59] Lunardini , V.H., "Heat Transfer with Freezing and Thawing" , Elsevier Science Publishers B.V., 1991.

[60] Bear J., Bacchmat Y., "Introduction to Modeling of Transport Phenomena in Porous Media", Kluwer Academic Publishers, Dordrecht, 1990.

[61] Chhabra R.P., Comiti J. ,Machac I. “Flow of non-newtonian fluids in fixed and fluidized beds” Chemical Engineering Science, 56 (1), pp.1-27, 2001.

[62] Tsilingiris P.T., “Thermophysical and transport properties of humid air at temperature range between 0 and 100 ºC”, Energy Conversion and Management, 49, pp 1098-1110, 2008.

[63] Bird, R.B., Stewart W.E., Lightfoot E.N., “Transport Phenomena”, John Wiley and Sons Inc., Madison, USA, 2001.

[64] Poling B.E,.Prausnitz J.M., O’Connell J.P., “The properties of gases and liquids “McGraw Hill, NewYork, USA, 2001.

[65] Ruthven D.M., “Principles of Adsorption and Adsorption Processes”, John Wiley and Sons, Inc., Frederickton, USA, 1984.

[66] Cal M.P., Rood M.J., Larson S.M., ”Gas phase adsorption of volatile organic compounds and water vapor on activated carbon cloth”, Energy and Fuels, 11, pp 311-315, 1997.

[67] Hager J.,Wimmerstedt R., Whitaker S., “Steam drying a bed of porous spheres: Theory and experiment”, Chemical Engineering Science, 55, pp 1675-1698, 2000.

[68] Carman P.C., ”Flow of Gases through Porous Media”, Butterworths Scientific Publications, London, UK, 1956.

[69]Valdes-Prada F.J.,Goyeau B., Ochoa-Tapia A.J.,“Diffusive mass transfer between a microporous medium and an homogeneous fluid: Jump boundary conditions”, Chemical Engineering Science,61, pp 1692-1704, 2005.

[70] Altevgot A.S., Rolston D.E., Whitaker S.” New equations for binary gas transport in porous media,Part 1: equation development”, Advances in Water Resources, 26, pp 695-715, 2003.

[71] Quintard M., Bletzacker L.,Chenu D.,Whitaker S., “Nonlinear, multicomponent, mass transport in porous media” Chemical Engineering Science, 61, pp 2643-2669, 2006.

[72] Zarate E.M., Valdes-Prada F.J.,Goyeau B., Ochoa-Tapia A.J., “Diffusion and reaction in three-phase systems: Average transport equations and jump boundary conditions” Chemical Engineering Journal, 138, pp 307-332, 2008.

[73] Kuwahara F., Shirota M., Nakayama A.,“A numerical study of interfacial convective heat transfer coefficient in two-energy equation model for convection in

porous media" International Journal of Heat and Mass Transfer, 44, pp 1153-1159, 2000.

[74] Yang C., Kuwahara F., Liu W., Nakayama A.,"Thermal Non-Equilibrium Forced Convective Flow in an Annulus Filled with a Porous Medium", The Open Tranpsort Phenomena Journal, 3, pp 31-39, 2001.

[75] Nield A.D., Bejan A., "Convection in Porous Media" 4th Edition, Springer, New York, USA, 2013.

[76] Vafai K.,"Handbook of Porous Media", 2nd Edition, CRC Press, Boca Ralton, USA, 2005.

[77] Ni J., Beckerman C.,"Volume-Averaged Two-Phase Model for transport Phenomena during Solidification" Metallurgical Transactions, 22B, pp 349-361, 1991.

[78] Taylor, R., Krishna, R.,. "Multicomponent Mass Transfer" John Wiley and Sons, Inc., New York,USA, 1993.

[79] Chua H.T., Ng K.C., Wang W., Yap C., Wang X.L., "Transient modeling of a two bed silica gel-water adsorption chiller", International Journal of Heat and Mass Transfer,47, pp 659-669, 2004.

[80] Wang D., Zhang J., Tian X., Liu D., Sumathy K., "Progress in silica gel–water adsorption refrigeration technology" , Renewable and Sustainable Energy Reviews, 30, pp 85-104, 2014.

[81] Wang D., Zhang J.,Yang Q., Li N., Sumathy K., "Study of adsorption characteristics in silica gel-water adsorption refrigeration", Applied Energy, 113, pp 734-741, 2014.

[82] Zheng X., Wang L.W., Wang R.Z., Ge T.S., Ishugah T.F., " Thermal conductivity, pore structure and adsorption performance of compact composite silica gel", International Journal of Heat and Mass Transfer, 68, pp 435-443, 2014.

[83] Li T.X., Wang R.Z., Li H., "Progress in the development of solid-gas sorption refrigeration thermodynamic cycle driven by low grade thermal energy", Progress in Energy and Combustion Science, 40, pp 1-58, 2014.

[84] Youssef G.Y., Mahmoud S.M., AL-Dadah R.K.," Performance analysis of four bed adsorption water desalination/refrigeration system, comparsion of AQSOA-Z02 to silica-gel", Desalination, 375,pp 100-107, 2015.

[85] Mitra S., Kumar P., Srinivasan K., Dutta P., “Performance evaluation of a two stage silica gel+ water adsorption based cooling-cum-desalination system”, International Journal of Refrigeration, 58,pp 186-198, 2015.

[86] Sah R.P., Choudhury B., Das R.K., “A review on adsorption cooling systems with silica gel and carbon as adsorbents”, Renewable and Sustainable Energy Reviews, 45, pp 123-134, 2015.

[87] Goyal P.,Baredar P., Mittal A.,Siddiqui A.R., “Adsorption refrigeration technology- An overview of theory and its solar energy applications”, Renewable and Sustainable Energy Reviews, 53, pp 1389-1410, 2016.

[88] Sapienza A.,Glaznev I.S., Santamaria S.,Freni A.,Aristov Y.I.,” Adsorption chilling driven by low temperature heat: New adsorbent and cycle optimization”, Applied Thermal Engineering, 32, pp 141-146, 2012.

[89] Vasta S., Freni A., Sapienza A., Costa F., Restuccia G., “Development and lab-test of a mobile adsorption air-conditioner” , International Journal of Refrigeration, 35,pp 701-708, 2011.

[90] Chakraborty A., Saha B.B., Aristov Y.I., “Dynamic behaviors of adsorption chiller: Effects of the silica gel grain size and layers”, Energy, 78, pp 304-312, 2014.

[91] Brites G.J.V.N., Costa J.J., Costa V.A.F., “Influence of the design parameters on the overall performance of a solar adsorption refrigerator”, Renewable Energy, 86, pp 238-250, 2016.

[92] Hadj Ammar M.A., Benhaoua B., Balghouthi M., “Simulation of tubular adorber for adsorption refrigeration system powered by solar energy in sub-Sahara region of Algeria”, Energy Conversion and Management, 106, pp 31-40, 2015.

[93] Ji X., Song X., Li M., Liu J., Wang Y., “Performance investigation of a solar hot water driven adsorption ice-making system”, Energy Conversion and Management, 106, pp 753-765, 2015.

[94] Ariful kabir K.M., Amanul Alam K.C., Sarker M.M.A. Rouf R.A., Saha B.B., “Effect of mass recovery on the performance of solar adsorption cooling system”, Energy Procedia 79, pp 67-72, 2015.

[95] Qasem N.A.A., El-Shaarawi “Thermal analysis and modeling study of an activated carbon solar adsorption icemaker:Dhahran case study”, Energy Conversion and Management, 100, pp 310-323, 2015.

[96] El Fadar A., “Thermal behavior and performance assesment of a solar adsorption cooling system with finned adsorber”, Energy, 83, pp 674-684, 2015.

[97] Allouhi A., Kousksou T., Jamil A., El Rhafiki T., Mourad Y., Zeraouli Y., "Optimal working pairs for solar adsorption cooling applications", Energy, 79, 235-247, 2015.

[98] Habib K.,Saha B.B., Koyama S., "Study of various adsorbent-refrigerant pairs for application of solar driven adsorption cooling in tropical climates",Applied Thermal Engineering, 72, pp 266-274, 2014.

[99] Song X., Ji X., Li M., Wang Q.,Dai Y., Liu J.,"Effect of desorption parameters on performance of solar water bath solid adsorption ice-making system", Applied Thermal Engineering, 89, pp 316-322, 2015.

[100] Islam M.P., Morimoto T., "A new zero energy cool chamber with a solar-driven adorption refrigerator", Renewable Energy, 72, pp 367-376, 2014.

[101] Fernandes M.S., Brites G.J.V.N., Costa J.J., Costa V.A.F., "Review and future trends of solar adsorption refrigeration systems", Renewable and Sustainable Energy Reviews, 39, pp 102-123, 2014.

[102] Chekirou W., Chikouche A., Boukreit N., Karaali A., Phalippou S., " Dynamic modelling and simulation of the tubular adsorber of a solid adsorption machine powered by solar energy" International Journal of Refrigeration, 39, pp 137-151, 2014.

[103] Santori G., Santamaria S., Sapienza A., Brandani S., Freni A., "A stand-alone solar adsorption refrigerator for humanitarian aid", Solar Energy, 100, pp 172-178, 2014.

[104] Abu-Hamdeh N.H., Alnefaie K.A., Almitani K.H., "Design and performance characteristics of solar adsorption refrigeration system using parabolica trough collector: Experimental and statistical optimization technique", Energy Conversion and Management, 74 pp 162-170, 2013.

[105] Li C., Wang R.Z.,Wang L.W., Li T.X., Chen Y.,"Experimental study on an adsorption icemaker driven by parabolica trough solar collector", Renewable Energy, 57, pp 223-233, 2013.

[106] Dassler I., Mittelbach W.,"Solar cooling with adsorption chillers" , Energy Procedia,30, pp 921-929, 2012.

[107] Zhang G., Wang D.C., Zhang J.P., Han Y.P., Sun W., "Simulation of operating characteristics of the silica gel water adsorption chiller powered by solar energy", Solar Energy,85, pp 1469-1478, 2011.

[108] Hassan H.Z., Mohamad A.A., Bennacer R.,"Simulation of an adsorption solar cooling system", Energy, 36, pp 530-537, 2011.

[109] Choudhury B., Chatterjee P.K., Sarkar J.P., "Review paper on solar-powered air-conditioning through adsorption route", Renewable and Sustainable Energy Reviews, 14, pp 2189-2195, 2010.

[110] Chang W.S., Wang C.C., Shieh C.C., "Design and performance of a solar-powered heating and cooling system using silica gel/water adsorption chiller", Applied Thermal Engineering, 29, pp 2100-2105, 2009.

[111] Henninger S.K.,Munz G.,Ratzsch K.F.,Schossig P., "Cycle stability of sorption materials and composites for the use in heat pumps and cooling machines", Renewable Energy, 36, 2011,3043–3049.

[112] Fan Y., Luo L., Souyri B., "Review of solar sorption refrigeration technologies: Development and applications", Renewable and sustainable Energy Reviews, 11, pp 1758-1775, 2007.

[113] Tchernev D.I., Emerson D.T., "High-efficiency regenerative zeolite heat pump."ASHRAE Trans, 14 , pp 2024-2032, 1988.

[114] de Boer R., Smeding S.F., "Thermally operated mobile air conditioning systems; development and test of a laboratory prototype", International Sorption Heat Pump Conference, September 23-26, Seoul, South Korea, 2008.

[115] Saha B.B., El-Sharkawy I.I., Chakraborty A., Koyama S.," Study on an activated carbon fiber–ethanol adsorption chiller. Part II. Performance evaluation." International Journal of Refrigeration, 30, pp 96–102, 2007.

[116] Chen S.G., Yang R.T., "Theoretical basis for the potential theory adsorption isotherms. The Dubinin-radushkevic and dubinin-ashtakov equations", Langmuir, 10, pp 4244-4249, 1994.

[117] Alghoul M.A., Sulaiman M.Y., Azmi B.Z., Wahab M.A., "Advances on multipurpose solar adsorption systems for domestic refrigeration and water heating", Applied Thermal Engineering, 27, pp 813-822, 2007.

[118] Sapienza A., Frazzica A., Freni A., Aristov Y., "Dramatic effect of residual gas on dynamics of isobaric adsorption stage of an adsorptive chiller", Applied Thermal Engineering, 96, pp 385-390, 2016.

[119] Critoph R.E., Vogel R., "Possible adsorption pairs for use in solar cooling" International Journal of Ambient Energy, 7, pp 183–90, 1986.

[120] Hajji A., Worek W.M., Lavan Z., "Dynamic analysis of a closed cycle solar adsorption refrigerator using two adsorbent–adsorbate pairs", ASME Journal of Solar Energy Engineering, 113,pp 73–9, 1991.

[121] Wang D.C.,Li Y.H.,Li D.,Xia Y.Z., Zhang J.P.,"A review on adsorption refrigeration technology and adsorption deterioration in physical adsorption systems", Renewable and Sustainable Energy Reviews, 14, pp 344–53, 2010.

[122] San J.Y.,Hsu H.C., "Performance of a multi-bed adsorption heat pump using SWS-1L composite adsorbent and water as the working pair", Applied Thermal Engineering, 29, pp 1606-13, 2009.

[123] Saha B.B.,Chakraborty A.,Koyama S.,Aristov Y.I., "A new generation cooling device employing CaCl2-in-silica gel-water system" International Journal of Heat and Mass Transfer, ,52, pp 516–524, 2009.

[124] Zhu D.,Wang S.," Experimental investigation of contact resistance in adsorber of solar adsorption refrigeration", Solar Energy, 73 , pp 177–185, 2002.

[125] Yong L., Wang R.Z.," Adsorption refrigeration: a survey of novel technologies", Recent Patents on Engineering, 1, pp 1-21 ,2007.

[126] Schnabel L., Tatlier M., Schmidt F., Erdem-Senatalar A., "Adsorption kinetics of zeolite coatings directly crystallized on metal supports for heat pump applications" Applied Thermal Engineering, 30, pp 1409-1416, 2010

[127] Freni A., Santamaria S., Calabrese L., Frazzia A., Sapienza A., Bonaccorsi L., Proverbio E., Restuccia G.," Experimental testing of a coated adsorber", HPC12 Conference , 2012.

[128] Freni A., "Adsorption heat pumps, research activity at CNR ITAE", IEA Workshop, Rome, 2009.

[129] Waszkiewicz S.D., M.J. Tierney, H. Saidini Scott, Development of coated, annular fins for adsorption chillers, Applied Thermal Engineering, 29, pp 2222-2227, 2009.

[130] Freni A.,Russo F.,Vasta S.,Tokarev M., Aristov Y.,Restuccia G., "An advanced solid sorption chiller using SWS-1L ", Applied Thermal Engineering;27 pp 2200–4, 2007.

[131] Rezk A. Al-Dadah R.K., Mahmoud S., Elsayed A., "Effect of contact resistance and metal additives in finned tube adsorbent beds on the performance of silica gel/water adsorption chiller", Applied Thermal Engineering, 53, pp 278-284, 2013.

[132] Rezk A., “Theoretical and experimental investigation of silica gel/water adsorption refrigeration systems”, PhD Thesis, University of Birmingham, UK, 2012.

[133] Freni A., Maggio G., Cipiti F., Aristov Y., “Simulation of water sorption dynamics in adsorption chillers: One, two and four layers of loose silica grains”, Applied Thermal Engineering, 44, pp 69-77, 2012.

[134] Wang X.L.,Chua H.T.,Ng K.C., “Experimental investigation of silica gel–water adsorption chillers with and without a passive heat recovery scheme”, International Journal of Refrigeration, 28, pp 756–65, 2005.

[135] Akahira A., Alam K.C.A., Hamamoto Y., Akisawa A., Kashiwagi T.,” Experimental investigation of mass recovery adsorption refrigeration cycle”, International Journal of Refrigeration, 28 ,pp 565-572, 2005

[136] Akahira A., Alam K.C.A., Hamamoto Y., Akisawa A., Kashiwagi T., “Mass recovery adsorption refrigeration cycle—improving cooling capacity”, International Journal of Refrigeration, 27, pp 225-234, 2004.

[137] EIA U.S Energy Information Administration Statistics, www.eia.gov, -Last Visited-10.01.2016.

[138] Lior N., “Sustainable energy development with some game changers”, Energy, 40, pp 3–18. 2012.

[139] Mesut A., Murat E., Amir R., Shihab A., “Model predictive HVAC load control in buildings using real-time electricity pricing”, Energy and Buildings, 60, pp 199–209, 2013.

[140] Gupta Y., Metchop L., Frantzis A., Phelan P.E., “Comperative analysis of thermally activated environmentally friendly cooling systems”, Energy Conversion and Management, 49, pp 1091-1097, 2008.

[141] Tatlıer M., Tantekin-Ersolmaz B., Erdem-Senatalar A.,” A novel approach to enhance heat and mass transfer in adsorption heat pumps using the zeolite– water pair”, Microporous Mesoporous Materials, 27, pp 1–10, 1999.

[142] Mhiri F., El Golli S., “Etude d’un réfrigérateur solaire à adsorption solide avec le couple charbon actif-méthanol”, Revue Génerale de Thermique, 35, pp 269–77, 1996.

[143] Tchernev D.I., “Solar energy application of natural zeolites. Naturalzeolites: occurrence, properties and use” Pergamon Press, pp 479–85, 1978.

[144] Grenier Ph.,Guilleminot J.J., Meunier F., Pons M., “Solar powered solid adsorption cold store”, Journal of Solar Energy Engineering 110, pp 192-7, 1988.

[145] Wang R.Z.,Li M., Xu Y.X., Wu J.Y., “An energy efficient hybrid system of solar powered water heater and adsorption ice maker”, Solar Energy, 68 , pp 189–95, 2000.

[146] Passos E.F., Escobedo J.F., Meunier F., “Simulation of an intermittent adsorptive solar cooling system.” Solar Energy, 42, pp 103–11, 1989.

[147] Zhang L.Z., Wang L., “Effects of coupled heat and mass transfers in adsorbent on the performance of a waste heat adsorption cooling unit”, Applied Thermal Engineering, 19, pp 195–215, 1999.

[148] Jemni A., Nasrallah S.B., “Study of two-dimensional heat and mass transfer during absorption in a metal-hydrogen reactor” ,International Journal of Hydrogen Energy, 20, pp 43-52, 1995.

[149] Chahbani M. H., Labidi J., Paris J.,” Effect of mass transfer kinetics on the performance of adsorptive heat pump system”, Applied Thermal Engineering, 22 , pp 23-40, 2002.

[150] Pons M, Szarzynski S. “Accounting for the real properties of the heat transfer fluid in heat -regenerative adsorption cycles for refrigeration”, International Journal of Refrigeration, 23, pp 284-91, 2000.

[151] Comsol Multiphysics User’s Guide, Version 5.1, COMSOL AB., 2015.

[152] Gong L., Wang Y., Cheng X., Zhang R., Zhang H., “A novel effective medium theory for modelling thermal conductivity of porous materials” , International Journal of Heat and Mass Transfer, 68, pp 295-298, 2014.

[153] Sapienza A., Frazzica A., Freni A., Aristov Y., “Dramatic effect of residual gas on dynamics of isobaric adsorption stage of an adsorptive chiller”, Applied Thermal Engineering, 96, pp 385-390, 2016.

[154] Kakaç S., Yener Y.,”Convective Heat Transfer”,CRC Press, Second Edition, 1994, Florida, USA.

[155] Anderson J.D., “Computational Fluid Dynamics: The basics with applications” McGraw-Hill, 1995, Maryland, USA

[156] Schlichting H., “Boundary-Layer Theory” Translated by Dr. L. Kestin, 7th Edition, McGraw-Hill, 1979.

[157] Akın S.," Lecture notes on: Fluid Flow in Porous Media", Petroleum and Natural Gas Engineering Department, Middle East Technical University, Ankara, Turkey, 2011.

[158] Aris, R.," Vectors, Tensors, and the Basic Equations of Fluid Mechanics" Prentice Hall Inc., Englewood Cliffs, New Jersey, USA 1962.

[159] Carbonell R.G., Whitaker S., "Adsorption and reaction on a catalytic surface: the quasi steady condition", Chemical Engineering Science , 39, pp 1319-1321, 1984.

[160] Wang R.Z., Xia Z.Z., Wang L.W., Lu Z.S., Li S.L., Li T.X., Wu J.Y., He S., "Heat transfer design in adsorption refrigeration systems for efficient use of low-grade thermal energy", Energy, 36, pp 5425-5439, 2011.

[161] www.nist.gov, National Institute of Standards and Technology, NIST Standard Reference Databases- Last Visited, 11.2015.

[162] F.P. Incropera, D.P. DeWitt, T.L. Bergman, A.S. Lavine, "Fundamentals of Heat and Mass Transfer", John Wiley and Sons Inc., Indiana, USA, 2007.

[163] Reid R.C., Sherwood T.K." Properties of Gases and Liquids", McGraw Hill Book Company,New York, USA, 1958.

[164] Ng K.C., Chua H.T., Chung C.Y.," Loke C.H., Kashiwagi T., Akisawa A., Saha B.B.," Experimental investigation of the silica gel-water adsorption isotherm characteristics", Applied Thermal Engineering, 21, pp 1631-1642, 2001.

APPENDIX A

BASIC CONCEPTS AND RELATIONS IN VOLUME AVERAGING METHOD

Porous structures, interface boundaries between different phases could be unique, extremely irregular and complex. This geometric complexity together with required excessive effort in mathematical formulation will impose an extreme difficulty in solution of the governing equations within the microscale. Additionally the microscale equations systems and numerical models could not be solved by using the today available computational methods and facilities. Therefore of instead of directly modeling microstructures, the governing equations and properties belonging to porous media, these equations and properties should be described conveniently at macroscopic level. Regarding the concerns of transition from micro to macro scale it could be said that the pore sizes and the microstructures within the porous media is still larger than the continuum microscale and for this reason continuum approach is valid for micro and macro scale. Consequently it could be noted that governing equations and phase properties for the macroscopic level could be derived by using microscopic level properties and equations with an appropriate approach [56].

As a general method, the governing equations for the microstructures in porous media are averaged over a finite volume for obtaining the governing equations for macro scale. The governing equations within the microstructures are named as microscopic equations while the macro scale governing equations are called as macroscopic equations [56].

As mentioned above the transition from microscopic equations to macroscopic ones are based on the averaging process. There are various volume averaging approaches exist in the literature such as; time, representative elementary volume, mass-weighted volume and time-space double averaging [57]. Since, Representative Elementary Volume (REV) yields more consistent description for the governing equations and multiphase properties, this approach will be used in the scope of this work. REV is defined as the element of a continuum which consists of range of volumes where any quantity and variable could have a single value at definite time and location [58]. Moreover REV need to be large enough to contain enough number of particles and pore space on which averaging procedure can be applied. On the other hand REV should be small enough compared to the overall dimensions of the medium. [55] A simple sketch of a REV taken from a porous medium can be seen in Figure 2.2.

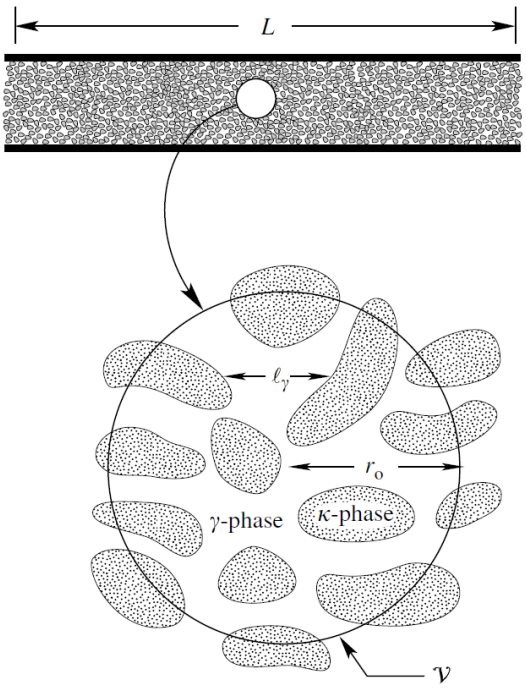

Figure 2.1 Sketch demonstrating the representative elementary volume (REV) taken from porous medium [76]

There are two different type of average values exists in the REV averaging method, which are intrinsic phase average and the superficial average. The superficial average is also called as phase average. The intrinsic phase average is also known as individual phase volume average. The main difference between these two average values is the volume on which the average values are calculated. In the phase average (superficial average) the average is calculated by dividing the integrated value by REV. The intrinsic phase average is calculated by division of the integrated value with the volume occupied by the discrete phase. The phase average of an arbitrary variable could be written as;

$$\langle \psi_\beta \rangle_R = \frac{1}{V_R} \int_{V_R} \psi_\beta dV \qquad (A.1)$$

In Equation (A.1) ψ_β is an arbitrary scalar quantity ψ belongs to phase β and has a distribution. The value of property or scalar quantitiy ψ is zero for the other phases. $\langle \psi_\beta \rangle_R$ is the phase (superficial) average of the arbitrary quantity ψ_β over the REV
V_R is the volume of the REV

Additionally phase average of ψ could be rewritten as follows;

$$\langle \psi_\beta \rangle_R = \frac{1}{V_R} \int_{V_R} \psi_\beta dV = \frac{1}{V_R} \int_{V_\beta} \psi_\beta dV \qquad (A.2)$$

Similarly the arbitrary scalar quantity ψ belonging to phase β can also be averaged over the volume of β phase only. This average is called as intrinsic phase average and can be expressed as;

$$\langle \psi_\beta \rangle_\beta = \frac{1}{V_\beta} \int_{V_\beta} \psi_\beta dV \qquad (A.3)$$

In equation A.3 $\langle\psi_\beta\rangle_\beta$ is the intrinsic phase average of arbitrary quantity ψ_β V_β is the fraction of REV occupied by the β phase.

When Equation A.1 A.2 and A.3 are considered together, it is possible to obtain a relation between phase average and intrinsic phase average expressions. For instance, dividing Equation A.3 with the second term on right hand side of Equation A.2, the result will be;

$$\frac{\langle\psi_\beta\rangle_R}{\langle\psi_\beta\rangle_\beta} = \frac{V_\beta}{V_R} \qquad (A.4)$$

$$\varepsilon_\beta = \frac{V_\beta}{V} \qquad (A.5)$$

The volume fraction of β phase is denoted by ε_β . The intrinsic phase average of quantity ψ then can be written in terms of phase average and the volume fraction of β phase as follows;

$$\langle\psi_\beta\rangle_R = \varepsilon_\beta\langle\psi_\beta\rangle_\beta \qquad (A.6)$$

Another important concept in the averaging theorem is the deviation from the averaged values. The deviation of scalar quantity ψ in β phase can be defined as;

$$\psi_\beta = \langle\psi_\beta\rangle_\beta + \hat{\psi}_\beta \qquad (A.7)$$

In Equation A.7 $\hat{\psi}_\beta$ represents the deviation of quantity ψ. The deviation from the average value also has a spatial distribution over the β phase. When Equation A.7 is averaged over phase β and the REV, the result will be;

$$\langle\psi_\beta\rangle_\beta = \langle\langle\psi_\beta\rangle_\beta\rangle_\beta + \langle\hat{\psi}_\beta\rangle_\beta \qquad (A.8)$$

$$\langle \psi_\beta \rangle_R = \langle \langle \psi_\beta \rangle_\beta \rangle_R + \langle \hat{\psi}_\beta \rangle_R \qquad (A.9)$$

As stated in [5] the average of averaged values will be equal to;

$$\langle \langle \psi_\beta \rangle_\beta \rangle_\beta = \langle \psi_\beta \rangle_\beta \qquad (A.10)$$

$$\langle \langle \psi_\beta \rangle_\beta \rangle_R = \langle \psi_\beta \rangle_R \qquad (A.11)$$

When Equation A.8, A.9, A.10 and A.11 considered together, the averaged values of the deviations will be equal to zero,

$$\langle \hat{\psi}_\beta \rangle_\beta = \langle \hat{\psi}_\beta \rangle_R = 0 \qquad (A.12)$$

Additionally, there are a few useful rules exist for the volume averaging procedure. For instance the product of two arbitrary quantities can be averaged as follows;

$$\psi_\beta \varphi_\beta = \left(\langle \psi_\beta \rangle_\beta + \hat{\psi}_\beta\right)\left(\langle \varphi_\beta \rangle_\beta + \hat{\varphi}_\beta\right) \qquad (A.13)$$

Equation A.13 could also be expressed as;

$$\psi_\beta \varphi_\beta = \langle \psi_\beta \rangle_\beta \langle \varphi_\beta \rangle_\beta + \langle \psi_\beta \rangle_\beta \hat{\varphi}_\beta + \langle \varphi_\beta \rangle_\beta \hat{\psi}_\beta + \hat{\psi}_\beta \hat{\varphi}_\beta \qquad (A.14)$$

After Equation A.14 is averaged over volume of phase β the result will be;

$$\langle \psi_\beta \varphi_\beta \rangle_\beta = \langle \langle \psi_\beta \rangle_\beta \langle \varphi_\beta \rangle_\beta \rangle_\beta + \langle \langle \psi_\beta \rangle_\beta \hat{\varphi}_\beta \rangle_\beta + \langle \langle \varphi_\beta \rangle_\beta \hat{\psi}_\beta \rangle_\beta + \langle \hat{\psi}_\beta \hat{\varphi}_\beta \rangle_\beta \qquad (A.15)$$

Since the intrinsic phase averaged values has a uniform distribution over phase β, Equation A.15 could be rewritten as;

$$\langle\psi_\beta\varphi_\beta\rangle_\beta = \langle\langle\psi_\beta\rangle_\beta\langle\langle\varphi_\beta\rangle_\beta\rangle_\beta + \langle\langle\psi_\beta\rangle_\beta\langle\hat{\varphi}_\beta\rangle_\beta + \langle\langle\varphi_\beta\rangle_\beta\rangle_\beta\langle\hat{\psi}_\beta\rangle_\beta + \langle\hat{\psi}_\beta\hat{\varphi}_\beta\rangle_\beta \quad (A.16)$$

When rules given in Equation A.10 and A.12 are applied Equation A.16 can be simplified to;

$$\langle\psi_\beta\varphi_\beta\rangle_\beta = \langle\psi_\beta\rangle_\beta\langle\varphi_\beta\rangle_\beta + \langle\hat{\psi}_\beta\hat{\varphi}_\beta\rangle_\beta \quad (A.17)$$

In Equation A.6, φ is another arbitrary scalar quantity similar to the quantity ψ and has a spatial distribution over phase β. $\langle\psi_\beta\varphi_\beta\rangle_\beta$ is the intrinsic phase average of product of these two arbitrary quantities over phase β. Equation A.17 and Equation A.6 can be combined to obtain the expression for phase average of the product of quantities ψ and φ in terms of intrinsic phase averages and deviations.

$$\langle\psi_\beta\varphi_\beta\rangle_R = \varepsilon_\beta\langle\psi_\beta\rangle_\beta\langle\varphi_\beta\rangle_\beta + \varepsilon_\beta\langle\hat{\psi}_\beta\hat{\varphi}_\beta\rangle_\beta \quad (A.18)$$

$$\langle\psi_\beta\varphi_\beta\rangle_R = \varepsilon_\beta\langle\psi_\beta\rangle_\beta\langle\varphi_\beta\rangle_\beta + \langle\hat{\psi}_\beta\hat{\varphi}_\beta\rangle_R \quad (A.19)$$

$$\langle\psi_\beta\varphi_\beta\gamma_\beta\rangle_R = \varepsilon_\beta\langle\psi_\beta\rangle_\beta\langle\varphi_\beta\rangle_\beta\langle\gamma_\beta\rangle_\beta + \langle\psi_\beta\rangle_\beta\langle\hat{\varphi}_\beta\hat{\gamma}_\beta\rangle_R + \langle\varphi_\beta\rangle_\beta\langle\hat{\psi}_\beta\hat{\gamma}_\beta\rangle_R + \langle\gamma_\beta\rangle_\beta\langle\hat{\psi}_\beta\hat{\varphi}_\beta\rangle_R + \langle\hat{\psi}_\beta\hat{\varphi}_\beta\widehat{\gamma_\beta}\rangle_R \quad (A.20)$$

In addition to the multiplication operation also, time derivative gradients and the divergence of any quantity of property within a phase could be averaged by using the REV averaging procedures. The time derivative of a property could be averaged and its phase average could be expressed as [56];

$$\langle\frac{\partial\psi_\beta}{\partial t}\rangle_R = \frac{\partial\langle\psi_\beta\rangle_R}{\partial t} - \frac{1}{V_R}\int_{A_\beta}\psi_\beta\,\mathbf{v}_{\mathbf{A_\beta}}\cdot\mathbf{n}_{\boldsymbol{\beta}}dA \quad (A.21)$$

In Equation A.21 A_β indicates the surface area of phase β. The term $\mathbf{v_{A_\beta}}$ is the velocity vector which belongs to the surface of phase β. The surface of β phase is assumed to be moving with this velocity. $\mathbf{n_\beta}$ unit normal vector of β phase surface which encloses the volume occupied by the same phase.

Similar to the time average, the gradient of a property could also be averaged. The expression for the phase average of gradient of quantity ψ over phase β could be written as follows;

$$\langle \nabla \psi_\beta \rangle_R = \langle \psi_\beta \rangle_R + \frac{1}{V_R} \int_{A_\beta} \hat{\psi}_\beta \cdot \mathbf{n_\beta} dA \qquad (A.22)$$

In Equation A.22 is $\langle \nabla \psi_\beta \rangle_R$ the phase average of the gradient of quantity ψ belonging to phase β.

In addition to the volume averaging rules also, surface area average of the quantities will be used while deriving the governing equations. For this purpose, the interface surface averaged quantity ψ of phase β averaged over the interface surface between phase β and α can be expressed as follows;

$$\langle \psi_\beta \rangle_{\beta\alpha} = \frac{1}{A_{\beta\alpha}} \int_{A_{\beta\alpha}} \psi_\beta dA \qquad (A.23)$$

In Equation A.23 $\langle \psi_\beta \rangle_{\beta\alpha}$ is the interface surface average value of quantitiy ψ of phase β. $A_{\beta\alpha}$ is the total interface area between phase β and α.

APPENDIX B

CALCULATION OF THERMOPHYSICAL PROPERTIES OF BINARY MIXTURES

In addition to the rules regarding the volume averaging method, some preliminaries related with mixtures and mass transport will be given in this part. In some of the models both adsorbate vapor and air exist at the same time in the gas phase and in such cases, the gas phase will be treated as a mixture of two discrete species. The laws and concepts related to the binary mixture (constituent of two species) will be discussed.

The major quantities related with the mixture are the mass density and molar concentration and mole fraction. The molar concentration of a species i, could be defined as [162];

$$C_i = \frac{n_i}{V} \qquad (B.1)$$

Here is the n_i number of moles and V is the total volume occupied by the mixture composed of species. The unit for the molar concentration is (kmol/m^3). Another important property is the mass density of species. Mass density ρ_i of species i can be expressed as;

$$\rho_i = M_i C_i \qquad (B.2)$$

In Equation B.2 M_i is the molecular weight of the species i, C_i and is the molar concentration of same species in the mixture.

Molar density (total moles per unit volume), and the mass density of a mixture can be expressed in terms of molar concentration of species and mass densities of species.

$$C = \sum_i C_i \qquad (B.3)$$

$$\rho = \sum_i \rho_i \qquad (B.4)$$

In Equation B.3, C is the total mole per unit volume. Similarly in Equation B.4 ρ is the mass density of the mixture. Two other quantities related with the molar and mass concentration are, mass fraction and mole fraction of species. The mass fraction and mole fraction of species i can be expressed as;

$$\omega_i = \frac{\rho_i}{\rho} \qquad (B.5)$$

$$x_i = \frac{C_i}{C} \qquad (B.6)$$

Mass fraction of species i is denoted with ω_i and similarly mole fraction of species i is denoted as x_i. Sum of both mass and mole fractions of species in a mixture should be equal to 1.

$$\sum_i \omega_i = 1 \qquad (B.7)$$

$$\sum_i x_i = 1 \qquad (B.8)$$

In an ideal gas mixture, both mass density and mole density of species could be expressed in terms of partial pressure and ideal gas law. The mass density and mole density expressions for species i can be written as;

$$\rho_i = \frac{p_i}{R_i T} \qquad (B.9)$$

$$C_i = \frac{p_i}{RT} \qquad (B.10)$$

In Equation B.9 and B.10 p_i is the partial pressure of species i and T is the temperature in Kelvin. In Equation B.9 R_i is the gas constant for species i while R in Equation B.10 is the universal gas constant.

Similar to the molar concentration and mass density, pressure of the mixture is also sum of the partial pressure values of species.

$$p = \sum_i p_i \qquad (B.11)$$

Additionally by combining Equation B.6 and Equation B.10 it is possible to obtain;

$$x_i = \frac{C_i}{C} = \frac{p_i}{p} \qquad (B.12)$$

Also by using the ideal gas relation one can express the volume occupied by species is as;

$$V_i = \frac{n_i RT}{p} \qquad (B.13)$$

Similarly the total volume occupied by the mixture can be expressed as:

$$V = \frac{nRT}{p} \qquad (B.14)$$

When Equation B.13 is divided with Equation B.14 side by side, the relation between volume fraction of species i and the mole fraction could be obtained.

$$\frac{V_i}{V} = \frac{n_i}{n} = x_i \qquad (B.15)$$

Also it is possible to obtain a relation between mass fraction and mole fraction by using the ideal gas relation in Equation B.9. Since gas constant for any substance is equal to the universal gas constant divided by molecular weight as given below,

$$R_i = \frac{R}{M_i} \qquad (B.16)$$

Then the mixture density could be expressed by suing ideal gas relation and molecular weight of mixture *M* as,

$$\rho = \frac{pM}{RT} \qquad (B.17)$$

Division of Equation B.9 with Equation B.17 would yield,

$$\frac{\rho_i}{\rho} = \frac{M_i}{M}\frac{p_i}{p} \qquad (B.18)$$

With the help of Equation B.5 and Equation B.12 it is possible to rewrite Equation B.18 to express the relation between mass fraction and mole fraction.

$$\omega_i = \frac{M_i}{M} x_i \qquad (B.19)$$

Consequently it could be seen that volume fraction of species i is equal to its mole fraction. The main point of interest for this study will be binary mixture of f vapor and air, which are assumed to be ideal gases. From this point the subscript *v* will denote the properties and quantities belonging the vapor component, whereas quantities and properties with subscript *a* are belonging to air component in the mixture. Likewise the properties and quantities that belong to the mixture of air and vapor will be denoted with a subscript of *g* referring to the gas phase. Since the gas phase is a mixture of vapor and air the thermophysical properties of the mixture should be expressed in terms of components' properties. For this purpose the viscosity, thermal conductivity and specific heat capacity of the ideal gas mixture of air and vapor will be expressed based on the Chapman-Enskog theory as [62,63] ;

$$\mu = \sum_{i=1}^{N} \frac{x_i \mu_i}{\sum_{j=1}^{N} x_j \Phi_{ij}} \qquad (B.20)$$

Equation B.20 is a general expression of mixture viscosity of multicomponent gas mixtures. The Φ_{ij} is the interaction parameter which will be defined below. Specifically for this study the viscosity of the gas phase composed of air and vapor could be expressed as;

$$\mu_g = \frac{x_a \mu_a}{x_a \Phi_{aa}} + \frac{x_a \mu_a}{x_v \Phi_{av}} + \frac{x_v \mu_v}{x_a \Phi_{va}} + \frac{x_v \mu_v}{x_v \Phi_{vv}} \qquad (B.21)$$

Since the interaction parameter is defined as;

$$\Phi_{ij} = \frac{\left[1 + \left(\frac{\mu_i}{\mu_j}\right)^{\frac{1}{2}} \left(\frac{M_j}{M_i}\right)^{\frac{1}{4}}\right]^2}{\left[8\left(1 + \frac{M_i}{M_j}\right)\right]^{\frac{1}{2}}} \qquad (B.22)$$

$$\Phi_{ii} = \Phi_{jj} = 1 \qquad (B.23)$$

$$\Phi_{ij} = \frac{\mu_j}{\mu_i} \frac{M_i}{M_j} \Phi_{ji} \qquad (B.24)$$

By combining the Equation B.21, Equation B.22, Equation B.23 and Equation B.24 one could obtain,

$$\mu_g = \mu_a + \mu_v + \frac{1}{\Phi_{av}} \left[\frac{x_a \mu_a}{x_v} + \frac{x_v \mu_v}{x_a} \frac{\mu_a}{\mu_v} \frac{M_v}{M_a}\right] \qquad (B.25)$$

It is possible to rewrite Equation B.25 since the sum of mole fractions of air and vapor are equal to 1.

$$x_a = 1 - x_v \qquad (B.26)$$

$$\mu_g = \mu_a + \mu_v + \frac{1}{\Phi_{av}} \left[\frac{(1 - x_v)\mu_a}{x_v} + \frac{x_v \mu_a}{(1 - x_v)} \frac{M_v}{M_a}\right] \qquad (B.27)$$

Where,

$$\Phi_{av} = \frac{\left[1 + \left(\frac{\mu_a}{\mu_v}\right)^{\frac{1}{2}} \left(\frac{M_v}{M_a}\right)^{\frac{1}{4}}\right]^2}{\left[8\left(1 + \frac{M_a}{M_v}\right)\right]^{\frac{1}{2}}} \qquad (B.28)$$

Substituting the Equation B.28 into Equation B.27 the final form of the expression for mixture viscosity will be;

$$\mu_g = \mu_a + \mu_v + \frac{\left[8\left(1+\frac{M_a}{M_v}\right)\right]^{\frac{1}{2}}}{\left[1+\left(\frac{\mu_a}{\mu_v}\right)^{\frac{1}{2}}\left(\frac{M_v}{M_a}\right)^{\frac{1}{4}}\right]^2}\left[\frac{(1-x_v)\mu_a}{x_v}+\frac{x_v\mu_a}{(1-x_v)}\,\frac{M_v}{M_a}\right] \qquad (B.29)$$

In Equation B.29 the μ denotes the dynamic viscosity. Throughout this study the variation of viscosity will assumed to be independent of temperature. For this reason Equation B.29 is composed of constant values except the mole fraction of vapor and air. The mole fraction of air and vapor will have a distribution in space varying with time. Distribution of mole fraction and its variation with time will be determined by solving the conservation of mass equations for species.

In addition to the viscosity also it is possible to express the thermal conductivity value of the gas phase in terms of air and vapor viscosity [64]. The relation given in Equation B.18 can also be used for calculating the gas phase thermal conductivity. As a result the expression for the mixture thermal conductivity will be;

$$k_g = \frac{x_a k_a}{x_a \Phi_{aa}} + \frac{x_a k_a}{x_v \Phi_{av}} + \frac{x_v k_v}{x_a \Phi_{va}} + \frac{x_v k_v}{x_v \Phi_{vv}} \qquad (B.30)$$

Using the relations given in Equation B.22 and Equation B.23 it is possible to simplify Equation B.27 as;

$$k_g = k_a + k_v + \frac{1}{\Phi_{av}}\left[\frac{x_a k_a}{x_v} + \frac{x_v k_v}{x_a}\frac{\mu_a}{\mu_v}\,\frac{M_v}{M_a}\right] \qquad (B.31)$$

$$k_g = k_a + k_v + \frac{\left[8\left(1+\frac{M_a}{M_v}\right)\right]^{\frac{1}{2}}}{\left[1+\left(\frac{\mu_a}{\mu_v}\right)^{\frac{1}{2}}\left(\frac{M_v}{M_a}\right)^{\frac{1}{4}}\right]^2}\left[\frac{(1-x_v)k_a}{x_v}+\frac{x_v k_v}{(1-x_v)}\frac{\mu_a}{\mu_v}\frac{M_v}{M_a}\right] \qquad (B.32)$$

In addition to the dynamic viscosity and thermal conductivity another parameter that will be used in computations is the specific heat capacity value of the gas phase. Heat capacity of a mixture could also be expressed in terms of constituents'' specific heat capacities as [62];

$$c_{pg} = c_{pa}x_a\frac{M_a}{M_g} + c_{pv}x_v\frac{M_v}{M_g} \qquad (B.33)$$

The relation and rules that are going to be used in mathematical formulation and equation derivation are tried to be summarized. In the following sections derivation of governing equations will be presented with the help of given relations and rules.

APPENDIX C

DERIVATION OF GOVERNING EQUATIONS

C.1 Conservation Equations for the Heat Transfer Fluid (HTF)

C.1.1 Mass Conservation Equation for the HTF

As a common practice, the derivation of 3-D conservation equations on Cartesian coordinates will be demonstrated on an elemental control volume. The cubic elemental control volume with fixed size, shape and position in space can be seen in Figure C.1.

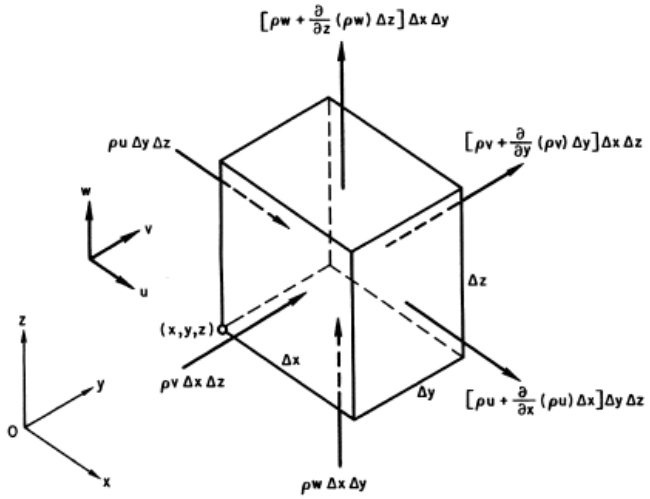

Figure C.1 The elemental control volume that will be used in derivation of mass conservation equation [154]

The flow through the control volume is assumed to be single phase with homogenous composition with x, y and z velocity components u, v and z respectively. The mass flux expressions are shown in Figure C.1 with the arrows and by using these expressions net rate of mass leaving the control volume in x, y and z direction can be expressed as;

$$Net\ \ rate\ of\ mass\ leaving\ C.V.\ in\ x\ direction$$
$$= -\left(-(\rho u)\Delta y\Delta z + \left[(\rho u) + \frac{\partial(\rho u)}{\partial x}\Delta x\right]\Delta y\Delta z\right) \qquad (C.1)$$

$$Net\ \ rate\ of\ mass\ leaving\ C.V.\ in\ y\ direction$$
$$= -\left(-(\rho v)\Delta x\Delta z + \left[(\rho v) + \frac{\partial(\rho v)}{\partial y}\Delta y\right]\Delta x\Delta z\right) \qquad (C.2)$$

$$Net\ \ rate\ of\ mass\ leaving\ C.V.\ in\ z\ direction$$
$$= -\left(-(\rho w)\Delta x\Delta y + \left[(\rho w) + \frac{\partial(\rho w)}{\partial z}\Delta z\right]\Delta x\Delta y\right) \qquad (C.3)$$

Also the rate of net mass increase within the volume can be expressed as;

$$Net\ \ rate\ of\ mass\ increase\ in\ C.V. = \frac{\partial\rho}{\partial t}\Delta x\Delta y\Delta z \qquad (C.4)$$

Since the mass is conserved for the elemental control volume, the net rate of mass entering the volume will be equal to the net rate of mass increase in the control volume. This equality could be written as;

$$\frac{\partial\rho}{\partial t}\Delta x\Delta y\Delta z = -\left[\frac{\partial(\rho u)}{\partial x} + \frac{\partial(\rho v)}{\partial y} + \frac{\partial(\rho w)}{\partial z}\right]\Delta x\Delta y\Delta z \qquad (C.5)$$

Rearranging the Equation C.5 it is possible to obtain continuity equation or the mass conservation equation in differential form, for the compressible and unsteady flows as;

$$\frac{\partial \rho}{\partial t} + \frac{\partial (\rho u)}{\partial x} + \frac{\partial (\rho v)}{\partial y} + \frac{\partial (\rho w)}{\partial z} = 0 \qquad (C.6)$$

Equation C.53 can also be written in more general form which applies to all coordinate systems as;

$$\frac{\partial \rho}{\partial t} + \boldsymbol{\nabla}(\rho \mathbf{V}) = 0 \qquad (C.7)$$

Since, the HTF fluid is liquid and assumed to be incompressible; the Equation C.53 can be rewritten as;

$$\rho_f \boldsymbol{\nabla}.\mathbf{V_f} = 0 \qquad (C.8)$$

The subscripts *f* refers to the quantities and properties belong to the HTF throughout the study.

C.1.2 Momentum Conservation Equation for the HTF

Similar to the mass conservation equation, the elemental differential volume will be used for the derivation of momentum conservation equation. The derivation will be made for 3-D Cartesian coordinates. The momentum conservation equation of a fluid particle is based on the Newton's second law of motion which can be written for a fluid particle with definite mass as;

$$\mathbf{F} = \frac{d\mathbf{M}}{dt} = \frac{d(m\mathbf{V})}{dt} = m\mathbf{a} \qquad (C.9)$$

In Equation C.9 the **M** denotes the momentum vector, and **a** denotes the acceleration vector.

Since the elemental fluid volume which is situated at x, y and z at time instant t, its position will be x+Δx, y+Δy and z+Δz at time t+Δt. According to this movement, the total change in velocity components of the fluid element can be expressed as;

$$\Delta u = \frac{\partial u}{\partial x}\Delta x + \frac{\partial u}{\partial y}\Delta y + \frac{\partial u}{\partial z}\Delta z + \frac{\partial u}{\partial t}\Delta t \qquad (C.10)$$

$$\Delta v = \frac{\partial v}{\partial x}\Delta x + \frac{\partial v}{\partial y}\Delta y + \frac{\partial v}{\partial z}\Delta z + \frac{\partial v}{\partial t}\Delta t \qquad (C.11)$$

$$\Delta w = \frac{\partial w}{\partial x}\Delta x + \frac{\partial w}{\partial y}\Delta y + \frac{\partial w}{\partial z}\Delta z + \frac{\partial w}{\partial t}\Delta t \qquad (C.12)$$

Dividing both sides of the Equations C.10, C.11 and C.12 with Δt as it approaches to 0, one will obtain expressions for the acceleration components for the fluid element as;

$$a_x = \lim_{\Delta t \to 0} \frac{\Delta u}{\Delta t} = u\frac{\partial u}{\partial x} + v\frac{\partial u}{\partial y} + w\frac{\partial u}{\partial z} + \frac{\partial u}{\partial t} \qquad (C.13)$$

$$a_y = \lim_{\Delta t \to 0} \frac{\Delta v}{\Delta t} = u\frac{\partial v}{\partial x} + v\frac{\partial v}{\partial y} + w\frac{\partial v}{\partial z} + \frac{\partial v}{\partial t} \qquad (C.14)$$

$$a_z = \lim_{\Delta t \to 0} \frac{\Delta v}{\Delta t} = u\frac{\partial w}{\partial x} + v\frac{\partial w}{\partial y} + w\frac{\partial w}{\partial z} + \frac{\partial w}{\partial t} \qquad (C.15)$$

The right hand side of the Equation C.13, C.14 and C.15 can be named as substantial derivative of velocity and can be expressed as;

$$a_x = \frac{Du}{Dt} \qquad (C.16)$$

$$a_y = \frac{Dv}{Dt} \qquad (C.17)$$

$$a_z = \frac{Dw}{Dt} \qquad (C.18)$$

In addition to the acceleration, other quantities that will be used in the momentum conservation equation will be the shear stresses, normal stresses and the body forces. The body forces can be assumed to be acting on the center of gravity of the fluid element located at x, y and z. The source of body forces could be gravitational, electrical or magnetic. The body force vector for the 3-D fluid element can be expressed as;

$$\mathbf{f} = f_x\mathbf{i} + f_y\mathbf{j} + f_z\mathbf{k} \qquad (C.19)$$

In Equation C.19 **i**, **j** and **k** are the unit normal vectors in x, y and z directions.

The other component of the force acting on the fluid element is the stresses. The normal and shear stresses on the surfaces of 3-D fluid element is similar to the a solid element and for this reason the stress tensor for the elemental fluid volume can be written as;

$$\boldsymbol{\pi} = \begin{bmatrix} \sigma_{xx} & \tau_{xy} & \tau_{xz} \\ \tau_{yx} & \sigma_{yy} & \tau_{yz} \\ \tau_{zx} & \tau_{zy} & \sigma_{zz} \end{bmatrix} \qquad (C.20)$$

In Equation C.20 the normal stresses are denoted by σ while, shear stresses are denoted by τ. The stresses are illustrated with their location on the elemental fluid volume in Figure C.2.

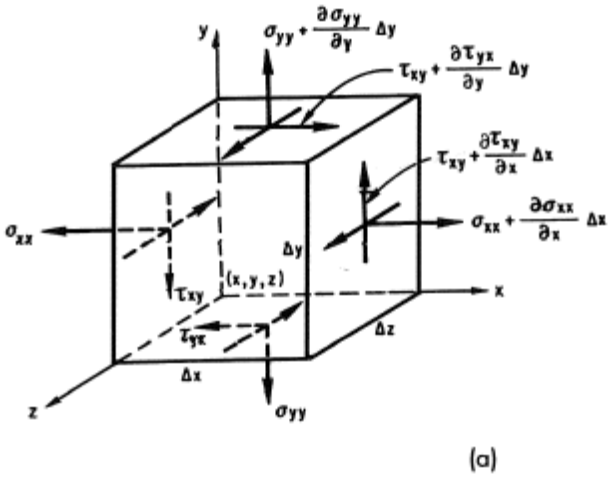

Figure C.2 The stresses on the surfaces of the elemental fluid volume [154]

These stresses are expressed in terms of strain rates in the fluid element, but before going through the detailed definition of stresses, it would be useful to discuss the relation between shear stresses and the torque that is expected to be imposed on the fluid element by these stresses. The shear stresses on xy-surface are illustrated by the sketch given in Figure C.3.

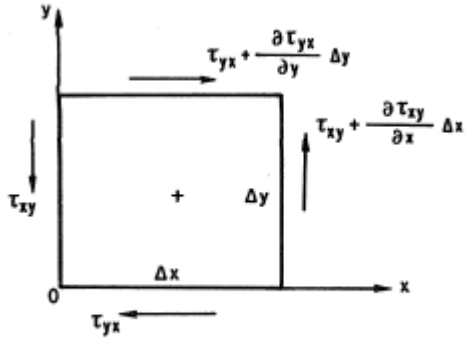

Figure C.3 The shear stresses on xy-surface of the elemental fluid volume [154]

Regarding the Figure C.6 it is possible to calculate the torque applied to the center of gravity of the illustrated surface. The torque applied could be expressed in terms of shear stresses after neglecting the higher order terms as follows;

$$\Gamma = \left(\tau_{xy} - \tau_{yx}\right)\Delta x \Delta y \qquad (C.21)$$

Since this torque is exist for the surface, according to the laws of motion it should be equal to the moment of inertia multiplied by the angular acceleration.

$$\Gamma = I\ddot{\theta}_z \qquad (C.22)$$

In Equation C.67 *I* is the moment of inertia of the surface and it equals to;

$$I = \frac{\rho}{12}((\Delta x)^2 + (\Delta y)^2)\Delta x \Delta y \qquad (C.23)$$

When Equation C.21 and C.22 are placed into Equation C.23 one will get;

$$\left(\tau_{xy} - \tau_{yx}\right) = \frac{\rho}{12}((\Delta x)^2 + (\Delta y)^2)\ddot{\theta}_z \qquad (C.24)$$

Δx and *Δy* are infinitesimal quantities and as they approach to zero, the only way to obtain a finite torque value is to have an infinitely large angular acceleration which is impractical. As a consequence, Equation C.24 could be barely satisfied when shear stress values are equal and the applied torque is equal to zero. Regarding to this equality it could be told that the shear stresses located symmetrically in the stress tensor matrix equal to each other for an infinitesimal 3-D cubic fluid element. This relationship between shear stresses will simplify the derivation procedure of the momentum conservation equation in the following parts.

The linear acceleration components were expressed in terms of flow velocities and their gradients. The left hand side of the Newton's second law of motion is the force

term. The forces acting on surfaces of a elemental fluid volume could be written in terms of stresses with the help of Figure C.3. According to the illustration given, the x,y and z components of resultant forces could be expressed as;

$$F_x = \rho f_x \Delta x \Delta y \Delta z + \left(\sigma_{xx} + \frac{\partial \sigma_{xx}}{\partial x}\Delta x\right)\Delta y \Delta z + \left(\tau_{yx} + \frac{\partial \tau_{yx}}{\partial y}\Delta y\right)\Delta x \Delta z$$
$$+ \left(\tau_{zx} + \frac{\partial \tau_{zx}}{\partial z}\Delta z\right)\Delta x \Delta y - \sigma_{xx}\Delta y \Delta z + \tau_{yx}\Delta x \Delta z + \tau_{zx}\Delta x \Delta y \qquad (C.25)$$

$$F_y = \rho f_y \Delta x \Delta y \Delta z + \left(\tau_{xy} + \frac{\partial \tau_{xy}}{\partial x}\Delta x\right)\Delta y \Delta z + \left(\sigma_{yy} + \frac{\partial \sigma_{yy}}{\partial y}\Delta y\right)\Delta x \Delta z$$
$$+ \left(\tau_{zy} + \frac{\partial \tau_{zy}}{\partial z}\Delta z\right)\Delta x \Delta y - \tau_{xy}\Delta y \Delta z + \sigma_{yy}\Delta x \Delta z + \tau_{zy}\Delta x \Delta y \qquad (C.26)$$

$$F_z = \rho f_z \Delta x \Delta y \Delta z + \left(\tau_{xz} + \frac{\partial \tau_{xz}}{\partial x}\Delta x\right)\Delta y \Delta z + \left(\tau_{yz} + \frac{\partial \tau_{yz}}{\partial y}\Delta y\right)\Delta x \Delta z$$
$$+ \left(\sigma_{zz} + \frac{\partial \sigma_{zz}}{\partial z}\Delta z\right)\Delta x \Delta y - \tau_{xz}\Delta y \Delta z + \tau_{yz}\Delta x \Delta z + \sigma_{zz}\Delta x \Delta y \qquad (C.27)$$

Substituting the Equation C.16 and Equation C.25 into Equation C.9 the Newton's second law of motion in x direction can be rewritten for a infinitesimal cubic fluid element in terms of velocities, velocity gradients and stresses as;

$$\left(\rho f_x + \frac{\partial \sigma_{xx}}{\partial x} + \frac{\partial \tau_{yx}}{\partial y} + \frac{\partial \tau_{zx}}{\partial z}\right)\Delta x \Delta y \Delta z = m\frac{Du}{Dt} \qquad (C.28)$$

Equation C.73 can be rearranged where mass of the fluid particle is $m = \rho \Delta x \Delta y \Delta z$,

$$\rho\frac{Du}{Dt} = \rho f_x + \frac{\partial \sigma_{xx}}{\partial x} + \frac{\partial \tau_{yx}}{\partial y} + \frac{\partial \tau_{zx}}{\partial z} \qquad (C.29)$$

The second law of motion can be written for y and z directions similarly,

$$\rho \frac{Dv}{Dt} = \rho f_y + \frac{\partial \tau_{xy}}{\partial x} + \frac{\partial \sigma_{yy}}{\partial y} + \frac{\partial \tau_{zy}}{\partial z} \qquad (C.30)$$

$$\rho \frac{Dw}{Dt} = \rho f_z + \frac{\partial \tau_{xz}}{\partial x} + \frac{\partial \tau_{yz}}{\partial y} + \frac{\partial \sigma_{zz}}{\partial z} \qquad (C.31)$$

The Newton's second law of motion had been written for the 3-D infinitesimal cubic fluid element in terms of velocities, velocity gradients and the stresses acting on the surfaces of the fluid element. However the stresses are also related with the deformations and strain rates, which mean they are also related with the velocity gradients [154, 155]. The relation with the stresses acting on the surfaces of the elemental fluid volume and the strain rates for a Newtonian fluid can be written as [156];

$$\sigma_{xx} = -p + \lambda\left(\frac{\partial u}{\partial x} + \frac{\partial v}{\partial y} + \frac{\partial w}{\partial z}\right) + 2\mu \frac{\partial u}{\partial x} \qquad (C.32)$$

$$\sigma_{yy} = -p + \lambda\left(\frac{\partial u}{\partial x} + \frac{\partial v}{\partial y} + \frac{\partial w}{\partial z}\right) + 2\mu \frac{\partial v}{\partial y} \qquad (C.33)$$

$$\sigma_{zz} = -p + \lambda\left(\frac{\partial u}{\partial x} + \frac{\partial v}{\partial y} + \frac{\partial w}{\partial z}\right) + 2\mu \frac{\partial w}{\partial z} \qquad (C.34)$$

$$\tau_{xy} = \tau_{yx} = \mu\left(\frac{\partial v}{\partial x} + \frac{\partial u}{\partial y}\right) \qquad (C.35)$$

$$\tau_{yz} = \tau_{zy} = \mu\left(\frac{\partial w}{\partial y} + \frac{\partial v}{\partial z}\right) \qquad (C.36)$$

$$\tau_{xz} = \tau_{zx} = \mu\left(\frac{\partial w}{\partial x} + \frac{\partial u}{\partial z}\right) \qquad (C.37)$$

In the above equations the μ represents the dynamic viscosity of the fluid. Additionally is named as second coefficient of viscosity and according to the Stoke's hypothesis [154] it is defined as;

$$\lambda = -\frac{2}{3}\mu \qquad (C.38)$$

Moreover the p in the above expressions represents the average pressure value which is also related with the normal stresses as;

$$p = -\frac{1}{3}(\sigma_{xx} + \sigma_{yy} + \sigma_{zz}) \qquad (C.39)$$

The final form of the conservation of momentum equation in terms of velocities, velocity gradients and pressure can be obtained by substitution of Equation C.37-Equation C.37 in Equations C.29, Equation C.30 and Equation C.31. The resultant equations can be written as;

$$\rho\frac{Du}{Dt} = \rho f_x - \frac{\partial p}{\partial x} + \frac{\partial}{\partial x}\left[2\mu\frac{\partial u}{\partial x} - \frac{2}{3}\mu\boldsymbol{\nabla}.\mathbf{V}\right] + \frac{\partial}{\partial y}\left[\mu\left(\frac{\partial v}{\partial x} + \frac{\partial u}{\partial y}\right)\right] + \frac{\partial}{\partial z}\left[\mu\left(\frac{\partial w}{\partial x} + \frac{\partial u}{\partial z}\right)\right] \qquad (C.40)$$

$$\rho\frac{Dv}{Dt} = \rho f_y - \frac{\partial p}{\partial y} + \frac{\partial}{\partial x}\left[\mu\left(\frac{\partial v}{\partial x} + \frac{\partial u}{\partial y}\right)\right] + \frac{\partial}{\partial y}\left[2\mu\frac{\partial v}{\partial y} - \frac{2}{3}\mu\boldsymbol{\nabla}.\mathbf{V}\right] + \frac{\partial}{\partial z}\left[\mu\left(\frac{\partial w}{\partial x} + \frac{\partial u}{\partial z}\right)\right] \qquad (C.41)$$

$$\rho\frac{Dw}{Dt} = \rho f_z - \frac{\partial p}{\partial z} + \frac{\partial}{\partial x}\left[\mu\left(\frac{\partial w}{\partial x} + \frac{\partial u}{\partial z}\right)\right] + \frac{\partial}{\partial y}\left[\mu\left(\frac{\partial v}{\partial x} + \frac{\partial u}{\partial y}\right)\right]$$
$$+ \frac{\partial}{\partial z}\left[2\mu\frac{\partial v}{\partial y} - \frac{2}{3}\mu\boldsymbol{\nabla}.\mathbf{V}\right] \qquad (C.42)$$

The relations given above is known as Navier-Stokes equations, however it is possible to make further simplification on these equations. As given in Equation C.9 for an incompressible fluid gradient of the velocity vector will be equal to 0. Additionally in most of the applications, viscosity of the fluid is assumed to be constant which is also the situation in this case. After the mentioned simplifications, the conservation of momentum equation for an incompressible Newtonian fluid with constant viscosity will be;

$$\rho\frac{Du}{Dt} = \rho f_x - \frac{\partial p}{\partial x} + \mu\left(\frac{\partial^2 u}{\partial x^2} + \frac{\partial^2 u}{\partial y^2} + \frac{\partial^2 u}{\partial z^2}\right) \qquad (C.43)$$

$$\rho\frac{Dv}{Dt} = \rho f_y - \frac{\partial p}{\partial y} + \mu\left(\frac{\partial^2 v}{\partial x^2} + \frac{\partial^2 v}{\partial y^2} + \frac{\partial^2 v}{\partial z^2}\right) \qquad (C.44)$$

$$\rho\frac{Dw}{Dt} = \rho f_z - \frac{\partial p}{\partial z} + \mu\left(\frac{\partial^2 w}{\partial x^2} + \frac{\partial^2 w}{\partial y^2} + \frac{\partial^2 w}{\partial z^2}\right) \qquad (C.45)$$

It is also possible to express the above equations in vector form. The vector form of momentum conservation equation for a Newtonian, incompressible fluid with constant viscosity which is also applicable to cylindrical and spherical coordinates can be written as;

$$\frac{D\mathbf{V}}{Dt} = \mathbf{f} - \frac{1}{\rho}\boldsymbol{\nabla}p + \frac{\mu}{\rho}\boldsymbol{\nabla}^2\mathbf{V} \qquad (C.46)$$

In this study where heat transfer fluid (HTF) is a component of the adsorption system, the velocity distribution will be determined with the solution of momentum conservation equation. According to the assumptions that had been made, the effect of body forces neglected in the mathematical models. The final form of the momentum conservation equations that will be used for the HTF will be;

$$\frac{D\mathbf{V_f}}{Dt} = -\frac{1}{\rho_f}\nabla p_f + \frac{\mu_f}{\rho_f}\nabla^2\mathbf{V_f} \qquad (C.47)$$

C.1.3 Energy Conservation Equation for the HTF

The energy conservation equation for the HTF will also be done on the 3-D infinitesimal cubic fluid element. The derivation will be done for the Cartesian coordinates but the final form of the conservation equation could be applied to the all coordinate systems. The energy equation is based on the first law of thermodynamics. The cubic elemental fluid volume with a mass of ρΔxΔyΔz is illustrated in Figure C.7 with the heat fluxes on the surfaces of this volume.

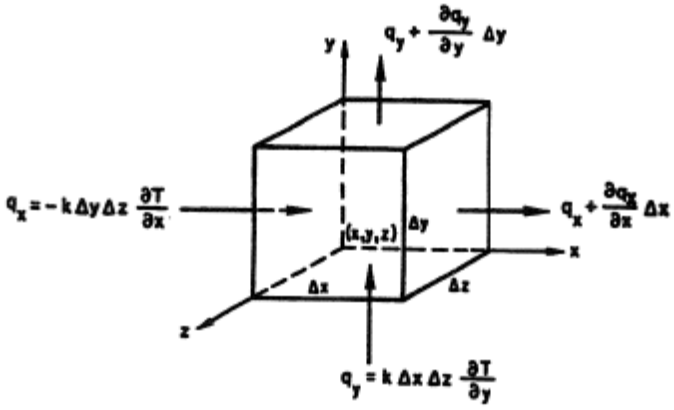

Figure C.4 The 3-D infinitesimal cubic fluid volume and the heat fluxes on the surfaces [154]

The first law of thermodynamics could be written for this elemental fluid volume in rate form as;

$$\dot{E} = \dot{Q} - \dot{W} \qquad (C.48)$$

$\dot{E}$ is the net rate of change of energy of the infinitesimal fluid element, $\dot{Q}$ while is the net rate of heat transfer to the system and $\dot{W}$ is the net rate of work done by the fluid element against the surface and body forces.

The energy of the fluid volume is composed of internal energy and the kinetic energy of the fluid particle. The fluid particle center of gravity is at x, y and z at time t and then it moves to its new position which is $x+\Delta x$ $y+\Delta y$ $z+\Delta z$ at time $t+\Delta t$.The expression for the change of energy for the elemental cubic fluid volume can be seen below;

$$\Delta e = \frac{\partial e}{\partial x}\Delta x + \frac{\partial e}{\partial y}\Delta y + \frac{\partial e}{\partial z}\Delta z + \frac{\partial e}{\partial t}\Delta t \qquad (C.49)$$

In Equation C.49 e is the energy per unit mass of the fluid. At instant t the rate of change of energy per unit mass of the fluid element could be written as;

$$\lim_{\Delta t \to 0} \frac{\Delta e}{\Delta t} = u\frac{\partial e}{\partial x} + v\frac{\partial e}{\partial y} + w\frac{\partial e}{\partial z} + \frac{\partial e}{\partial t} \qquad (C.50)$$

The rate of change of energy of the elemental fluid volume can be expressed with the substantial derivative which had been used for the definition of acceleration in momentum conservation equations as follows;

$$\dot{E} = \rho \Delta x \Delta y \Delta z \frac{De}{Dt} \qquad (C.51)$$

The energy per unit mass of the fluid element is assumed to be consisting of two main components. These components are internal energy and the kinetic energy. The internal energy per unit mass is denoted with $\mathfrak{U}$ while kinetic energy per unit mass is expressed in terms of velocity components. The total expression for the energy per unit mass in extended form can be written as;

$$e = \mathfrak{U} + \frac{u^2 + v^2 + w^2}{2} \qquad (C.52)$$

The second term in the energy conservation equation represents the net rate of heat transfer to the infinitesimal cubic fluid element. The net rate of heat transfer to the fluid element can be written regarding the fluxes shown in Figure C.4 can be written as;

$$\begin{aligned}\dot{Q} = &-k\frac{\partial T}{\partial x}\Delta y\Delta z - \left(-k\frac{\partial T}{\partial x} - \frac{\partial}{\partial x}\left(k\frac{\partial T}{\partial x}\right)\Delta x\right)\Delta y\Delta z - k\frac{\partial T}{\partial y}\Delta x\Delta z \\ &- \left(-k\frac{\partial T}{\partial y} - \frac{\partial}{\partial y}\left(k\frac{\partial T}{\partial y}\right)\Delta y\right)\Delta x\Delta z - k\frac{\partial T}{\partial z}\Delta x\Delta y \\ &- \left(-k\frac{\partial T}{\partial z} - \frac{\partial}{\partial z}\left(k\frac{\partial T}{\partial z}\right)\Delta y\right)\Delta x\Delta y \qquad (C.53)\end{aligned}$$

$$\dot{Q} = \left[\frac{\partial}{\partial x}\left(k\frac{\partial T}{\partial x}\right) + \frac{\partial}{\partial y}\left(k\frac{\partial T}{\partial y}\right) + \frac{\partial}{\partial z}\left(k\frac{\partial T}{\partial z}\right)\right]\Delta x\Delta y\Delta z \qquad (C.54)$$

According to the assumptions made the radiative heat transfer to the fluid element is neglected.

The third element of the energy conservation equation is the net rate of work done by the fluid element against the body and surface forces. The net rate of work done by

the fluid element can be expressed in terms of stresses and velocity components shown in Figure C.5 as;

$$\dot{W} = -\left[\frac{\partial}{\partial x}\left(u\sigma_{xx} + v\tau_{xy} + w\tau_{xz}\right) + \frac{\partial}{\partial y}\left(u\tau_{yx} + v\sigma_{yy} + w\tau_{yz}\right)\right.$$
$$\left. + \frac{\partial}{\partial z}\left(u\tau_{zx} + v\tau_{zy} + w\sigma_{zz}\right) + \rho\left(uf_x + vf_y + wf_z\right)\right]\Delta x\Delta y\Delta z \qquad (C.55)$$

If the Equation C.51, Equation C.54 and Equation C.55 is substituted into Equation C.48 the final form of the energy conservation equation will be;

$$\rho\Delta x\Delta y\Delta z\frac{D}{Dt}\left[\mathfrak{A} + \frac{u^2 + v^2 + w^2}{2}\right]$$
$$= \left[\frac{\partial}{\partial x}\left(k\frac{\partial T}{\partial x}\right) + \frac{\partial}{\partial y}\left(k\frac{\partial T}{\partial y}\right) + \frac{\partial}{\partial z}\left(k\frac{\partial T}{\partial z}\right)\right]\Delta x\Delta y\Delta z$$
$$+ \left[\frac{\partial}{\partial x}\left(u\sigma_{xx} + v\tau_{xy} + w\tau_{xz}\right) + \frac{\partial}{\partial y}\left(u\tau_{yx} + v\sigma_{yy} + w\tau_{yz}\right)\right.$$
$$+ \frac{\partial}{\partial z}\left(u\tau_{zx} + v\tau_{zy} + w\sigma_{zz}\right)$$
$$+ \rho\left(uf_x + vf_y\right.$$
$$\left.\left. + wf_z\right)\right]\Delta x\Delta y\Delta z \qquad (C.56)$$

The Equation C.56 is the also known as the total energy equation and it contains both thermal and mechanical energy terms. The ultimate goal of this derivation is to obtain the thermal energy equation which will be used in the mathematical model. The thermal energy equation can be obtained by subtracting the mechanical energy equation from the total energy equation which is given in Equation C.56. The mechanical energy equation can be obtained by using the momentum conservation equations and laws of mechanics. The first step to obtain the mechanical energy equation is to multiply the momentum conservation equation for x, y and z with the corresponding velocities. After multiplication, the resultant equations will be;

$$\rho u \frac{Du}{Dt} = u\left(\rho f_x + \frac{\partial \sigma_{xx}}{\partial x} + \frac{\partial \tau_{yx}}{\partial y} + \frac{\partial \tau_{zx}}{\partial z}\right) \qquad (C.57)$$

$$\rho v \frac{Dv}{Dt} = v\left(\rho f_y + \frac{\partial \tau_{xy}}{\partial x} + \frac{\partial \sigma_{yy}}{\partial y} + \frac{\partial \tau_{zy}}{\partial z}\right) \qquad (C.58)$$

$$\rho w \frac{Dw}{Dt} = w\left(\rho f_z + \frac{\partial \tau_{xz}}{\partial x} + \frac{\partial \tau_{yz}}{\partial y} + \frac{\partial \sigma_{zz}}{\partial z}\right) \qquad (C.59)$$

When Equation C.57, Equation C.58 and Equation C.59 are summed the result will be;

$$\rho \frac{D}{Dt}\left[\frac{u^2 + v^2 + w^2}{2}\right] = u\left(\frac{\partial \sigma_{xx}}{\partial x} + \frac{\partial \tau_{yx}}{\partial y} + \frac{\partial \tau_{zx}}{\partial z}\right) + v\left(\frac{\partial \tau_{xy}}{\partial x} + \frac{\partial \sigma_{yy}}{\partial y} + \frac{\partial \tau_{zy}}{\partial z}\right)$$
$$+ w\left(\frac{\partial \tau_{xz}}{\partial x} + \frac{\partial \tau_{yz}}{\partial y} + \frac{\partial \sigma_{zz}}{\partial z}\right) + \rho\left(u f_x + v f_y + w f_z\right) \qquad (C.60)$$

Since the mechanical energy equation is obtained it is possible to obtain the thermal energy equation or the energy equation by subtracting it from the total energy equation given in Equation C.56. The obtained energy equation can be written as;

$$\rho \frac{D\mathfrak{U}}{Dt} = \frac{\partial}{\partial x}\left(k \frac{\partial T}{\partial x}\right) + \frac{\partial}{\partial y}\left(k \frac{\partial T}{\partial y}\right) + \frac{\partial}{\partial z}\left(k \frac{\partial T}{\partial z}\right) + \sigma_{xx} \frac{\partial u}{\partial x} + \sigma_{yy} \frac{\partial v}{\partial y} + \sigma_{zz} \frac{\partial w}{\partial z}$$
$$+ \tau_{xy}\left(\frac{\partial v}{\partial x} + \frac{\partial u}{\partial y}\right) + \tau_{yz}\left(\frac{\partial w}{\partial y} + \frac{\partial v}{\partial z}\right) + \tau_{zx}\left(\frac{\partial u}{\partial z} + \frac{\partial w}{\partial x}\right) \qquad (C.61)$$

By using the stress definitions for a Newtonian fluid which were given earlier, the terms in the thermal energy equation can be expanded as;

$$\sigma_{xx} \frac{\partial u}{\partial x} = \left[-p - \frac{2}{3}\mu(\boldsymbol{\nabla}.\mathbf{V}) + 2\mu \frac{\partial u}{\partial x}\right] \frac{\partial u}{\partial x} \qquad (C.62)$$

$$\sigma_{yy}\frac{\partial v}{\partial y} = \left[-p - \frac{2}{3}\mu(\boldsymbol{\nabla}.\mathbf{V}) + 2\mu\frac{\partial v}{\partial y}\right]\frac{\partial v}{\partial y} \qquad (C.63)$$

$$\sigma_{zz}\frac{\partial w}{\partial z} = \left[-p - \frac{2}{3}\mu(\boldsymbol{\nabla}.\mathbf{V}) + 2\mu\frac{\partial w}{\partial z}\right]\frac{\partial w}{\partial z} \qquad (C.64)$$

Then the sum of Equation C.62, Equation C.63 and Equation C.64 will yield;

$$\sigma_{xx}\frac{\partial u}{\partial x} + \sigma_{yy}\frac{\partial v}{\partial y} + \sigma_{zz}\frac{\partial w}{\partial z}$$
$$= -p\boldsymbol{\nabla}.\mathbf{V} - \frac{2}{3}\mu(\boldsymbol{\nabla}.\mathbf{V})^2 + 2\mu\left[\left(\frac{\partial u}{\partial x}\right)^2 + \left(\frac{\partial v}{\partial y}\right)^2 + \left(\frac{\partial w}{\partial z}\right)^2\right] \qquad (C.65)$$

Additionally the last three terms in the energy equation can be expressed in terms of velocity gradients for a Newtonian fluid as;

$$\tau_{xy}\left(\frac{\partial v}{\partial x} + \frac{\partial u}{\partial y}\right) = \mu\left(\frac{\partial v}{\partial x} + \frac{\partial u}{\partial y}\right)^2 \qquad (C.66)$$

$$\tau_{yz}\left(\frac{\partial w}{\partial y} + \frac{\partial v}{\partial z}\right) = \mu\left(\frac{\partial w}{\partial y} + \frac{\partial v}{\partial z}\right)^2 \qquad (C.67)$$

$$\tau_{zx}\left(\frac{\partial u}{\partial z} + \frac{\partial w}{\partial x}\right) = \mu\left(\frac{\partial u}{\partial z} + \frac{\partial w}{\partial x}\right)^2 \qquad (C.68)$$

Since the mass conservation equation given in C.6 can also be written in terms of a substantial derivative of density as;

$$\frac{D\rho}{Dt} + \rho\boldsymbol{\nabla}.\mathbf{V} = 0 \qquad (C.69)$$

The energy equation can be rewritten in terms of velocity gradients, velocities, pressure and density by using the relations between stresses and strain rates for a Newtonian fluid. Rearranged representation energy equation after substitution is as follows,

$$\rho\frac{D\mathfrak{A}}{Dt}=\frac{\partial}{\partial x}\left(k\frac{\partial T}{\partial x}\right)+\frac{\partial}{\partial y}\left(k\frac{\partial T}{\partial y}\right)+\frac{\partial}{\partial z}\left(k\frac{\partial T}{\partial z}\right)+\frac{p}{\rho}\frac{D\rho}{Dt}-\frac{2}{3}\mu(\boldsymbol{\nabla}.\mathbf{V})^2$$
$$+2\mu\left[\left(\frac{\partial u}{\partial x}\right)^2+\left(\frac{\partial v}{\partial y}\right)^2+\left(\frac{\partial w}{\partial z}\right)^2\right]$$
$$+\mu\left(\frac{\partial v}{\partial x}+\frac{\partial u}{\partial y}\right)^2+\mu\left(\frac{\partial w}{\partial y}+\frac{\partial v}{\partial z}\right)^2+\mu\left(\frac{\partial u}{\partial z}+\frac{\partial w}{\partial x}\right)^2 \qquad (C.70)$$

The last 5 terms in Equation C.70 are represents the rate of work done by the viscous forces. The work done by the viscous forces are irreversible and have a contribution to the energy increase of the fluid element. In literature these terms are called as dissipation function [157] and represented by Φ. The dissipation function is;

$$\Phi=2\mu\left[\left(\frac{\partial u}{\partial x}\right)^2+\left(\frac{\partial v}{\partial y}\right)^2+\left(\frac{\partial w}{\partial z}\right)^2\right.$$
$$\left.+\frac{1}{2}\left(\frac{\partial v}{\partial x}+\frac{\partial u}{\partial y}\right)^2+\frac{1}{2}\left(\frac{\partial w}{\partial y}+\frac{\partial v}{\partial z}\right)^2+\frac{1}{2}\left(\frac{\partial u}{\partial z}+\frac{\partial w}{\partial x}\right)^2-\frac{1}{3}(\boldsymbol{\nabla}.\mathbf{V})^2\right] \qquad (C.71)$$

The energy equation can also be written in terms of fluid enthalpy which will yield a more usable form for the mathematical modeling purposes. The fluid enthalpy can be defined as;

$$h=\mathfrak{A}+\frac{p}{\rho} \qquad (C.72)$$

The substantial derivative of Equation C.72 after rearrangement will be,

$$\frac{D\mathfrak{A}}{Dt} = \frac{Dh}{Dt} - \frac{1}{\rho}\frac{Dp}{Dt} - p\frac{D\rho}{Dt} \qquad (C.73)$$

The substitution of Equation C.73 into energy equation which is given by Equation C.70 will result in;

$$\rho\frac{Dh}{Dt} = \frac{\partial}{\partial x}\left(k\frac{\partial T}{\partial x}\right) + \frac{\partial}{\partial y}\left(k\frac{\partial T}{\partial y}\right) + \frac{\partial}{\partial z}\left(k\frac{\partial T}{\partial z}\right) + \frac{Dp}{Dt} + \Phi \qquad (C.74)$$

The substantial derivative of pressure represents the reversible work done by the compression on the fluid particle and generally negligibly low for subsonic velocities. Additionally if the fluid is a perfect gas then the fluid enthalpy can be related to fluid temperature as;

$$dh = c_p dT \qquad (C.75)$$

Consequently for a low speed flow of a perfect gas with constant specific heat the energy equation will be;

$$\rho c_p \frac{DT}{Dt} = \boldsymbol{\nabla}(k\boldsymbol{\nabla}T) + \Phi \qquad (C.76)$$

In case of an incompressible fluid where the constant pressure and constant volume specific heat values are identical,

$$d\mathfrak{A} = c_p dT = c_v dT = cdT \qquad (C.77)$$

Additionally the continuity equation will be reduced to,

$$\boldsymbol{\nabla}.\mathbf{V} = \mathbf{0} \qquad (C.78)$$

Then the energy equation for incompressible fluid with constant specific heat can be written as follows;

$$\rho c \frac{DT}{Dt} = \boldsymbol{\nabla}(k\boldsymbol{\nabla}T) + \Phi \qquad (C.79)$$

Where viscous dissipation function is a bit different for the incompressible fluids and can be written as;

$$\Phi = 2\mu\left[\left(\frac{\partial u}{\partial x}\right)^2 + \left(\frac{\partial v}{\partial y}\right)^2 + \left(\frac{\partial w}{\partial z}\right)^2 + \frac{1}{2}\left(\frac{\partial v}{\partial x} + \frac{\partial u}{\partial y}\right)^2 + \frac{1}{2}\left(\frac{\partial w}{\partial y} + \frac{\partial v}{\partial z}\right)^2 + \frac{1}{2}\left(\frac{\partial u}{\partial z} + \frac{\partial w}{\partial x}\right)^2\right] \qquad (C.80)$$

Effect of viscous dissipation may be neglected when flow velocity is not high. As a measure of justification generally Eckert number is used. Eckert number can be defined as the ratio of kinetic energy of the flow to the enthalpy difference between heat transfer surface and fluid. The Eckert number can be expressed as follows,

$$Ec = \frac{U_{flow}^2}{c_p\left|T_{fluid} - T_{surface}\right|} \qquad (C.81)$$

For low flow velocities the Eckert number will be small and under this circumstance the effect of viscous dissipation will be small and can be neglected.

Consequently the derived energy equation can be used for mathematical modeling of the HTF temperature distribution. As mentioned above the HTF flow is assumed to be incompressible, and the thermophysical properties of HTF will be constant. Additionally the flow velocities will be small therefore; the viscous dissipation effect could be neglected. The energy equation that will be used for describing the

temperature field of the HTF can be written under these assumptions and simplifications as;

$$\rho_f c_f \frac{DT_f}{Dt} = k_f \boldsymbol{\nabla^2} T_f \qquad (C.82)$$

The required velocity values for the HTF energy equations will be obtained from the solution of the momentum conservation equation which is discussed in previous section.

C.2 Conservation Equations for the Heat Transfer Tube (HTT)

C.2.1 Energy Conservation Equation for the HTT

The energy conservation equation for the heat transfer tube (HTT) is derived similar to the HTF. However HTT is rigid, solid and immobile and thus the derivation will be shorter. The beginning point for derivation is the first law of thermodynamics which is expressed in Equation C.90. The rate of work done will be equal to zero, for an infinitesimal solid particle since the particle will not be moving. In this case the first law of thermodynamics can be written as;

$$\dot{E} = \dot{Q} \qquad (C.83)$$

In brief the rate of change of energy of the system will be equal to the net rate of heat transferred to the system. Since the elemental solid volume is immobile the energy of the system is composed of the internal energy of the infinitesimal volume. Therefore it is possible to express the net rate of energy increase in the system as;

$$\dot{E} = \frac{\Delta E}{\Delta t} = \rho \frac{\Delta \mathfrak{U}}{\Delta t} \Delta x \Delta y \Delta z \qquad (C.84)$$

The differential form of Equation C.84 can be obtained by taking the limit. Since the relation between internal energy and temperature had been stated in Equation C.83 the net rate of energy increase for the infinitesimal solid element can be written as;

$$\lim_{\Delta t \to 0} \frac{\Delta \mathfrak{U}}{\Delta t} \rho \Delta x \Delta y \Delta z = \frac{\partial \mathfrak{U}}{\partial t} \rho \Delta x \Delta y \Delta z = \rho c \frac{\partial T}{\partial t} \Delta x \Delta y \Delta z \qquad (C.85)$$

The heat fluxes had been shown in Figure C.4 for an infinitesimal cubic element. The net rate of heat transferred to the system is identical for the one which had been expressed for fluid element and was given in Equation C.54. When both Equation C.54 and Equation C.83 are substituted into Equation C.85, the energy conservation equation for the solid element can be obtained as;

$$\rho c \frac{\partial T}{\partial t} = \left[\frac{\partial}{\partial x} \left(k \frac{\partial T}{\partial x} \right) + \frac{\partial}{\partial y} \left(k \frac{\partial T}{\partial y} \right) + \frac{\partial}{\partial z} \left(k \frac{\partial T}{\partial z} \right) \right] \qquad (C.86)$$

As mentioned above for the HTT density and the specific heat and thermal conductivity values are assumed to be constant. The parameters and quantities belong to the HTT will be denoted by a subscript t in this study. Regarding the assumptions simplified form of the energy conservation equation can be rewritten as follows,

$$\rho_t c_t \frac{\partial T_t}{\partial t} = k_t \boldsymbol{\nabla^2} T_t \qquad (C.87)$$

C.3 Conservation Equations for the Packed Bed

As stated above, there are various approaches in mathematical modeling of the packed bed. The derivation of governing equations procedure is mainly based on the treatment of the phases. Based on the LTNE assumption, phases are treated separately and the governing equations for each phase will be derived by using volume averaging method. On the other hand when phases are assumed to be at local

thermal equilibrium (LTE) and all the phases within the packed bed will be treated as a single phase, the governing equation derivation will be based on control volume approach.

Moreover it should be noted that the mobile phase within the packed bed is gas and, this phase may be pure vapor or mixture of vapor and air depending on the case. There are also immobile phases exist in the packed bed. The immobile phases are liquid and solid phases but according to the assumptions solid and liquid phases are treated as a single phase which will be mentioned as solid phase. Throughout this work the quantities and parameters that belong to mobile phase will be denoted with the subscript g referring to the gas state of the phase. Similarly, the quantities and parameters that belong to solid phase will be denoted with subscript s.

C.3.1 Mass Conservation Equation Based on Local Thermal Non-Equilibrium (LTNE) Approach

The mass conservation equation for the mobile, gas phase can be written in differential form as;

$$\frac{\partial \rho_g}{\partial t} + \boldsymbol{\nabla}.(\rho_g \mathbf{V_g}) = 0 \qquad (C.88)$$

As mentioned earlier, to obtain the governing equations in the packed bed, the volume averaging will be applied for the differential form of equations over the representative elementary volume. The averaged form of Equation C.88 can be rewritten as;

$$\langle\frac{\partial \rho_g}{\partial t}\rangle_R + \langle\boldsymbol{\nabla}.(\rho_g \mathbf{V_g})\rangle_R = 0 \qquad (C.89)$$

At the solid and gas phase interface the condition can be written as;

$$\mathbf{n_{gs}}.\mathbf{V_g}\,\rho_g = C_g \qquad (C.90)$$

In Equation C.90 $\mathbf{n}_{gs}$ is the unit normal vector of the phase interface of gas and solid phase where the area of this interface is A_{gs}. Applying the transport theorem and averaging on the REV, differential form of mass conservation will yield;

$$\frac{\partial\left(\varepsilon_g\langle\rho_g\rangle_g\right)}{\partial t} + \boldsymbol{\nabla}.\left(\langle\rho_g\rangle_g\langle\mathbf{V_g}\rangle_R\right) + \boldsymbol{\nabla}.\langle\hat{\rho}_g\hat{\mathbf{V}}_\mathbf{g}\rangle_R + \frac{1}{V_R}\int_{A_{gs}}\rho_g\mathbf{n_{gs}}.(\mathbf{V_g}-\mathbf{v_{gs}})\,dA = 0 \qquad (C.91)$$

As mentioned above the $\mathbf{v_{gs}}$ is the velocity vector which defines the velocity of the phase interface between gas and solid phase.

The spatial deviation of density of the gas phase is relatively small compared to the intrinsic phase average [67].

$$\hat{\rho}_g \ll \langle\rho_g\rangle_g \qquad (C.92)$$

Thus the third term in Equation C.91 can be omitted according to the imposition of the order of magnitude estimate shown below,

$$\boldsymbol{\nabla}.\langle\hat{\rho}_g\hat{\mathbf{V}}_\mathbf{g}\rangle_R \ll \boldsymbol{\nabla}.\left(\langle\rho_g\rangle_g\langle\mathbf{V_g}\rangle_R\right) \qquad (C.93)$$

Additionally the last term on the left hand side of Equation C.91 which represents the area adsorptive or desorptive transport can be rewritten as [67];

$$\frac{1}{V_R}\int_{A_{gs}}\rho_g\mathbf{n_{gs}}.(\mathbf{V_g}-\mathbf{v_{gs}})\,dA = a_{gs}\langle\Omega_g\rangle_{gs} \qquad (C.94)$$

In Equation C.94 specific interfacial area between solid and gas phase is denoted by a_{gs} and the area averaged adsorptive or desorptive mass flux is represented by $\langle \Omega_g \rangle_{gs}$ which is defined as;

$$\langle \Omega_g \rangle_{gs} = \frac{1}{A_{gs}} \int_{A_{gs}} \Omega_g \, dA \qquad (C.95)$$

Assuming that the interface velocity $\mathbf{v_{gs}}$ is equal to zero Ω_g will be,

$$\Omega_g = \rho_g \mathbf{n_{gs}}.\mathbf{V_g} \qquad (C.96)$$

After the simplifications and representations shown above implemented into Equation C.94, the equation will take the following form,

$$\frac{\partial(\varepsilon_g \langle \rho_g \rangle_g)}{\partial t} + \boldsymbol{\nabla}.\langle \rho_g \rangle_g \langle \mathbf{V_g} \rangle_R + a_{gs} \langle \Omega_g \rangle_{gs} = 0 \qquad (C.97)$$

In the above equation first term represents the net rate of mass change of the gas phase, the second term is the convective mass transport as a result of bulk fluid motion and the third term is the adsorptive of desorptive mass transfer rate to or from the liquid phase. As mentioned above the liquid phase is assumed to be at same temperature with the solid phase at every spatial location of the adsorbent bed domain. For this reason the adsorptive or desorptive mass transfer assumed to be taking place between gas and solid phases.

A more simplified approach used in mathematical modeling of the adsorptive or desorptive mass transfer rate term is to define the adsorption or desorption rate per unit volume by using an expression which relates the adsorption rate per unit volume [36]. The expression that will be used for defining the adsorptive mass transfer rate can be written as;

$$a_{gs}\langle \Omega_g \rangle_{gs} \cong (1-\varepsilon_t)\rho_s \frac{\partial X}{\partial t} \qquad (C.98)$$

In Equation C.98 X represents the adsorption capacity which is the adsorbed amount of adsorbate in kilograms per kilogram of solid adsorbent. For this reason the rate of change of adsorbed amount per unit volume of packed bed could be obtained by multipliying the $\frac{\partial X}{\partial t}$ term with the adsorbent density and the $(1-\varepsilon_t)$. Before going through the approach that will be used for defining the rate of change of adsorption capacity, it could be useful to define the equilibrium adsorption capacity term which will be an input for the expression that is going be used for defining the rate of change of adsorption capacity.

The equilibrium adsorption capacity of an adsorbent is the maximum amount of adsorbate that can be adsorbed by the adsorbent at definite temperature and pressure. Therefore equilibrium adsorption capacity is a function of adsorbate pressure and the adsorbent temperature. The equilibrium adsorption capacity of an adsorbate/adsorbent pair can be defined by using adsorption equilibrium models which are a function of pressure and temperature [39]. In this study the adsorption equilibrium for silica gel-water vapor adsorption equilibrium is defined by using the Dubinin-Ashtakov (D-A) equation which is defined as follows [10],

$$X_{eq} = 0.346 \exp\left[-5.6\left(\frac{T_s}{T_{sat}} - 1\right)^{1.6}\right] \qquad (C.99)$$

In Equation C.99 the X_{eq} is the equilibrium adsorption capacity. The constants 0.346, 5.6 and 1.6 are the coefficients of D-A adsorption equilibrium equation which are experimentally determined for the silica gel-water vapor adsorbent-adsorbate pair [12]. T_s is the adsorbent temperature and T_{sat} is the saturation temperature of the water vapor at definite adsorbate pressure. The relation between adsorbate (water

vapor) pressure p_g and the saturation temperature can be expressed by an empirically derived function which is [17],

$$T_{sat} = \left[\frac{1730.63}{8.0713 - \log_{10}(7.0063 p_g)} + 39.724\right] \qquad (C.100)$$

In some of the cases the gas phase is composed of air and water vapor, and under this circumstance, the partial pressure of vapor is used since it is the adsorbing species, while air is assumed to be inert and not adsorbed by the adsorbent.

At this point by utilizing the relations given above, it is possible to determine the equilibrium adsorption capacity at any spatial location within the packed bed as long as adsorbent temperature and adsorbate pressure is known. However as stated earlier, the main concern here is to obtain an expression for the rate of change of adsorption capacity. In this study the adsorption equilibrium assumption is not made, which means the adsorption capacity at each spatial location may be different than the equilibrium value at any instant. As a result of this non-equilibrium assumption it is possible to account for the internal mass transfer resistances within the adsorbent particles while expressing the rate of change of adsorption capacity. The approach that will be used for defining the rate of change of adsorption capacity by accounting the internal mass transfer resistance within the adsorbent particles is the Linear Driving Force (LDF) approach. The LDF approach had been used by various researchers [36, 39, and 9]. The LDF approach linearly relates the rate of change of adsorption capacity at any spatial location with equilibrium adsorption capacity and the adsorption capacity at that instant. This model can be expressed as [12];

$$\frac{\partial X}{\partial t} = k_m(X_{eq} - X) \qquad (C.101)$$

In Equation C.101 X_{eq} is the equilibrium adsorption capacity value while X is the adsorption capacity at that insant. The internal mass transfer coefficient is denoted by k_m and it is defined as [12];

$$k_m = 15\frac{D_e}{r_p^2} \qquad (C.102)$$

In Equation C.102 r_p represents the radii of the adsorbent particles and D_e represents the equivalent diffusivity. The equivalent diffusivity is expressed as [12],

$$D_e = D_0 \exp\left(\frac{E_a}{R_g T_s}\right) \qquad (C.103)$$

In Equation C.103 D_0 represents the reference diffusivity, E_a represents the activation energy for surface diffusion, T_s represents the adsorbent temperature and R_g represents the specific gas constant for the adsorbate.

In addition to the above simplification, assuming that the gas phase density does not vary significantly within the averaging volume the intrinsic phase average of density could be replaced with the density value at that location. Moreover the gas phase volume fraction is assumed to be equal to the total porosity ε_t . Regarding these simplifications and assumptions, the macroscopic form of mass conservation equation can be written as,

$$\varepsilon_t \frac{\partial \rho_g}{\partial t} + \boldsymbol{\nabla}.\rho_g \mathbf{V_g} + (1-\varepsilon_t)\rho_s \frac{\partial X}{\partial t} = 0 \qquad (C.104)$$

C.3.2 Momentum Conservation Equation Based on Local Thermal Non-Equilibrium (LTNE) Approach

As mentioned earlier the mobile phase is gas and the velocity field needs to be determined for this phase only. These velocity values will be used in the mass conservation and energy conservation equations. One of the basic equations that can be used for definition of the velocity field of a fluid flowing in porous media is the Darcy's Law [68]. According to the Darcy's Law the rate of flow is directly proportional with pressure gradient which is the driving force causing the fluid flow.

The derivation of Darcy's Law is based on the differential formulation of momentum conservation equation by omitting some of the terms as a result of order of magnitude analyses. As stated earlier, the porosity of the packed bed is assumed to be constant and the volume of the adsorbed phase is neglected. In this case the differential form of the momentum conservation gas phase as;

$$\frac{D\left(\rho_g \mathbf{V_g}\right)}{Dt} = \boldsymbol{\nabla}.\boldsymbol{\pi} + \rho_g \mathbf{f} \qquad (C.105)$$

The normal stresses in the stress tensor $\boldsymbol{\pi}$ can be rewritten by decomposition into pressure and the stress terms separately as;

$$\boldsymbol{\pi} = \begin{bmatrix} \sigma_{xx} & \tau_{xy} & \tau_{xz} \\ \tau_{yx} & \sigma_{yy} & \tau_{yz} \\ \tau_{zx} & \tau_{zy} & \sigma_{zz} \end{bmatrix} = \begin{bmatrix} \tau_{xx} - p & \tau_{xy} & \tau_{xz} \\ \tau_{yx} & \tau_{yy} - p & \tau_{yz} \\ \tau_{zx} & \tau_{zy} & \tau_{zz} - p \end{bmatrix}$$
$$= \begin{bmatrix} \tau_{xx} & \tau_{xy} & \tau_{xz} \\ \tau_{yx} & \tau_{yy} & \tau_{yz} \\ \tau_{zx} & \tau_{zy} & \tau_{zz} \end{bmatrix} - p \begin{bmatrix} 1 & 0 & 0 \\ 0 & 1 & 0 \\ 0 & 0 & 1 \end{bmatrix} \qquad (C.106)$$

The stress tensor can be rewritten by using the above expression to get a more compatible representation with the [79].

$$\boldsymbol{\pi} = \boldsymbol{\tau} - p \begin{bmatrix} 1 & 0 & 0 \\ 0 & 1 & 0 \\ 0 & 0 & 1 \end{bmatrix} \qquad (C.107)$$

Replacing the tensor notation given in Equation C.107 into Equation C.105 one will obtain,

$$\frac{D\left(\rho_g \mathbf{V_g}\right)}{Dt} = -\boldsymbol{\nabla} p_g + \boldsymbol{\nabla}.\boldsymbol{\tau} + \rho_g \mathbf{f} \qquad (C.108)$$

The first term in Equation C.108 is the net rate of momentum change in the elemental fluid volume and the net rate of convective momentum flux into the system. In brief the left hand side of the equation corresponds to mass multiplied by acceleration and also known as the inertial terms of the momentum conservation equation. Since the inertial terms are more important for the flows with high velocity and high Reynolds number these terms can be neglected for the momentum transport in porous medium [157]. Effect of body forces in momentum conservation are neglected for sake of simplicity throughout the study, for this reason the last term on right hand side will also be neglected. The second term on the right hand side represents the rate of viscous momentum gain per unit volume. The viscous momentum exchange is the dominant component for the fluid flow in porous media, therefore after omitting the neglected terms the momentum conservation equation will take the following form,

$$0 = -\boldsymbol{\nabla} p_g + \boldsymbol{\nabla}.\boldsymbol{\tau} \qquad (C.109)$$

By using the linear relations between stress and strain rates for Newtonian fluids Equation C.109 can be rewritten in terms of velocity and viscosity of the gas phase as,

$$0 = -\boldsymbol{\nabla} p_g + \mu_g \boldsymbol{\nabla^2} \mathbf{V_g} \qquad (C.110)$$

Equation C.110 is the Stoke's equation without the body forces. In general superficial average velocity is preferred for the representation of macroscopic velocity field in porous media [57].

After taking the volume average of Equation C.110 over a representative elementary volume (REV), it will take the form given below,

$$0 = -\langle \nabla p_g \rangle_R + \langle \mu_g \nabla . \nabla \mathbf{V_g} \rangle_R \qquad (\mathrm{C}.111)$$

Assuming that the variations of gas phase viscosity in averaging volume is small, during momentum conservation equation derivation, one can write Equation C.111 as,

$$0 = -\langle \nabla p_g \rangle_R + \mu_g \langle \nabla . \nabla \mathbf{V_g} \rangle_R \qquad (\mathrm{C}.112)$$

$$\langle \nabla p_g \rangle_R = \nabla \langle p_g \rangle_R + \frac{1}{V_R} \int_{A_{gs}} p_g \cdot \mathbf{n_\beta} dA \qquad (C.113)$$

Expressing the phase average of pressure in terms of intrinsic phase average the Equation C.113 can be rewritten as,

$$\langle \nabla p_g \rangle_R = \varepsilon_g \nabla \langle p_g \rangle_g + \langle p_g \rangle_g \nabla \varepsilon_g + \frac{1}{V_R} \int_{A_{gs}} p_g \cdot \mathbf{n_\beta} dA \qquad (C.114)$$

Additionally the pressure value can be expressed in terms of its intrinsic phase average and spatial deviation and then Equation C.114 can be rewritten as,

$$\langle \nabla p_g \rangle_R = \varepsilon_g \nabla \langle p_g \rangle_g + \langle p_g \rangle_g \nabla \varepsilon_g + \frac{1}{V_R} \int_{A_{gs}} \langle p_g \rangle_g \cdot \mathbf{n_\beta} dA$$

$$+ \frac{1}{V_R} \int_{A_{gs}} \widehat{p_g} \cdot \mathbf{n_\beta} dA \qquad (C.115)$$

The intrinsic volume average of pressure can be taken out of integral which will yields [57].

$$\langle p_g \rangle_g \frac{1}{V_R} \int_{A_{gs}} \mathbf{n_\beta} \, dA = -\langle p_g \rangle_g \nabla \varepsilon_g \qquad (C.116)$$

Substituting this term will cancel the second term on the right hand side of Equation C.115 and it will take the following form,

$$\langle \nabla p_g \rangle_R = \varepsilon_g \nabla \langle p_g \rangle_g + \frac{1}{V_R} \int_{A_{gs}} \widehat{p_g} \cdot \mathbf{n_\beta} dA \qquad (C.117)$$

After completing the expansion of the pressure gradient term in Equation C.146, expansion of the second term can be discussed. The second term on the right hand side of Equation C.112 can be written as;

$$\langle \nabla . \nabla \mathbf{V_g} \rangle_R = \nabla . \langle \nabla \mathbf{V_g} \rangle_R + \frac{1}{V_R} \int_{A_{gs}} \mathbf{n_\beta} . \nabla \mathbf{V_g} dA \qquad (C.118)$$

Similar to the pressure variable also velocity field can be expressed in terms of intrinsic phase average and its spatial deviation which will yields.

$$\langle \nabla . \nabla \mathbf{V_g} \rangle_R = \nabla . \langle \nabla \mathbf{V_g} \rangle_R + \frac{1}{V_R} \int_{A_{gs}} \mathbf{n_\beta} . \nabla \langle \mathbf{V_g} \rangle_\mathbf{g} dA$$

$$+ \frac{1}{V_R} \int_{A_{gs}} \mathbf{n_\beta} . \nabla \widehat{\mathbf{V_g}} dA \qquad (C.119)$$

It is possible to express the second term on the right hand side of Equation C.119 by taking the intrinsic averaged term out of the integral as,

$$\boldsymbol{\nabla}\langle \mathbf{V_g} \rangle_{\mathbf{g}} \frac{1}{V_R} \int\limits_{A_{gs}} \mathbf{n_\beta} \, . \, dA = -\boldsymbol{\nabla}\varepsilon_g . \boldsymbol{\nabla}\langle \mathbf{V_g} \rangle_{\mathbf{g}} \qquad (C.120)$$

This term can be moved out of area integral regarding the length scale analysis given by Whitaker [57].

By using the expression given above Equation C.119 can be rewritten as,

$$\langle \boldsymbol{\nabla} . \boldsymbol{\nabla} \mathbf{V_g} \rangle_R = \boldsymbol{\nabla} . \langle \boldsymbol{\nabla} \mathbf{V_g} \rangle_R - \boldsymbol{\nabla}\varepsilon_g . \boldsymbol{\nabla}\langle \mathbf{V_g} \rangle_{\mathbf{g}} + \frac{1}{V_R} \int\limits_{A_{gs}} \mathbf{n_\beta} \, . \, \boldsymbol{\nabla}\widehat{\mathbf{V_g}} dA \qquad (C.121)$$

The first term of Equation C.121 can be expressed by using the averaging theorem as,

$$\boldsymbol{\nabla} . \langle \boldsymbol{\nabla} \mathbf{V_g} \rangle_R = \boldsymbol{\nabla^2} \langle \mathbf{V_g} \rangle_R + \boldsymbol{\nabla} . \left(\frac{1}{V_R} \int\limits_{A_{gs}} \mathbf{n_\beta} \, . \, \mathbf{V_g} dA \right) \qquad (C.122)$$

For the derivation of the momentum conservation equation, effect of adsorption-desorption will not be taken into account and for this reason, at the gas-solid phase interface no slip condition will be assumed. Additionally the interface velocity is assumed to be equal to zero as previously done. Regarding this assumption second term on the right hand side of Equation C.122 will be equal to zero. Substituting Equation C.122 into Equation C.121 after this simplification will yields,

$$\langle \boldsymbol{\nabla} . \boldsymbol{\nabla} \mathbf{V_g} \rangle_R = \boldsymbol{\nabla^2} \langle \mathbf{V_g} \rangle_R - \boldsymbol{\nabla}\varepsilon_g . \boldsymbol{\nabla}\langle \mathbf{V_g} \rangle_{\mathbf{g}} + \frac{1}{V_R} \int\limits_{A_{gs}} \mathbf{n_\beta} \, . \, \boldsymbol{\nabla}\widehat{\mathbf{V_g}} dA \qquad (C.123)$$

Substituting the decomposed forms of the volume averaged pressure gradient and viscous force terms into Equation C.113 will result in,

$$0 = -\varepsilon_g \boldsymbol{\nabla}\langle p_g\rangle_g - \frac{1}{V_R}\int_{A_{gs}} \widehat{p_g}\cdot \mathbf{n_\beta} dA \; + \mu_g \boldsymbol{\nabla^2}\langle \mathbf{V_g}\rangle_R - \mu_g \boldsymbol{\nabla}\varepsilon_g . \boldsymbol{\nabla}\langle \mathbf{V_g}\rangle_\mathbf{g}$$

$$+ \mu_g \frac{1}{V_R}\int_{A_{gs}} \mathbf{n_\beta} . \boldsymbol{\nabla}\widehat{\mathbf{V_g}} dA \qquad (C.124)$$

The superficial velocity can be replaced by the intrinsic phase average by using the relation given below,

$$\langle \mathbf{V_g}\rangle_R = \varepsilon_g \langle \mathbf{V_g}\rangle_g \qquad (C.125)$$

$$\boldsymbol{\nabla^2}\langle \mathbf{V_g}\rangle_R = \varepsilon_g \boldsymbol{\nabla^2}\langle \mathbf{V_g}\rangle_g + \langle \mathbf{V_g}\rangle_g \boldsymbol{\nabla^2}\varepsilon_g \qquad (C.126)$$

Additionally the spatial deviation of pressure can be expressed as a tensor by multiplying with the unit tensor as,

$$\widehat{p_g}\begin{bmatrix}1 & 0 & 0\\ 0 & 1 & 0\\ 0 & 0 & 1\end{bmatrix} = \mathbf{I}\widehat{p_g} \qquad (C.127)$$

Replacing the expressions given above into Equation C.124, it could be rewritten after a rearrangement as,

$$0 = -\varepsilon_g \boldsymbol{\nabla}\langle p_g\rangle_g - \frac{1}{V_R}\int_{A_{gs}} \mathbf{n_\beta}.\mathbf{I}\widehat{p_g}\, dA \; + \mu_g \varepsilon_g \boldsymbol{\nabla^2}\langle \mathbf{V_g}\rangle_g + \mu_g \langle \mathbf{V_g}\rangle_g \boldsymbol{\nabla^2}\varepsilon_g$$

$$- \mu_g \boldsymbol{\nabla}\varepsilon_g . \boldsymbol{\nabla}\langle \mathbf{V_g}\rangle_\mathbf{g} + \frac{1}{V_R}\int_{A_{gs}} \mathbf{n_\beta} . \mu_g \boldsymbol{\nabla}\widehat{\mathbf{V_g}} dA \qquad (C.128)$$

Since the gas phase volume fraction is assumed to be equal to total porosity and porosity is assumed to be uniformly distributed within the packed bed, terms with the gas phase volume fraction gradient will yield a value of zero. After dividing each term with the volume fraction of gas phase, Equation C.128 will take the following form,

$$0 = -\boldsymbol{\nabla}\langle p_g\rangle_g + \frac{1}{V_g}\int\limits_{A_{gs}} \mathbf{n_\beta}.\left(-\mathbf{I}\widehat{p_g} + \mu_g\boldsymbol{\nabla}\widehat{\mathbf{V_g}}\right) dA \; + \mu_g\boldsymbol{\nabla}^{\mathbf{2}}\langle \mathbf{V_g}\rangle_g \qquad (C.129)$$

The third term on the right hand side of Equation C.129 is known as Brinkman correction term and can be neglected as a result of order of magnitude estimates given below,

$$\boldsymbol{\nabla}\widehat{\mathbf{V_g}} = \mathbf{O}\left(\frac{\widehat{\mathbf{V_g}}}{L_g}\right) \qquad (C.130)$$

Since the no slip boundary condition is assumed during derivation of the momentum conservation equation, the magnitude of spatial deviation of velocity will be equal to the order of magnitude of intrinsic phase average of velocity which can be expressed as,

$$\widehat{\mathbf{V_g}} = \mathbf{O}\left(\langle \mathbf{V_g}\rangle_g\right) \qquad (C.131)$$

Regarding the order of magnitude estimates given above, the order of magnitude for the second term on the right hand side of Equation C.161 can be expressed as,

$$\frac{1}{V_g}\int\limits_{A_{gs}} \mathbf{n_\beta}.\left(-\mathbf{I}\widehat{p_g} + \mu_g\boldsymbol{\nabla}\widehat{\mathbf{V_g}}\right) dA = \mathbf{O}\left(\frac{\mu_g\langle \mathbf{V_g}\rangle_g}{L_g^2}\right) \qquad (C.132)$$

The length scale associated with the interface area divided by the phase averaging volume is taken as L_g and the magnitude of spatial deviation of pressure is assumed to be same with the$\mu_g \nabla \widehat{\mathbf{V_g}}$.

The order of magnitude estimate for Brinkman correction term will contain two different length scales which are defined by Whitaker [57] in detail and can be written as,

$$\mu_g \nabla^2 \langle \mathbf{V_g} \rangle_g = \mathbf{O}\left(\frac{\mu_g \langle \mathbf{V_g} \rangle_g}{L_v L_{v1}}\right) \qquad (C.133)$$

Since $L_v L_{v1} \gg L_g^2$ the Brinkman correction term will be much smaller than the integral term and can be neglected. After discarding the Brinkman correction, the final form of the volume averaged momentum conservation equation will be,

$$0 = -\nabla \langle p_g \rangle_g + \frac{1}{V_g} \int_{A_{gs}} \mathbf{n_\beta} . \left(-\mathbf{I}\widehat{p_g} + \mu_g \nabla \widehat{\mathbf{V_g}}\right) dA \qquad (C.134)$$

At this point instead of solving a complex closure problem to determine the expression for the second term on the right hand side of Equation C.134, by adopting the result obtained from the closure problem which is solved by Whitaker [57].

$$\frac{1}{V_g} \int_{A_{gs}} \mathbf{n_\beta} . \left(-\mathbf{I}\widehat{p_g} + \mu_g \nabla \widehat{\mathbf{V_g}}\right) dA = -\frac{\mu_g \varepsilon_g}{\boldsymbol{\kappa_g}} \langle \mathbf{V_g} \rangle_g \qquad (C.135)$$

In Equation C.135 $\boldsymbol{\kappa_g}$ represents the permeability tensor which is assumed to be isotropic in this study. The permeability tensor can be expressed in terms of a permeability value as,

$$\boldsymbol{\kappa}_{\mathbf{g}} = \kappa_g \begin{bmatrix} 1 & 0 & 0 \\ 0 & 1 & 0 \\ 0 & 0 & 1 \end{bmatrix} \qquad (C.136)$$

By using the expressions given above it is possible to write Equation C.134 as,

$$0 = -\boldsymbol{\nabla}\langle p_g \rangle_g - \frac{\mu_g \varepsilon_g}{\kappa_g} \langle \mathbf{V_g} \rangle_g \qquad (C.137)$$

Rearranging Equation C.137 an expression for the superficial velocity could be obtained as,

$$\langle \mathbf{V_g} \rangle_R = -\frac{\kappa_g}{\mu_g} \boldsymbol{\nabla}\langle p_g \rangle_g \qquad (C.138)$$

As previously done, the intrinsic phase averages will be replaced with the point properties assuming that variations are negligibly small [57, 17]. The velocity can be defined as,

$$\mathbf{V_g} = -\frac{\kappa_g}{\mu_g} \boldsymbol{\nabla} p_g \qquad (C.139)$$

The permeability value is defined by the well-known Kozeny-Carman equation as a function of adsorbent particle diameter and bed porosity as [68];

$$\kappa_g = \frac{d_p^2 \varepsilon_b^3}{180(1-\varepsilon_b)^2} \qquad (C.140)$$

In Equation C.140 κ_g denotes the permeability of the packed bed while d_p represents the diameter of the solid particles.

C.3.3 Energy Conservation Equation for the Gas Phase Based on Local Thermal Non-Equilibrium (LTNE) Approach

As mentioned earlier, the energy equation for different phases within the packed bed will be derived by using the volume averaging approach. In this section the macroscopic energy equation for the gas phase within the packed bed will be derived form the microscopic pore scale equations by using the averaging approach. As a starting point differential form of energy conservation equation with convective, conductive terms can be written for the pore scale as,

$$\frac{\partial(\rho_g c_{pg} T_g)}{\partial t} + \boldsymbol{\nabla}.\left(\rho_g \mathbf{V_g} c_{pg} T_g\right) = \boldsymbol{\nabla}.\left(k_g \boldsymbol{\nabla} T_g\right) \qquad (C.141)$$

Before going through the averaging procedure, it should be noted that at the solid and gas phase interface heat fluxes to and from each phase and the temperature of the phases are equal. The interface area is denoted as A_{gs} and the heat flux and temperature conditions can be shown as;

$$T_g = T_s \qquad (C.142)$$

$$k_g \mathbf{n_{gs}}.\boldsymbol{\nabla} T_g = k_s \mathbf{n_{gs}}.\boldsymbol{\nabla} T_s \qquad (C.143)$$

In Equation C.143 $\mathbf{n_{gs}}$ represents the outward normal vector of the phase interface surface.

After phase averaging applied to the energy conservation equation given in Equation C.141, the result will be,

$$\langle\frac{\partial(\rho_g c_{pg} T_g)}{\partial t}\rangle_R + \langle\boldsymbol{\nabla}.\left(\rho_g \mathbf{V_g} c_{pg} T_g\right)\rangle_R = \langle\boldsymbol{\nabla}.\left(k_g \boldsymbol{\nabla} T_g\right)\rangle_R \qquad (C.144)$$

The averaged form of the energy conservation equation will be discussed term by term starting with the first term on the left hand side. The first term represents the net rate of change of energy of the REV and can be expanded as;

$$\frac{\partial\langle(\rho_g c_{pg} T_g)\rangle_R}{\partial t} = \frac{\partial\left(\varepsilon_g\langle c_{pg}\rangle_g\langle\rho_g\rangle_g\langle T_g\rangle_g\right)}{\partial t} + \frac{\partial(\langle c_{pg}\rangle_g\langle\widehat{\rho_g}\widehat{T_g}\rangle_R)}{\partial t}$$
$$+ \frac{\partial(\langle\rho_g\rangle_g\langle\widehat{c_{pg}}\widehat{T_g}\rangle_R)}{\partial t} + \frac{\partial(\langle T_g\rangle_g\langle\widehat{c_{pg}}\widehat{\rho_g}\rangle_R)}{\partial t} + \frac{\partial(\langle\widehat{c_{pg}}\widehat{\rho_g}\widehat{T_g}\rangle_R)}{\partial t} \qquad (C.145)$$

Since the variation of the specific heat, density and the temperature of the gas phase within the averaging volume is very small, it is assumed to be constant and taken as a point property for the averaging volume. For this reason terms which include the product of deviations of these variables C.145 can be neglected due to the order of magnitude estimates which can be expressed as [67],

$$\frac{\partial(\langle c_{pg}\rangle_g\langle\widehat{\rho_g}\widehat{T_g}\rangle)}{\partial t} \ll \frac{\partial\left(\varepsilon_g\langle c_{pg}\rangle_g\langle\rho_g\rangle_g\langle T_g\rangle_g\right)}{\partial t} \qquad (C.146)$$

$$\frac{\partial(\langle\rho_g\rangle_g\langle\widehat{c_{pg}}\widehat{T_g}\rangle)}{\partial t} \ll \frac{\partial\left(\varepsilon_g\langle c_{pg}\rangle_g\langle\rho_g\rangle_g\langle T_g\rangle_g\right)}{\partial t} \qquad (C.147)$$

$$\frac{\partial(\langle T_g\rangle_g\langle\widehat{c_{pg}}\widehat{\rho_g}\rangle)}{\partial t} \ll \frac{\partial\left(\varepsilon_g\langle c_{pg}\rangle_g\langle\rho_g\rangle_g\langle T_g\rangle_g\right)}{\partial t} \qquad (C.148)$$

$$\frac{\partial(\langle\widehat{c_{pg}}\widehat{\rho_g}\widehat{T_g}\rangle)}{\partial t} \ll \frac{\partial\left(\varepsilon_g\langle c_{pg}\rangle_g\langle\rho_g\rangle_g\langle T_g\rangle_g\right)}{\partial t} \qquad (C.149)$$

The second term in the energy equation which represents the rate of convective heat transfer can be expanded as follows, after phase averaging.

$$\langle \nabla . \left(\rho_g \mathbf{V_g} c_{pg} T_g\right)\rangle_R = \nabla . \langle \rho_g \mathbf{V_g} c_{pg} T_g \rangle_R + \frac{1}{V_R} \int_{A_{gs}} \rho_g c_{pg} \mathbf{n_{gs}} . \mathbf{V_g} T_g \, dA = 0 \qquad (C.150)$$

The first term in the right hand side can be expanded after expressing the each variable in terms of its intrinsic phase average and deviation as;

$$\rho_g = \langle \rho_g \rangle_g + \widehat{\rho_g} \qquad (C.151)$$

$$\mathbf{V_g} = \langle \mathbf{V_g} \rangle_g + \widehat{\mathbf{V_g}} \qquad (C.152)$$

$$c_{pg} = \langle c_{pg} \rangle_g + \widehat{c_{pg}} \qquad (C.153)$$

$$T_g = \langle T_g \rangle_g + \widehat{T_g} \qquad (C.154)$$

After the intrinsic phase average and deviations are substituted into the first term on the right hand side of Equation C.150 and multiplied, the equation will take the following form,

$$\begin{aligned}
&\nabla . \langle \rho_g \mathbf{V_g} c_{pg} T_g \rangle_R \\
&= \nabla . \langle \langle \rho_g \rangle_g \langle \mathbf{V_g} \rangle_g \langle c_{pg} \rangle_g \langle T_g \rangle_g \rangle_R + \nabla . \langle \langle \rho_g \rangle_g \langle \mathbf{V_g} \rangle_g \langle c_{pg} \rangle_g \widehat{T_g} \, \rangle_R \\
&+ \nabla . \langle \langle \rho_g \rangle_g \langle \mathbf{V_g} \rangle_g \widehat{c_{pg}} \langle T_g \rangle_g \rangle_R + \nabla . \langle \langle \rho_g \rangle_g \widehat{\mathbf{V_g}} \langle c_{pg} \rangle_g \langle T_g \rangle_g \rangle_R \\
&+ \nabla . \langle \widehat{\rho_g} \, \langle \mathbf{V_g} \rangle_g \langle c_{pg} \rangle_g \langle T_g \rangle_g \rangle_R + \nabla . \langle \langle \rho_g \rangle_g \langle \mathbf{V_g} \rangle_g \widehat{c_{pg}}_g \widehat{T_g} \, \rangle_R \\
&+ \nabla . \langle \langle \rho_g \rangle_g \widehat{\mathbf{V_g}} \langle c_{pg} \rangle_g \widehat{T_g} \, \rangle_R + \nabla . \langle \widehat{\rho_g} \, \langle \mathbf{V_g} \rangle_g \langle c_{pg} \rangle_g \widehat{T_g} \, \rangle_R + \nabla . \langle \langle \rho_g \rangle_g \widehat{\mathbf{V_g}} \widehat{c_{pg}}_g \widehat{T_g} \, \rangle_R \\
&+ \nabla . \langle \widehat{\rho_g} \langle \mathbf{V_g} \rangle_g \widehat{c_{pg}}_g \widehat{T_g} \, \rangle_R + + \nabla . \langle \widehat{\rho_g} \widehat{\mathbf{V_g}} \langle c_{pg} \rangle_g \widehat{T_g} \, \rangle_R + \nabla . \langle \widehat{\rho_g} \widehat{\mathbf{V_g}} \widehat{c_{pg}}_g \langle T_g \rangle_g \rangle_R \\
&+ \nabla . \langle \langle \rho_g \rangle_g \widehat{\mathbf{V_g}} \widehat{c_{pg}} \langle T_g \rangle_g \rangle_R + \nabla . \langle \widehat{\rho_g} \, \langle \mathbf{V_g} \rangle_g \widehat{c_{pg}} \langle T_g \rangle_g \rangle_R \\
&+ \nabla . \langle \widehat{\rho_g} \widehat{\mathbf{V_g}} \langle c_{pg} \rangle_g \langle T_g \rangle_g \rangle_R + \nabla . \langle \widehat{\rho_g} \widehat{\mathbf{V_g}} \widehat{c_{pg}}_g \widehat{T_g} \rangle_R \qquad (C.155)
\end{aligned}$$

Since the phase average of terms containing single deviation will be equal to zero these variables as can be discarded. The deviation of variables except the velocity is relatively small compared to the average values. The velocity deviations are on the order of the average value of the velocity term, therefore the terms with products of two deviations except velocity will be neglected. Moreover, the terms including the product three or more deviations are negligibly small compared to other terms and will be discarded [17, 67]. Consequently after discarding the negligible terms the Equation C.155 will take the following form,

$$\begin{aligned}
&\boldsymbol{\nabla}.\langle \rho_g \mathbf{V_g} c_{pg} T_g \rangle_R \\
&= \boldsymbol{\nabla}.\langle \langle \rho_g \rangle_g \langle \mathbf{V_g} \rangle_g \langle c_{pg} \rangle_g \langle T_g \rangle_g \rangle_R + \boldsymbol{\nabla}.\langle \langle \rho_g \rangle_g \widehat{\mathbf{V_g}} \langle c_{pg} \rangle_g \widehat{T_g} \, \rangle_R \\
&+ \boldsymbol{\nabla}.\langle \langle \rho_g \rangle_g \widehat{\mathbf{V_g}} \widehat{c_{pg}} \langle T_g \rangle_g \rangle \\
&+ \boldsymbol{\nabla}.\langle \widehat{\rho_g} \widehat{\mathbf{V_g}} \langle c_{pg} \rangle_g \langle T_g \rangle_g \rangle_{R_R} \qquad (C.156)
\end{aligned}$$

As mentioned earlier the phase average of intrinsic phase average of a variable will be equal to the phase average of this variable. Applying this rule for the velocity variable, Equation C.155 can be rewritten as,

$$\begin{aligned}
&\boldsymbol{\nabla}.\langle \rho_g \mathbf{V_g} c_{pg} T_g \rangle_R \\
&= \boldsymbol{\nabla}.\left(\langle \rho_g \rangle_g \langle \mathbf{V_g} \rangle_R \langle c_{pg} \rangle_g \langle T_g \rangle_g \right) + \boldsymbol{\nabla}.\left(\langle \rho_g \rangle_g \langle c_{pg} \rangle_g \langle \widehat{\mathbf{V_g}} \widehat{T_g} \rangle_R \right) \\
&+ \boldsymbol{\nabla}.\left(\langle \rho_g \rangle_g \langle \widehat{\mathbf{V_g}} \widehat{c_{pg}} \rangle_R \langle T_g \rangle_g \right) \\
&+ \boldsymbol{\nabla}.\left(\langle \widehat{\rho_g} \widehat{\mathbf{V_g}} \rangle_R \langle c_{pg} \rangle_g \langle T_g \rangle_g \right) \qquad (C.157)
\end{aligned}$$

In Equation C.157 the averaged values are taken out of the integral. The first term on the right hand side of Equation C.157 can be rewritten after application of chain rule for differentiation.

$$\nabla.\left(\langle\rho_g\rangle_g\langle\mathbf{V_g}\rangle_R\langle c_{pg}\rangle_g\langle T_g\rangle_g\right)$$
$$=\langle T_g\rangle_g\nabla.\left(\langle\rho_g\rangle_g\langle c_{pg}\rangle_g\langle\mathbf{V_g}\rangle_R\right)+\left(\langle\rho_g\rangle_g\langle c_{pg}\rangle_g\langle\mathbf{V_g}\rangle_R\right).\nabla\langle T_g\rangle_g \qquad (C.158)$$

Similarly the third and fourth terms on the right hand side of Equation C.157 can be rewritten as;

$$\nabla.\left(\langle\rho_g\rangle_g\langle\widehat{\mathbf{V_g}}\widehat{c_{pg}}\rangle_R\langle T_g\rangle_g\right)$$
$$=\langle T_g\rangle_g\nabla.\left(\langle\rho_g\rangle_g\langle\widehat{\mathbf{V_g}}\widehat{c_{pg}}\rangle_R\right)$$
$$+\left(\langle\rho_g\rangle_g\langle\widehat{\mathbf{V_g}}\widehat{c_{pg}}\rangle_R\right).\nabla\langle T_g\rangle_g \qquad (C.159)$$

$$\nabla.\left(\langle\widehat{\rho_g}\widehat{\mathbf{V_g}}\rangle_R\langle c_{pg}\rangle_g\langle T_g\rangle_g\right)$$
$$=\langle T_g\rangle_g\nabla.\left(\langle\widehat{\rho_g}\widehat{\mathbf{V_g}}\rangle_R\langle c_{pg}\rangle_g\right)+\left(\langle\widehat{\rho_g}\widehat{\mathbf{V_g}}\rangle_R\langle c_{pg}\rangle_g\right).\nabla\langle T_g\rangle_g \qquad (C.160)$$

Substitution of the expanded form of the terms into Equation C.157 results in,

$$\nabla.\langle\rho_g\mathbf{V_g}c_{pg}T_g\rangle_R$$
$$=\langle T_g\rangle_g\nabla.\left(\langle\rho_g\rangle_g\langle c_{pg}\rangle_g\langle\mathbf{V_g}\rangle_R\right)+\left(\langle\rho_g\rangle_g\langle c_{pg}\rangle_g\langle\mathbf{V_g}\rangle_R\right).\nabla\langle T_g\rangle_g$$
$$+\nabla.\left(\langle\rho_g\rangle_g\langle c_{pg}\rangle_g\langle\widehat{\mathbf{V_g}}\widehat{T_g}\rangle_R\right)+\langle T_g\rangle_g\nabla.\left(\langle\rho_g\rangle_g\langle\widehat{\mathbf{V_g}}\widehat{c_{pg}}\rangle_R\right)$$
$$+\left(\langle\rho_g\rangle_g\langle\widehat{\mathbf{V_g}}\widehat{c_{pg}}\rangle_R\right).\nabla\langle T_g\rangle_g+\langle T_g\rangle_g\nabla.\left(\langle\widehat{\rho_g}\widehat{\mathbf{V_g}}\rangle_R\langle c_{pg}\rangle_g\right)$$
$$+\left(\langle\widehat{\rho_g}\widehat{\mathbf{V_g}}\rangle_R\langle c_{pg}\rangle_g\right).\nabla\langle T_g\rangle_g \qquad (C.161)$$

Since expansion and rearrangement of the first term in Equation C.150 had been completed, the second term on the left hand side of Equation C.150 can be revisited. Same volume averaging procedure will be followed here with the derivation of mass conservation equation. Therefore using the definition given in Equation C.97 this term can be rewritten as,

$$\frac{1}{V_R}\int_{A_{gs}}\rho_g c_{pg}\mathbf{n_{gs}}.\mathbf{V_g}T_g\,dA=\frac{1}{V_R}\int_{A_{gs}}c_{pg}T_g\Omega_g\,dA \qquad (C.162)$$

It is possible to express the right hand side of Equation C.162 in terms of intrinsic area average at the interface area of solid and gas phases.

$$\frac{A_{gs}}{V_R}\frac{1}{A_{gs}}\int_{A_{gs}} c_{pg}T_g\Omega_g\,dA \;=\; a_{gs}c_{pg}\langle T_g\Omega_g\rangle_{gs} \qquad (C.163)$$

It had been stated that the solid and gas phase temperatures are equal at the phase interface, thus Equation C.163 can be written in terms of solid phase temperature as,

$$a_{gs}c_{pg}\langle T_g\Omega_g\rangle_{gs} = a_{gs}c_{pg}\langle T_s\Omega_g\rangle_{gs} \qquad (C.164)$$

The Equation C.164 can be expressed in terms of intrinsic interface area average of the variables and their deviations as,

$$a_{gs}c_{pg}\langle T_s\Omega_g\rangle_{gs} = a_{gs}c_{pg}\langle T_s\rangle_{gs}\langle\Omega_g\rangle_{gs} + a_{gs}c_{pg}\langle\widehat{T_s}\widehat{\Omega_g}\rangle_{gs} \qquad (C.165)$$

In the equation given above the last term on the right hand side is named as the dispersive energy flux and discarded by Hager et al.[67]. Although the justification of this simplification had not been done yet this term will also be ignored in this study.

Up this point the volume averages of terms representing rate of energy change within the REV and the rate of convective heat transfer had been expanded, simplified, and rearranged. The next step will be the investigation of the term on the right hand side of Equation C.144 which represents rate of conductive energy transfer. After averaging this term can be written as,

$$\langle\boldsymbol{\nabla}.\left(k_g\boldsymbol{\nabla}T_g\right)\rangle_R = \boldsymbol{\nabla}.\langle k_g\boldsymbol{\nabla}T_g\rangle_R + \frac{1}{V_R}\int_{A_{gs}} k_g\mathbf{n_{gs}}.\boldsymbol{\nabla}T_g\,dA \qquad (C.166)$$

Assuming that the thermal conductivity of the gas phase is not varying over the averaging volume first term on the right hand side of Equation C.166 can be expanded as,

$$\boldsymbol{\nabla}.\langle k_g \boldsymbol{\nabla} T_g \rangle_R = \boldsymbol{\nabla}.\left(k_g \boldsymbol{\nabla} \langle T_g \rangle_R + \frac{k_g}{V_R} \int\limits_{A_{gs}} \mathbf{n_{gs}} T_g \, dA \right) \tag{C.167}$$

$$\boldsymbol{\nabla}.\langle k_g \boldsymbol{\nabla} T_g \rangle_R = \boldsymbol{\nabla}.\left(\varepsilon_g k_g \boldsymbol{\nabla} \langle T_g \rangle_g + \frac{k_g}{V_R} \int\limits_{A_{gs}} \mathbf{n_{gs}} \langle T_g \rangle_g \, dA \right.$$

$$\left. + \frac{k_g}{V_R} \int\limits_{A_{gs}} \mathbf{n_{gs}} \widehat{T_g} \, dA \right) \tag{C.168}$$

The second term on the right hand side of Equation C.168 will be equal to zero since the average temperature is constant over the area of integration and the remaining terms will yield a zero value after integration [158]. After substituting the Equation C.168 into Equation C.166 the result will be,

$$\langle \boldsymbol{\nabla}.\left(k_g \boldsymbol{\nabla} T_g \right) \rangle_R = \boldsymbol{\nabla}.\left(\varepsilon_g k_g \boldsymbol{\nabla} \langle T_g \rangle_g + \frac{k_g}{V_R} \int\limits_{A_{gs}} \mathbf{n_{gs}} \widehat{T_g} dA \right)$$

$$+ \frac{1}{V_R} \int\limits_{A_{gs}} k_g \mathbf{n_{gs}}.\boldsymbol{\nabla} T_g \, dA \tag{C.169}$$

After replacing the all expanded terms into the energy conservation equation given in Equation C.144, the final form of the equation will be,

$$\frac{\partial\left(\varepsilon_g\langle c_{pg}\rangle_g\langle\rho_g\rangle_g\langle T_g\rangle_g\right)}{\partial t}+\langle T_g\rangle_g\boldsymbol{\nabla}.\left(\langle\rho_g\rangle_g\langle c_{pg}\rangle_g\langle\mathbf{V_g}\rangle_R\right)$$
$$+\left(\langle\rho_g\rangle_g\langle c_{pg}\rangle_g\langle\mathbf{V_g}\rangle_R\right).\boldsymbol{\nabla}\langle T_g\rangle_g+\boldsymbol{\nabla}.\left(\langle\rho_g\rangle_g\langle c_{pg}\rangle_g\langle\widehat{\mathbf{V_g}}\widehat{T_g}\rangle_R\right)$$
$$+\langle T_g\rangle_g\boldsymbol{\nabla}.\left(\langle\rho_g\rangle_g\langle\widehat{\mathbf{V_g}}\widehat{c_{pg}}\rangle_R\right)+\left(\langle\rho_g\rangle_g\langle\widehat{\mathbf{V_g}}\widehat{c_{pg}}\rangle_R\right).\boldsymbol{\nabla}\langle T_g\rangle_g$$
$$+\langle T_g\rangle_g\boldsymbol{\nabla}.\left(\langle\widehat{\rho_g}\widehat{\mathbf{V_g}}\rangle_R\langle c_{pg}\rangle_g\right)+\left(\langle\widehat{\rho_g}\widehat{\mathbf{V_g}}\rangle_R\langle c_{pg}\rangle_g\right).\boldsymbol{\nabla}\langle T_g\rangle_g+a_{gs}c_{pg}\langle T_s\rangle_{gs}\langle\Omega_g\rangle_{gs}$$
$$=\boldsymbol{\nabla}.\left(\varepsilon_g k_g\boldsymbol{\nabla}\langle T_g\rangle_g+\frac{k_g}{V_R}\int\limits_{A_{gs}}\mathbf{n_{gs}}\widehat{T_g}\,dA\right)+\frac{1}{V_R}\int\limits_{A_{gs}}k_g\mathbf{n_{gs}}.\boldsymbol{\nabla}T_g\,dA \qquad (C.170)$$

A further simplification can be done on Equation C.170 based on the order of magnitude comparisons given below [67],

$$\widehat{\rho_g}\ll\langle\rho_g\rangle_g \qquad (C.171)$$

As mentioned earlier the specific heat deviation within the averaging volume is also assumed to be negligibly small compared to its intrinsic phase average.

$$\widehat{c_{pg}}\ll\langle c_{pg}\rangle_g \qquad (C.172)$$

However the deviation of the velocity field within the averaging volume is assumed to be on the order of intrinsic phase average which yields,

$$\langle\widehat{\rho_g}\widehat{\mathbf{V_g}}\rangle_R\ll\langle\rho_g\rangle_g\langle\mathbf{V_g}\rangle_R \qquad (C.173)$$

$$\langle\widehat{c_{gp}}\widehat{\mathbf{V_g}}\rangle_R\ll\langle c_{pg}\rangle_g\langle\mathbf{V_g}\rangle_R \qquad (C.174)$$

Thus the terms with the product of deviations given in Equation C.173 and Equation C.174 can be neglected. After discarding these terms Equation C.170 can be rewritten as,

$$\frac{\partial\left(\varepsilon_g\langle c_{pg}\rangle_g\langle\rho_g\rangle_g\langle T_g\rangle_g\right)}{\partial t}+\langle c_{pg}\rangle_g\langle T_g\rangle_g\boldsymbol{\nabla}.\left(\langle\rho_g\rangle_g\langle\mathbf{V_g}\rangle_R\right)$$
$$+\langle\rho_g\rangle_g\langle\mathbf{V_g}\rangle_R\langle T_g\rangle_g\boldsymbol{\nabla}.\left(\langle c_{pg}\rangle_g\right)+\left(\langle\rho_g\rangle_g\langle c_{pg}\rangle_g\langle\mathbf{V_g}\rangle_R\right).\boldsymbol{\nabla}\langle T_g\rangle_g$$
$$+\boldsymbol{\nabla}.\left(\langle\rho_g\rangle_g\langle c_{pg}\rangle_g\langle\widehat{\mathbf{V_g}}\widehat{T_g}\rangle_R\right)+a_{gs}c_{pg}\langle T_s\rangle_{gs}\langle\Omega_g\rangle_{gs}$$
$$=\boldsymbol{\nabla}\varepsilon_g k_g\boldsymbol{\nabla}\langle T_g\rangle_g+\boldsymbol{\nabla}\left(\frac{k_g}{V_R}\int\limits_{A_{gs}}\mathbf{n_{gs}}\widehat{T_g}\,dA\right)+\frac{1}{V_R}\int\limits_{A_{gs}}k_g\mathbf{n_{gs}}.\boldsymbol{\nabla}T_g\,dA \qquad (C.175)$$

A further simplification can be done on Equation C.175 by subtracting the volume averaged continuity equation which is derived earlier after multiplication with intrinsic phase average of temperature and the heat capacity. The volume averaged continuity equation after multiplication with the mentioned variables can be expressed as,

$$\langle c_{pg}\rangle_g\langle T_g\rangle_g\frac{\partial\left(\varepsilon_g\langle\rho_g\rangle_g\right)}{\partial t}+\langle c_{pg}\rangle_g\langle T_g\rangle_g\boldsymbol{\nabla}.\langle\rho_g\rangle_g\langle\mathbf{V_g}\rangle_R+\langle c_{pg}\rangle_g\langle T_g\rangle_g a_{gs}\langle\Omega_g\rangle_{gs}$$
$$=0 \qquad (C.176)$$

After subtracting Equation C.176 from Equation C.175 one will obtain,

$$\varepsilon_g\langle\rho_g\rangle_g\frac{\partial\left(\langle c_{pg}\rangle_g\langle T_g\rangle_g\right)}{\partial t}+\langle\rho_g\rangle_g\langle\mathbf{V_g}\rangle_R\langle T_g\rangle_g\boldsymbol{\nabla}.\left(\langle c_{pg}\rangle_g\right)$$
$$+\left(\langle\rho_g\rangle_g\langle c_{pg}\rangle_g\langle\mathbf{V_g}\rangle_R\right).\boldsymbol{\nabla}\langle T_g\rangle_g+\boldsymbol{\nabla}.\left(\langle\rho_g\rangle_g\langle c_{pg}\rangle_g\langle\widehat{\mathbf{V_g}}\widehat{T_g}\rangle_R\right)$$
$$+a_{gs}c_{pg}\left(\langle T_s\rangle_{gs}-\langle T_g\rangle_g\right)\langle\Omega_g\rangle_{gs}$$
$$=\boldsymbol{\nabla}\left(\varepsilon_g k_g\boldsymbol{\nabla}\langle T_g\rangle_g+\frac{k_g}{V_R}\int\limits_{A_{gs}}\mathbf{n_{gs}}\widehat{T_g}\,dA\right)+\frac{1}{V_R}\int\limits_{A_{gs}}k_g\mathbf{n_{gs}}.\boldsymbol{\nabla}T_g\,dA \qquad (C.177)$$

Theoretical evaluation of the terms including the deviations could be extremely cumbersome and complicated. Therefore in the literature [67,158] these terms are interpreted by considering the phenomena which they corresponds. For instance the

fourth term on the left hand side of Equation C.177 represents the mechanical or convective dispersion and could be expressed similar to the diffusion process. For this purpose the dispersion process is modeled as gradient of the averaged variable which will be the driving force multiplied by a coefficient. According to this approach the dispersive flux term can be expressed as [67];

$$\langle \rho_g \rangle_g \langle c_{pg} \rangle_g \langle \widehat{\mathbf{V}_\mathbf{g}} \widehat{T_g} \rangle_R = -\mathbf{K_{gm}} \boldsymbol{\nabla} \langle T_g \rangle_g \qquad (C.178)$$

In Equation C.178 $\mathbf{K_{gm}}$, is the hydrodynamic dispersion tensor; however it would not be possible to evaluate this coefficient theoretically. Another term which contains the deviation of temperature is the first term on the right hand side of the Equation C.177. This term represents the molecular or conductive dispersion and similar to the mechanical or convective dispersion, modeled by using the gradient of the averaged variable and a coefficient [67].

$$\varepsilon_g k_g \boldsymbol{\nabla} \langle T_g \rangle_g + \frac{k_g}{V_R} \int_{A_{gs}} \mathbf{n_{gs}} \widehat{T_g} \, dA = \mathbf{K_{ge}} \boldsymbol{\nabla} \langle T_g \rangle_g \qquad (C.179)$$

In Equation C.179 $\mathbf{K_{ge}}$ represents the effective thermal conductivity tensor of the gas phase. The last term on the right hand side of Equation C.177 represents the interfacial heat flux. This term can also be expressed as a simple function of the averaged variables. As a result of the approach followed by Hager et al. [67] this term can be represented by a heat transfer coefficient multiplied by the volume averaged temperature and gas solid phase interface temperature difference which is given as,

$$\frac{1}{V_R} \int_{A_{gs}} k_g \mathbf{n_{gs}} . \boldsymbol{\nabla} T_g \, dA = a_{gs} h_{gs} \left(\langle T_g \rangle_g - \langle T_g \rangle_{gs} \right) \qquad (C.180)$$

As mentioned earlier, at the gas-solid phase interface solid and gas temperatures are equal so it is possible to rewrite Equation C.180 by using the solid temperature as,

$$-\frac{1}{V_R}\int_{A_{gs}} k_g \mathbf{n_{gs}}.\boldsymbol{\nabla} T_g \, dA = a_{gs} h_{gs}\left(\langle T_g\rangle_g - \langle T_s\rangle_{gs}\right) \qquad (C.181)$$

Before writing the final form of the energy conservation equation of the gas phase it should be noted that, the intrinsic phase average of specific heat, density and temperature values are assumed to be equal to the point values since variations within the averaging volume are negligibly small. Using this assumption and expressions redefined above the final form of the energy conservation equation for the gas phase will be written as,

$$\begin{aligned}&\varepsilon_g \rho_g \frac{\partial\left(c_{pg} T_g\right)}{\partial t} + \rho_g \mathbf{V_g}.\boldsymbol{\nabla}\left(c_{pg} T_g\right) - \boldsymbol{\nabla}\left(\mathbf{K_{gm}}.\boldsymbol{\nabla} T_g\right)\\ &+ c_{pg}\left(T_s - T_g\right)(1-\varepsilon_t)\rho_s \frac{\partial X}{\partial t}\\ &= \boldsymbol{\nabla}\left(\mathbf{K_{ge}}.\boldsymbol{\nabla}\langle T_g\rangle_g\right) - a_{gs} h_{gs}\left(T_g - T_s\right) \qquad (C.182)\end{aligned}$$

It would be possible to rearrange Equation C.182 to obtain a more compact form as;

$$\begin{aligned}&\varepsilon_g \rho_g \frac{\partial\left(c_{pg} T_g\right)}{\partial t} + \rho_g \mathbf{V_g}.\boldsymbol{\nabla}\left(c_{pg} T_g\right) + c_{pg}\left(T_s - T_g\right)(1-\varepsilon_t)\rho_s \frac{\partial X}{\partial t}\\ &= \boldsymbol{\nabla}\left(\mathbf{K_{geq}}.\boldsymbol{\nabla}\langle T_g\rangle_g\right) - a_{gs} h_{gs}\left(T_g - T_s\right) \qquad (C.183)\end{aligned}$$

In Equation C.182 K_{geq} represents the equivalent thermal conductivity which is the sum of hydrodynamic dispersion and effective thermal conductivity tensors. The equivalent thermal conductivity tensor will be composed of constant values since the conductive heat transfer for the gas phase is assumed to be isotropic. The equivalent thermal conductivity can be defined as a linear function of total porosity as [75],

$$\mathbf{K_{geq}} = \mathbf{K_{ge}} + \mathbf{K_{gm}} = K_{geq}\begin{bmatrix}1 & 0 & 0\\ 0 & 1 & 0\\ 0 & 0 & 1\end{bmatrix} \qquad (C.184)$$

Where,

$$K_{geq} = \varepsilon_t k_g \qquad (C.185)$$

Additionally the a_{gs} variable in Equation C.183 which represents the gas-solid phase interface area is represented as a specific surface area per unit volume as a function of total porosity and adsorbent particle diameter as [39] ,

$$a_{gs} = \frac{6(1-\varepsilon_t)}{d_p} \qquad (C.186)$$

As mentioned earlier the volume fraction of the gas phase is assumed to be equal to the total porosity of the packed bed since the volume occupied by the adsorbed phase is neglected in this study. Regarding these information a final rearrangement can be made on the energy conservation equation for the gas phase and the final form can be rewritten as follows,

$$\varepsilon_t \rho_g \frac{\partial(c_{pg}T_g)}{\partial t} + \rho_g \mathbf{V_g}.\boldsymbol{\nabla}(c_{pg}T_g) + c_{pg}(T_s - T_g)(1-\varepsilon_t)\rho_s \frac{\partial X}{\partial t}$$
$$= \boldsymbol{\nabla}\left(K_{geq}.\boldsymbol{\nabla}\langle T_g\rangle_g\right) - a_{gs}h_{gs}(T_g - T_s) \qquad (C.187)$$

More details on the volume averaging procedure and the assumptions made during derivation of the energy conservation equation can be found in [45, 67, 159, and 75].

C.3.4 Energy Conservation Equation for the Solid Phase Based on Local Thermal Non-Equilibrium (LTNE) Approach

Upon completing the derivation of energy conservation equation for the gas phase, next step will be the derivation of energy conservation equation for the solid phase in the packed bed. As stated in the previous section there will be thermal equilibrium between solid and gas phases at the phase interface. Since the solid phase is immobile the microscopic energy conservation equation will be composed of rate of change of energy, the conductive energy transfer rate and a heat source. The differential expression of the microscopic energy conservation equation for solid phase can be written as follows,

$$\frac{\partial(\rho_s c_{ps} T_s)}{\partial t} = \boldsymbol{\nabla}.(k_s \boldsymbol{\nabla} T_s) + \dot{Q} \qquad (C.188)$$

The volume averaging procedure that will be applied to Equation C.188 is totally same with the procedure followed during derivation of the energy conservation equation of the gas phase; therefore these steps will be skipped in this section. The volume averaged form of the microscopic energy conservation equation given in Equation C.188 can be written as,

$$\varepsilon_s \langle \rho_s \rangle_s \frac{\partial\left(\langle c_{ps} \rangle_s \langle T_s \rangle_s\right)}{\partial t} + \\ = \boldsymbol{\nabla}\left(\varepsilon_s k_s \boldsymbol{\nabla} \langle T_s \rangle_{\mathbf{s}} + \frac{k_s}{V_R} \int_{A_{gs}} \mathbf{n_{sg}} \widehat{T_s}\, dA \right) + \frac{1}{V_R} \int_{A_{gs}} k_s \mathbf{n_{sg}}.\boldsymbol{\nabla} T_s\, dA + \langle \dot{Q} \rangle_R \qquad (C.189)$$

The simplification made previously for the first term on the right hand side will be done here also as,

$$\varepsilon_s k_s \nabla\langle T_s\rangle_s + \frac{k_s}{V_R}\int_{A_{gs}} \mathbf{n_{sg}}\widehat{T_s}\, dA = \mathbf{K_{se}}\nabla\langle T_s\rangle_s \qquad (C.190)$$

In Equation C.190 $\mathbf{K_{se}}$ is defined as the effective thermal conductivity tensor of the solid phase in presence of gas phase. Similar to the gas phase it will be isotropic and can be represented by a scalar as,

$$\mathbf{K_{seq}} = \mathbf{K_{se}} = K_{seq}\begin{bmatrix}1 & 0 & 0\\ 0 & 1 & 0\\ 0 & 0 & 1\end{bmatrix} \qquad (C.191)$$

The K_{seq} also can be expressed in terms of the volume fraction of solid phase and thermal conductivity of the solid phase as,

$$K_{seq} = (1-\varepsilon_t)k_s \qquad (C.192)$$

After this simplification Equation C.189 will take the following form,

$$\varepsilon_s\langle\rho_s\rangle_s \frac{\partial\left(\langle c_{ps}\rangle_s\langle T_s\rangle_s\right)}{\partial t} +$$
$$= \nabla\left(K_{seq}\nabla\langle T_s\rangle_s\right) + \frac{1}{V_R}\int_{A_{gs}} k_s\mathbf{n_{sg}}.\nabla T_s\, dA + \langle\dot{Q}\rangle_R \qquad (C.193)$$

The second term on the right hand side of Equation C.193 represents the interfacial heat transfer rate and would be equal to the negative of the interfacial heat transfer rate from solid phase to gas phase which was defined by Equation C.181.

$$\frac{1}{V_R}\int_{A_{gs}} k_s\mathbf{n_{sg}}.\nabla T_s\, dA = -\frac{1}{V_R}\int_{A_{gs}} k_g\mathbf{n_{gs}}.\nabla T_g\, dA$$
$$= a_{gs}h_{gs}\left(\langle T_g\rangle_g - \langle T_s\rangle_{gs}\right) \qquad (C.194)$$

The last term on the right hand side of Equation C.189 represents the heat addition to solid phase due to adsorption or heat rejection from solid phase due to desorption. The heat addition or rejection is defined in terms of rate of adsorption-desorption and heat of adsorption as [36],

$$\langle \dot{Q} \rangle_R = (1 - \varepsilon_t)\rho_s \frac{\partial X}{\partial t} \Delta H_{ad} \qquad (C.195)$$

Additionally the heat capacity of the solid phase per unit mass needs to be defined by accounting the effect of adsorbed phase. For this reason the heat capacity of the adsorbed amount is added on the heat capacity of the solid phase. The expression representing the equivalent heat capacity of the solid phase is given as,

$$c_{ps} = c_{ps} + X c_{pl} \qquad (C.196)$$

In Equation C.196 X represents the amount adsorbed per unit mass of adsorbent while c_{pl} represents the specific heat capacity of the adsorbed phase which is liquid.

Similar to the gas phase in solid phase energy conservation equation the intrinsic phase averaged quantities can be expressed as point properties disregarding the variations. In addition to this simplification, the specific heat value and the volume fraction of the solid phase is also assumed to be constant throughout the packed bed. Utilizing the assumptions and expressions given above, final form the energy conservation equation for the solid phase can be rewritten as;

$$(1 - \varepsilon_t)\rho_s \left(c_{ps} + X c_{pl}\right) \frac{\partial T_s}{\partial t} +$$
$$= \boldsymbol{\nabla}\left(K_{seq} \boldsymbol{\nabla} T_s\right) + a_{gs} h_{gs} \left(T_g - T_s\right) + (1 - \varepsilon_t)\rho_s \frac{\partial X}{\partial t} \Delta H_{ad} \qquad (C.197)$$

C.3.5 Mass Transport Equations Where Gas Phase is Composed of Vapor and Air Based on Local Thermal Non-Equilibrium (LTNE) Approach

As mentioned earlier in some of the cases the adsorbate phase is consisting of air and vapor. In this subsection transport equation for both air and vapor will be derived by using the volume averaging procedure which had been used in the previous parts. Actually these transport equations are separate mass conservation equations for both air and vapor phases and composed of convective and diffusive transport terms. As it had been stated earlier air is assumed to be non-adsorbing component while vapor is adsorbed on the solid phase. The governing equations will be derived in terms of mass quantities in this study for the purpose of compatibility with the other governing equations.

C.3.5.1 Mass Transport Equation for Vapor Based on LTNE Approach

The microscopic transport equation for the vapor component will be averaged over the gas phase. The derivation of transport equation will be similar to the energy conservation equation derivation since both of them are composed of convective and diffusive transport terms. The properties and quantities belonging to the vapor component will be denoted by a subscript of v in the equations. The governing equation for vapor transport can be written as [63];

$$\frac{\partial\left(\rho_g \omega_v\right)}{\partial t} + \boldsymbol{\nabla}.\left(\rho_g \omega_v \mathbf{V_g}\right) = -\boldsymbol{\nabla}.\left(\mathbf{j}_v\right) \qquad (C.198)$$

In Equation C.198 ω_v represents the mass fraction of the vapor phase and **j** represents the diffusive mass flux vector. Diffusive mass flux vector can be expressed in terms of mass fraction and a diffusion coefficient as,

$$\mathbf{j}_v = -\rho_g \mathfrak{D}_{va} \boldsymbol{\nabla} \omega_v \qquad (C.199)$$

In Equation C.199 $\mathcal{D}_{va}$ represents the mass diffusivity for vapor-air pair. The diffusivity value will be the same for the diffusive transport of both air and vapor. Replacing the diffusive mass flux vector into Equation C.198 and assuming that the mass diffusivity $\mathcal{D}_{va}$ is constant, the microscopic transport equation for the vapor component will take the following form [63],

$$\frac{\partial(\rho_g \omega_v)}{\partial t} + \nabla.(\rho_g \omega_v \mathbf{V_g}) = \nabla.\mathfrak{D}_{va}(\rho_g \nabla \omega_v) \qquad (C.200)$$

After this microscopic equation is averaged over the REV to obtain the macroscopic transport equation for vapor phase, the equation will be written as,

$$\langle\frac{\partial(\rho_g \omega_v)}{\partial t}\rangle_R + \langle\nabla.(\rho_g \omega_v \mathbf{V_g})\rangle_R = \langle\nabla.\mathfrak{D}_{va}(\rho_g \nabla \omega_v)\rangle_R \qquad (C.201)$$

The first term on right hand side of Equation C.201 represents the accumulation of vapor in the averaging volume and can be rewritten as,

$$\langle\frac{\partial(\rho_g \omega_v)}{\partial t}\rangle_R = \frac{\partial\langle\rho_g \omega_v\rangle_R}{\partial t} \qquad (C.202)$$

The phase average of the mass quantity can be rewritten in terms of intrinsic phase average since; in the final form of equation intrinsic phase average will be needed.

$$\langle\rho_g \omega_v\rangle_R = \varepsilon_g\langle\rho_g \omega_v\rangle_g + \langle\widehat{\rho_g}\widehat{\omega_v}\rangle_R \qquad (C.203)$$

As previously stated, the deviation of density will be much smaller than the intrinsic phase average of density [67].Regarding this order of magnitude evaluation the last term on the right hand side of Equation C.203 can be discarded. By replacing the simplified expression for the accumulation term and assuming that gas phase volume

fraction is independent of time, the volume averaged transport equation for the vapor component can be rewritten as,

$$\varepsilon_g \frac{\partial \langle \rho_g \omega_v \rangle_g}{\partial t} + \langle \nabla . \left(\rho_g \omega_v \mathbf{V_g} \right) \rangle_R = \langle \nabla . \mathfrak{D}_{va} \left(\rho_g \nabla \omega_v \right) \rangle_R \qquad (C.204)$$

The second term in the right hand side of equation represents the convective mass transfer rate of the vapor and the average of this term can be expanded as,

$$\langle \nabla . \left(\rho_g \omega_v \mathbf{V_g} \right) \rangle_R = \nabla . \langle \rho_g \omega_v \mathbf{V_g} \rangle_R + \frac{1}{V_R} \int_{A_{gs}} \rho_g \omega_v \mathbf{n_{gs}} . \left(\mathbf{V_g} - \mathbf{v_{gs}} \right) dA \qquad (C.205)$$

Similar to the derivation of the mass conservation equation for pure vapor the second term on the left hand side represents the convective mass flux through the gas-solid phase interface since the vapor is only adsorbing-desorbing species in the mixture.

The second term on the left hand side of Equation C.205 is expressed in terms of point quantities; next step will be the expansion of the first term on the left hand side. This term can be rewritten by using the spatial decomposition of each quantity in brackets as,

$$\rho_g = \langle \rho_g \rangle_g + \widehat{\rho_g} \qquad (C.208)$$

$$\omega_g = \langle \omega_g \rangle_g + \widehat{\omega_g} \qquad (C.209)$$

$$\mathbf{V_g} = \langle \mathbf{V_g} \rangle_g + \widehat{\mathbf{V_g}} \qquad (C.210)$$

The next step will be the multiplication of these terms in a similar manner with the expansion of the convective term in energy conservation equation.

$$\nabla.\langle\rho_g\omega_v\mathbf{V_g}\rangle_R = \nabla.\langle\langle\rho_g\rangle_g\langle\omega_g\rangle_g\langle\mathbf{V_g}\rangle_g\rangle_R + \nabla.\langle\langle\rho_g\rangle_g\langle\omega_g\rangle_g\widehat{\mathbf{V_g}}\rangle_R +$$
$$\nabla.\langle\langle\rho_g\rangle_g\widehat{\omega_g}\langle\mathbf{V_g}\rangle_g\rangle_R + \nabla.\langle\widehat{\rho_g}\langle\omega_g\rangle_g\langle\mathbf{V_g}\rangle_g\rangle_R + \nabla.\langle\langle\rho_g\rangle_g\widehat{\omega_g}\widehat{\mathbf{V_g}}\rangle_R + \nabla.\langle\widehat{\rho_g}\langle\omega_g\rangle_g\widehat{\mathbf{V_g}}\rangle_R +$$
$$\nabla.\langle\widehat{\rho_g}\widehat{\omega_g}\langle\mathbf{V_g}\rangle_g\rangle_R + \nabla.\langle\widehat{\rho_g}\widehat{\omega_g}\widehat{\mathbf{V_g}}\rangle_R \qquad (C.211)$$

Similar to the simplifications made in the derivation of the convective term in energy conservation equation, also in Equation C.211 all terms with a single deviation will be discarded since averaged terms will be taken outside the integral and the volume average of deviations will be equal to zero [63,67]. Additionally the term containing three deviations will yield a relatively small value and can be neglected as it had been done earlier. After these simplifications the Equation C.211 can be rewritten as,

$$\nabla.\langle\rho_g\omega_v\mathbf{V_g}\rangle_R = \nabla.\langle\langle\rho_g\rangle_g\langle\omega_g\rangle_g\langle\mathbf{V_g}\rangle_g\rangle_R + \nabla.\langle\langle\rho_g\rangle_g\widehat{\omega_g}\widehat{\mathbf{V_g}}\rangle_R$$
$$+ \nabla.\langle\widehat{\rho_g}\langle\omega_g\rangle_g\widehat{\mathbf{V_g}}\rangle_R + \nabla.\langle\widehat{\rho_g}\widehat{\omega_g}\langle\mathbf{V_g}\rangle_g\rangle_R \qquad (C.212)$$

Moreover, the deviations of the mass fraction and density are relatively small compared to the deviation of velocity and the term containing the product of density and mass fraction deviation can also be discarded [17, 67].As stated earlier, the phase average of intrinsic phase averages are equal to intrinsic phase average of that quantity multiplied by the volume fraction of that phase. Regarding the information given above further simplified form of Equation C.212 can be written as,

$$\nabla.\langle\rho_g\omega_v\mathbf{V_g}\rangle_R = \nabla.\left(\langle\rho_g\rangle_g\langle\omega_g\rangle_g\langle\mathbf{V_g}\rangle_R\right) + \nabla.\langle\rho_g\rangle_g\langle\widehat{\omega_g}\widehat{\mathbf{V_g}}\rangle_R$$
$$+ \langle\omega_g\rangle_g\nabla.\langle\widehat{\rho_g}\widehat{\mathbf{V_g}}\rangle_R \qquad (C.213)$$

Moreover as it had been done in the previous parts as a result of order of magnitude analyses given below,

$$\hat{\rho}_g \ll \langle\rho_g\rangle_g \qquad (C.214)$$

$$\widehat{\mathbf{V_g}} = \mathbf{O}\langle \mathbf{V_g} \rangle_R \qquad (C.215)$$

$$\boldsymbol{\nabla}.\left(\langle \omega_v \rangle_g \langle \hat{\rho}_g \widehat{\mathbf{V}}_\mathbf{g} \rangle_R\right) \ll \boldsymbol{\nabla}.\left(\langle \omega_v \rangle_g \langle \rho_g \rangle_g \langle \mathbf{V_g} \rangle_R\right) \qquad (C.216)$$

Regarding the order of magnitude estimate given above, the last term in the right hand side of Equation C.213 can be discarded and final form of the averaged convective transport term can be rewritten as [67],

$$\boldsymbol{\nabla}.\langle \rho_g \omega_v \mathbf{V_g} \rangle_R = \boldsymbol{\nabla}.\left(\langle \rho_g \rangle_g \langle \omega_v \rangle_g \langle \mathbf{V_g} \rangle_R\right) + \boldsymbol{\nabla}.\langle \rho_g \rangle_g \langle \widehat{\omega_v} \widehat{\mathbf{V_g}} \rangle_R \qquad (C.217)$$

The next step is to obtain an expression for the diffusive transport term which is the right hand side of Equation C.204.

$$\langle \boldsymbol{\nabla}.\left(\mathfrak{D}_{va} \rho_g \boldsymbol{\nabla} \omega_v\right) \rangle_R = \boldsymbol{\nabla}.\langle \mathfrak{D}_{va} \rho_g \boldsymbol{\nabla} \omega_v \rangle_R + \frac{1}{V_R} \int_{A_{gs}} \mathfrak{D}_{va} \rho_g \mathbf{n_{gs}} \boldsymbol{\nabla} \omega_v dA \qquad (C.218)$$

The first term on the right hand side of Equation C.218 can be expanded as follows,

$$\boldsymbol{\nabla}.\langle \mathfrak{D}_{va} \rho_g \boldsymbol{\nabla} \omega_v \rangle_R = \boldsymbol{\nabla}.\left(\mathfrak{D}_{va} \varepsilon_g \left(\langle \rho_g \rangle_g \boldsymbol{\nabla} \langle \omega_v \rangle_g + \langle \widehat{\rho_g} \boldsymbol{\nabla} \widehat{\omega_v} \rangle_g\right)\right) \qquad (C.219)$$

Regarding the order of magnitude estimate given in [70],

$$\widehat{\omega_v} = \mathbf{O}\left(\langle \omega_v \rangle_g \frac{L_g}{L}\right) \qquad (C.220)$$

In Equation C.220 L_g represents the length scale related to gas phase and L represents the macro length scale. It should be noted that L_g is much smaller than L. Using the expression given above; the order of magnitude for the gradient of deviation can be expressed as,

$$\boldsymbol{\nabla}\widehat{\omega_v} = \mathbf{O}\left(\Delta\langle\omega_v\rangle_g \frac{1}{L_g}\frac{L_g}{L}\right) \tag{C.221}$$

Whereas, the order of magnitude for the gradient of the intrinsic phase average of the mass fraction of vapor will be,

$$\boldsymbol{\nabla}\langle\omega_v\rangle_g = \mathbf{O}\left(\Delta\langle\omega_v\rangle_g \frac{1}{L_g}\right) \tag{C.222}$$

Additionally as stated previously deviation of density is much smaller than the intrinsic phase average,

$$\hat{\rho}_g \ll \langle\rho_g\rangle_g \tag{C.223}$$

Consequently as a result of this order of magnitude analyses the last term in Equation C.214 can be discarded and simplified form of the diffusive term can be written as,

$$\boldsymbol{\nabla}.\langle\mathfrak{D}_{va}\rho_g\boldsymbol{\nabla}\omega_v\rangle_R = \boldsymbol{\nabla}.\left(\mathfrak{D}_{va}\varepsilon_g\left(\langle\rho_g\rangle_g\boldsymbol{\nabla}\langle\omega_v\rangle_g\right)\right) \tag{C.224}$$

Procedure that will be followed for expanding the diffusive term is going to be similar to the procedure followed for the expansion of the conductive term in energy conservation equation. The expanded form of Equation C.224 will be,

$$\boldsymbol{\nabla}.\langle\mathfrak{D}_{va}\rho_g\boldsymbol{\nabla}\omega_v\rangle_R = \boldsymbol{\nabla}.\left[\varepsilon_g\mathfrak{D}_{va}\langle\rho_g\rangle_g\left(\varepsilon_g\boldsymbol{\nabla}\langle\omega_v\rangle_g + \frac{1}{V_R}\int_{A_{gs}}\mathbf{n_{gs}}\langle\omega_v\rangle_g\,dA + \frac{1}{V_R}\int_{A_{gs}}\mathbf{n_{gs}}\widehat{\omega_v}\,dA\right)\right] \tag{C.225}$$

The second term in the parenthesis on the right hand side of Equation C.225 can be taken out of the integral. In this case the normal of the interface surface will be integrated which yields a value of zero. Thus Equation C.224 can be rewritten as,

$$\langle \boldsymbol{\nabla}.\left(\mathfrak{D}_{va}\rho_g \boldsymbol{\nabla}\omega_v\right)\rangle_R = \boldsymbol{\nabla}.\left(\mathfrak{D}_{va}\varepsilon_g^2\langle\rho_g\rangle_g \boldsymbol{\nabla}\langle\omega_v\rangle_{\mathbf{g}}\right)$$
$$+\boldsymbol{\nabla}.\left(\frac{\varepsilon_g \mathfrak{D}_{va}\langle\rho_g\rangle_g}{V_R}\int\limits_{A_{gs}} \mathbf{n_{gs}}\widehat{\omega_v}\, dA\right)$$
$$+\frac{1}{V_R}\int\limits_{A_{gs}} \mathfrak{D}_{va}\rho_g \mathbf{n_{gs}}\,\boldsymbol{\nabla}\omega_v dA \qquad (C.226)$$

The first two terms on the right hand side of Equation C.226 represents the diffusive transport and instead of solving a complex closure problem to identify these terms a similar procedure will be followed with the derivation of diffusive transport terms in energy equation. The diffusive transport of vapor will be expressed in terms of gradient of mass fraction of vapor and an effective diffusivity tensor. The effective diffusivity for the vapor will assumed to be isotropic. The expression can be written as follows [67],

$$\left[\left(\mathfrak{D}_{va}\varepsilon_g \boldsymbol{\nabla}\langle\omega_v\rangle_{\mathbf{g}}\right) + \left(\frac{\mathfrak{D}_{va}}{V_R}\int\limits_{A_{gs}} \mathbf{n_{gs}}\widehat{\omega_v}\, dA\right)\right] = \mathbf{D_{ve}}\boldsymbol{\nabla}\langle\omega_v\rangle_g \qquad (C.227)$$

After substituting the volume averaged expanded form of the diffusive and convective terms into the mass transport equation the Equation C.204 will take the following form.

$$\varepsilon_g \frac{\partial \langle \rho_g \omega_v \rangle_g}{\partial t} + \nabla . \left(\langle \rho_g \rangle_g \langle \omega_v \rangle_g \langle \mathbf{V_g} \rangle_R \right) + \nabla . \langle \rho_g \rangle_g \langle \widehat{\omega_v} \widehat{\mathbf{V_g}} \rangle_R$$
$$+ \frac{1}{V_R} \int_{A_{gs}} \rho_g \omega_v \mathbf{n_{gs}} . \left(\mathbf{V_g} - \mathbf{v_{gs}} \right) dA$$
$$= \nabla . \left(\varepsilon_g \langle \rho_g \rangle_g \mathbf{D_{ve}} \nabla \langle \omega_v \rangle_\mathbf{g} \right) + \frac{\varepsilon_g \langle \rho_g \rangle_g}{V_R} \int_{A_{gs}} \mathfrak{D}_{va} \mathbf{n_{gs}} . \nabla \omega_v \, dA \qquad (C.228)$$

After rearranging the equation given above,

$$\varepsilon_g \frac{\partial \langle \rho_g \omega_v \rangle_g}{\partial t} + \nabla . \left(\langle \rho_g \rangle_g \langle \omega_v \rangle_g \langle \mathbf{V_g} \rangle_R \right)$$
$$= \nabla . \left(\varepsilon_g \langle \rho_g \rangle_g \mathbf{D_{ve}} \nabla \langle \omega_v \rangle_\mathbf{g} \right) - \frac{1}{V_R} \int_{A_{gs}} \rho_g \omega_v \mathbf{n_{gs}} . \left(\mathbf{V_g} - \mathbf{v_{gs}} \right) dA$$
$$+ \frac{1}{V_R} \int_{A_{gs}} \mathfrak{D}_{va} \rho_g \mathbf{n_{gs}} \nabla \omega_v dA \; - \nabla . \left(\varepsilon_g \langle \rho_g \rangle_g \langle \widehat{\omega_v} \widehat{\mathbf{V_g}} \rangle_g \right) \qquad (C.229)$$

Similar to the derivation of energy conservation equation by using volume averaging method, the last term on the right hand side of Equation C.229 represents the dispersive transport and can be expressed in terms of an hydrodynamic dispersion tensor and the gradient of intrinsic phase average of mass fraction as[63,67],

$$- \langle \widehat{\omega_v} \widehat{\mathbf{V_g}} \rangle_g = \mathbf{D_{vm}} \nabla \langle \omega_v \rangle_g \qquad (C.230)$$

A more simplified form of the equation can be rewritten after the substituting the term given above and assuming that phase interface velocity $\mathbf{v_{gs}}$ is equal to zero,

$$\varepsilon_g \frac{\partial \langle \rho_g \omega_v \rangle_g}{\partial t} + \nabla . \left(\langle \rho_g \rangle_g \langle \omega_v \rangle_g \langle \mathbf{V_g} \rangle_R \right)$$
$$+ \frac{1}{V_R} \int_{A_{gs}} \left(\rho_g \omega_v \mathbf{n_{gs}} . \mathbf{V_g} - \rho_g \mathfrak{D}_{va} \mathbf{n_{gs}} . \nabla \omega_v \right) dA$$
$$= \nabla . \left(\langle \rho_g \rangle_g \varepsilon_g (\mathbf{D_{ve}} + \mathbf{D_{vm}}) \nabla \langle \omega_v \rangle_\mathbf{g} \right) \qquad (C.231)$$

As declared by Altevogt et al.[70] The second term on the left hand side of Equation C.229 represents the combined diffusive and convective mass flux rate at the gas-solid phase interface which would be equal to total rate of adsorption-desorption. However a more comprehensive representation of this interfacial flux will be governed by expressing the velocity of species. As given in [67], in a diffusing mixture species are moving with different velocities. The velocity of a component in a mixture can be derived by using the Fick's first law of diffusion. According to Fick's first law of diffusion mass flux for vapor can be expressed as,

$$\mathbf{j_v} = \rho_v\left(\mathbf{v_v} - \mathbf{V_g}\right) = -\rho_g \mathfrak{D}_{va} \boldsymbol{\nabla} \omega_v \qquad (C.232)$$

In Equation C.232 represents the velocity of vapor species, which is the velocity of vapor component in the gas phase. The velocity of gas phase is a mass average of both air and vapor species. Rearranging the Equation C.232 an expression for the velocity of vapor species could be obtained as,

$$\frac{\rho_v}{\rho_g}(\mathbf{v_v}) = \left(\frac{\rho_v}{\rho_g}\mathbf{V_g} - \mathfrak{D}_{va}\boldsymbol{\nabla}\omega_v\right) \qquad (C.233)$$

Since the mass fraction of vapor species is equal to,

$$\frac{\rho_v}{\rho_g} = \omega_v \qquad (C.234)$$

Equation C.230 can be rewritten as,

$$\omega_v(\mathbf{v_v}) = \left(\omega_v \mathbf{V_g} - \mathfrak{D}_{va}\boldsymbol{\nabla}\omega_v\right) \qquad (C.235)$$

Substituting the expression given in Equation C.235 into the integral term which represents the net interfacial mass flux yields,

$$\frac{1}{V_R}\int_{A_{gs}} \mathbf{n_{gs}}\rho_g\left(\omega_v \mathbf{V_g} - \mathfrak{D}_{va}\nabla\omega_v\right) dA = \frac{1}{V_R}\int_{A_{gs}} \mathbf{n_{gs}}\rho_g\left(\omega_v(\mathbf{v_v})\right) dA \qquad (C.236)$$

As described previously since vapor is an adsorbing-desorbing species, the velocity of vapor species multiplied by the interfacial area normal will yield a non-zero value for this situation. However, as described by Whitaker [57] in case of an impermeable phase interface the integral will yield a value of zero since the velocity variable in the integral will be zero due to no slip condition. No slip condition for velocity is applicable where there is no mass transfer between phases thus the phase interface assumed to be impermeable.

$$\frac{1}{V_R}\int_{A_{gs}} \mathbf{n_{gs}}\rho_g\left(\omega_v(\mathbf{v_v})\right) dA = a_{gs}\langle\Omega_g\rangle_{gs} \qquad (C.237)$$

The net rate of interfacial mass flux can be related with the rate of adsorption capacity variation as follows,

$$\frac{1}{V_R}\int_{A_{gs}} \mathbf{n_{gs}}\rho_g\left(\omega_v(\mathbf{v_v})\right) dA = (1-\varepsilon_t)\rho_s\frac{\partial X}{\partial t} \qquad (C.238)$$

An equivalent diffusivity value can be defined as a sum of the effective and hydrodynamic diffusivity tensors. The effective and hydrodynamic diffusivity tensors are assumed to be isotropic. Additionally these tensors are intrinsic quantities [57] and their sum will be expressed as an intrinsic equivalent diffusivity.

$$\mathbf{D_{veq}} = \mathbf{D_{ve}} + \mathbf{D_{vm}} = D_{vaeq}\begin{bmatrix}1 & 0 & 0\\ 0 & 1 & 0\\ 0 & 0 & 1\end{bmatrix} \qquad (C.239)$$

The superficial equivalent diffusivity value of the vapor in the gas phase can be expressed in terms of intrinsic diffusivity and gas phase volume fraction, which was assumed to be equal to the total porosity of the packed bed.

$$D_{vaeq} = \varepsilon_t D_{va} \qquad (C.240)$$

For this case the gas phase is a binary mixture of vapor and air. In this case the binary diffusivities for vapor and air will be identical.[79]

$$D_{va} = D_{av} \qquad (C.241)$$

Using the ideal gas law the binary diffusion coefficient for vapor and air can be expressed based on Chapman-Enskog kinetic theory as [79],

$$D_{va} = D_{av} = 0.0018583\sqrt{T_g^3\left(\frac{1}{M_a}+\frac{1}{M_v}\right)}\frac{1}{p\sigma_{av}^2\omega_{av}} \qquad (C.242)$$

In Equation C.242 the M_a and M_v represents the molecular weight of air and vapor respectively. Where σ_{av} represents the collision diameter for Lennard-Jones potential and ω_{av} represents the collision integral.

As previously done on the derivation of energy conservation equation the final form of mass transport equation for vapor can be obtained by replacing the point properties with the intrinsic phase averages based on the assumption stated earlier. [70] Only the superficial velocity values will be replaced with the point velocity values since directly the superficial velocity values are obtained from conservation of momentum equation.

$$\varepsilon_t \frac{\partial(\rho_g \omega_v)}{\partial t} + \boldsymbol{\nabla}.(\rho_g \omega_v \mathbf{V_g}) + (1-\varepsilon_t)\rho_s \frac{\partial X}{\partial t} = \boldsymbol{\nabla}.(\rho_g D_{vaeq} \boldsymbol{\nabla} \omega_v) \qquad (C.243)$$

C.3.5.1 Mass Transport Equation for Air Based on LTNE Approach

The second step is to derive the transport equation for the air. The main difference between the derivation of transport equation for air and derivation of transport equation for vapor will be the terms representing the interfacial mass transfer. As mentioned in the assumptions, air is assumed to be non-adsorbing component in the gas phase. For this reason the interfacial mass flux at the gas-solid phase interface will be discarded. All the other terms will be identical with the mass transport equation of the vapor. The parameters belonging to air component will be denoted by a subscript of a in the following relations.

As a starting point for the derivation of mass transport equation for air species, the volume averaged and simplified form of the mass transport equation can be expressed by using quantities of air species since, all the boundary conditions and assumptions are same up to that point. Regarding this fact the volume averaged and simplified form of mass transport equation for air species can be written as,

$$\varepsilon_g \frac{\partial \langle \rho_g \omega_a \rangle_g}{\partial t} + \boldsymbol{\nabla}.\left(\langle \rho_g \rangle_g \langle \omega_a \rangle_g \langle \mathbf{V_g} \rangle_R\right) + \frac{1}{V_R} \int_{A_{gs}} \left(\rho_g \omega_a \mathbf{n_{gs}}.\mathbf{V_g} - \rho_g \mathfrak{D}_{av} \mathbf{n_{gs}}.\boldsymbol{\nabla}\omega_a\right) dA = \boldsymbol{\nabla}.\left(\langle \rho_g \rangle_g \varepsilon_g (\mathbf{D_{ae}} + \mathbf{D_{am}}) \boldsymbol{\nabla} \langle \omega_a \rangle_g\right) \qquad (C.244)$$

As previously stated for the vapor species the equivalent diffusivity tensor can be defined in terms of equivalent diffusivity as,

$$\mathbf{D_{aeq}} = \mathbf{D_{ae}} + \mathbf{D_{am}} = D_{aveq}\begin{bmatrix}1 & 0 & 0\\ 0 & 1 & 0\\ 0 & 0 & 1\end{bmatrix} \qquad (C.245)$$

The equivalent diffusivity can be expressed similarly since diffusivity value for air and vapor species will be identical,

$$D_{aveq} = \varepsilon_t D_{av} = \varepsilon_t D_{va} \qquad (C.246)$$

The second term in the left hand side of Equation C.244 represents the interfacial mass flux as stated earlier. This term can be written by using the velocity and mass fraction of air species as stated earlier.

$$\frac{1}{V_R}\int_{A_{gs}} \left(\rho_g \omega_a \mathbf{n_{gs}}.\mathbf{V_g} - \rho_g \mathfrak{D}_{av}\mathbf{n_{gs}}.\boldsymbol{\nabla}\omega_a\right) dA = \frac{1}{V_R}\int_{A_{gs}} \mathbf{n_{gs}}\rho_g\left(\omega_a(\mathbf{v_a})\right) dA \qquad (C.247)$$

Unlike the vapor species air is assumed not to be adsorbing-desorbing. Since air will not be adsorbed or desorbed at the phase interface air species velocity will be equal to zero due to no slip condition. As a consequence the integral will yield a value of zero which means that the gas-solid phase interface is impermeable for the air species. In addition to the expression given above also the intrinsic phase averages will be replaced with the point properties since the variations are assumed to be small. As a result final form of the mass transport equation for the air species can be written as,

$$\varepsilon_t \frac{\partial\left(\rho_g \omega_a\right)}{\partial t} + \boldsymbol{\nabla}.\left(\rho_g \omega_a \mathbf{V_g}\right) = \boldsymbol{\nabla}.\left(\rho_g D_{aveq}\boldsymbol{\nabla}\omega_v\right) \qquad (C.248)$$

Upon completion of the derivation of governing equation for Local Thermal Non-Equilibrium (LTNE) assumption, next step is to derive the governing equations for the mathematical model based on the Local Thermal Equilibrium (LTE) assumption. In the LTE model both solid and gas phases are at the same temperature and will be treated as single continuous phase. Therefore the governing equation derivation procedure will be based on the control volume approach.

C.3.6 Mass Conservation Equation Based on Local Thermal Equilibrium (LTE) Approach

As previously done for the derivation of mass conservation equation for the Heat Transfer Fluid (HTF), the derivation of mass conservation equation based on LTE assumption will also be based on the elemental cubic control volume. Since the net rate of mass change within the control volume will be equal to net rate of mass leaving the control volume in 3-D. The derivation will be based on the elemental cubic volume element demonstrated in Figure C.1. As stated earlier, the quantities and parameters belonging the gas phase will be denoted by a subscript of g while the parameters and quantities belonging the solid phase will be denoted by subscript s and for the adsorbed phase subscript of l will be used. Net rate of mass leaving the control volume can be expressed for x, y and z directions in terms of gas phase velocity and density since gas phase is the only mobile phase. It should be noted that the velocities are face averaged velocity quantities since in porous control volume, a portion of the wall will be composed of solid phase and impermeable however face averaged velocity could be defined to make the derivation more straightforward.

$$Net\ \ rate\ of\ mass\ leaving\ C.V.\ in\ x\ direction$$

$$= -\left(-(\rho_g u_g)\Delta y\Delta z + \left[(\rho_g u_g) + \frac{\partial(\rho_g u_g)}{\partial x}\Delta x\right]\Delta y\Delta z\right) \qquad (C.249)$$

$$Net\ \ rate\ of\ mass\ leaving\ C.V.\ in\ y\ direction$$

$$= -\left(-(\rho_g v_g)\Delta x\Delta z + \left[(\rho_g v_g) + \frac{\partial(\rho_g v_g)}{\partial y}\Delta y\right]\Delta x\Delta z\right) \qquad (C.250)$$

$$Net\ \ rate\ of\ mass\ leaving\ C.V.\ in\ z\ direction$$

$$= -\left(-(\rho_g w_g)\Delta x\Delta y + \left[(\rho_g w_g) + \frac{\partial(\rho_g w_g)}{\partial z}\Delta z\right]\Delta x\Delta y\right) \qquad (C.251)$$

Also the rate of net mass increase within the volume can be expressed as;

$$Net\ \ rate\ of\ mass\ increase\ in\ C.V. = \frac{\partial m}{\partial t} \qquad (C.252)$$

The elemental cubic volume contains, gas phase, solid phase and the adsorbed phase, for this reason the mass of the elemental cubic volume will be expressed in terms of intrinsic quantities as,

$$m\ = \left(\rho_g \varepsilon_g + \left(1-\varepsilon_g\right)\rho_s + \left(1-\varepsilon_g\right)\rho_s X\ \right)\Delta x\Delta y\Delta z \qquad (C.253)$$

As stated previously the X represents the amount adsorbed as a ratio to the solid phase mass. Additionally the volume of the adsorbed phase had been neglected and thus sum of gas phase and solid phase volume fractions is equal to 1. The net rate of mass increase in the control volume can be rewritten by substituting Equation C.253 into Equation C.252.

$$Net\ \ rate\ of\ mass\ increase\ in\ C.V.$$

$$= \frac{\partial}{\partial t}\left(\rho_g \varepsilon_g + \left(1-\varepsilon_g\right)\rho_s + \left(1-\varepsilon_g\right)\rho_s X\ \right)\Delta x\Delta y\Delta z \qquad (C.254)$$

Substituting the expressions for net rate of mass increase in control volume and net rate of mass leaving the control volume one can obtain a total expression for the mass conservation equation.

$$\frac{\partial}{\partial t}\left(\rho_g \varepsilon_g + (1-\varepsilon_g)\rho_s + (1-\varepsilon_g)\rho_s X\right)\Delta x \Delta y \Delta z$$
$$= (\rho_g u_g)\Delta y \Delta z - \left[(\rho_g u_g) + \frac{\partial(\rho_g u_g)}{\partial x}\Delta x\right]\Delta y \Delta z + (\rho_g v_g)\Delta x \Delta z$$
$$- \left[(\rho_g v_g) + \frac{\partial(\rho_g v_g)}{\partial y}\Delta y\right]\Delta x \Delta z + (\rho_g w_g)\Delta x \Delta y$$
$$- \left[(\rho_g w_g) + \frac{\partial(\rho_g w_g)}{\partial z}\Delta z\right]\Delta x \Delta y \qquad (C.255)$$

After rearranging Equation 2.243 can be expressed in terms of superficial gas phase velocity components as,

$$\frac{\partial}{\partial t}\left(\rho_g \varepsilon_g + (1-\varepsilon_g)\rho_s + (1-\varepsilon_g)\rho_s X\right)$$
$$= -\frac{\partial(\rho_g u_g)}{\partial x} - \frac{\partial(\rho_g v_g)}{\partial y} - \frac{\partial(\rho_g w_g)}{\partial z} \qquad (C.256)$$

The volume fraction of gas phase is equal to total porosity and total porosity is assumed to be uniform and constant within the packed bed. Moreover the solid phase is assumed to be rigid and density of the solid phase is invariant within the packed bed. Regarding these assumptions differential relation on the left hand side can be expanded and Equation C.255 can be rewritten by using the gas phase velocity vector as,

$$\varepsilon_t \frac{\partial \rho_g}{\partial t} + (1-\varepsilon_g)\rho_s \frac{\partial X}{\partial t} + \boldsymbol{\nabla}.\mathbf{V_g} = 0 \qquad (C.257)$$

In Equation C.257 the time derivative of the adsorption capacity represents the rate of mass exchange between gas phase and the adsorbed phase.

C.3.7 Momentum Conservation Equation Based on Local Thermal Equilibrium (LTE) Approach

The momentum conservation equation will also be derived for the only mobile phase which is the gas phase. Again derivation approach will be the equating the net momentum change of the control volume and the momentum influx to the forces applied. The net rate of change of momentum and the momentum influx to the system will corresponds to mass multiplied by acceleration. The acceleration components are previously derived for the conservation of momentum equation of HTF are also applicable to the gas phase and can be rewritten in terms of substantial derivatives of velocity components as ,

Regarding this concern, the components of the conservation equation can be listed as,

$$Net\ \ rate\ of\ change\ in\ momentum\ of\ C.V.\ in\ x\ direction$$
$$= \varepsilon_g \frac{\partial(\rho_g u_g)}{\partial t} \Delta x \Delta y \Delta z \qquad (C.258)$$

$$Net\ \ rate\ of\ change\ in\ momentum\ of\ C.V.\ in\ y\ direction$$
$$= \varepsilon_g \frac{\partial(\rho_g v_g)}{\partial t} \Delta x \Delta y \Delta z \qquad (C.259)$$

$$Net\ \ rate\ of\ change\ in\ momentum\ of\ C.V.\ in\ z\ direction$$
$$= \varepsilon_g \frac{\partial(\rho_g w_g)}{\partial t} \Delta x \Delta y \Delta z \qquad (C.260)$$

The term for the momentum influx can be written in terms the mass flow rates derived in the previous section and face averaged velocities as,

.

$$Net\ \ rate\ of\ momentum\ inflow\ to\ C.V.\ in\ x\ direction$$

$$= \left((\rho_g u_g u_g) \Delta y \Delta z - \left[(\rho_g u_g u_g) + u_g \frac{\partial (\rho_g u_g)}{\partial x} \Delta x \right] \Delta y \Delta z \right) \qquad (C.261)$$

$$Net\ \ rate\ of\ momentum\ inflow\ to\ C.V.\ in\ y\ direction$$

$$= \left((\rho_g v_g v_g) \Delta x \Delta z - \left[(\rho_g v_g v_g) + v_g \frac{\partial (\rho_g v_g)}{\partial y} \Delta y \right] \Delta x \Delta z \right) \qquad (C.262)$$

$$Net\ \ rate\ of\ momentum\ inflow\ to\ C.V.\ in\ x\ direction$$

$$= \left((\rho_g v_g v_g) \Delta x \Delta y - \left[(\rho_g v_g v_g) + v_g \frac{\partial (\rho_g v_g)}{\partial z} \Delta z \right] \Delta x \Delta y \right) \qquad (C.263)$$

The net rate of momentum inflow to the control volume can be expressed as a substantial derivative of superficial velocity vector and gas phase density as,

$$Net\ \ rate\ of\ momentum\ change\ and\ momentum\ inflow\ to\ C.V.$$

$$= \frac{D(\rho_g \mathbf{V_g})}{Dt} \Delta x \Delta y \Delta z \qquad (C.264)$$

As mentioned above net rate of momentum change net rate of momentum inflow and net rate of momentum change in the control volume will be equal to the forces applied. The forces acting on the surfaces of the elemental fluid volume could be expressed by a stress tensor which is given below. The normal stresses in the stress tensor $\boldsymbol{\pi}$ can be rewritten by decomposition into pressure and the stress terms separately as;

$$\boldsymbol{\pi} = \begin{bmatrix} \sigma_{xx} & \tau_{xy} & \tau_{xz} \\ \tau_{yx} & \sigma_{yy} & \tau_{yz} \\ \tau_{zx} & \tau_{zy} & \sigma_{zz} \end{bmatrix} = \begin{bmatrix} \tau_{xx} - p & \tau_{xy} & \tau_{xz} \\ \tau_{yx} & \tau_{yy} - p & \tau_{yz} \\ \tau_{zx} & \tau_{zy} & \tau_{zz} - p \end{bmatrix}$$

$$= \begin{bmatrix} \tau_{xx} & \tau_{xy} & \tau_{xz} \\ \tau_{yx} & \tau_{yy} & \tau_{yz} \\ \tau_{zx} & \tau_{zy} & \tau_{zz} \end{bmatrix} - p \begin{bmatrix} 1 & 0 & 0 \\ 0 & 1 & 0 \\ 0 & 0 & 1 \end{bmatrix} \qquad (C.265)$$

The stress tensor can be decomposed into stresses formed by pressure and stresses formed by viscous forces to get a more compatible representation with the [79].

$$\boldsymbol{\pi} = \boldsymbol{\tau} - p \begin{bmatrix} 1 & 0 & 0 \\ 0 & 1 & 0 \\ 0 & 0 & 1 \end{bmatrix} \qquad (C.266)$$

The forces acting on the elemental cubic volume due to the stresses on the faces will be the divergence of the stress tensor which had been derived earlier for the HTF. Additionally one other source of the force acting on the infinitesimal element is the body forces which will be expressed in the vector form as **f**. Regarding these definitions the forces acting on the elemental cubic volume can be written as;

$$\mathbf{F} = \boldsymbol{\nabla}\boldsymbol{\pi} + \rho_g \mathbf{f} = \boldsymbol{\nabla}.\boldsymbol{\tau} - \boldsymbol{\nabla} p_g + \rho_g \mathbf{f} \qquad (C.267)$$

Since net momentum change and momentum inflow rate will be equal to the forces acting on the elemental cubic volume, the conservation of momentum equation per unit volume can be written in vector form as,

$$\frac{D(\rho_g \mathbf{V_g})}{Dt} = \boldsymbol{\nabla}.\boldsymbol{\tau} - \boldsymbol{\nabla} p_g + \rho_g \mathbf{f} \qquad (C.268)$$

The first term in Equation C.268 is the net rate of momentum change in the elemental fluid volume and the net rate of convective momentum flux into the system. In brief the left hand side of the equation corresponds to mass multiplied by acceleration and also known as the inertial terms of the momentum conservation equation. Since the inertial terms are more important for the flows with high velocity

and high Reynolds number these terms can be neglected for the momentum transport in porous medium [157]. Effect of body forces in momentum conservation are neglected for sake of simplicity throughout the study, for this reason the last term on right hand side will also be neglected. The second term on the right hand side represents the rate of viscous momentum gain per unit volume. The viscous momentum exchange is the dominant component for the fluid flow in porous media, therefore after omitting the neglected terms the momentum conservation equation will take the following form,

$$0 = -\boldsymbol{\nabla} p_g + \boldsymbol{\nabla}.\boldsymbol{\tau} \qquad (\mathrm{C}.269)$$

Since the elemental cubic volume is composed of pore space and locations occupied by solid phase a simple order of magnitude estimate will be done in terms of volume average. The volume average of the second term in Equation C.269 on a the cubic element which is representative of the whole domain and has a characteristic length of L^3, can be expressed as follows [158],

$$\langle \boldsymbol{\nabla}.\boldsymbol{\tau} \rangle_R = \frac{\int_V \boldsymbol{\nabla}.\boldsymbol{\tau}}{V} = \frac{\int_{A_{gs}} \boldsymbol{\tau}.\mathbf{n}\mathrm{dA}}{V} + \frac{\int_{A_R} \boldsymbol{\tau}.\mathbf{n}\mathrm{dA}}{V} \qquad (C.270)$$

In Equation C.270 A_{gs} is the area of the gas and solid phase interface whereas, A_R is the external surface area of the volume enclosed by the infinitesimal cubic element. The area of the phase interface between gas and solid phase is assumed to be equal to the pore wall surface. The averaging volume to pore wall surface area ratio is proportional with the diameter of the pore spaces in the packed bed [39]. On the other hand the ratio of the averaging volume and the surface area of are proportional with characteristic length of cubic element which is L. Therefore Equation C.270 can be rewritten as;

$$\langle \boldsymbol{\nabla}.\boldsymbol{\tau} \rangle = \frac{\int_{V_R} \boldsymbol{\nabla}.\boldsymbol{\tau}}{V} \cong \boldsymbol{\tau}.\mathbf{n}\left(\frac{1}{d_{pore}} + \frac{1}{L}\right) \qquad (C.271)$$

Since the characteristic length of the averaging volume need to be much more larger than the pore space characteristic dimensions, ($L >> d_{pore}$), Equation C.271 can be reduced to,

$$\langle \boldsymbol{\nabla}.\boldsymbol{\tau} \rangle_R = \frac{\int_{V_R} \boldsymbol{\nabla}.\boldsymbol{\tau}}{V_R} \cong \boldsymbol{\tau}.\mathbf{n}\left(\frac{1}{d_{pore}}\right) \qquad (C.272)$$

The dot product of pore wall surface normal and the stress tensor can be expressed in terms of average velocity vector, fluid viscosity and a function of the pore space diameter as [157],

$$\boldsymbol{\tau}.\mathbf{n} \cong -\frac{\boldsymbol{\mu}\overline{\mathbf{V_g}}}{f(d_{pore})} \qquad (C.273)$$

In Equation C.273 $\overline{\mathbf{V_g}}$ is the average velocity vector of the gas phase, and $f(d_{pore})$ denotes the function of pore space diameter. Assuming that the velocity variation within the averaging volume is not significant, the averaged velocity values are taken as identical with the superficial velocity values. When Equation C.258 and Equation C.273 is replaced into Equation C.268, the final form of the momentum conservation equation for the gas phase will be,

$$\mathbf{V_g} = -\frac{f(d_{pore})}{\mu}\boldsymbol{\nabla} p_g \qquad (C.274)$$

Regarding the derived momentum conservation equation or Darcy's Law it is possible to conclude that the relation between velocity within the porous media and the pressure gradient is inversely proportional with fluid viscosity and proportional to the function of pore space diameter. The proportionality constant given as $f(d_{pore})$ is

defined by the well-known Kozeny-Carman equation as a function of adsorbent particle diameter and bed porosity as[68];

$$f(d_{pore}) = \kappa_g = \frac{d_p^2 \varepsilon_b^3}{180(1-\varepsilon_b)^2} \qquad (C.275)$$

In Equation C.275 κ_g denotes the permeability of the packed bed while d_p represents the diameter of the solid particles. The final form of the momentum conservation equation, which is also known as Darcy's Law can be written as,

$$\mathbf{V_g} = -\frac{\kappa_g}{\mu}\nabla p_g \qquad (C.276)$$

C.3.8 Energy Conservation Equation Based on Local Thermal Equilibrium (LTE) Approach

Similar to the conservation equation for LTNE Approach, for LTE approach follows the first law of thermodynamics. According to first law of thermodynamics, the net rate of energy change in the control volume will be equal to the difference between net rate of heat transfer to the system and net rate of work done by the control volume as expressed below.

$$\dot{E} = \dot{Q} - \dot{W} \qquad (C.277)$$

The energy per unit volume of packed bed will be expressed in terms of internal energy of the vapor, solid, and adsorbed phases. It should be noted that the kinetic energy of mobile fluid particles are assumed to be negligible and will not be included in the energy expression. Regarding this definition energy contained in the control volume can be expressed as,

$$E = \left(\varepsilon_g \rho_g \mathfrak{U}_g + \left(1-\varepsilon_g\right)\rho_s \mathfrak{U}_s + \left(1-\varepsilon_g\right)\rho_s X \mathfrak{U}_l\right)\Delta x \Delta y \Delta z \qquad (C.278)$$

In Equation C.278 $\mathfrak{U}_g$, $\mathfrak{U}_s$ and $\mathfrak{U}_l$ represents the internal energy of gas phase, solid phase and adsorbed phase respectively. Then net rate of energy change in the control volume can be expressed as a time derivative as,

$$\dot{E} = \frac{\partial}{\partial t}\left(\varepsilon_g \rho_g \mathfrak{U}_g + \left(1-\varepsilon_g\right)\rho_s \mathfrak{U}_s + \left(1-\varepsilon_g\right)\rho_s X \mathfrak{U}_l\right)\Delta x \Delta y \Delta z \qquad (C.279)$$

Since gas phase is the only mobile phase, the convective energy transfer and pressure work done on the control volume will be related with the gas phase only. Net rate of convective energy transfer to the control volume combined with the rate of work done by the by the flow of gas phase can be expressed as net rate of enthalpy transfer to the control volume. Considering a infinitesimal fluid element with dimensions Δx, Δy and Δz, net rate of enthalpy inflow to the system can be expressed for x, y, and z axis as,

$$Net\ \ rate\ of\ enthalpf\ inflow\ to\ C.V.\ in\ x\ direction$$
$$= \left(\rho_g u_g h_g\right)\Delta y \Delta z - \left[\left(\rho_g u_g h_g\right) + \frac{\partial\left(\rho_g u_g h_g\right)}{\partial x}\Delta x\right]\Delta y \Delta z \qquad (C.280)$$

$$Net\ \ rate\ of\ enthalpf\ inflow\ to\ C.V.\ in\ y\ direction$$
$$= \left(\rho_g v_g h_g\right)\Delta x \Delta z - \left[\left(\rho_g v_g h_g\right) + \frac{\partial\left(\rho_g v_g h_g\right)}{\partial y}\Delta y\right]\Delta x \Delta z \qquad (C.281)$$

$$Net\ \ rate\ of\ enthalpf\ inflow\ to\ C.V.\ in\ y\ direction$$
$$= \left(\rho_g w_g h_g\right)\Delta x \Delta y - \left[\left(\rho_g w_g h_g\right) + \frac{\partial\left(\rho_g w_g h_g\right)}{\partial z}\Delta z\right]\Delta x \Delta y \qquad (C.282)$$

The net rate of enthalpy flow into the control volume can be expressed as,

$$Net\ rate\ of\ enthalpf\ inflow\ to\ C.V = \nabla.\left(\rho_g h_g \mathbf{V_g}\right)\Delta x\Delta y\Delta z \qquad (C.283)$$

As mentioned earlier the velocity components and the velocity belong to the superficial velocity so they do not need to be multiplied by the volume fraction of the gas phase. Next step is to find an expression for the net rate of conductive heat transfer to the system. Since there will be only a single temperature parameter due to the local thermal equilibrium assumption, conductive heat transfer rate can be expressed by using a single temperature variable. The temperature belonging both phases will be denoted by a subscript of *gs*. However, before going through the conductive heat transfer equivalent thermal conductivity concept needs to be discussed for the infinitesimal control volume which contains both, solid gas and adsorbed phases. According to Nield and Bejan [75] for a packed bed, equivalent conductivity need to be expressed as a function of both gas and solid phase thermal conductivity values. However in case of adsorption or desorption there is also adsorbed phase within the packed bed and its effect should be included in the equivalent value. Therefore equivalent thermal conductivity for the packed bed can be expressed as a function of solid, gas and adsorbed phase thermal conductivity values as[37],

$$k_{eq} = {k_s}^{(1-\varepsilon_g)}{k_g}^{\varepsilon_g} \qquad (C.284)$$

For an infinitesimal cubic element with dimensions of Δx, Δy and Δz, net rate of conductive heat transfer to the control volume can be expressed as,

$$\dot{Q} = -k_{eq}\frac{\partial T_{gs}}{\partial x}\Delta y\Delta z - \left(-k_{eq}\frac{\partial T_{gs}}{\partial x} - \frac{\partial}{\partial x}\left(k_{eq}\frac{\partial T_{gs}}{\partial x}\right)\Delta x\right)\Delta y\Delta z$$
$$- k_{eq}\frac{\partial T_{gs}}{\partial y}\Delta x\Delta z - \left(-k_{eq}\frac{\partial T_{gs}}{\partial y} - \frac{\partial}{\partial y}\left(k_{eq}\frac{\partial T_{gs}}{\partial y}\right)\Delta y\right)\Delta x\Delta z - k_{eq}\frac{\partial T_{gs}}{\partial z}\Delta x\Delta y$$
$$- \left(-k_{eq}\frac{\partial T_{gs}}{\partial z} - \frac{\partial}{\partial z}\left(k_{eq}\frac{\partial T_{gs}}{\partial z}\right)\Delta y\right)\Delta x\Delta y \qquad (C.285)$$

Replacing the decomposed form of net rate of energy change, heat transfer to the control volume and the work done by the control volume expressions into the energy conservation equation one can obtain the equation of energy conservation as,

$$\frac{\partial}{\partial t}\left(\varepsilon_g\rho_g\mathfrak{U}_g + \left(1-\varepsilon_g\right)\rho_s\mathfrak{U}_s + \left(1-\varepsilon_g\right)\rho_s X\mathfrak{U}_l\right)$$
$$= \nabla\left(k_{eq}\nabla T_{gs}\right) - \boldsymbol{\nabla}.\left(\rho_g h_g \mathbf{V_g}\right) \qquad (C.286)$$

The last term on the right hand side of Equation C.286 can be expanded by using the chain rule for differentiation as,

$$\boldsymbol{\nabla}.\left(\rho_g h_g \mathbf{V_g}\right) = h_g\boldsymbol{\nabla}.\left(\rho_g \mathbf{V_g}\right) + \rho_g \mathbf{V_g}\boldsymbol{\nabla}.\left(h_g\right) \qquad (C.287)$$

The first term in the right hand side of Equation C.287 can be rewritten by using the mass conservation equation given in Equation C.257 as,

$$h_g\boldsymbol{\nabla}.\left(\rho_g \mathbf{V_g}\right) = -h_g\frac{\partial}{\partial t}\left(\rho_g\varepsilon_g + \left(1-\varepsilon_g\right)\rho_s + \left(1-\varepsilon_g\right)\rho_s X\right) \qquad (C.288)$$

The enthalpy term can be written as,

$$h_g = \mathfrak{U}_g + \frac{p_g}{\rho_g} = \mathfrak{U}_g + p_g v_g \qquad (C.289)$$

In Equation C.289 v_g represents the specific volume of the gas phase. In addition to these rearrangements also the internal energy and enthalpy values need to be related with the temperature to obtain a plausible energy conservation equation. Thus the relations for the gas phase, solid phase and adsorbed phase internal energy and enthalpy values are written in terms of specific heat and temperature given below.

$$d\mathfrak{U}_g = c_{vg} dT_{gs} \qquad (C.290)$$

$$d\mathfrak{U}_l = c_{vl} dT_{gs} = c_{pl} dT_{gs} \qquad (C.291)$$

$$d\mathfrak{U}_s = c_{vs} dT_{gs} = c_{ps} dT_{gs} \qquad (C.292)$$

$$dh_g = c_{pg} dT_{gs} \qquad (C.293)$$

It should be noted that for the adsorbed phase and solid phase constant volume specific heat and constant pressure specific heat values are identical. Also as a simplifying assumption, the specific volume of adsorbed phase is assumed to be very small which yields,

$$\mathfrak{U}_l = h_l - pv_l \cong h_l \qquad (C.294)$$

Regarding the expressions given above the energy conservation equation given in Equation C.286 can be rewritten as,

$$\begin{aligned} &\frac{\partial}{\partial t}\left[\varepsilon_g \rho_g \left(h_g - \frac{p_g}{\rho_g}\right)\right] + (1-\varepsilon_g)\rho_s c_{ps} \frac{\partial T_{gs}}{\partial t} + (1-\varepsilon_g)\rho_s X c_{pl} \frac{\partial T_{gs}}{\partial t} \\ &= \nabla\left(k_{eq} \nabla T_{gs}\right) + h_g \frac{\partial}{\partial t}\left(\rho_g \varepsilon_g + (1-\varepsilon_g)\rho_s\right. \\ &\left. + (1-\varepsilon_g)\rho_s X\right) - \rho_g \mathbf{V_g} \boldsymbol{\nabla}.\left(h_g\right) \end{aligned} \qquad (C.295)$$

Assuming that the volume fraction of the gas phase is constant within the packed bed and in time the Equation C.295 will results in the following form,

$$\varepsilon_g \rho_g c_{pg} \frac{\partial T_{gs}}{\partial t} + \varepsilon_g h_g \frac{\partial \rho_g}{\partial t} - \varepsilon_g \frac{\partial p_g}{\partial t} + (1-\varepsilon_g)\rho_s c_{ps} \frac{\partial T_{gs}}{\partial t} + (1-\varepsilon_g)\rho_s X c_{pl} \frac{\partial T_{gs}}{\partial t} + (1-\varepsilon_g)\rho_s \frac{\partial X}{\partial t} h_l = \nabla(k_{eq} \nabla T_{gs}) + \varepsilon_g h_g \frac{\partial \rho_g}{\partial t} + (1-\varepsilon_g)\rho_s \frac{\partial X}{\partial t} h_g - \rho_g \mathbf{V_g} c_{pg} \boldsymbol{\nabla}. T_{gs} \quad (C.296)$$

Assuming that volume fraction of the gas phase is equal to the total porosity and defining the heat of adsorption as,

$$\Delta H_{ad} = h_g - h_l \quad (C.297)$$

Regarding these definitions the final form of the energy conservation equation can be written as,

$$\varepsilon_t \rho_g c_{pg} \frac{\partial T_{gs}}{\partial t} - \varepsilon_g \frac{\partial p_g}{\partial t} + (1-\varepsilon_g)\rho_s c_{ps} \frac{\partial T_{gs}}{\partial t} + (1-\varepsilon_g)\rho_s X c_{pl} \frac{\partial T_{gs}}{\partial t} = \nabla(k_{eq} \nabla T_{gs}) + (1-\varepsilon_g)\rho_s \frac{\partial X}{\partial t} \Delta H_{ad} - \rho_g \mathbf{V_g} c_{pg} \boldsymbol{\nabla}. T_{gs} \quad (C.298)$$

C.3.9 Mass Transport Equations Where Gas Phase is Composed of Vapor and Air Based on Local Thermal Equilibrium (LTE) Approach

C.3.9.1 Mass Transport Equation for Vapor Based on LTNE Approach

As mentioned in the previous parts in some of the cases, the gas phase is a binary mixture of air and vapor. In such cases the mass transport equations for each phase will be used for constructing the mathematical model. These equations will define

the transport of species within the packed bed by convection and diffusion. The derivation procedure for the mass transport equation for each species will be based on the mass conservation principle. Regarding the conservation laws, the net rate of mass of a species in the control volume will be equal to the net rate of mass of the same species leaving the control volume. Additionally if there is any the rate of mass of any species generated in the control volume will act as a source for the conservation equation. In this study as mentioned above the gas phase will be treated as a mixture of vapor and air. In such cases the properties and variables belonging the vapor species will be denoted by a subscript of v similarly properties and variables belonging air species will be denoted by a subscript a. Regarding the fact that each species in the mixture will be moving with different velocities in a diffusive mixture [63], deriving the mass conservation equation for each phase separately will yield the mass transport of species. For this purpose the mass conservation equation for the vapor species will be derived first, on an infinitesimal cubic control volume which has dimension of Δx Δy and Δz. Just as a reminder it should be noted that the velocity quantities used in the derivations are face averaged superficial velocity components since the values obtained by solution of momentum conservation equation will be these values.

$$Net\ \ rate\ of\ vapor\ mass\ \ leaving\ C.V.\ in\ x\ direction$$

$$= -(\rho_v u_v)\Delta y\Delta z - \left[(\rho_v u_v) + \frac{\partial(\rho_v u_v)}{\partial x}\Delta x\right]\Delta y\Delta z \qquad (C.299)$$

$$Net\ \ rate\ of\ \ vapor\ mass\ leaving\ C.V.\ in\ y\ direction$$

$$= -(\rho_v v_v)\Delta x\Delta z - \left[(\rho_v v_v) + \frac{\partial(\rho_v v_v)}{\partial y}\Delta y\right]\Delta x\Delta z \qquad (C.300)$$

$$Net\ \ rate\ of\ vapor\ mass\ leaving\ C.V.\ in\ z\ direction$$

$$= -(\rho_v w_v)\Delta x\Delta y - \left[(\rho_v w_v) + \frac{\partial(\rho_v w_v)}{\partial z}\Delta z\right]\Delta x\Delta y \qquad (C.301)$$

Similar to previous governing equations the rate of change of vapor mass within the control volume can be expressed in terms of vapor density can be expressed as,

$$Rate\ of\ vapor\ mass\ change\ in\ C.V.\ due\ to\ accumulation$$
$$= \frac{\partial \rho_v}{\partial t} \Delta x \Delta y \Delta z \qquad (C.302)$$

In addition to the rate of mass change in the control volume due to accumulation, there is another contribution to the rate of mass change of vapor species in the control volume. This extra contribution stems from the adsorption or desorption since the vapor species is assumed to be the only adsorbing species. The rate of change of vapor mass within the control volume due to adsorption can be defined as rate of change of adsorbed mass as,

$$Rate\ of\ vapor\ mass\ change\ in\ C.V.\ due\ to\ adsorption\ or\ desorption$$
$$= (1-\varepsilon_t)\rho_s \frac{\partial X}{\partial t}\ \Delta x \Delta y \Delta z \qquad (C.303)$$

As a reminder it should be noted that X is named as adsorption capacity and equal to the mass of adsorbed amount per unit mass of adsorbent. The time rate of change adsorption capacity will be positive or negative in case of adsorption or desorption. The contribution of adsorption is only accounted in the mass transport equation of vapor species. For the mass transport of equation the effect of adsorption is discarded since air is assumed to be non-adsorbing species in this study. The mass transport equation for the vapor species can be obtained by using the expressions given above as follows,

$$\frac{\partial \rho_v}{\partial t} + (1-\varepsilon_t)\rho_s \frac{\partial X}{\partial t} + \frac{\partial (\rho_v u_v)}{\partial x} + \frac{\partial (\rho_v v_v)}{\partial y} + \frac{\partial (\rho_v w_v)}{\partial z} = 0 \qquad (C.304)$$

The equation can be also written by using the velocity vector of the vapor species as,

$$\frac{\partial \rho_v}{\partial t} + (1 - \varepsilon_t)\rho_s \frac{\partial X}{\partial t} + \boldsymbol{\nabla}(\rho_v \mathbf{v_v}) = 0 \qquad (C.305)$$

At this point the density and velocity of the vapor species need to be represented by using the available mixture quantities since solving additional conservation equations will only impose extra complexity into the mathematical modeling problem. In the previous parts the relations between mixture and species quantities were given. According to these relations the density of vapor species in the mixture can be expressed in terms of mixture density and mass fraction of vapor as,

$$\rho_v = \omega_v \rho_g \qquad (C.306)$$

In Equation C.306, ω_v represents the mass fraction of vapor in the mixture.
The second concern is to express the vapor species velocity in terms of known quantities. Since the solution of momentum conservation equation will give the velocity distribution of the gas phase which contains both air and vapor, the vapor species velocity need to be related with this parameter. The velocity of the mixture (gas phase) will be equal to the mass averaged velocity of the species which can be written as,

$$\mathbf{V_g} = \omega_v \mathbf{v_v} + \omega_a \mathbf{v_a} \qquad (C.307)$$

To obtain a relation between mass averaged velocity and the species velocity, the Fick first law of diffusion which defines the transport of species in a mixture due to molecular motions, will be utilized. According to the Fick's first law of diffusion the molecular mass flux of a species for a binary mixture is expressed as [63],

$$\mathbf{j_v} = \rho_v(\mathbf{v_v} - \mathbf{V_g}) = -\rho_g D_{va} \boldsymbol{\nabla} \omega_a \qquad (C.308)$$

In Equation C.308 $\mathbf{j_v}$ represents the molecular mass flux and represents the diffusivity. The term in the parentheses is referred as diffusion velocity of the vapor phase. Since there is also solid phase exists in the control volume mass diffusivity value need to be redefined to account for the molecular mass flux in porous packed bed. The equivalent diffusivity value for the porous packed bed is defined by Nield and Bejan [75] as,

$$D_{vaeq} = \varepsilon_t D_{va} \qquad (C.309)$$

In addition to this definition it had been stated by Bird et al.[63] the mass diffusivity value both species in a binary mixture will be identical which means,

$$D_{va} = D_{av} \qquad (C.310)$$

By using Equation C.310 it is possible to obtain and expression for the vapor species velocity as,

$$\frac{\rho_v}{\rho_g}(\mathbf{v_v}) = \left(\frac{\rho_v}{\rho_g}\mathbf{V_g} - \mathfrak{D}_{va}\boldsymbol{\nabla}\omega_v\right) \qquad (C.311)$$

$$\rho_v(\mathbf{v_v}) = \rho_g\left(\omega_v\mathbf{V_g} - \mathfrak{D}_{va}\boldsymbol{\nabla}\omega_v\right) \qquad (C.312)$$

Substituting Equation C.312 into Equation C.305 will yield the final form of the mass transport equation for the vapor species,

$$\frac{\partial\left(\rho_g\omega_v\right)}{\partial t} + (1-\varepsilon_t)\rho_s\frac{\partial X}{\partial t} + \boldsymbol{\nabla}.\left(\rho_g\omega_v\mathbf{V_g}\right) = \boldsymbol{\nabla}.\left(\rho_g\mathfrak{D}_{vaeq}\boldsymbol{\nabla}\omega_v\right) \qquad (C.313)$$

C.3.5.1 Mass Transport Equation for Air Based on LTE Approach

The derivation procedure for the mass transport equation for air species will also be the same except the effect of adsorption. As mentioned previously air is assumed to be non-adsorbing and for this reason there will not be any term representing the rate of change of air mass in the control volume as a result of adsorption or desorption. Thus the mass transport equation can be written by discarding the second term on the left hand side of Equation C.313.

$$\frac{\partial(\rho_g \omega_a)}{\partial t} + \boldsymbol{\nabla}.(\rho_g \omega_a \mathbf{V_g}) = \boldsymbol{\nabla}.(\rho_g \mathfrak{D}_{aveq} \boldsymbol{\nabla} \omega_a) \qquad (C.314)$$

APPENDIX D

MESH INDEPENDENCE STUDY OF NUMERICAL ANALYSES

The independence of the solved quantities from the number of grid elements is demonstrated with the comparison made on the time variation of integrated surface heat flux at the HTT-packed bed interface. The interface which is used for integration of the heat flux can be seen in Figure D.1 for Bed Design 1 and Bed Design 2.

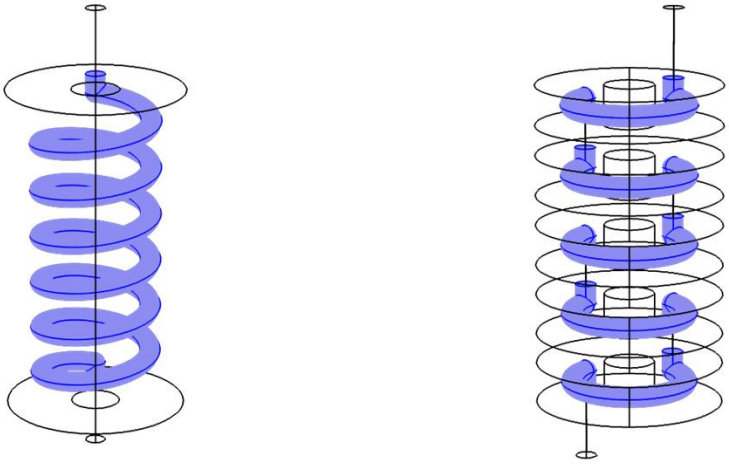

Figure D.1 The HTT-Packed Bed interface where, surface heat flux is integrated

The results obtained by using medium mesh density had been presented in the previous chapters. Therefore the mesh density that had been used in the numerical analyses of this study is labeled as “medium”. Coarser and finer computational grids

are also used for demonstrating the effect of mesh density on the numerical solutions. The results obtained from coarser grid are labeled as “coarse” while the results obtained from finer grid is labeled as “fine”. The time variations of the integrated heat flux values are given in comparison for all the bed designs and modeling approaches. The analysis conditions and the number of mesh elements used in the mesh independence study is tabulated in Table D.1.The maximum number of elements used in the mesh independence study is restricted with the available computer resources.

Table D.1 The analysis conditions and number of mesh element used in the grid independence study.

		Number of Mesh Elements			
	Modeling Approach	Coarse	Medium	Fine	Analysis Conditions
Bed Design 1	LTE	350450	659429	1215242	Experiment 1
	LTNE	659429	1195841	161378	Experiment 1
Bed Design 2	LTE	244287	585623	1052711	Experiment 1
	LTNE	585623	1065634	1528632	Experiment 1

The time variation of the integrated heat flux at the HTT-packed bed interface can be seen for different mesh densities at the figures below. The integral that had been calculated for the comparison purpose can be expressed for LTE and LTNE based models respectively as,

$$\int_{A_{interface}} -\boldsymbol{n} \cdot (k_{eq} \boldsymbol{\nabla} T_{gs})\, dA = \dot{q} \qquad (D.1)$$

$$\int_{A_{interface}} -\boldsymbol{n} \cdot (k_{seq} \boldsymbol{\nabla} T_{s})\, dA = \dot{q} \qquad (D.2)$$

In the LTNE based numerical solutions solid phase temperature is used for heat flux calculation. In LTE based models since there is single temperature variable exists for the heat flux is calculated by using that temperature variable. The area of integration is equal to the area of the interface between HTT and packed bed.

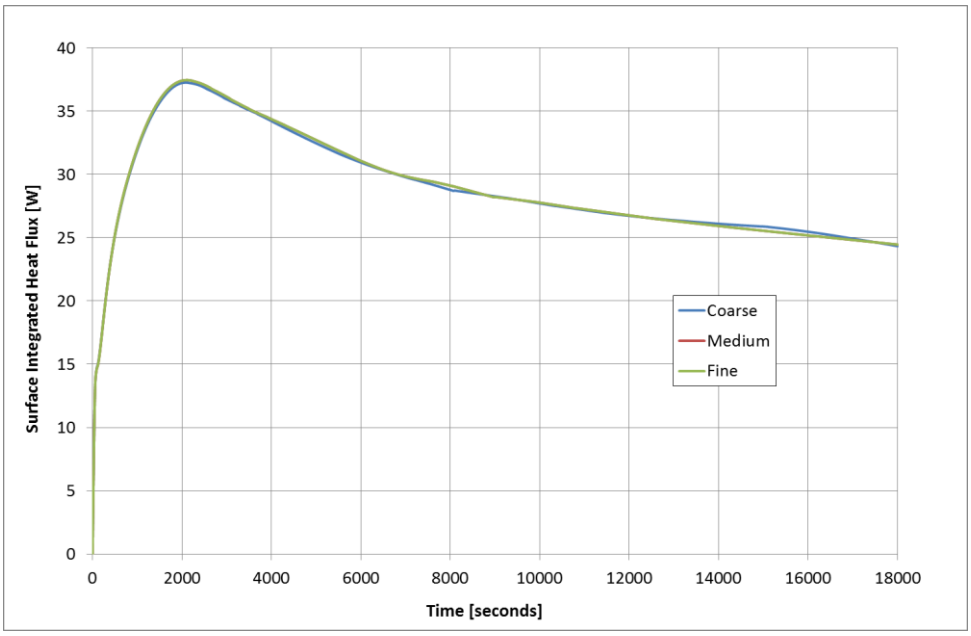

Figure D.2 The variation of integrated surface heat flux with time for the Bed Design 1 obtained from LTE based model for different number of mesh elements.

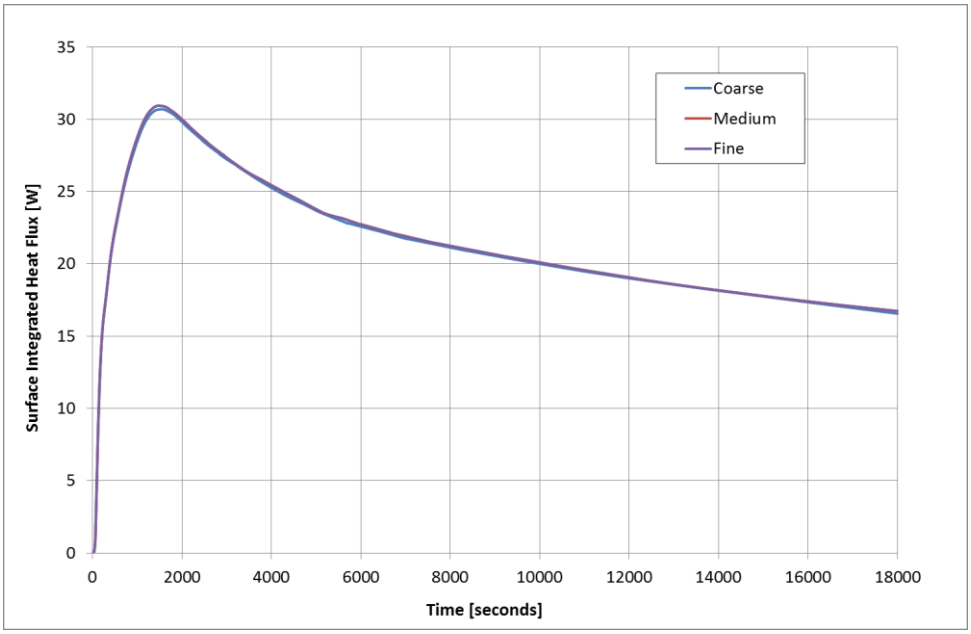

Figure D.3 The variation of integrated surface heat flux with time for the Bed Design 2 obtained from LTE based model for different number of mesh elements.

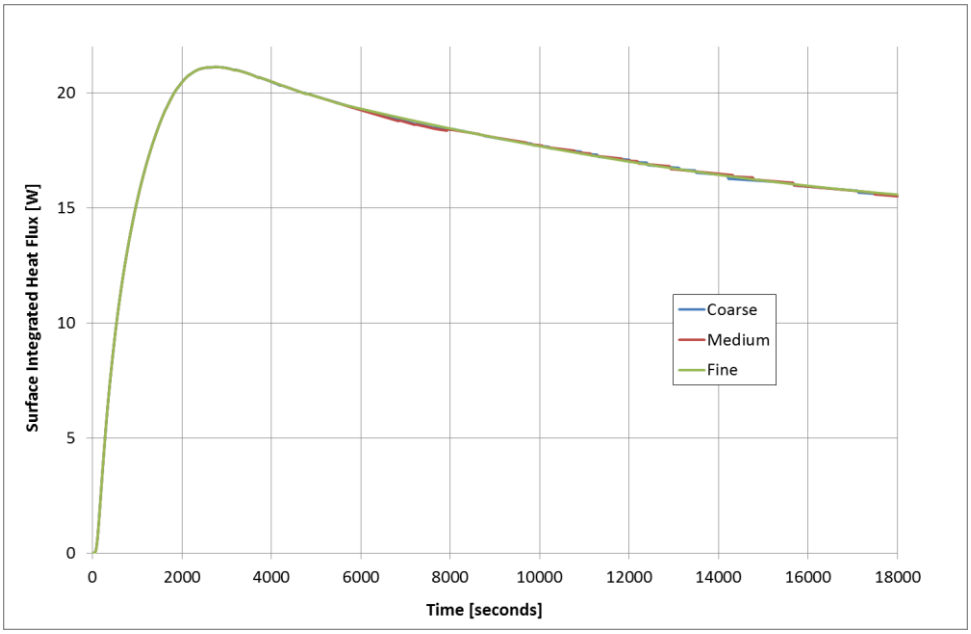

Figure D.4 The variation of integrated surface heat flux with time for the Bed Design 1 obtained from LTNE based model for different number of mesh elements.

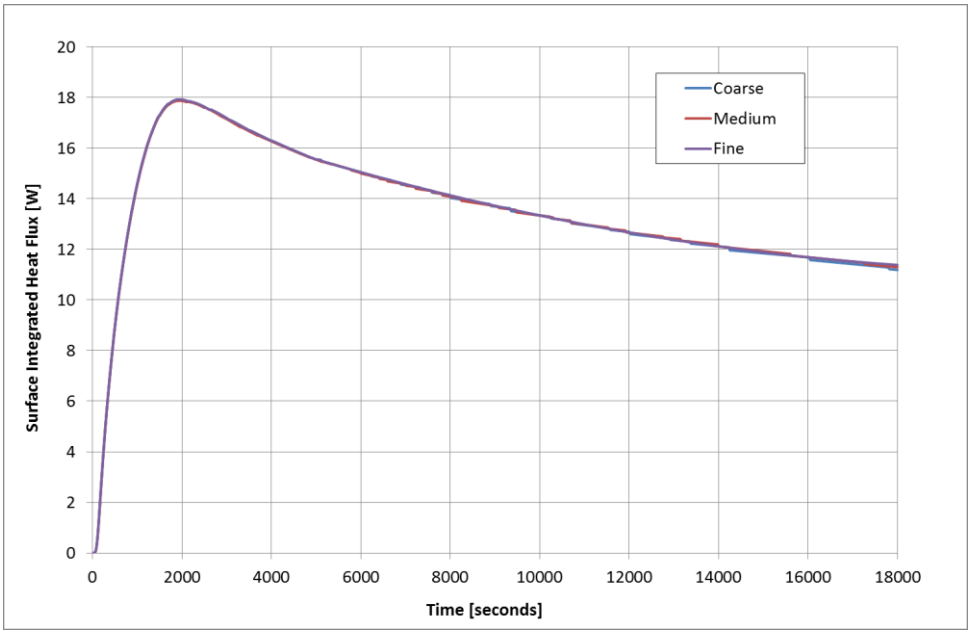

Figure D.5 The variation of integrated surface heat flux with time for the Bed Design 2 obtained from LTNE based model for different number of mesh elements.

Regarding the comparisons made for the time variation of the integrated heat flux values at the HTT packed bed interface, no significant difference could be observed for the analyses performed by using different number of mesh elements. The differences for the time variation of the integrated heat flux between coarse, medium and fine mesh solutions is less than 1.5 % for all cases and modeling approaches during 18000 seconds. Therefore to reduce the run time and obtain reasonable spatial resolution the medium mesh density solutions had been performed for the numerical analayses. As stated earlier, upper limit for the number of mesh elements used in the grid independence study is imposed by the available computational resources.

APPENDIX E

UNCERTAINITY ANALYSIS OF THE EXPERIMENTAL RESULTS

The uncertainty for the measured values during experimentation can be calculated by using the Gauss error propagation law. The measured value can be treated as a function of independent variables as, $y=f(x_1,x_2,..x_n)$. Here y is the measured value and y can be calculated by using independent variables x. Therefore according to law of error propagation, the uncertainty value for the measured value y, can be related with the uncertainty of the independent variables x as follows,

$$w_y = \left[\left(\frac{\delta y}{\delta x_1} w_1\right)^2 + \left(\frac{\delta y}{\delta x_2} w_2\right)^2 + \cdots \left(\frac{\delta y}{\delta x_n} w_n\right)^2\right]^{\frac{1}{2}} \qquad (E.1)$$

In Equation E.1 w_y is the uncertainty of the measured value y while, w_1, $w2$ and w_n are the uncertainty values associated with the independent variables x.

The uncertainty of the temperature measurements can be expressed as a combination of with the uncertainty associated with thermocouples, data logger and the sensor connections. The uncertainty associated with thermocouples of type T and K is taken as ± 0.5 ^oC. The error associated with data logger for temperature measurements is ±0.02 ^oC. Similarly the uncertainty associated with connections on the temperature measurements is ± 0.1 ^oC. As a result uncertainty for temperature measurements can be calculated as follows,

$$w_T = [(0.5)^2 + (0.02)^2 + (0.1)^2]^{\frac{1}{2}} = 0.51 \qquad (E.2)$$

The uncertainty for the temperature measurements in the experiments is calculated as ±0.51 ºC.

The uncertainty for the pressure measurements also associated with the same kind of independent variables. The uncertainty values associated with the pressure transducers at a mean measured pressure of 42 mbar is approximately 0.5 mbar. The uncertainty associated with data logger and sensor connections are 0.15 mbar and 0.1 mbar respectively. As a result the uncertainty of the pressure measurements can be calculated as,

$$w_T = [(0.5)^2 + (0.15)^2 + (0.1)^2]^{\frac{1}{2}} = 0.53 \qquad (E.2)$$

According to the error propagation law the uncertainty value for the pressure measurements is ±0.53 mbar.

Another quantity that had been measured during experiments is the volumetric flow rate of the HTF. The volume of HTF flow during a 18000 seconds long experiment is 9 liters with an uncertainty of ± 0.05 liters. The time of experiments are measured to be 18000 ± 0.5 seconds. The uncertainty of the volumetric flow rate measurements can be expressed as a function of uncertainty values associated with volume and time as,

$$w_{\dot{V}} = \left[\left(\frac{\delta \dot{V}}{\delta V} w_V\right)^2 + \left(\frac{\delta \dot{V}}{\delta t} w_t\right)^2\right]^{\frac{1}{2}} \qquad (E.3)$$

In Equation E.3 the first and second terms can be expressed as follows,

$$\frac{\delta \dot{V}}{\delta V} = \frac{V}{t}\frac{1}{V} = 0.000556 \qquad (E.4)$$

$$\frac{\delta \dot{V}}{\delta V} = \frac{V}{t}\frac{1}{t} = 0.000000028 \qquad (E.5)$$

$$w_{\dot{V}} = [(0.000556 \cdot 0.05)^2 + (0.000000028 \cdot 0.5)^2]^{\frac{1}{2}} = 0.0000278 \qquad (E.6)$$

The uncertainty associated with the volumetric flow rate measurements is calculated as ± 0.0000278 liters/min.

APPENDIX F

HTF INLET TEMPERATURE ANALYSIS AT THE VACUUM CHAMBER CAP

The vacuum chamber used in the experimental investigations is a massive structure manufactured from stainless steel. The cap of the vacuum chamber is required to be in physical contact with the HTT of the adsorbent bed for assuring the vacuum sealing. However this physical contact also involves in a heat exchange relationship between HTT and the vacuum chamber cap. The HTF temperature is measured at a location different than the location that is used for defining the inlet conditions in numerical analyses of the bed designs. Therefore to determine the deviation of HTF temperature between the measurement location and the inlet boundary used in the numerical analyses a more detailed sub model of the HTT and the vacuum chamber cap is prepared. Using this sub model the effect of vacuum chamber cap on the HTF temperatures tried to be determined. The obtained mass weighted average HTF temperature values are used in the three dimensional numerical analyses which are simulating the experimental conditions. The model used in the analysis can be seen in Figure F.1

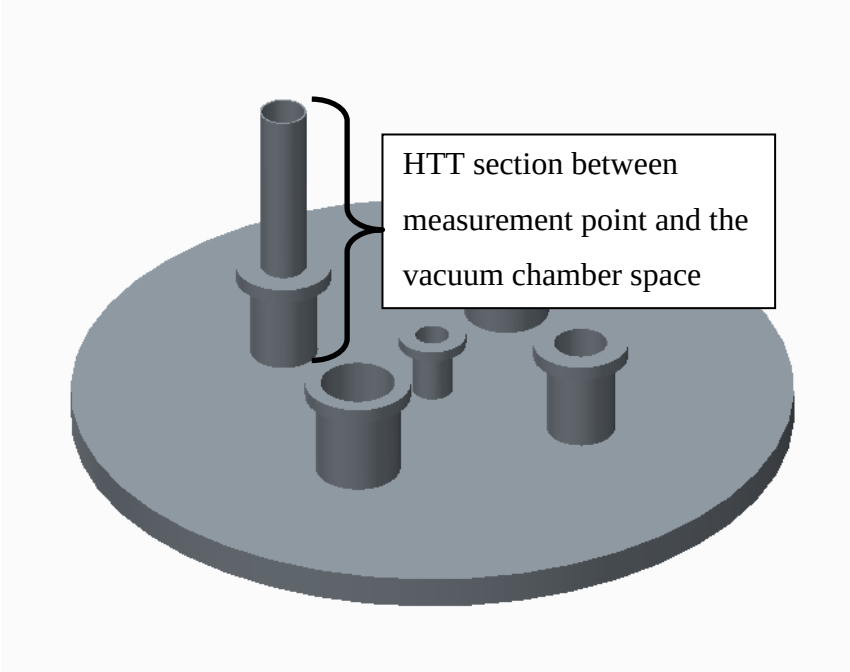

Figure F.1 The CAD data used in the sub model analyses

The mesh used in the analysis of sub model for the vacuum chamber cap and the HTT can be seen in Figure F.2

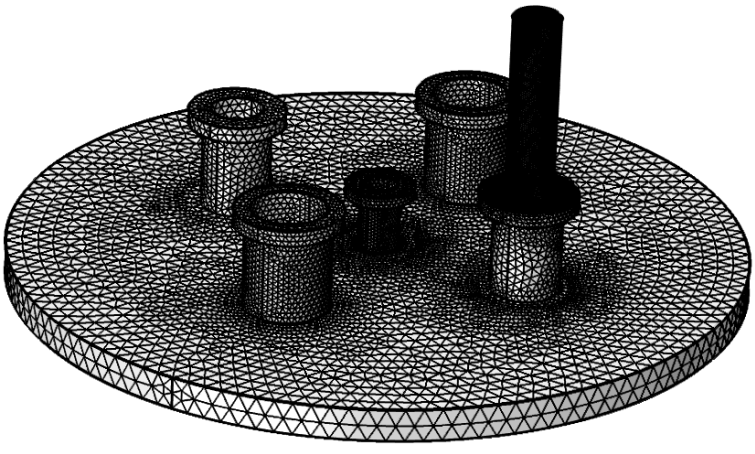

Figure F.2 The mesh used in the sub model analyses

The HTT thickness also meshed and conduction in the HTT solid domain is solved together with the HTF flow inside. At the same time HTT is in contact with the vacuum chamber cap. The bottom face and the inner surfaces of the ports on the cap is defined as insulated boundaries. Also the side surfaces of the HTT tube which were insulated in the real case, is defined to be insulated. At these boundaries heat flux is defined to be equal to zero. The insulation boundaries of the numerical model can be seen in Figure F.3.

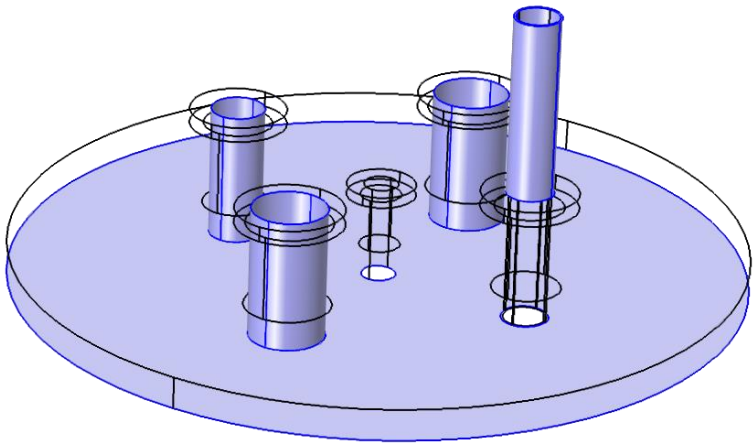

Figure F.3 Boundaries at which zero heat flux is defined

The air surrounding the top surfaces of the cap had not been modeled for reducing the need for computational resources. The boundaries of the vacuum chamber cap facing to the ambient a constant heat flux value of 5 W/(m^2K) had been defined. The value is determined by using the estimated temperature of the cap and the correlation given in [154]. The boundaries at which a heat transfer coefficient defined can be seen in Figure F.4. The ambient temperature is assumed to be constant and equal to 20^{o}C in the analyses.

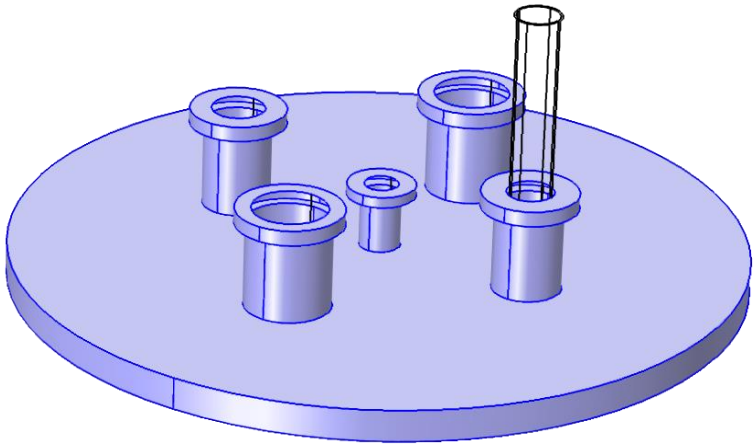

Figure F.4 The boundaries of the analysis model at which a heat transfer coefficient is defined.

The HTF inlet temperature and velocity is defined at the top section of the HTT in the model. This inlet boundary of the HTF is the HTF inlet temperature measurement location of the experimental setup. Therefore the temperature value measured in experiments is defined at this location. The outlet boundary for the HTF in the analyses is the section of the HTT which is at the bottom face of the cap. The outlet boundary for the HTF in the sub model analyses can be seen in Figure F.5.

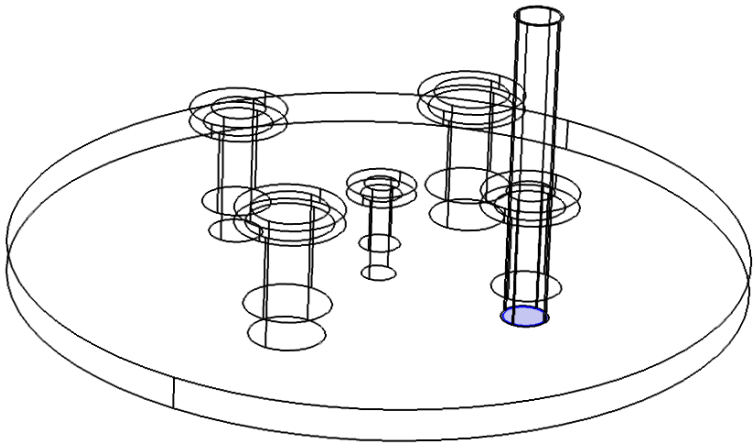

Figure F.5 Outlet boundary for the HTF domain in the analysis model

The analyses with this sub model is performed for each of the HTF velocity and HTF inlet temperature combinations to obtain the HTF inlet temperature values that will be used in the simulations of experiments. The HTF temperature values required for the desorption analyses are obtained by calculating the mean value of the mass weighted average of the HTF temperatures in time at the outlet surface shown above. The conditions analyzed and the obtained HTF temperatures can be seen in Table F.1

Table F.1 HTF temperature values that will be used in desorption analyses

		HTF Inlet Temperature [K]	HTF Inlet Velocity [m/s]	HTF Inlet Temperature Used in The Analysis [K]
Bed Design 1	Experiment 1	397	0.0012	384
	Experiment 2	397	0.002	388
	Experiment 3	370	0.002	364
	Experiment 4	394	0.002	385
Bed Design 2	Experiment 1	397	0.0012	384
	Experiment 2	390	0.002	381
	Experiment 3	370	0.002	364
	Experiment 4	390	0.002	381

The surface temperature contours obtained from the simulations of the conditions of Experiment 1 for Bed Design 1 can be seen in Figure F.6

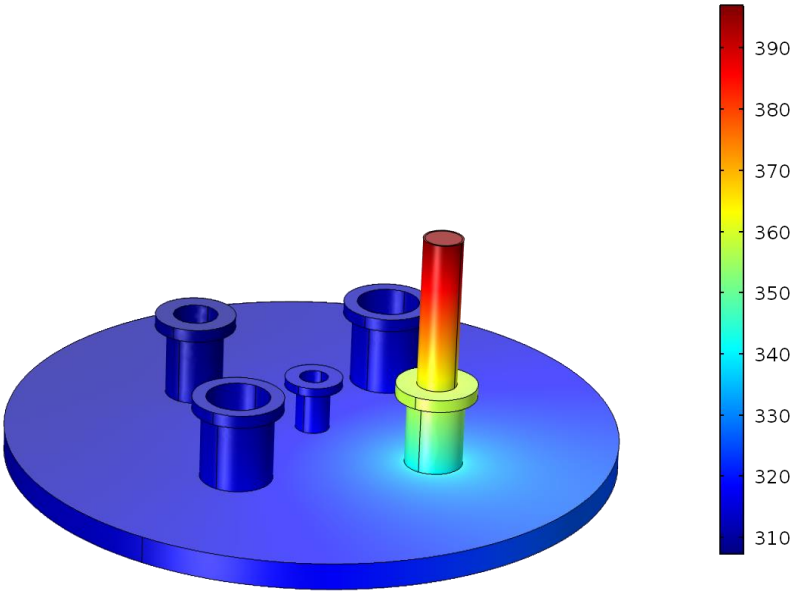

Figure F.6 Surface temperature contours obtained from sub-model analysis